



The
University
Of
Sheffield.

Modelling and Analysis of DC-DC
Converters for Bidirectional EV Charging
Applications

By:

Lais Farias Martins

A thesis submitted in partial fulfilment of the requirements for the
degree of Doctor of Philosophy

The University of Sheffield
Faculty of Engineering
Department of Electrical and Electronic Engineering

November 2019

Abstract

This thesis is focused on the modelling and analysis of DC-DC converter topologies used for bidirectional charging of electric vehicles. Bidirectional converters are used in vehicle-to-grid (V2G) systems to allow bidirectional power transfer between the vehicle and the grid. Following the investigation in the literature review of potential converter topologies used in V2G applications and modelling techniques, this research proposes the application of the cyclic-averaging method for analysis of the Dual Active Bridge, 4th order resonant CLLC converter, and series compensated Inductive Power Transfer (IPT) converter.

First, the cyclic-averaging method is applied for analysis of a phase-shift modulated Dual Active Bridge converter (DAB). For implementation of the cyclic analysis, the operation of the converter is first analysed using a Spice simulation to determine the system's operation modes and duty cycles. The cyclic-averaging model is validated against a Spice simulation and employed to predict the converter's output and to perform harmonic analysis of the inductor current.

Following the analysis of the DAB, a 4th order CLLC converter is evaluated considering frequency and phase-shift modulations. The cyclic-averaging model is derived to model the behaviour of the converter's output and state-variables in steady state. Additionally, a Fundamental Mode Approximation (FMA) model and a novel piecewise-linear state-variable model are also implemented for comparison. The models obtained are validated using Spice and, for the phase-shift modulated converter, experimental results.

Finally, the series compensated IPT converter is analysed considering operation under phase-shift modulation. A FMA model is derived and, using circuit transformation, the state-variable and cyclic-averaging models previously defined for the CLLC converter are adapted for the analysis of the IPT converter. A prototype is built for validation of the cyclic model.

Overall, for all converters analysed in this research, the cyclic-averaging method showed good performance with considerably fast execution and accuracy similar to Spice simulations.

List of publications

L. Farias Martins, D. A. Stone and M. P. Foster, "State-Variable and Cyclic-Averaging Analysis of Bidirectional CLLC Resonant Converters," The 10th International Conference on Power Electronics, Machines and Drives (PEMD 2018), 2018.

L. Farias Martins, D. A. Stone and M. P. Foster, "State-Variable and Cyclic-Averaging Analysis of Bidirectional CLLC Resonant Converters," in The Journal of Engineering, vol. 2019, no. 17, pp. 4364-4368, 6 2019.

L. Farias Martins, D. A. Stone and M. P. Foster, "Modelling of Bidirectional CLLC Resonant Converter Operating under Frequency Modulation," The IEEE Energy Conversion Congress and Exposition (ECCE 2019), 2019.

Manuscripts under preparation:

L. Farias Martins, D. A. Stone and M. P. Foster, "Modelling of Phase-Shift Modulated Bidirectional CLLC Resonant Converters", to be submitted to IET Power Electronics.

L. Farias Martins, D. A. Stone and M. P. Foster, "Analysis of Dual Active Bridge Converter Using Cyclic-Averaging", to be submitted to IEEE Transactions on Power Electronics.

L. Farias Martins, D. A. Stone and M. P. Foster, "Modelling and Analysis of Series-Compensated IPT Converter", to be submitted to IEEE Transactions on Power Electronics.

Acknowledgments

First, I would like to thank my supervisors Prof. David Stone and Prof. Martin Foster for all the support, guidance and patience throughout my studies. Many thanks to the EMD group colleagues and staff for the friendly and supportive environment.

A sincere acknowledgement to my family, especially my mother, and to the great friends I made in Sheffield. A special thanks to Alistair for all the encouragement and support through the good and bad times.

Finally, I would also like to thank the Brazilian National Council for Scientific and Technological Development (CNPq) for the financial support with the scholarship 201065/2015-0.

Table of Contents

Abstract	i
List of publications	ii
Acknowledgments	iii
Table of contents	iv
Acronyms	vii
List of Symbols	viii
List of Figures	xi
List of Tables	xviii
1 Introduction	1
1.1 Background and motivation.....	1
1.2 Thesis structure.....	3
1.3 References.....	5
2 Literature Review	6
2.1 Introduction.....	6
2.2 Bidirectional DC-DC converters.....	7
2.2.1 Dual Active Bridge.....	7
2.2.2 Resonant topologies.....	11
2.2.3 Wireless power transfer systems.....	15
2.3 Modelling techniques review.....	19
2.3.1 Fundamental Mode Approximation (FMA).....	19
2.3.2 State-variable.....	20
2.3.3 Cyclic-averaging.....	22
2.4 Conclusions.....	30
2.5 References.....	31
3 Cyclic-Averaging Analysis of Dual Active Bridge Converter	40
3.1 Introduction.....	40
3.2 State-variable description.....	41
3.3 Cyclic-averaging analysis.....	45
3.4 Simulation results.....	49
3.5 Conclusions.....	56
3.6 References.....	57

4 Modelling of Frequency Modulated CLLC Converter	58
4.1 Introduction	58
4.2 Operation.....	59
4.3 Fundamental Mode Approximation (FMA).....	59
4.4 State-variable model.....	64
4.4.1 Implementation in Simulink	70
4.5 Cyclic-averaging model	73
4.5.1 Estimation of duty cycle	79
4.6 Case study	82
4.7 Simulation results.....	85
4.8 Conclusions	91
4.9 References	92
5 Modelling of Phase-shift Modulated CLLC Converter.....	93
5.1 Introduction	93
5.2 Phase-shift modulation technique	93
5.3 Fundamental Mode Approximation (FMA).....	95
5.4 State-variable analysis.....	98
5.4.1 Implementation in Simulink	102
5.5 Cyclic-averaging analysis	104
5.6 Design and simulation.....	112
5.6.1 Converter design	112
5.6.2 Simulation results.....	117
5.7 Conclusions	128
5.8 References	129
6 CLLC Converter Design and Prototype.....	131
6.1 Introduction	131
6.2 Converter design	132
6.2.1 Switching circuit.....	132
6.2.2 PCB: Deadtime, gate driver and H-bridge circuits	135
6.2.3 Resonant tank design	137
6.2.4 Load	141
6.3 Experimental results.....	142
6.4 Conclusions	157

6.5	References	158
7	CLLC Converter Design and Prototype	159
7.2	Fundamental Mode Approximation (FMA) applied to inductive power transfer ...	160
7.3	State-variable and cyclic-averaging analysis	163
7.4	Simulation results	164
7.4.1	Converter design based on FMA model	164
7.4.2	Verification of FMA model	165
7.4.3	Verification of state-variable and cyclic-averaging method	169
7.5	Magnetics design of coil pad structures	172
7.6	Experimental results	183
7.6.1	Construction of coil pad structures	183
7.6.2	Evaluation of converter operation	192
7.7	Conclusions	203
7.8	References	204
8	Conclusions and Further Work	205
8.1	Conclusions	205
8.2	Further work	208
8.3	References	209
	Appendix A.1	210
	Appendix A.2	213

Acronyms

AC	- Alternating Current
BBP	- Bipolar Pad
CPS	- Conventional Phase-Shift
DAB	- Dual Active Bridge
DBSRC	- Dual-Bridge Series Resonant Converter
DC	- Direct Current
DDP	- Double D Pad
DDQP	- Double D Quadrature Pad
DPS	- Dual Phase-Shift
EPS	- Extended Phase-Shift
EV	- Electric vehicle
FEA	- Finite Element Analysis
FMA	- Fundamental Mode Approximation
GaN	- Gallium Nitride
IPT	- Inductive Power Transfer
MOSFET	- Metal Oxide Semiconductor Field-Effect Transistor
PCB	- Printed Circuit Board
PPM	- Pulse-Phase Modulation
RCFMA	- Rectifier Compensated Fundamental Mode Approximation
RMS	- Root Mean Square
RTFMA	- Rectifier Transformed Fundamental Mode Approximation
SiC	- Silicon Carbide
SPS	- Single Phase-Shift
SRDAB	- Series Resonant Dual Active Bridge
TPS	- Triple Phase-Shift
V2G	- Vehicle-to-grid
WPT	- Wireless Power Transfer
ZCS	- Zero-Current Switching
ZVS	- Zero-Voltage Switching

Symbol list

ϕ	- Phase shift angle between primary and secondary bridge voltages
α_1	- Phase shift angle between the two legs of bridge 1
α_2	- Phase shift angle between the two legs of bridge 2
α_{ratio}	- Normalized phase shift angle between the bridge legs
k	- Coupling coefficient or coupling factor
M	- Mutual inductance
n	- Transformer's turns ratio
DC_{Gain}	- DC gain of transfer function
L_s	- Series inductance of Dual Active Bridge converter
L_{s1}	- Primary series inductance
L_1	- Primary coil self-inductance
L_2	- Secondary coil self-inductance
L_m	- Magnetizing branch inductance
C_{s1}	- Primary series capacitance
C_{s2}	- Secondary series capacitance
C'_{s2}	- Secondary series capacitance reflected to primary
C_i, C_f	- Filter capacitors
r_{dc}	- DC bus series resistance
r_{bat}	- Battery series resistance
r_{SWITCH}	- Switching device resistance
r_d	- Diode forward-biased resistance
r_{Ls1}	- Series inductor resistance
r_{Lm}	- Magnetizing inductor resistance
r_{Cs1}	- Primary capacitor resistance
r_{C2}	- Secondary capacitor resistance
r_1, r_2	- Primary and secondary series resistances
r_2'	- Secondary series resistance reflected to primary
r_{Cf}, r_{Ci}	- Filter capacitors resistance
R_{eq}	- Equivalent load resistance
R_{load}	- Load resistance
X_n	- Base reactance

X_{L1}	- Reactance of primary series inductor
X_{C1}	- Reactance of primary series capacitor
X_{Lm}	- Reactance of magnetizing inductor
$X_{C2'}$	- Reactance of secondary series capacitor reflected to primary
v_1	- Output voltage of bridge 1
v_2	- Output voltage of bridge 2
v_i	- Input voltage of resonant tank for FMA analysis
$v_{i,FMA}$	- Fundamental component of input voltage of resonant tank
$V_{i,RMS}$	- RMS input voltage of resonant tank
v_o	- Output voltage of resonant tank for FMA analysis
$v_{o,FMA}$	- Fundamental component of output voltage of resonant tank
$V_{o,RMS}$	- RMS output voltage of resonant tank
v_{Cf}, v_{Ci}	- Filter capacitors voltage
v_L	- Inductor voltage for DAB converter
v_{Ls1}	- Primary series inductor voltage
v_{Lm}	- Primary magnetizing inductor voltage
v_{Cs1}	- Primary capacitor voltage
v_{Cs2}	- Secondary capacitor voltage
V_{bat}	- Battery voltage
V_{dc}	- DC bus voltage
V_d	- Diode forward voltage
V_{out}	- Output voltage of converter
I_{out}	- Output current of converter
i_L	- Current through inductor for DAB converter
i_{Ls1}	- Current through series inductor
i_{Lm}	- Current through magnetizing inductor
i_{Cs1}	- Current through primary capacitor
i_{Cs2}	- Current through secondary capacitor
i_{Cf}, i_{Ci}	- Current through filter capacitors
i_{bridge}	- Input current to slow subsystem
i_{rect}	- Current through bridge rectifier
I_1	- Primary current phasor
I_2	- Secondary current phasor referred to primary

I_{sec}	- Secondary current phasor
I_m	- Phasor of current through magnetizing branch
P_{out}	- Converter output power
ω_n	- Normalized frequency
ω_r	- Angular resonant frequency
ω_{sr}	- Angular series resonant frequency
ω_{sw}	- Angular switching frequency
f_s	- Switching frequency
f_{sr}	- Series resonant frequency
f_{li}	- Frequency at load independent point
Q_1	- Quality factor
g	- Capacitance ratio
h	- Inductance ratio
$x(t)$	- State-vector at time t
$z(t)$	- Augmented state-vector at time t
A_i	- State-variable dynamic matrix for the i^{th} operation mode
B_i	- State-variable input matrix for the i^{th} operation mode
\hat{A}_i	- Augmented state-variable system matrix for the i^{th} operation mode
\tilde{A}_i	- Augmented state-variable system matrix for averaging calculation
$\hat{\Phi}_{tot}$	- Augmented state-variable system matrix for period of operation
$x(t_0)$	- State-vector initial condition
$z(t_0)$	- Augmented state-vector initial condition
x_{avg}	- Averaged state-vector
c_k	- Fourier coefficient vector for the k^{th} harmonic
\hat{c}_k	- Augmented Fourier coefficient vector for the k^{th} harmonic
$\delta_k(t)$	- State-vector of fictitious system for harmonic calculation
$\hat{A}_{i,k}$	- Augmented state-variable system matrix for fictitious system
d_i	- Normalized time interval, or duty cycle, for operation mode i
T	- Time period of a cycle

List of Figures

Figure 1.1: Typical V2G system.....	2
Figure 2.1: Typical vehicle-to-grid system.....	7
Figure 2.2: Wireless charging system.....	7
Figure 2.3: Dual Active Bridge converter	8
Figure 2.4: Diagrams for (a) Single Phase-Shift modulation (b) Extended Phase-Shift modulation and (c) Dual Phase-Shift or Triple Phase-Shift modulation	10
Figure 2.5: Resonant tank of Series-Resonant Dual Active Bridge converter	12
Figure 2.6: Resonant tank of LLC converter	13
Figure 2.7: Resonant tank of CLLC converter	14
Figure 2.8: IPT converter.....	16
Figure 2.9: LC-series compensation circuit.....	16
Figure 2.10: LC-parallel compensation circuit.....	16
Figure 2.11: LCL compensation circuit.....	17
Figure 2.12: Pad structures comparison: (a) Double D pad (DDP), (b) Double D Quadrature pad (DDQP) and (c) Bipolar pad (BPP)	18
Figure 3.1: Dual Active Bridge converter	40
Figure 3.2: Single Phase-Shift (SPS) modulation, forward mode	41
Figure 3.3: Equivalent circuits for DAB converter in (a) forward mode and (b) reverse mode.....	42
Figure 3.4: Typical waveforms of bridge voltages for DAB converters operating in (a) forward mode and (b) reverse mode	45
Figure 3.5: Simulation results for SPS modulation (a) forward mode and (b) reverse mode.....	51
Figure 3.6: Bridge voltages and inductor current in forward operation for (a) $\phi = 90^\circ$ and (b) $\phi = 45^\circ$	51
Figure 3.7: Bridge voltages and inductor current in reverse operation for (a) $\phi = 90^\circ$ and (b) $\phi = 45^\circ$	53
Figure 3.8: Inductor current waveform from (a) Spice (b) cyclic method with 1 st , 3 rd and 5 th harmonics considered and (c) cyclic method with 1 st , 3 rd , 5 th , 7 th and 9 th harmonics considered.....	55
Figure 4.1: CLLC topology	59

Figure 4.2: Equivalent circuit for FMA analysis in forward mode, referred to primary .. 60

Figure 4.3: Equivalent circuit for FMA analysis in reverse mode, referred to primary ... 60

Figure 4.4: Equivalent circuit for state-variable analysis, forward mode..... 64

Figure 4.5: DC voltage gain versus switching frequency for CLLC converter in forward operation 66

Figure 4.6: Typical bridge voltages and rectifier current in forward mode (a) $f_{sw} \geq f_{li}$ (b) $f_{sw} < f_{li}$ 67

Figure 4.7: Equivalent circuit during non-conduction mode, forward operation 67

Figure 4.8: Equivalent circuit for state-variable analysis, reverse mode..... 68

Figure 4.9: Equivalent circuit during non-conduction mode, reverse operation 69

Figure 4.10: Fast subsystem, forward mode 71

Figure 4.11: Slow subsystem, forward mode 72

Figure 4.12: Rectifier and coupling equations, forward mode 72

Figure 4.13: Typical voltage and current sequence for operation in region I, forward mode..... 75

Figure 4.14: Typical voltage and current sequence for operation in region II, forward mode..... 76

Figure 4.15: Typical voltage and current sequence for operation in region I, reverse mode 78

Figure 4.16: Typical voltage and current sequence for operation in region II, reverse mode..... 78

Figure 4.17: Battery current versus battery voltage for forward operation 83

Figure 4.18: DC link current versus battery voltage for reverse operation 84

Figure 4.19: DC voltage gain versus switching frequency for converter operating in (a) forward mode and (b) reverse mode 85

Figure 4.20: Switching frequency for different battery voltage operation points for (a) forward and (b) reverse operation..... 87

Figure 4.21: Waveforms comparison for (a) State-variable and (b) Spice simulations in forward mode and $V_{bat} = 350V$ 89

Figure 4.22: Waveforms comparison for (a) State-variable and (b) Spice simulations in reverse mode and $V_{bat} = 350V$ 90

Figure 5.1: CLLC topology 94

Figure 5.2: Bridge output voltages for (a) SPS modulation, operating in reverse mode and (b) PPM modulation, operating in forward mode	95
Figure 5.3: Simplified circuit for FMA analysis, referred to primary	96
Figure 5.4: Equivalent circuit for state-variable analysis, forward mode.....	99
Figure 5.5: Equivalent circuit for state-variable analysis, reverse mode.....	100
Figure 5.6: Definition of bridge voltages, forward mode	102
Figure 5.7: Coupling equation, forward mode.....	102
Figure 5.8: Slow subsystem, forward mode	103
Figure 5.9: Fast subsystem, forward mode	103
Figure 5.10: Typical bridge voltage and current sequence for SPS operation in (a) forward mode and (b) reverse mode	106
Figure 5.11: Typical bridge voltage and current sequence for PPM operation and $90^\circ \leq \alpha \leq 180^\circ$ in (a) forward mode and (b) reverse mode.....	107
Figure 5.12: Typical bridge voltage and current sequence for PPM operation and $\alpha < 90^\circ$ in (a) forward mode and (b) reverse mode.....	107
Figure 5.13: Final circuit for simulation of CLLC converter	113
Figure 5.14: Output power versus α_1 and α_2 for (a) $\phi = 90^\circ$ (b) $\phi = 22.5^\circ$	117
Figure 5.15: Primary current magnitude versus α_1 and α_2 for (a) $\phi = 90^\circ$ (b) $\phi = 22.5^\circ$	118
Figure 5.16: Secondary current magnitude versus α_1 and α_2 for (a) $\phi = 90^\circ$ (b) $\phi = 22.5^\circ$	118
Figure 5.17: Magnetizing branch current magnitude versus α_1 and α_2 for (a) $\phi = 90^\circ$ (b) $\phi = 22.5^\circ$	118
Figure 5.18: Output power for (a) FMA and (b) Spice simulations	119
Figure 5.19: Primary current for (a) FMA and (b) Spice simulations	120
Figure 5.20: Secondary current for (a) FMA and (b) Spice simulations	120
Figure 5.21: Magnetizing branch current for (a) FMA and (b) Spice simulations.....	120
Figure 5.22: Efficiency from Spice simulation.....	122
Figure 5.23: Simulation results for SPS modulation (a) forward mode and (b) reverse mode.....	123
Figure 5.24: Simulation results for PPM modulation (a) forward mode and (b) reverse mode.....	124

Figure 5.25: Waveform comparison for α ratio = 0.25 (a) state-variable and (b) Spice, forward mode	126
Figure 6.1: Simplified block diagram for prototype construction	131
Figure 6.2: Switching circuit diagram	132
Figure 6.3: Inverting circuit	132
Figure 6.4: Implementation of 90 degrees phase-shift, Ch2_count = 52	134
Figure 6.5: Implementation of 180 degrees phase-shift, Ch1_count = 104.....	134
Figure 6.6: Implementation of angles greater than 180 degrees phase-shift, Ch0_count = 0 , Ch3_count = 104 and Inv_flag = 1	134
Figure 6.7: Implementation of CLLC converter	135
Figure 6.8: Deadtime circuit	136
Figure 6.9: Gate driver circuit.....	136
Figure 6.10: Resonant tank	137
Figure 6.11: Inductor non-ideal model	138
Figure 6.12: Series resistance of inductor in function of frequency	139
Figure 6.13: Capacitor non-ideal model	140
Figure 6.14: Transformer non-ideal model.....	141
Figure 6.15: Load resistor for forward operation	142
Figure 6.16: Experimental set-up.....	145
Figure 6.17: Resonant tank circuits employed for (a) Spice simulation and (b) cyclic-averaging simulation.....	146
Figure 6.18: Spice, cyclic-averaging and prototype results comparison for (a) PPM modulation and (b) SPS modulation in forward operation	147
Figure 6.19: Spice, cyclic-averaging and prototype results comparison for (a) PPM modulation and (b) SPS modulation in reverse operation	147
Figure 6.20: CLLC converter circuit	148
Figure 6.21: Drain source voltages for 10° phase-shift test case in forward mode	148
Figure 6.22: Inductor equivalent circuit for cyclic-averaging implementation	149
Figure 6.23: Secondary capacitor equivalent circuit for cyclic-averaging implementation	149
Figure 6.24: Optimized Spice, cyclic-averaging and prototype results comparison for (a) PPM modulation and (b) SPS modulation in forward operation	150

Figure 6.25: Optimized Spice, cyclic-averaging and prototype results comparison for (a) PPM modulation and (b) SPS modulation in reverse operation	151
Figure 6.26: Comparison between (a) Spice and (b) experimental results for the primary current	152
Figure 6.27: Comparison between (a) Spice and (b) experimental results for the secondary current.....	152
Figure 6.28: Comparison between (a) Spice and (b) experimental results for the primary capacitor voltage	152
Figure 6.29: Comparison between (a) Spice and (b) experimental results for the secondary capacitor voltage.....	153
Figure 7.1: Series compensated IPT converter	159
Figure 7.2: Equivalent circuits for series compensated IPT converter with (a) coupled inductors representation and (b) T-model representation	160
Figure 7.3: Equivalency between series compensated IPT converter and CLLC converter	163
Figure 7.4: Spice and FMA results for RMS value of primary current in function of (a) coupling coefficient and (b) self-inductance	166
Figure 7.5: Spice and FMA results for secondary current in function of (a) coupling coefficient and (b) self-inductance	168
Figure 7.6: Spice and FMA results for output power in function of (a) coupling coefficient and (b) self-inductance	169
Figure 7.7: Equivalent circuits for Spice simulation (a) series compensated IPT converter and (b) CLLC equivalent circuit.....	170
Figure 7.8: Model comparison SPS modulation (a) forward operation and (b) reverse operation	171
Figure 7.9: Model comparison PPM modulation (a) forward operation and (b) reverse operation	171
Figure 7.10: 3D model of double D coil (a) top view of coil pad (b) primary and secondary coil pads.....	173
Figure 7.11: Mesh plot for coil pad structures, cross section area perpendicular to Y axis	174
Figure 7.12: Coupling coefficient and self-inductance in function of coil length.....	175
Figure 7.13: Coupling coefficient and self-inductance in function of coil width.....	176

Figure 7.14: Coupling coefficient and self-inductance in function of number of ferrite cores per row.....	176
Figure 7.15: Coupling coefficient and self-inductance in function of space between rows of ferrite bars.....	177
Figure 7.16: Coupling coefficient and self-inductance in function of pitch.....	177
Figure 7.17: Implementation of offset in the X axis.....	178
Figure 7.18: Coupling coefficient in function of distance between pads in the X axis..	179
Figure 7.19: Implementation of offset in the Y axis.....	179
Figure 7.20: Coupling coefficient in function of distance between pads in the Y axis..	179
Figure 7.21: Implementation of offset in the Z axis	180
Figure 7.22: Coupling coefficient in function of distance between pads in the Z axis ..	180
Figure 7.23: Flux density distribution in the cross-section area perpendicular to Y axis (a) with aluminium shield (b) no aluminium shield placed	182
Figure 7.24: Current density distribution for primary and secondary coils and aluminium shields	183
Figure 7.25: Coil pad structure	184
Figure 7.26: 3D printed structure to implement 4mm pitch	184
Figure 7.27: Gain curve measured with Bode 100	185
Figure 7.28: Inductance measurement in (a) series-aiding and (b) series-opposing configurations	186
Figure 7.29: Experimental measurement of coupling coefficient in function of misalignment in the X axis	188
Figure 7.30: Experimental measurement of coupling coefficient in function of misalignment in the Y axis	188
Figure 7.31: Experimental measurement of coupling coefficient in function of distance between pads in the Z axis.....	188
Figure 7.32: Coupling coefficient in function of (a) offset in X axis (b) offset in Y axis and (c) distance between pads in Z axis	189
Figure 7.33: Primary and secondary compensation capacitors.....	192
Figure 7.34: Experimental and theoretical coupling coefficients in function of (a) offset in X axis (b) offset in Y axis.....	193
Figure 7.35: Experimental and simulation results for 48-12V SPS modulated converter operating in (a) forward and (b) reverse modes.....	196

Figure 7.36: Experimental and simulation results for 48-12V PPM modulated converter operating in (a) forward and (b) reverse modes.....	197
Figure 7.37: Experimental and simulation results for 24-24V SPS modulated converter operating in (a) forward and (b) reverse modes.....	200
Figure 7.38: Experimental and simulation results for 24-24V PPM modulated converter operating in (a) forward and (b) reverse modes.....	200
Figure 7.39: Prototype tests: input voltage and current	202
Figure 7.40: Prototype tests: output voltage and current	202
Figure 8.1: Coil resistance versus frequency	209

List of Tables

Table 3.1: Mode descriptions for DAB converter operating under SPS modulation, forward mode.....	46
Table 3.2: Mode descriptions for DAB converter operating under SPS modulation, reverse mode.....	46
Table 3.3: Simulation parameters.....	49
Table 3.4: Simulation results for SPS modulation.....	50
Table 3.5: Inductor current states across a cycle considering forward operation and $\phi = 90^\circ$	52
Table 3.6: Inductor current states across a cycle considering forward operation and $\phi = 45^\circ$	52
Table 3.7: Inductor current states across a cycle considering reverse operation and $\phi = 90^\circ$	53
Table 3.8: Inductor current states across a cycle considering forward operation and $\phi = 45^\circ$	53
Table 3.9: Harmonics analysis of inductor current i_L , forward mode.....	54
Table 4.1: Mode descriptions for converter operating in region I, forward mode.....	75
Table 4.2: Mode descriptions for converter operating in region II, forward mode.....	76
Table 4.3: Mode descriptions for converter operating in region I, reverse mode.....	78
Table 4.4: Mode descriptions for converter operating in region II, reverse mode.....	79
Table 4.5: Simulation parameters.....	83
Table 4.6: Equivalent output load resistor across operating range.....	84
Table 4.7: Operation frequency forward mode.....	86
Table 4.8: Operation frequency reverse mode.....	86
Table 4.9: Percentage error between proposed models and Spice, forward mode.....	87
Table 4.10: Percentage error between proposed models and Spice, reverse mode.....	88
Table 4.11: Comparison of duty estimation techniques for cyclic-averaging implementation, forward mode.....	88
Table 4.12: Execution time comparison.....	91
Table 5.1: Mode descriptions for SPS modulation, forward mode.....	106
Table 5.2: Mode descriptions for SPS modulation, reverse mode.....	106

Table 5.3: Mode descriptions for PPM modulation and $90^\circ \leq \alpha \leq 180^\circ$, forward mode	108
Table 5.4: Mode descriptions for PPM modulation and $90^\circ \leq \alpha \leq 180^\circ$, reverse mode	108
Table 5.5: Mode descriptions for PPM modulation and $\alpha \leq 90^\circ$, forward mode	109
Table 5.6: Mode descriptions for PPM modulation and $\alpha \leq 90^\circ$, reverse mode	109
Table 5.7: Mode descriptions for PPM modulation and $\alpha = 90^\circ$, forward mode	111
Table 5.8: Mode descriptions for PPM modulation and $\alpha = 90^\circ$, reverse mode	111
Table 5.9: Resonant tank parameters calculated for different values of k	115
Table 5.10: Spice simulation results for different values of k	116
Table 5.11: Design parameters	116
Table 5.12: Influence of voltage variations on output power	117
Table 5.13: Simulation results for SPS modulation	124
Table 5.14: Simulation results for PPM modulation	125
Table 5.15: State-variable model results for variables states considering $\alpha_{ratio} = 0.25$, forward mode	127
Table 5.16: Cyclic-averaging model results for variables states considering $\alpha_{ratio} = 0.25$, forward mode	127
Table 5.17: Spice model results for variables states considering $\alpha_{ratio} = 0.25$, forward mode	127
Table 5.18: Execution time comparison	128
Table 6.1: Values of ChN_count and Inv_flag for different modulation cases,	133
Table 6.2: Ls1 (design value: 54.04 μ H)	138
Table 6.3: Lm (design value: 27.02 μ H)	139
Table 6.4: Cs1 (recalculated design value: 29.70 nF)	140
Table 6.5: Cs2 (recalculated design value: 1.25 μ F)	140
Table 6.6: Measured transformer parameters	141
Table 6.7: Inductors and capacitor equivalent parameters referred to primary	150
Table 6.8: Difference between Spice and experimental results in waveform analysis	153
Table 6.9: Influence of additional resistances on output current	154
Table 6.10: Influence of capacitor Cs1 on output current	155
Table 6.11: Influence of capacitor Cs2 on output current	155
Table 6.12: Influence of inductor Ls1 on output current	155

Table 6.13: Influence of inductor L_m on output current	155
Table 6.14: Influence of frequency on output current	156
Table 6.15: Influence of output resistor on output current in forward mode.....	156
Table 6.16: Influence of output resistor on output current in reverse mode.....	156
Table 7.1: Design parameters	165
Table 7.2: Comparison between Spice and FMA models for primary current (I_1).....	167
Table 7.3: Comparison between Spice and FMA models for current I_2	168
Table 7.4: Simulation parameters for IPT and CLLC-equivalent converters.....	170
Table 7.5: Initial parameters for Double D coil in the FEA simulations.....	175
Table 7.6: Parameters for Double D coil in the FEA simulations	178
Table 7.7: Parameters used in Double D coil construction.....	181
Table 7.8: Coupling coefficient when primary and secondary pads are separated by 150 mm	187
Table 7.9: Coupling coefficient (k) in function of misalignment on X axis.....	190
Table 7.10: Coupling coefficient (k) in function of misalignment on Y axis.....	191
Table 7.11: Coupling coefficient (k) in function of distance between pads	191
Table 7.12: Equivalent circuit parameters measured with Bode 100	194
Table 7.13: Equivalent circuit parameters for reduced IPT converter and CLLC converter	195
Table 7.14: Load definition for forward and reverse tests.....	195
Table 7.15: Results for SPS modulation (48 – 12 V)	197
Table 7.16: Results for PPM modulation (48 – 12 V).....	198
Table 7.17: Influence of converter voltage ratio in the output power and efficiency of the system at maximum modulation	199
Table 7.18: Load definition for forward and reverse tests for 24-24V tests.....	199
Table 7.19: Results for SPS modulation (24 – 24 V)	201
Table 7.20: Results for PPM modulation (24 – 24 V).....	201
Table A1.1: Output power relative error (%) between FMA and Spice considering $\phi =$ 90° , where: Green: <5%, Orange : 5-10% and Red: >10%.....	210
Table A1.2: Primary current ($ I_1 $) relative error (%) between FMA and Spice, considering $\phi = 90^\circ$, where: Green: <5%, Orange: 5-10% and Red: >10%.....	211
Table A1.3: Secondary current ($ I_2 $) relative error (%) between FMA and Spice considering $\phi = 90^\circ$, where: Green: <5%, Orange: 5-10% and Red: >10%.....	211

Table A1.4: Magnetizing current ($ I_m $) relative error (%) between FMA and Spice considering $\phi = 90^\circ$, where: Green: $<5\%$, Orange: 5-10% and Red: $>10\%$	212
Table A1.5: Efficiency in Spice considering $\phi = 90^\circ$, where: Green: ≥ 0.98 , Orange: 0.95-0.98 and Red <0.95	212
Table A2.1: Results for single phase-shift modulation forward operation.....	213
Table A2.2: Results for single phase-shift modulation reverse operation.....	214
Table A2.3: Results for pulse-phase modulation forward operation	214
Table A2.4: Results for pulse-phase modulation reverse operation	215
Table A2.5: Measured input voltage SPS tests.....	215
Table A2.6: Measured input voltage PPM tests	216

1 Introduction

1.1 Background and motivation

The interest in low-carbon vehicles has been increasing, mostly due to climate change and environment pollution concerns. In the current scenario, the electric vehicle (EV) is seen as a clean, environment-friendly transport option due to its reduced emission levels. The increased government incentives, number of charging stations and rapid development of EV technology has contributed to the popularization of these vehicles. In 2017, as a strategy to reduce air pollution, the UK government announced plans to end the sale of petrol and diesel vehicles by 2040 [1].

Despite the environmental benefits, the prospect of a large EV population in the future raises concerns about the overload of the grid or possible grid instability. Smart-grid technologies such as vehicle-to-grid (V2G) have been studied in order to reduce impacts, improve the current EV technology and consequently contribute to the further popularization of EVs [2].

Typical EV charging systems are unidirectional, where the power flow direction is from the grid to the battery. Vehicle-to-grid systems enable a bidirectional power transfer between the grid and the battery pack of an EV. Since electric vehicles are usually connected to the grid for long periods of time while charging (during the night or when the owner is at work), the vehicle's battery may work as a temporary energy storage element. If the vehicle-to-grid interface allows bidirectional power flow, the battery may be available for grid support during peak times, when the energy demand is high. During off-peak time the battery may also absorb the excess generation. This way, the battery may work as support for the grid, contributing to the grid stability and efficient use of energy. All these benefits contribute to a reduction of the impact of EV's on the power grid.

In Figure 1.1 a simplified diagram for a V2G system is presented. An AC-DC converter is connected to the grid for power factor correction and voltage/current AC-DC or DC-AC conversion, depending on the power flow direction. The DC-DC converter connects the DC bus at the output of the AC-DC converter to the battery and it is mainly used for voltage and current regulation and galvanic isolation [3].

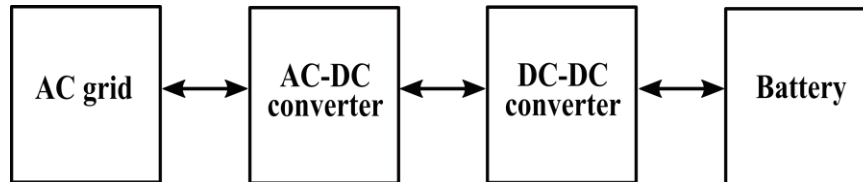


Figure 1.1: Typical V2G system

The majority of EV's charging systems are plug-in, where a cable is used to establish a wired connection between vehicle and charging station. However, with the performance improvement of wireless power transfer (WPT) systems in the recent years, bidirectional wireless chargers are a great option for use in V2G applications, especially due to flexibility, reliability and safe operation under harsh environmental conditions.

This thesis is focused on the analysis of bidirectional DC-DC converter topologies for V2G applications. The cyclic-averaging modelling method, proposed in [4] to achieve rapid and accurate analysis of periodically switching systems, will be applied here to model the bidirectional operation of a Dual Active Bridge (DAB) converter, a 4th order resonant CLLC converter and a series compensated Inductive Power Transfer (IPT) converter, three popular topologies used in V2G systems. The cyclic method was previously applied for analysis of frequency modulated 3rd order LLC converters in [5] and LCC converters in [6], in both cases only unidirectional operation was considered.

The analysis of high order resonant converters with circuit simulation software (Spice, Simulink) can be very time-consuming, therefore, research of more computationally efficient modelling techniques is essential. For validation of the cyclic-averaging model, simulations of Fundamental Mode Approximation (FMA), state-variable and Spice models will also be evaluated along this thesis and performance will be compared.

The main novelty of this thesis is the use of the cyclic-averaging technique to model the behaviour of the bidirectional DAB, CLLC and series compensated IPT converters with high accuracy and faster execution compared to more traditional models, as Spice, FMA and state-variable. Therefore, the models developed in this thesis are useful during the converter design and control processes, where simulations are performed multiple times to evaluate the influence of components values or control variables and, consequently, a reduced execution time is crucial.

The main contribution topics for this thesis are summarized below.

- **Development of piecewise-linear state-variable description for DAB and CLLC converters:** Equivalent circuits for the converters are defined and a state-variable description is obtained considering all possible operating modes of the converter. The DAB converter is analysed when operating under single phase-shift modulation, while frequency and phase-shift modulation cases are considered for the CLLC converter.
- **Development of cyclic-averaging models to DAB and CLLC converters:** Based on the state-variable description and analysis of the converters operating modes, the cyclic-averaging method is applied. Verification of accuracy of the cyclic-averaging model is performed using Spice simulation. For phase-shift modulated CLLC converters, a prototype is built for experimental verification.
- **Analysis of the series-compensated IPT converter using the cyclic-averaging method:** Due to similarities between the CLLC topology and the series compensated IPT converter, circuit transformation is employed to extend the cyclic analysis to the wireless converter. The cyclic-averaging model previously developed for the CLLC converter is therefore applied to an equivalent CLLC circuit that models the behaviour of the IPT converter. A prototype of the series compensated IPT converter is built and the model results are verified against a Spice simulation and experimental results.

1.2 Thesis structure

In this section the organization of the thesis in chapters will be discussed.

A literature review is conducted in Chapter 2. Prior research on bidirectional topologies of DC-DC converters, as Dual Active Bridge, resonant variants of the DAB (series resonant DAB, LLC and CLLC) and topologies for wireless power transfer applications, will be analysed. Additionally, potential modulation techniques used for the converter control are discussed. A review on modelling techniques applied for converter analysis is also provided, including a detailed equation description and implementation methodology for the cyclic-averaging method.

In Chapter 3 the cyclic-averaging modelling technique is employed to analyse a Dual Active Bridge converter operating with single phase-shift modulation. The state-variable description is obtained considering bidirectional operation and the cyclic-averaging method is applied for calculation of the converter's output current and harmonic analysis of the state-variables.

The cyclic analysis is applied to a frequency modulated CLLC converter in Chapter 4. Here, Fundamental Mode Approximation (FMA) and state-variable simulations are also conducted for comparison of accuracy and execution performance with the cyclic-averaging method. In Chapters 3 and 4 the models are verified using a component-based simulation (Spice).

The analysis of the CLLC converter operating under phase-shift modulation is performed in Chapter 5. Models are developed and verified at simulation stage considering two types of phase-shift modulation (single phase-shift and pulse-phase modulation). Furthermore, a detailed analysis of the influence of the phase-shift angles on the converter operation is performed.

Following the simulation study, experimental verification is performed for the phase-shift modulated CLLC converter in Chapter 6, where the prototype construction process and experimental results are discussed.

In Chapter 7, the models developed for the phase-shift modulated CLLC converter in Chapters 5 and 6 are adapted to model a series compensated wireless converter, also operating with phase-shift modulation. The design and construction of the IPT converter prototype followed by the experimental verification are also presented in this chapter.

The thesis conclusions and further work possibilities are presented in Chapter 8.

1.3 References

- [1] “Plan for roadside NO₂ concentrations published,” *Press release: Department for Environment, Food & Rural Affairs*, 2017. [Online]. Available: <https://www.gov.uk/government/news/plan-for-roadside-no2-concentrations-published>. [Accessed: 22-Oct-2019].
- [2] A. Kriukov and M. Gavrilas, “Energy/Cost efficiency study on V2G operating mode for EVs and PHEVs,” in *2019 8th International Conference on Modern Power Systems (MPS)*, 2019, pp. 1–6.
- [3] C. Liu, J. Wang, K. Colombage, C. Gould, and B. Sen, “A CLLC Resonant Converter Based Bidirectional EV Charger with Maximum Efficiency Tracking,” in *8th IET International Conference on Power Electronics, Machines and Drives (PEMD 2016)*, 2016, pp. 1–6.
- [4] H. R. Visser and P. P. J. van den Bosch, “Modelling of periodically switching networks,” *PESC '91 Record 22nd Annual IEEE Power Electronics Specialists Conference*, no. 1, pp. 67–73, 1991.
- [5] C. Gould, “Rapid Analysis and Design of CLL Resonant Power Converters,” PhD Thesis. University of Sheffield, 2006.
- [6] M. P. Foster, “Analysis and Design of High-order Resonant Power Converters,” PhD Thesis. University of Sheffield, 2003.

2 Literature Review

2.1 Introduction

In the previous chapter an introduction to vehicle-to-grid charging systems was given and the importance of bidirectional DC-DC converters for this application was identified. Additionally, the structure and novelty elements of this thesis were presented. Following the background, motivations and structure of this work previously discussed, a review on the base subjects for this research will be conducted in this chapter.

Firstly, bidirectional DC-DC converter topologies suitable for wired vehicle-to-grid (V2G) charging systems are analysed. The Dual Active Bridge (DAB) and its resonant variants will be evaluated and compared. These topologies of DC-DC converter use a conventional tightly coupled transformer for galvanic isolation and voltage regulation, therefore, they are not suitable for wireless charging systems.

Following the analysis of resonant bidirectional topologies of DC-DC converters for conventional chargers, a review of the topologies adopted for wireless power transfer (WPT) systems will be given. A conventional V2G system is shown in Figure 2.1 while a modified system using wireless charging is shown in Figure 2.2. In a wireless charging system, the DC-DC converter is divided in two parts: a DC-AC inverter bridge connected to a primary coil and compensation circuit placed in a charging base on the ground, and a second part placed in the vehicle composed by the secondary coil and compensation circuit connected to an AC-DC rectifying bridge. The primary and secondary coil pads are separated by a large air gap (100 to 250 mm). Different configurations of compensation circuits and coil pad structures will also be analysed.

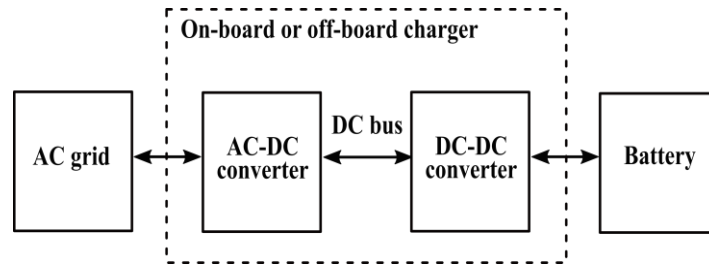


Figure 2.1: Typical vehicle-to-grid system

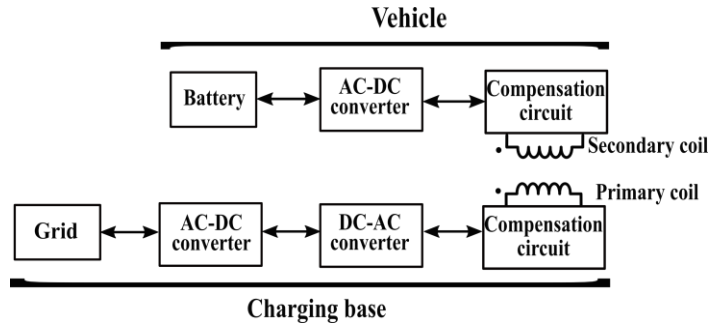


Figure 2.2: Wireless charging system

Lastly, after the analysis of wireless power transfer systems, a review on the modelling methods used to describe DC-DC converters will be performed. The main techniques analysed are Fundamental Mode Approximation (FMA), cyclic-averaging and methods based on state-variable description.

2.2 Bidirectional DC-DC converters

Bidirectional DC-DC converters are employed in V2G systems to provide voltage and current regulation and galvanic isolation. Various topologies of bidirectional DC-DC converters for V2G applications are analysed and compared in [1], [2] and [3].

Potential topologies suitable for high power V2G applications are reviewed in this section. Due to the safety requirement in V2G systems and consequent need of galvanic isolation, only isolated topologies are analysed. The converters evaluated are divided in two main categories: the converters suitable for conventional bidirectional charging systems, which includes the non-resonant Dual Active Bridge and its resonant variants, and topologies suitable for wireless charging systems.

2.2.1 Dual Active Bridge

The Dual Active Bridge (DAB) topology was first proposed in 1988 [4]. This soft-switching DC-DC converter was considered a suitable option for high power applications and, initially, only unidirectional power transfer was analysed. In [5] the bidirectional power flow and converter's performance are analysed and experimental results are presented. At first, the efficiency of this converter was low due to the switching technology in the early 1990's, however, with the evolution of the switching devices technology and development of new modulation and control techniques, the efficiency was reported as 92.2% for a 1 kW prototype in 2012 [6]. Also, in 2016, an efficiency value of nearly 98% was obtained for a 1.6 kW converter [7].

The DAB topology is presented in Figure 2.3, where n is the transformer turns ratio, v_1 is the output voltage of bridge 1 and v_2 the output voltage of bridge 2. The converter is composed of two full-bridge circuits connected by an isolated transformer and an additional inductor, L_s . The left-side full-bridge (bridge 1) is connected to a high-voltage DC bus while the right-side bridge (bridge 2) is connected to an energy storage device, which can be a battery or ultracapacitor. The converter operates in "forward mode" when power flows from the DC bus to charge the energy storage device. When operating in "reverse mode" the power direction is from the energy storage system to the DC bus, in a process of discharging the battery.

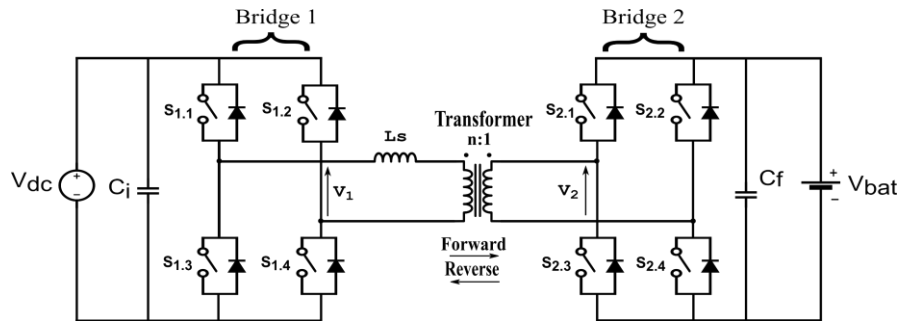


Figure 2.3: Dual Active Bridge converter

The main benefits of the topology are: bidirectional power transfer, galvanic isolation, reduced number of components, symmetric structure, high power density, soft-switching operation, high-frequency operation and reduced size [5], [6], [8]. The performance of the DAB converter was previously analysed for aircraft energy storage applications in [9] and for vehicle-to-grid/automotive applications in [6], [10], [11].

Various modulation techniques were proposed to operate the DAB converter. The Conventional Phase-Shift (CPS) or Single Phase-Shift (SPS) modulation [5], [12], [13] is the simplest and easiest method to implement, where the power can be controlled using a simple PI-based controller. The switching circuit is implemented to generate a high-frequency square-wave voltage with 50% duty cycle at each bridge terminal (voltages v_1 and v_2 in Figure 2.3), as shown in Figure 2.4-a, and the magnitude and direction of power transferred is controlled by the phase shift angle between the primary and secondary bridge voltages (ϕ), where the power flows from the bridge that generates the leading square-wave.

Despite the simple and fast implementation, the main drawback of the SPS method is the limited voltage operation range. As the input or output voltages deviate from the nominal operation values ($v_1 \neq nv_2$) the soft-switching range is reduced, a high circulating energy between the bridges appears and conduction losses increase, resulting in significant reduction in efficiency [7], [14]–[16].

To overcome the limitations of the CPS/SPS approach, alternative modulation techniques with increased complexity were proposed. Improved results could be found by increasing the control degrees of freedom instead of using only the bridge phase-shift angle as control variable.

The Extended Phase-Shift (EPS) control technique proposed in [17] adds a degree of freedom to the control, utilising the inner phase-shift ratio of a bridge (Figure 2.4-b). The output voltage of one of the bridges is maintained as a square wave with 50% duty cycle, as in the SPS modulation case. For the other bridge, an inner phase shift angle, α_1 for bridge 1 or α_2 for bridge 2, is introduced between the two legs of the bridge, resulting in a variable duty cycle that is used as an additional control variable.

The Dual Phase-Shift (DPS) control [18]–[20] is an extension of the EPS method, where the inner phase-shift of both bridges is modified but maintaining the same value for both primary and secondary bridges, as shown in Figure 2.4-c, where $\alpha_1 = \alpha_2$. In the Triple Phase-Shift (TPS) or Pulse-Phase Modulation (PPM) control, shown in Figure 2.4-c, the inner phase-shift ratios of the two bridges (α_1 and α_2) may have different values ($\alpha_1 = \alpha_2$ or $\alpha_1 \neq \alpha_2$) [6], [21]–[24]. Therefore, the DPS is a particular case of TPS modulation that occurs when $\alpha_1 = \alpha_2$.

It was observed that the use of EPS, DPS and TPS modulation techniques results in lower peak currents, reduced conduction losses, increased soft-switching range and improvement of efficiency [25], [26]. Although best results are obtained with the TPS method, the manipulation of three control variables significantly increases both the system and control complexity [7].

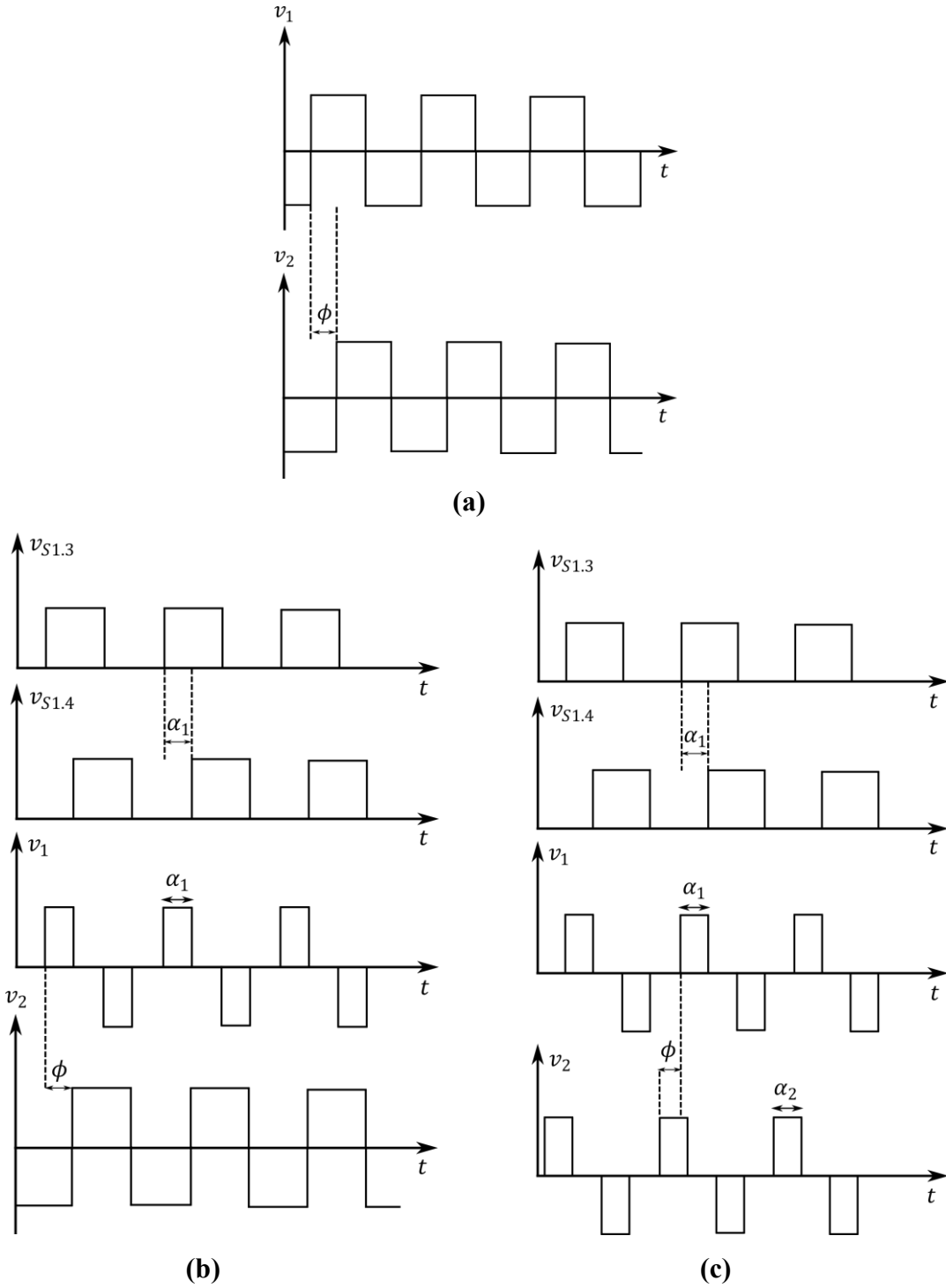


Figure 2.4: Diagrams for (a) Single Phase-Shift modulation (b) Extended Phase-Shift modulation and (c) Dual Phase-Shift or Triple Phase-Shift modulation

Advanced methods are proposed where the switching sequence is manipulated in order to obtain triangular or trapezoidal waveforms for the transformer current [6], [7], [27], [28]. Switching losses are reduced with the triangular method (TRM) but this technique should only be used when input and output voltage are significantly different, since the triangular current slope is defined based on the input and output bridge voltages [27]. For $v_1 \approx nv_2$ the positive slope of the triangular current becomes zero ($\frac{v_1 - nv_2}{L} = 0$) and the trapezoidal method (TZM) is preferred [28]. Improved efficiency and lower peak and rms currents are obtained with the trapezoidal method, however, for low voltage applications, when the input voltage is not sufficiently high, the trapezoidal current becomes triangular and this technique is no longer recommended [15]. Despite the reduction of switching losses, the use of trapezoidal or triangular methods results in higher rms current and a consequent increase of conduction losses when compared to SPS modulation. A hybrid method combining the triangular and trapezoidal methods depending on the voltage range is proposed in [28], performance is improved but increased computational effort on behalf of the controller is required.

The main phase-shift modulation techniques proposed for the DAB topology are reviewed and compared in [26]. Overall, the improvement of modulation techniques proposed in the literature results in higher efficiency and optimized operation of the DAB, but also leads to complex control systems, increasing the difficulty of physical implementation.

The most recent research on Dual Active Bridge converters is focused on transient analysis of the converter and development of novel modulation techniques to improve the operation and efficiency of the DAB [29].

2.2.2 Resonant topologies

The DAB converter presents large peak currents and limited operation range when operating with simpler modulation and control methods. To overcome the flaws of the DAB topology, alternative converters were proposed using the DAB topology as a base but incorporating a resonant tank in the interface between the two bridges. These resonant topologies can achieve higher efficiency, reduced peak currents and improved range of soft-switching operation [30]. Various resonant converters are analysed in [31] for renewable energy applications and in [1] for high voltage gain applications.

A simple resonant topology is obtained when a capacitor is added in series to the inductor of the conventional DAB topology, as shown in Figure 2.5. This converter is named Dual-Bridge Series Resonant converter (DBSRC) or Series-Resonant Dual Active Bridge (SRDAB) and its operation is analysed in [31]–[35]. The addition of a capacitor causes reduction of harmonics in the high-frequency transformer current, resulting in a waveform closer to a sine wave, while in a standard DAB converter the current has a triangular waveform. The capacitor is also responsible for blocking DC currents that could lead to saturation of the transformer [36].

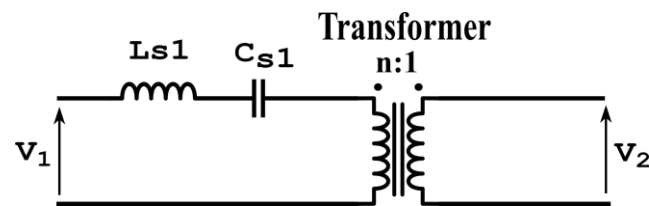


Figure 2.5: Resonant tank of Series-Resonant Dual Active Bridge converter

The SRDAB and DAB topologies were compared in [37]. Efficiency improvement and reduction of rms currents were noticed for the resonant topology. However, both topologies presented higher efficiency when the primary voltage was close to the reflected secondary voltage and performance degradation was observed for operation outside this range. Therefore, both DAB and DBSRC converters are not appropriate to operate in applications with a wide voltage range when using less complex modulation techniques.

Similar to the DAB converter, advanced control and modulation techniques may be applied to improve the operation of the resonant converter. The use of Single Phase-Shift modulation results in poor efficiency, therefore, various phase-shift modulation techniques are applied in [32], [35], [36] and [38] to reduce current stress and improve the efficiency of the SRDAB. Although most research is focused on phase-shift modulated SRDAB, variable frequency control is analysed in [37] and [39]. A drawback of the frequency modulation technique is the fact that, for resonant converters, maximum efficiency is achieved for operation close to the resonant frequency. Therefore, for converters operating with a wide voltage range, frequency modulation is not indicated since the switching frequency would significantly deviate from the resonant point during control.

The LLC converter [40], [41] is an alternative resonant topology where a shunt inductor (L_m) is added to the resonant tank of the SRDAB topology, as presented in Figure 2.6.

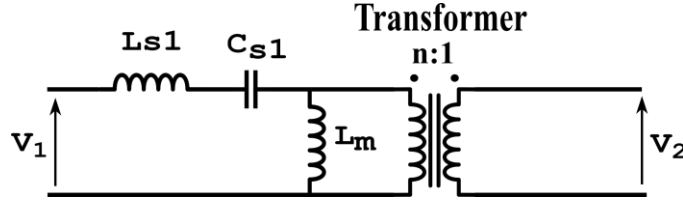


Figure 2.6: Resonant tank of LLC converter

The unidirectional version of the LLC converter is a popular topology for wide voltage range applications due to its ability of achieving soft-switching over the full operation range for all switching devices [42]. However, the behaviour of the bidirectional version is equal to the unidirectional converter only in forward mode (charging) operation. For reverse mode operation (discharging), the shunt inductor is clamped and the system behaves as a conventional series resonant converter, resulting in large losses, especially when switching frequency and resonant frequency are significantly different. The difference between the forward and reverse mode operations causes problems of voltage regulation, power control, waveform distortions and large circulating current, making this topology not suitable for bidirectional wide voltage range applications [42]–[44].

To overcome the limitations of the 3rd order LLC converter for bidirectional operation, a 4th order CLLC converter is proposed in [45]. For this topology, a series capacitor is added in the secondary side of the LLC converter resonant tank, as shown in Figure 2.7. Here, soft-switching is achieved for both power flow directions, zero-voltage switching (ZVS) for the primary side and zero-current switching (ZCS) for the secondary side, resulting in a minimization of switching losses and an overall improvement of efficiency. A maximum efficiency of 97.9% is obtained in [44] for a 3.5kW converter.

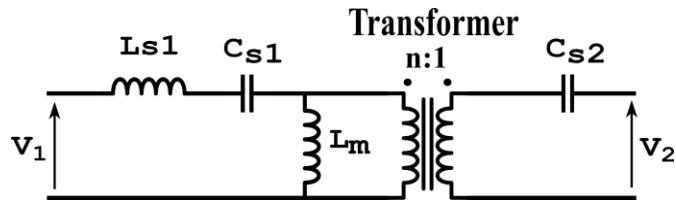


Figure 2.7: Resonant tank of CLLC converter

Most of the literature is focused on CLLC converters operating under frequency modulation [43]–[45], when the output power is regulated using the switching frequency as control variable. For conventional frequency control, both LLC and CLLC topologies present problems of performance when the difference between switching frequency and series resonant frequency significantly increases to regulate variations in the battery voltage. Operation close to the resonant frequency is desired to achieve high efficiency, therefore, a maximum efficiency tracking method is employed in [43] to avoid increased deviation from the resonant frequency, here, instead of using only the frequency as control variable, the DC bus voltage is also regulated using the front end control of the AC-DC converter to maintain the required output power level despite battery voltage fluctuations. Alternatively, phase-shift modulation can be applied to maintain the operating frequency constant.

A CLLC converter operating under triple phase-shift modulation is analysed in [46], where the phase-shift angle between primary and secondary bridges (ϕ) is fixed at $\pm 90^\circ$ to control only the power flow direction while the inner phase-shift angles of bridges 1 and 2 (α_1 and α_2) in Figure 2.3 are used to control the output power magnitude. Here, a maximum efficiency of 95% is achieved at maximum modulation in a 4kW prototype.

The main drawback of phase-shift modulation applied to CLLC converters is the loss of soft-switching as the inner phase-shift angles decrease and operation deviates from the maximum power transfer point. In [47] a solution for the soft-switching problem is proposed where the phase-shift angle between primary and secondary bridges is no longer constant at $\pm 90^\circ$, but adjusted to maintain soft turn-on transitions with either zero-voltage switching (ZVS) or zero-current switching (ZCS). Reduction of switching losses is achieved with this technique, however, the circulating current is slightly increased, consequently increasing conduction losses. Therefore, for systems

with low switching frequency and high tank currents the method proposed in [46], where $\phi = \pm 90^\circ$, is more appropriate.

2.2.3 Wireless power transfer systems

In the field of V2G systems, the optimization of the bidirectional charging process is a key point of research and is the basis for several studies focused on improvement of factors like cost, flexibility, efficiency and complexity of the charging/discharging system. Wireless Power Transfer (WPT) methods have been used in V2G systems with the objective to meet these demands avoiding the need of plugs or any physical connections for the charging process. The use of WPT systems is particularly important to guarantee the safety isolation between the vehicle and the grid and reliability in harsh environment conditions, when the systems are exposed to rain, dirt, chemicals or dust for example. The benefits of WPT make it suitable for different areas, including aerospace, automotive and biomedical applications.

Inductive Power Transfer (IPT) systems consists of two or more loosely coupled coils used for wireless power transfer by induction. Although most of research is focused on unidirectional systems, bidirectional IPT systems for V2G applications were analysed in [48]–[50].

A conventional IPT system is shown in Figure 2.8. The system is symmetrical and composed by a primary and secondary (or pickup) side, where the primary side is placed on the ground and the secondary side is placed inside the vehicle. Similar to the DAB converter, an active full-bridge (bridge 1) is connected to a DC-link while the secondary active bridge (bridge 2) is connected to the battery. In IPT systems, primary and secondary coil pads are separated by a large air gap. According to the Society of Automotive Engineers (SAE) standard for WPT for light duty EV's [51], the distance between the lower surface of the primary coil pad and ground surface must be in a range from 100 to 250 mm.

The primary and secondary compensation circuits are implemented to minimize the volt-ampere (VA) rating of the power supply, improve power factor in the primary and secondary circuits and achieve maximum power transfer capability, with consequent improvement of efficiency [52], [53].

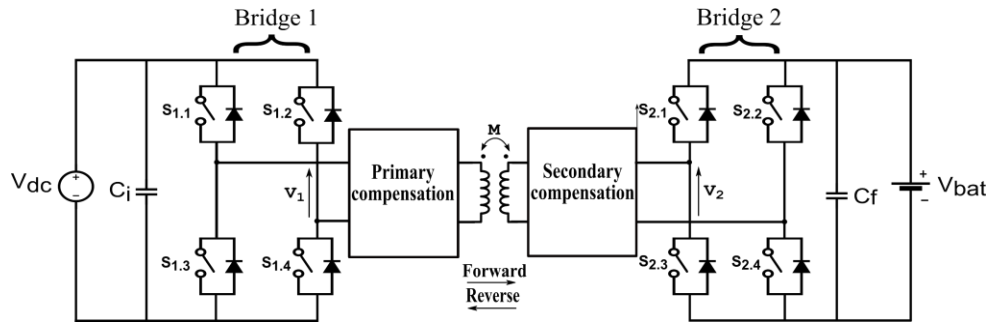


Figure 2.8: IPT converter

Various configurations were proposed for the compensation circuit, the series compensated, LC-series or Series-Series (SS) circuit [54]–[56], shown in Figure 2.9, is the most popular configuration, where a series capacitor is connected in series to the inductor in both primary and secondary sides.

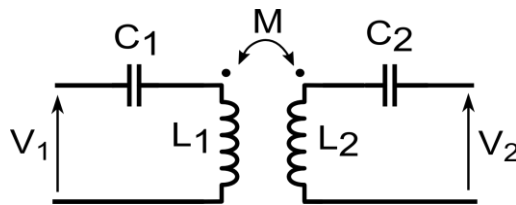


Figure 2.9: LC-series compensation circuit

In the LC-parallel or Parallel-Parallel (PP) compensation circuit, the capacitors are connected in parallel to the coils, as shown in Figure 2.10. This topology is not often used due to poor performance when compared to LC-series or LCL compensations.

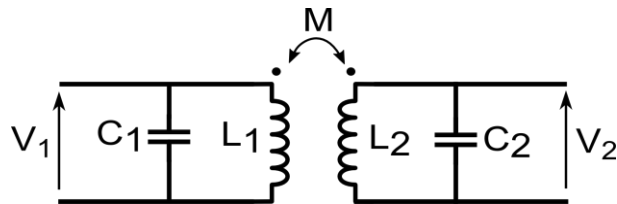


Figure 2.10: LC-parallel compensation circuit

The LCL compensation circuit [57], [58], shown in Figure 2.11, is more complex due to the increased number of components. In this topology, filter inductors (L_{s1} and L_{s2}) are added to the LC-parallel configuration in order to reduce harmonics of the inverter current.

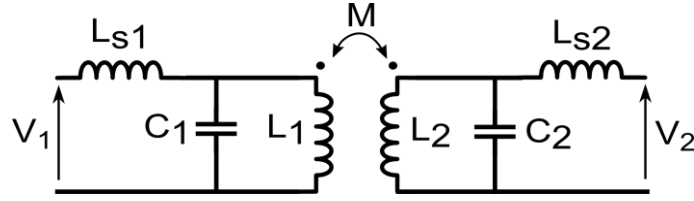


Figure 2.11: LCL compensation circuit

For all configurations, the mutual inductance M is defined based on the coupling coefficient k and coil self-inductances L_1 and L_2 . It is important to note that the coupling coefficient decreases as the distance between the primary and secondary pads increases.

$$M = k\sqrt{L_1 L_2} \quad (2.1)$$

The resonant frequency ω_r is defined based on the coil self-inductances and compensation capacitors:

$$\omega_r = \frac{1}{\sqrt{L_1 C_1}} = \frac{1}{\sqrt{L_2 C_2}} \quad (2.2)$$

The most used compensation circuits, LC-series and LCL, are evaluated in [59] while in [52] and [60] the LC-series, LC-parallel and LCL configurations are analysed and compared, where it was shown that LCL compensation is less sensitive to misalignments between the primary and secondary pads. However, better efficiency and higher power factor are achieved with the LC-series circuit. Due to the presence of large current spikes, the use of LC-parallel configuration results in the lowest efficiency and power factor. It was also observed that for an ideal converter, as the coupling coefficient reduces, the output power of the converter increases when using LC-series compensation but reduces when using LC-parallel or LCL. Experimental results obtained in [56] show that this behaviour is only observed for a higher range of coupling factor, as the coupling coefficient significantly decreases, the output power also starts to reduce for the series compensated converter.

For the coil pad design, various configurations have been proposed in the literature and the most popular structures are compared in [61]–[63]. Finite element analysis is often employed for the magnetic design process of the pad structures, as in [56], [64], [65].

Circular pads are simple and extensively researched structures but show poor coupling and high sensitivity to misalignment. The Double D pad (DDP) was proposed in [66] as an alternative to the circular pad, improving coupling and tolerance for misalignments in the Y axis. The charge zone of DDP structures is nearly two times larger than that of equivalent circular pads.

To improve performance for misalignment in the X axis, the Double D Quadrature pad (DDQP) was also proposed in [66], where a quadrature coil is added to a DDP structure. Using a DD coil in the primary and DDQ coil in the secondary results in a charge zone three times larger than the area obtained using DD coils on both sides, however, the cost and complexity of the pad structures are increased due to the extra quadrature coil.

The Bipolar pad (BPP) analysed in [67], has similar performance to a DDQ coil. The advantage of using this structure instead of a DDQP is the less amount of copper required for construction, since the third quadrature coil is not implemented and only two coils are used, as shown in Figure 2.12 where the DDP, DDQP and BPP structures are compared.

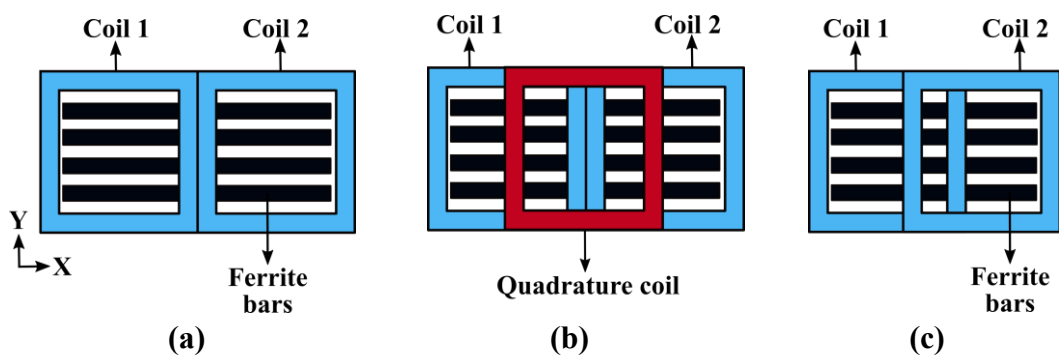


Figure 2.12: Pad structures comparison: (a) Double D pad (DDP), (b) Double D Quadrature pad (DDQP) and (c) Bipolar pad (BPP)

Phase-shift modulation techniques are usually applied for the analysis of IPT converters instead of frequency modulation, since best performance is obtained when operating around the resonant frequency.

Despite the safety, flexibility and reliability benefits, the main drawbacks of IPT systems are the reduced efficiency compared to the wired systems and the dependency on the misalignment between primary and secondary coils, which also affects the system overall performance and efficiency. Still, high efficiency systems were previously achieved with maximum of 95.4% at 3kW with 150mm gap in [68], 95.3% for a 6kW prototype with 150mm air gap in [69] and 97.4% for 22kW and gap of 135mm in [70].

2.3 Modelling techniques review

Modelling methods are employed to obtain a mathematical description for prediction of the converter's behaviour without the need of construction and experimental verification. Therefore, the development of a model is an important tool for the design and analysis process. Modelling techniques are constantly developed and improved aiming to obtain an accurate and rapid analysis of power electronics systems.

A review of modelling techniques previously applied to analyse DC-DC converters is presented in this section, showing the basic principles of each technique, advantages and limitations.

2.3.1 Fundamental Mode Approximation (FMA)

Fundamental Mode Approximation (FMA) [71] is one of the most used frequency-domain techniques for analysis and design of resonant DC-DC converters due to its simplicity and fast execution. Following this method, a linear equivalent circuit is obtained from the analysis of a non-linear converter. The behaviour of the input source combined with the switching devices is typically modelled as a sinusoidal voltage source, representing the fundamental component of the resonant tank input voltage, while the output is modelled as an equivalent resistor, representing the behaviour of transformer, output filter, output bridge and load. Conventional AC circuit analysis is utilized to solve the system and a transfer function is obtained to describe the converter's behaviour and frequency response [72], [73].

According to the FMA method, only the fundamental component of voltages and currents is considered. Therefore, despite the rapid and simple analysis, the method suffers from accuracy problems when the actual resonant tank currents/voltages are

more distant from perfect sine waves, and harmonics influence must be considered. Additionally, only steady-state results are obtained when using FMA.

The FMA technique was previously applied for analysis of LCC [73]–[75], LLC [76], [77] CLLLC converters [44], [78] and CLLC converters [45], [79] operating under frequency modulation. For the phase-shift modulated variant of the CLLC converter, the fundamental assumption is employed in [47] for calculation of resonant tank currents. FMA was also used to analyse wireless power converters in [52], [59], [80], [81]. In [31] the FMA method is applied to evaluate and compare five popular DC-DC resonant topologies: the series, parallel, series-parallel, LLC and CLLC converters.

To improve the accuracy of the FMA method, the Rectifier Compensated Fundamental Mode Approximation (RCFMA) is proposed in [82] for analysis of a series-parallel LCLC resonant converter. This method improves the modelling of the rectifier’s behaviour, but accuracy is reduced for operation around the resonant frequency and for low output voltage designs, since the rectifier voltage drop is neglected [83]. To overcome the RCFMA limitations, modifications to this method are proposed in [73], [83] to analyse a LCC resonant converter, resulting in the Rectifier Transformed Fundamental Mode Approximation (RTFMA). This method adds an iterative procedure to incorporate the rectifier voltage drop and the accuracy for operation around the resonant frequency is improved.

2.3.2 State-variable

The state-variable model is a time-domain description of the differential equations that represent a system [84]. In conventional converters circuits, the state-variables are the inductors currents and capacitors voltages, and the derivatives of these variables are described as a linear combination of the state-variables and inputs of the system, as shown in (2.3).

$$\begin{cases} \frac{dx(t)}{dt} = Ax(t) + Bu(t) \\ y(t) = Cx(t) + Du(t) \end{cases} \quad (2.3)$$

where $x(t)$ is the state-vector that contains all state-variables, A is the state (or dynamic) matrix, B is the input matrix, C is the output matrix and D is the direct transmission (or feedthrough) matrix.

The differential equations are solved based on the initial value of the state-variables and system inputs. From the state-variable description, the transient and steady state characteristics are obtained, therefore, this method is an important tool to analyse bidirectional DC-DC converters, serving as base to numerous modelling techniques.

Based on the state-variable description, state-space averaging [85], [86] is one of the most commonly used techniques to model switching power converters and obtain the average values of state-variables. According to this method, a piecewise linear state-variable model is obtained, and the time-averaged dynamic and input matrices are determined and used to calculate the average value of the state-variables (for many converters this method of decomposition is based on a priori knowledge of the operating modes and their duty/time duration). This method also relies on the small ripple approximation, where the natural frequencies of the converter and input signal variations are significantly slower compared to the switching frequency [84]. This assumption, however, does not apply to resonant topologies, since for these converters the switching frequency is usually close to the resonant tank frequency [72], [73], [87].

As an alternative to state-space averaging, DQ transformation [88] is used in [87] to analyse a CLLC converter operating under phase-shift modulation, where the converter's equivalent circuit is divided into a high frequency AC subsystem and a DC subsystem modelled as a voltage source. This analysis, however, uses fundamental mode approximation for the representation of the AC subsystem, resulting in accuracy problems when the harmonics influence is significant.

The waveform relaxation method [89], [90] is used in [91] for fast time-domain analysis of non-linear power electronics systems. According to this technique, a non-linear model is decomposed into two subsystems (separating the fast and slow dynamics elements) that are described by a set of linear equations and connected by a coupling equation, where each subsystem is integrated over its own time-step. The decoupling of the circuit into subsystems reduces the complexity of the equations to be solved, resulting in decreased simulation time. This decomposition method is used to

analyse 3rd order LCC resonant converters in [92], 4th order LCLC converters in [93] and to model LLC converters in [94], in all these analyses the converter's circuit is divided into a fast subsystem, representing the power switches and resonant tank behaviours, and a slow subsystem that represents the output filter and load. The fast and slow subsystem are then connected by a set of coupling equations that describe the action of the output rectifier. Similar analysis will be adopted here in the next chapters to analyse the DAB, CLLC and series compensated IPT converters.

2.3.3 Cyclic-averaging

The cyclic-averaging is a time-domain method proposed in [95] as a more accurate alternative to state-space averaging for analysis of periodically switching systems. This modelling technique was previously used in [76] to model LLC converters, in [93] for LCLC converters and in [96] to model LCC converters.

In this section, the equation description for this method will be presented, this will serve as basis for the analysis performed in Chapters 3 to 7 to model the DAB converter, CLLC converter and the series resonant wireless converter using the cyclic technique.

A system presents cyclic behaviour when the state-vector at the beginning and at the end of the period are equal, as defined in (2.4).

$$x(t) = x(t + cT) \tag{2.4}$$

where T is the period of a cycle calculated based on the operating frequency and c is an integer representing the number of cycles.

To perform the cyclic analysis, the periodically switched system is defined as a piecewise linear model. Based on the states of the switches, a cycle is divided into m operation modes, where m is the number of possible combinations of switches. The non-linear model is therefore decomposed into a set of m linear state-variable equations. From circuit analysis, the state-variable description is obtained for each mode i , where $i = 1, 2, \dots, m$:

$$\frac{dx(t)}{dt} = A_i x(t) + B_i$$

(2.5)

where $x(t)$ is the state-vector, A_i is the dynamic matrix and B_i represents the excitation term for the i^{th} mode.

The circuit operates in each mode for a fixed period, the calculation of this time is performed by analysing the circuit and input voltages behaviour over a cycle, and will depend on the type of modulation employed. Considering the system operates in mode i when $t_{i-1} \leq t \leq t_i$, the evolution of the state-vector through mode i is calculated as follows.

$$x(t) = e^{A_i(t-t_{i-1})}x(t_{i-1}) + \int_{t_{i-1}}^t e^{A_i(t-\tau)}B_i d\tau \quad (2.6)$$

The duty cycle d_i is defined as the normalized time interval for each operation mode and T is the period of a cycle. Therefore, the length of each mode is defined as $\Delta t_i = t_i - t_{i-1} = d_i T$ and the following notation is adopted:

$$\begin{aligned} \phi_i &= \phi(t_i, t_{i-1}) = e^{A_i(t_i-t_{i-1})} = e^{A_i d_i T} \\ \Gamma_i &= \int_{t_{i-1}}^{t_i} e^{A_i(t_i-\tau)}B_i d\tau = (e^{A_i d_i T} - I)A_i^{-1}B_i, \text{ if } A_i \text{ is invertible} \end{aligned} \quad (2.7)$$

The system can be solved recursively combining the initial condition $x(t_0)$ with equations (2.6) and (2.7). However, due to the complexity of the integral term, this calculation is considerably complicated, especially when A_i is a singular matrix. To simplify and speed up the analysis, the integration term in (2.7) can be eliminated by introducing an augmented vector that combines the dynamic and excitation matrices. The new augmented matrices are defined as follows.

$$\frac{d}{dt}\hat{x}(t) = \hat{A}_i \hat{x}(t) \quad (2.8)$$

where:

$$\hat{x}(t) = \begin{bmatrix} x(t) \\ 1 \end{bmatrix}$$

$$\hat{A}_i = \left[\begin{array}{c|c} A_i & B_i \\ \hline 0 & 0 \end{array} \right]$$
(2.9)

The solution for the i^{th} mode is given by (2.10).

$$\hat{x}(t_i) = e^{\hat{A}_i d_i T} \hat{x}(t_{i-1}) = \hat{\phi}_i \hat{x}(t_{i-1})$$
(2.10)

Considering a system with m modes, where $i = 1, 2, \dots, m$, the state-vector at the end of mode 1, at the end of mode 2 and after a complete period are calculated recursively as follows.

$$\hat{x}(t_1) = e^{\hat{A}_1 d_1 T} \hat{x}(t_0) = \hat{\phi}_1 \hat{x}(t_0)$$

$$\hat{x}(t_2) = e^{\hat{A}_2 d_2 T} \hat{x}(t_1) = \hat{\phi}_2 \hat{x}(t_1) = \hat{\phi}_2 \hat{\phi}_1 \hat{x}(t_0)$$

$$\hat{x}(t_m) = e^{\hat{A}_m d_m T} \hat{x}(t_{m-1}) = \hat{\phi}_m \hat{\phi}_{m-1} \dots \hat{\phi}_1 \hat{x}(t_0) = \hat{\phi}_{tot} \hat{x}(t_0)$$
(2.11)

where $\hat{x}(t_0) = \begin{bmatrix} x(t_0) \\ 1 \end{bmatrix}$ is the initial condition.

The augmented matrix $\hat{\phi}_i$ is also defined combining matrices ϕ_i and Γ_i from (2.7).

$$\hat{\phi}_i = e^{\hat{A}_i d_i T} = \left[\begin{array}{c|c} \phi_i & \Gamma_i \\ \hline 0 & 1 \end{array} \right]$$
(2.12)

The periodic solution is obtained using the definition of periodic system in (2.4).

$$\hat{x}(t_0 + T) = \hat{\phi}_{tot} \hat{x}(t_0) = \hat{x}(t_0)$$
(2.13)

where $\hat{\phi}_{tot} = \hat{\phi}_m \hat{\phi}_{m-1} \dots \hat{\phi}_1$.

The initial condition is calculated using (2.12) to solve (2.13).

$$x(t_0) = (I^n - \phi_{tot})^{-1} \Gamma_{tot} \quad (2.14)$$

where:

$$\begin{aligned} \phi_{tot} &= \phi_m \phi_{m-1} \dots \phi_1 \\ \Gamma_{tot} &= (\phi_m \phi_{m-1} \dots \phi_2) \Gamma_1 + (\phi_m \phi_{m-1} \dots \phi_3) \Gamma_2 + \dots + \phi_m \Gamma_{m-1} + \Gamma_m \end{aligned} \quad (2.15)$$

Thus, with knowledge of the circuit modes and duration times, the cyclic-mode initial condition, $x(t_0)$, can be precisely calculated. The values of all state-variables through a cycle are then calculated recursively using (2.9), (2.10) and (2.14).

2.3.3.1 Averaged state-vector

The cyclic method is also used to calculate the average value of the state-variables over a cycle. The averaged state-vector x_{avg} is obtained using the periodic solution previously defined and the average value definition in (2.16).

$$x_{avg} = \frac{1}{T} \int_{t_0}^{t_0+T} x(t) dt \quad (2.16)$$

The following system must be analysed to be solved.

$$\begin{cases} \dot{x}(t) = A_i x(t) + B_i \\ \dot{y}(t) = \dot{x}_{avg} = \frac{1}{T} x(t) \end{cases} \quad (2.17)$$

The augmented-vector technique is used once more to obtain a simplified and rapid solution. The new state-vector is obtained combining the variables $x(t)$ and $y(t)$, resulting in the following system.

$$\frac{d}{dt} z(t) = \tilde{A}_i z(t) \quad (2.18)$$

where:

$$\tilde{A}_i = \left[\begin{array}{c|c|c} A_i & B_i & 0 \\ \hline 0 & 0 & 0 \\ \hline I/T & 0 & 0 \end{array} \right]$$

$$z(t) = \left[\begin{array}{c} x(t) \\ \hline 1 \\ \hline x_{avg}(t) \end{array} \right]$$
(2.19)

The initial condition is defined in (2.20).

$$z(t_0) = \left[\begin{array}{c} x(t_0) \\ \hline 1 \\ \hline 0 \end{array} \right]$$
(2.20)

The system is solved recursively following the same methodology adopted to calculate the periodic state-vector over a full cycle and the averaged state-vector is finally obtained from (2.21).

$$z(t_0 + T) = \tilde{\phi}_m \tilde{\phi}_{m-1} \dots \tilde{\phi}_1 z(t_0) = \left[\begin{array}{c} x(t_0) \\ \hline 1 \\ \hline x_{avg} \end{array} \right]$$
(2.21)

where:

$$\tilde{\phi}_i = e^{\tilde{A}_i d_i T}$$
(2.22)

2.3.3.2 Harmonics analysis

The last application of the cyclic method here evaluated is the harmonics analysis. Using the Fourier theorem, a periodic function can be decomposed into an infinite sum of complex exponentials functions. Therefore, the periodic state-vector previously obtained is decomposed as follows:

$$x(t) = \sum_{k=-\infty}^{\infty} c_k e^{jk\omega t} \quad (2.23)$$

where $\omega = \frac{2\pi}{T}$, and c_k is the Fourier coefficient vector for the k^{th} harmonic defined by:

$$c_k = \frac{1}{T} \int_{t_0}^{t_0+T} x(t) e^{-jk\omega t} dt \quad (2.24)$$

Since the system analysed here is piecewise linear, the integral from (2.24) is separated into a sum of integrals for each mode i and the state-vector $x(t)$ is replaced by the augmented vector $\hat{x}(t)$. Consequently, for a system with m modes:

$$\hat{c}_k = \frac{1}{T} \sum_{i=1}^m \int_{t_{i-1}}^{t_i} e^{\hat{A}_i(t-t_{i-1})} \hat{x}(t_{i-1}) e^{-jk\omega t} dt \quad (2.25)$$

Equation (2.25) is reorganized splitting the complex exponential $e^{-jk\omega t}$ into two parts, resulting in the following equation:

$$\hat{c}_k = \sum_{i=1}^m \int_{t_{i-1}}^{t_i} \frac{1}{T} e^{-jk\omega t_{i-1}} e^{(\hat{A}_i - jk\omega I)(t-t_{i-1})} \hat{x}(t_{i-1}) dt \quad (2.26)$$

From (2.26) new variables $v_k(t)$ and $w_k(t)$ are defined in (2.27) in (2.28).

$$v_k(t) = e^{(\hat{A}_i - jk\omega I)(t-t_{i-1})} \hat{x}(t_{i-1})$$

$$w_k(t_i) = \int_{t_{i-1}}^{t_i} \frac{1}{T} e^{-jk\omega t_{i-1}} e^{(\hat{A}_i - jk\omega I)(t-t_{i-1})} \hat{x}(t_{i-1}) dt \quad (2.27)$$

$$\begin{cases} \dot{v}_k(t) = (\hat{A}_i - jk\omega I)v_k(t) \\ \dot{w}_k(t) = \frac{1}{T}e^{-jk\omega t_{i-1}}v_k(t) \end{cases} \quad (2.28)$$

where $v_k(t_{i-1}) = \hat{x}(t_{i-1})$ and $w_k(t_{i-1}) = 0$ are the initial conditions.

To simplify the solution, a new fictitious system is defined combining variables $v_k(t)$ and $w_k(t)$.

$$\dot{\delta}_k(t) = \hat{A}_{i,k}\delta_k(t) \quad (2.29)$$

where:

$$\delta_k(t) = \begin{bmatrix} v_k(t) \\ w_k(t) \end{bmatrix}$$

$$\hat{A}_{i,k} = \left[\begin{array}{c|c} \hat{A}_i - jk\omega I & 0 \\ \hline \frac{1}{T}e^{-jk\omega t_{i-1}}I & 0 \end{array} \right] \quad (2.30)$$

The system solution is defined in (2.31).

$$\begin{bmatrix} v_k(t_i) \\ w_k(t_i) \end{bmatrix} = e^{\hat{A}_{i,k}d_i T} \zeta(t_{i-1}) \quad (2.31)$$

where

$$\zeta(t_i) = \begin{bmatrix} \hat{x}(t_i) \\ 0 \end{bmatrix} \quad (2.32)$$

Comparing (2.26) and (2.27) it is possible to calculate the Fourier coefficients from the sum of $w_k(t_i)$ for all m modes.

$$\hat{c}_k = \sum_{i=1}^m w_k(t_i) \quad (2.33)$$

where $\hat{c}_k = \begin{bmatrix} c_k \\ 0 \end{bmatrix}$.

Based on the equation description presented in this section, the methodology for application of the cyclic-averaging method is summarized in the following steps:

1. Definition of circuit parameters, matrices A_i and B_i , number of modes ($i = 1, \dots, m$) and duty cycles d_i .
2. Calculation of \hat{A}_i using (2.9) and $\hat{\phi}_i$ from (2.12).
3. Calculation of ϕ_i and Γ_i from (2.12).
4. Calculation of ϕ_{tot} and Γ_{tot} from (2.15).
5. Calculation of $x(t_0)$ using (2.14).
6. Definition of $\hat{x}(t_0), \hat{x}(t_1), \dots, \hat{x}(t_m)$ using (2.10) and (2.11).
7. The values of the state-variables at the transition of each mode are defined, since $\hat{x}(t_i) = \begin{bmatrix} x(t_i) \\ 1 \end{bmatrix}$.

To calculate the average value of the state-variables in a full cycle the following steps are furtherly taken:

8. Calculation of \tilde{A}_i using (2.19).
9. Calculation of $\tilde{\phi}_i$ using (2.22) and $z(t_0)$ from (2.20).
10. The averaged state-vector is calculated from (2.21).

For harmonics calculation:

11. Calculation of $\hat{A}_{i,k}$ for all modes ($i = 1, \dots, m$) using (2.30).
12. Calculation of the Fourier coefficient vector for the k^{th} harmonic, c_k , from (2.31) and (2.33).

The cyclic-averaging is an attractive technique due to the rapid and accurate analysis. As previously shown in [96], the accuracy of the cyclic method is close to component-based simulations (Spice) but requiring $1/10,000^{\text{th}}$ of the computation time when analysing 3rd order LCC converters. The main drawback of this method, however, is the need for a priori knowledge of the circuit's behaviour during a cycle for the determination of the operation modes and calculation of duty cycles [76]. This analysis is required since the converter's behaviour and number of modes change depending on the choice of modulation and various circuit's variables, as the operating frequency and bridge/legs phase-shift angles.

2.4 Conclusions

In this chapter a literature review was conducted in fundamental topics for the development of this research. The most popular topologies of DC-DC converters applied to wired and wireless bidirectional charging applications were described and potential modelling techniques used to describe the behaviour of these converters were evaluated.

Based on the review of the DC-DC converters, the CLLC resonant converter was selected as a potential topology to be furtherly analysed due to its improved performance in bidirectional operation. From the modelling techniques described, the cyclic-averaging method, previously applied to analyse LCLC, LCC and LLC unidirectional converters, stands out for the accuracy and low execution time. Therefore, the cyclic analysis will be applied here to model a bidirectional CLLC converter operating under frequency and phase-shift modulations in Chapters 4 and 5, respectively. Due to the low complexity of the topology and lack of this analysis in the literature, the cyclic-averaging method will be applied first to model a Dual Active Bridge converter in the next chapter.

Considering the wireless topologies, the circuit of a LC series compensated converter shows a considerable similarity to the CLLC converter, therefore, in Chapter 7 the models obtained for the CLLC converter will be adapted for the analysis of a wireless converter with series compensation.

2.5 References

- [1] K. L. Jorgensen, M. C. Mira, Z. Zhang, and M. A. E. Andersen, "Review of high efficiency bidirectional DC-DC topologies with high voltage gain," in *2017 52nd International Universities Power Engineering Conference, UPEC 2017*, 2017, pp. 1–6.
- [2] P. He and A. Khaligh, "Comprehensive analyses and comparison of 1 kW isolated DC-DC converters for bidirectional EV charging systems," *IEEE Transactions on Transportation Electrification*, vol. 3, no. 1, pp. 147–156, 2017.
- [3] Y. Du, S. Lukic, B. Jacobson, and A. Huang, "Review of high power isolated bi-directional DC-DC converters for PHEV/EV DC charging infrastructure," in *2011 IEEE Energy Conversion Congress and Exposition*, 2011, pp. 553–560.
- [4] R. W. De Doncker, D. M. Divan, and M. H. Kheraluwala, "A three-phase soft-switched high power density Dc/Dc converter for high power applications," *Conference Record of the 1988 IEEE Industry Applications Society Annual Meeting*, vol. 1, pp. 796–805, 1988.
- [5] M. H. Kheraluwala, R. W. Gascoigne, D. M. Divan, and E. D. Baumann, "Performance characterization of a high-power dual active bridge dc-to-dc converter," *IEEE Transactions on Industry Applications*, vol. 28, no. 6, pp. 1294–1301, 1992.
- [6] F. Krismer and J. W. Kolar, "Efficiency-optimized high-current dual active bridge converter for automotive applications," *IEEE Transactions on Industrial Electronics*, vol. 59, no. 7, pp. 2745–2760, 2012.
- [7] G. Xu, D. Sha, J. Zhang, and X. Liao, "Unified boundary trapezoidal modulation control utilizing fixed duty cycle compensation and magnetizing current design for dual active bridge DC-DC converter," *IEEE Transactions on Power Electronics*, vol. 8993, no. c, pp. 1–1, 2016.
- [8] R. T. Naayagi, A. J. Forsyth, and R. Shuttleworth, "High-power bidirectional DC-DC converter for aerospace applications," *IEEE Transactions on Power Electronics*, vol. 27, no. 11, pp. 4366–4379, 2012.
- [9] R. T. Naayagi and A. J. Forsyth, "Bidirectional DC-DC converter for aircraft electric energy storage systems," *5th IET International Conference on Power Electronics, Machines and Drives (PEMD 2010)*, pp. 1–6, 2010.
- [10] R. J. Ferreira, L. M. Miranda, R. E. Araújo, and J. P. Lopes, "A new bi-directional charger for vehicle-to-grid integration," *2nd IEEE PES International Conference and Exhibition on Innovative Smart Grid Technologies*, pp. 1–5, 2011.

- [11] W. Yen-Ching, W. Yen-Chun, and L. Tzung-Lin, "Design and implementation of a bidirectional isolated dual-active-bridge-based DC/DC converter with dual-phase-shift control for electric vehicle battery," *2013 IEEE Energy Conversion Congress and Exposition*, pp. 5468–5475, 2013.
- [12] S. Inoue and H. Akagi, "A bidirectional DC-DC converter for an energy storage system with galvanic isolation," *IEEE Transactions on Power Electronics*, vol. 22, no. 6, pp. 2299–2306, 2007.
- [13] H. Bai, C. C. Mi, and S. Gargies, "The short-time-scale transient processes in high-voltage and high-power isolated bidirectional dc-dc converters," *IEEE Transactions on Power Electronics*, vol. 23, no. 6, pp. 2648–2656, 2008.
- [14] G. Xu, D. Sha, Y. Xu, and X. Liao, "Dual-transformer-based DAB converter with wide ZVS range for wide voltage conversion gain application," *IEEE Transactions on Industrial Electronics*, vol. 65, no. 4, pp. 3306–3316, 2018.
- [15] S. Zengin and M. Boztepe, "A novel current modulation method to eliminate low frequency harmonics in single-stage dual active bridge AC/DC converter," *IEEE Transactions on Industrial Electronics*, vol. 67, no. 2, pp. 1048–1058, 2019.
- [16] F. Krismer and J. W. Kolar, "Accurate small-signal model for the digital control of an automotive bidirectional dual active bridge," *IEEE Transactions on Power Electronics*, vol. 24, no. 12, pp. 2756–2768, 2009.
- [17] G. G. Oggier, G. O. Garcia, and A. R. Oliva, "Modulation strategy to operate the dual active bridge DC-DC converter under soft switching in the whole operating range," *IEEE Transactions on Power Electronics*, vol. 26, no. 4, pp. 1228–1236, 2011.
- [18] T. Hirose and H. Matsuo, "A consideration of bidirectional superposed dual active bridge dc-dc converter," *2nd International Symposium on Power Electronics for Distributed Generation Systems, PEDG 2010*, pp. 39–46, 2010.
- [19] B. Zhao, Q. Song, and W. Liu, "Power characterization of isolated bidirectional dual-active-bridge dc-dc converter with dual-phase-shift control," *IEEE Transactions on Power Electronics*, vol. 27, no. 9, pp. 4172–4176, 2012.
- [20] H. Bai and C. Mi, "Eliminate reactive power and increase system efficiency of isolated bidirectional dual-active-bridge dc-dc converters using novel dual-phase-shift control," *IEEE Transactions on Power Electronics*, vol. 23, no. 6, pp. 2905–2914, 2008.
- [21] K. Wu, C. W. De Silva, and W. G. Dunford, "Stability analysis of isolated bidirectional dual active full-bridge DC-DC converter with triple phase-shift control," *IEEE Transactions on Power Electronics*, vol. 27, no. 4, pp. 2007–2017, 2012.

- [22] A. Tong, L. Hang, G. Li, X. Jiang, and S. Gao, "Modeling and analysis of a Dual-Active-Bridge-isolated bidirectional DC/DC converter to minimize RMS current with whole operating range," *IEEE Transactions on Power Electronics*, vol. 33, no. 6, pp. 5302–5316, 2018.
- [23] S. S. Muthuraj, V. K. Kanakesh, P. Das, and S. K. Panda, "Triple Phase Shift Control of an LLL Tank Based Bidirectional Dual Active Bridge Converter," *IEEE Transactions on Power Electronics*, vol. 32, no. 10, pp. 8035–8053, 2017.
- [24] A. A. S. Mohamed, T. Youssef, and O. Mohammed, "Vehicle side predictive power-flow control of bidirectional WPT system for EV ancillary services," *2017 IEEE Applied Power Electronics Conference and Exposition (APEC)*, pp. 3211–3217, 2017.
- [25] B. Zhao, Q. Song, W. Liu, and Y. Sun, "Overview of dual-active-bridge isolated bidirectional DC-DC converter for high-frequency-link power-conversion system," *IEEE Transactions on Power Electronics*, vol. 29, no. 8, pp. 4091–4106, 2014.
- [26] N. Hou and Y. Li, "Overview and Comparison of Modulation and Control Strategies for Non-Resonant Single-Phase Dual-Active-Bridge dc-dc Converter," *IEEE Transactions on Power Electronics*, pp. 1–23, 2019.
- [27] H. Zhou and A. M. Khambadkone, "Hybrid modulation for dual-active-bridge bidirectional converter with extended power range for ultracapacitor application," *IEEE Transactions on Industry Applications*, vol. 45, no. 4, pp. 1434–1442, 2009.
- [28] F. Krismer, S. Round, and J. W. Kolar, "Performance optimization of a high current dual active bridge with a wide operating voltage range," *PESC Record - IEEE Annual Power Electronics Specialists Conference*, pp. 1–7, 2006.
- [29] J. Hong, Y. Liu, and J. Yin, "Modulation Strategy for Optimized Transient Performance of Dual Active Bridge Converter under Reverse of Power Flow Direction," *2019 IEEE International Conference on Industrial Technology (ICIT)*, pp. 510–514, 2019.
- [30] C. Gould, K. Colombage, J. Wang, D. Stone, and M. Foster, "A comparative study of on-board bidirectional chargers for electric vehicles to support vehicle-to-grid power transfer," *IEEE 10th International Conference on Power Electronics and Drive Systems (PEDS)*, pp. 639–644, 2013.
- [31] M. Arazi, A. Payman, M. B. Camara, and B. Dakyo, "Study of different topologies of DC-DC resonant converters for renewable energy applications," *13th International Conference on Ecological Vehicles and Renewable Energies, EVER 2018*, pp. 1–6, 2018.
- [32] B. Y. Luan and X. Li, "A new control strategy to reduce circulation current for a

- bidirectional resonant converter,” *2016 IEEE 8th International Power Electronics and Motion Control Conference, IPEMC-ECCE Asia 2016*, pp. 3477–3482, 2016.
- [33] L. Corradini, D. Seltzer, D. Bloomquist, R. Zane, D. Maksimović, and B. Jacobson, “Minimum current operation of bidirectional dual-bridge series resonant DC/DC converters,” *IEEE Transactions on Power Electronics*, vol. 27, no. 7, pp. 3266–3276, 2012.
- [34] X. Li and A. K. S. Bhat, “Analysis and design of high-frequency isolated dual-bridge series resonant DC/DC converter,” *IEEE Transactions on Power Electronics*, vol. 25, no. 4, pp. 850–862, 2010.
- [35] H. P. Park, M. Kim, and J. H. Jung, “Investigation of Zero Voltage Switching Capability for Bidirectional Series Resonant Converter Using Phase-Shift Modulation,” *IEEE Transactions on Power Electronics*, vol. 34, no. 9, pp. 8842–8858, 2019.
- [36] E. Prieto-Araujo, S. F. Fekriasl, and O. Gomis-Bellmunt, “Control and experimental validation of a Dual Active Bridge Series Resonant Converter,” *2015 IEEE 6th International Symposium on Power Electronics for Distributed Generation Systems, PEDG 2015*, pp. 1–8, 2015.
- [37] F. Krismer, J. Biela, and J. W. Kolar, “A comparative evaluation of isolated bi-directional DC/DC converters with wide input and output voltage range,” *Fourtieth IAS Annual Meeting. Conference Record of the 2005 Industry Applications Conference*, vol. 1, pp. 599–606, 2005.
- [38] W. Han and L. Corradini, “General closed-form zvs analysis of dual-bridge series resonant DC-DC converters,” *IEEE Transactions on Power Electronics*, vol. 34, no. 9, pp. 9289–9302, 2019.
- [39] M. Yaqoob, K. H. Loo, and Y. M. Lai, “Modeling the effect of dead-Time on the soft-switching characteristic of variable-frequency modulated series-resonant DAB converter,” *2017 IEEE 18th Workshop on Control and Modeling for Power Electronics, COMPEL 2017*, 2017.
- [40] G. Pledl, M. Tauer, and D. Buecherl, “Theory of operation, design procedure and simulation of a bidirectional LLC resonant converter for vehicular applications,” *2010 IEEE Vehicle Power and Propulsion Conference, VPPC 2010*, pp. 1–5, 2010.
- [41] C. Liu, J. W. Smiee, K. Colombage, C. Gould, B. Sen, and D. Stone, “Current Ripple Reduction in 4kW LLC Resonant Converter Based Battery Charger for Electric Vehicles,” *2015 IEEE Energy Conversion Congress and Exposition (ECCE)*, pp. 6014–6021, 2015.
- [42] S. Zong, H. Luo, W. Li, Y. Deng, and X. He, “High-power bidirectional resonant

- DC–DC converter with equivalent switching frequency doubler,” *IET Renewable Power Generation*, vol. 10, no. 6, pp. 834–842, 2016.
- [43] C. Liu, J. Wang, K. Colombage, C. Gould, and B. Sen, “A CLLC Resonant Converter Based Bidirectional EV Charger with Maximum Efficiency Tracking,” *8th IET International Conference on Power Electronics, Machines and Drives (PEMD 2016)*, pp. 1–6, 2016.
- [44] Z. U. Zahid, Z. M. Dalala, R. Chen, B. Chen, and J. S. Lai, “Design of bidirectional DC-DC resonant converter for Vehicle-to-Grid (V2G) applications,” *IEEE Transactions on Transportation Electrification*, vol. 1, no. 3, pp. 232–244, 2015.
- [45] W. Chen, P. Rong, and Z. Lu, “Snubberless bidirectional DC-DC converter with new CLLC resonant tank featuring minimized switching loss,” *IEEE Transactions on Industrial Electronics*, vol. 57, no. 9, pp. 3075–3086, 2010.
- [46] R. P. Twiname, D. J. Thrimawithana, U. K. Madawala, and C. A. Baguley, “A Dual-Active Bridge Topology with a Tuned CLC Network,” *IEEE Transactions on Power Electronics*, vol. 30, no. 12, pp. 6543–6550, 2015.
- [47] W. L. Malan, D. M. Vilathgamuwa, G. R. Walker, D. J. Thrimawithana, and U. K. Madawala, “Novel modulation strategy for a CLC resonant dual active bridge,” *9th International Conference on Power Electronics and ECCE Asia (ICPE-ECCE Asia)*, pp. 759–764, 2015.
- [48] U. K. Madawala and D. J. Thrimawithana, “A bidirectional inductive power interface for electric vehicles in V2G systems,” *IEEE Transactions on Industrial Electronics*, vol. 58, no. 10, pp. 4789–4796, 2011.
- [49] A. A. S. Mohamed, A. Berzoy, and O. Mohammed, “Power Flow Modeling of Wireless Power Transfer for EVs Charging and Discharging in V2G Applications,” *2015 IEEE Vehicle Power and Propulsion Conference (VPPC)*, pp. 1–6, 2015.
- [50] L. Zhao, D. J. Thrimawithana, and U. K. Madawala, “A hybrid bi-directional IPT system with improved spatial tolerance,” *2015 IEEE 2nd International Future Energy Electronics Conference, IFEEEC 2015*, 2015.
- [51] SAE International, “J2954™ Wireless Power Transfer for Light-Duty Plug-In/Electric Vehicles and Alignment Methodology,” *Surface Vehicle Information Report*, 2016.
- [52] A. A. S. Mohamed, A. Berzoy, F. G. N. Nogueira de Almeida, and O. Mohammed, “Modeling and Assessment Analysis of Various Compensation Topologies in Bidirectional IWPT System for EV Applications,” *IEEE Transactions on Industry Applications*, vol. 53, no. 5, pp. 4973–4984, 2017.

- [53] W. Zhang, S. C. Wong, C. K. Tse, and Q. Chen, "Design for efficiency optimization and voltage controllability of series-series compensated inductive power transfer systems," *IEEE Transactions on Power Electronics*, vol. 29, no. 1, pp. 191–200, 2014.
- [54] Y. Zhang, T. Kan, Z. Yan, and C. C. Mi, "Frequency and Voltage Tuning of Series-Series Compensated Wireless Power Transfer System to Sustain Rated Power under Various Conditions," *IEEE Journal of Emerging and Selected Topics in Power Electronics*, vol. 7, no. 2, pp. 1311–1317, 2019.
- [55] Z. U. Zahid *et al.*, "Modeling and control of series-series compensated inductive power transfer system," *IEEE Journal of Emerging and Selected Topics in Power Electronics*, 2015.
- [56] S. Wang, J. Chen, Z. Hu, C. Rong, and M. Liu, "Optimisation design for series-series dynamic WPT system maintaining stable transfer power," *IET Power Electronics*, vol. 10, no. 9, pp. 987–995, 2017.
- [57] A. A. S. Mohamed, F. G. N. De Almeida, and O. Mohammed, "Harmonics-based steady-state mathematical model of bidirectional inductive wireless power transfer system in V2G applications," *2016 IEEE Transportation Electrification Conference and Expo, ITEC 2016*, 2016.
- [58] D. J. Thrimawithana, U. K. Madawala, and Y. Shi, "Design of a bi-directional inverter for a wireless V2G system," *2010 IEEE International Conference on Sustainable Energy Technologies, ICSET 2010*, 2010.
- [59] L. Zhao, D. J. Thrimawithana, and U. K. Madawala, "A comparison of LCL and LC bi-directional inductive power transfer systems," *Proceedings - 2014 International Power Electronics and Application Conference and Exposition, IEEE PEAC 2014*, pp. 766–771, 2014.
- [60] S. Li and C. Mi, "Wireless Power Transfer for Electric Vehicle Applications," *IEEE Journal of Emerging and Selected Topics in Power Electronics*, vol. 3, no. 1, pp. 4–17, 2014.
- [61] C. Liu, C. Jiang, and C. Qiu, "Overview of coil designs for wireless charging of electric vehicle," *2017 IEEE PELS Workshop on Emerging Technologies: Wireless Power Transfer, WoW 2017*, pp. 15–18, 2017.
- [62] G. A. Covic and J. T. Boys, "Modern trends in inductive power transfer for transportation applications," *IEEE Journal of Emerging and Selected Topics in Power Electronics*, vol. 1, no. 1, pp. 28–41, 2013.
- [63] A. Zaheer, H. Hao, G. A. Covic, and D. Kacprzak, "Investigation of multiple decoupled coil primary pad topologies in lumped IPT systems for interoperable electric vehicle charging," *IEEE Transactions on Power Electronics*, vol. 30, no.

- 4, pp. 1937–1955, 2015.
- [64] A. A. S. Mohamed, A. Berzoy, and O. Mohammad, “Magnetic design considerations of bidirectional inductive wireless power transfer system for EV applications,” *IEEE Transactions on Magnetics*, vol. 53, no. 6, pp. 1–5, 2017.
 - [65] M. Budhia, G. Covic, and J. Boys, “A new IPT magnetic coupler for electric vehicle charging systems,” *IECON Proceedings (Industrial Electronics Conference)*, pp. 2487–2492, 2010.
 - [66] M. Budhia, J. T. Boys, G. A. Covic, and C. Y. Huang, “Development of a single-sided flux magnetic coupler for electric vehicle IPT charging systems,” *IEEE Transactions on Industrial Electronics*, vol. 60, no. 1, pp. 318–328, 2013.
 - [67] A. Zaheer, D. Kacprzak, and G. A. Covic, “A bipolar receiver pad in a lumped IPT system for electric vehicle charging applications,” in *2012 IEEE Energy Conversion Congress and Exposition, ECCE 2012*, 2012, pp. 283–290.
 - [68] F. Lu, H. Zhang, H. Hofmann, and C. Mi, “A high efficiency 3.3 kW loosely-coupled wireless power transfer system without magnetic material,” *2015 IEEE Energy Conversion Congress and Exposition, ECCE 2015*, pp. 2282–2286, 2015.
 - [69] W. Li, H. Zhao, S. Li, J. Deng, T. Kan, and C. C. Mi, “Integrated LCC Compensation Topology for Wireless Charger in Electric and Plug-in Electric Vehicles,” *IEEE Transactions on Industrial Electronics*, vol. 62, no. 7, pp. 4215–4225, 2015.
 - [70] J. Tritschler, S. Reichert, and B. Goeldi, “A practical investigation of a high power, bidirectional charging system for electric vehicles,” *2014 16th European Conference on Power Electronics and Applications, EPE-ECCE Europe 2014*, no. Fig 1, pp. 1–7, 2014.
 - [71] R. L. Steigerwald, “A Comparison of Half-Bridge Resonant Converter,” *IEEE Transactions on Power Electronics*, vol. 3, no. 2, pp. 174–182, 1988.
 - [72] C. Gould, “Rapid Analysis and Design of CLL Resonant Power Converters,” PhD Thesis. University of Sheffield, 2006.
 - [73] M. P. Foster, “Analysis and Design of High-order Resonant Power Converters,” PhD Thesis. University of Sheffield, 2003.
 - [74] A. J. Forsyth, G. A. Ward, and S. V. Mollov, “Extended Fundamental Frequency Analysis of the LCC Resonant Converter,” *IEEE Transactions on Power Electronics*, vol. 18, no. 6, pp. 1286–1292, 2003.
 - [75] A. J. Gilbert, D. A. Stone, and C. M. Bingham, “Rapid design of LCC current-output resonant converters with reduced electrical stresses,” *Electronics Letters*, vol. 41, no. 6, p. 365, 2005.

- [76] C. Gould, C. M. Bingham, D. A. Stone, and M. P. Foster, "CLL resonant converters with output short-circuit protection," *IEE Proceedings-Electric Power Applications*, vol. 152, no. 5, pp. 1296–1306, 2005.
- [77] J. Jung and J. Kwon, "Theoretical analysis and optimal design of LLC resonant converter," *2007 European Conference on Power Electronics and Applications*, pp. 1–10, 2007.
- [78] J. H. Jung, H. S. Kim, M. H. Ryu, and J. W. Baek, "Design methodology of bidirectional CLLC resonant converter for high-frequency isolation of DC distribution systems," *IEEE Transactions on Power Electronics*, vol. 28, no. 4, pp. 1741–1755, 2013.
- [79] C. Liu, J. Wang, K. Colombage, C. Gould, and B. Sen, "A CLLC Resonant Converter Based Bidirectional EV Charger with Maximum Efficiency Tracking," *8th IET International Conference on Power Electronics, Machines and Drives (PEMD 2016)*, pp. 1–6, 2016.
- [80] K. Song, Z. Li, J. Jiang, and C. Zhu, "Constant Current/Voltage Charging Operation for Series-Series and Series-Parallel Compensated Wireless Power Transfer Systems Employing Primary-Side Controller," *IEEE Transactions on Power Electronics*, vol. 33, no. 9, pp. 8065–8080, 2018.
- [81] E. Asa, K. Colak, D. Czarkowski, and B. Tamyurek, "Efficiency Analysis of a Bi-directional DC / DC Converter for Wireless Energy Transfer Applications," in *2015 IEEE Energy Conversion Congress and Exposition (ECCE)*, 2015, pp. 594–598.
- [82] J. G. Hayes and M. G. Egan, "Rectifier-compensated fundamental mode approximation analysis of the series parallel LCLC family of resonant converters with capacitive output filter and voltage-source load," in *30th Annual IEEE Power Electronics Specialists Conference. Record*, 1999, pp. 1030–1036.
- [83] H. I. Sewell, M. P. Foster, C. M. Bingham, D. A. Stone, D. Hente, and D. Howe, "Analysis of voltage output LCC resonant converters, including boost mode operation," *IEE Proceedings - Electric Power Applications*, vol. 150, no. 6, pp. 673–679, 2003.
- [84] R. W. Erickson and D. Maksimovic, *Fundamentals of power electronics*. 2001.
- [85] R. D. Middlebrook and S. Cuk, "A general unified approach to modelling switching-converter power stages," in *1976 IEEE Power Electronics Specialists Conference*, 1976, vol. 42, no. 6, pp. 18–34.
- [86] R. Dirkman, "Generalized state space averaging," *1983 IEEE Power Electronics Specialists Conference*, pp. 283–294, 1983.
- [87] W. L. Malan, D. M. Vilathgamuwa, G. R. Walker, D. J. Thrimawithana, and U.

- K. Madawala, "Modeling and Control of a CLC Resonant Dual Active Bridge," *IEEE Transactions on Power Electronics*, vol. 31, no. 10, pp. 7297–7310, 2016.
- [88] Y. Zhang and P. C. Sen, "D-Q models for resonant converters," *PESC Record - IEEE Annual Power Electronics Specialists Conference*, vol. 3, pp. 1749–1753, 2004.
- [89] A. E. Ruehli and A. L. Sangiovanni-Vincentelli, "The Waveform Relaxation Method for Time-Domain Analysis of Large Scale Integrated Circuits," *IEEE Transactions on Computer-Aided Design of Integrated Circuits and Systems*, vol. 1, no. 3, pp. 131–145, 1982.
- [90] R. A. Saleh and A. Richard Newton, "The Exploitation of Latency and Multirate Behavior Using Nonlinear Relaxation for Circuit Simulation," *IEEE Transactions on Computer-Aided Design of Integrated Circuits and Systems*, vol. 8, no. 12, pp. 1286–1298, 1989.
- [91] J. Sun and H. Grotstollen, "Fast Time-Domain Simulation by Waveform Relaxation Methods," *IEEE Transactions on Circuits and Systems*, vol. 44, no. 8, pp. 660–666, 1997.
- [92] M. P. Foster, H. I. Sewell, C. M. Bingham, and D. A. Stone, "State-variable modelling of LCC voltage-output resonant converters," *Electronics Letters*, vol. 37, no. 17, pp. 1065–1066, 2001.
- [93] Y. A. Ang, M. P. Foster, C. M. Bingham, D. A. Stone, H. I. Sewell, and D. Howe, "Analysis of 4th-order LCLC resonant power converters," *EE Proceedings - Electric Power Applications*, vol. 151, no. 2, pp. 169–181, 2004.
- [94] C. Gould, D. A. Stone, M. P. Foster, and C. Bingham, "State-variable modelling of CLL resonant converters," in *Second International Conference on Power Electronics, Machines and Drives (PEMD 2004)*, 2004, pp. 214–219.
- [95] H. R. Visser and P. P. J. van den Bosch, "Modelling of periodically switching networks," *PESC '91 Record 22nd Annual IEEE Power Electronics Specialists Conference*, no. 1, pp. 67–73, 1991.
- [96] M. P. Foster, H. I. Sewell, C. M. Bingham, D. A. Stone, D. Hente, and D. Howe, "Cyclic-averaging for high-speed analysis of resonant converters," *IEEE Transactions on Power Electronics*, vol. 18, no. 4, pp. 985–993, 2003.

3 Cyclic-Averaging Analysis of Dual Active Bridge Converter

3.1 Introduction

Following the literature review presented in the last chapter, the cyclic-averaging modelling method described in Chapter 2 will now be employed to analyse a Dual Active Bridge (DAB) converter, shown in Figure 3.1. One of the main objectives of this research is to employ this modelling method for analysis of resonant CLLC converters. As explained in the previous chapter, the CLLC is a resonant variant of the DAB converter, therefore the cyclic analysis is performed here first for the DAB converter, a simpler topology.

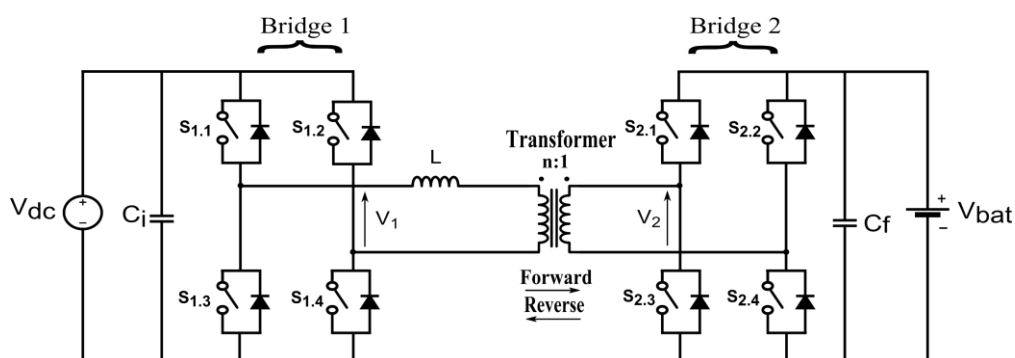


Figure 3.1: Dual Active Bridge converter

In this chapter, the DAB converter is considered to be operating under the simplest type of phase-shift modulation: the Single Phase-Shift (SPS) [1], [2]. The drain-to-source voltages of switches $S_{1.3}$ ($v_{S_{1.3}}$) and $S_{1.4}$ ($v_{S_{1.4}}$) and resulting primary and secondary bridge voltages (v_1 and v_2) for a converter operating in forward mode are presented in Figure 3.2.

The bridge waveforms have fixed frequency and duty cycle of 50%. The phase-shift angle between primary and secondary bridges (ϕ) is the only variable manipulated

to control the power flow direction and magnitude. The power flow direction is determined by the signal of the bridge phase-shift angle, forward operation occurs when v_1 leads v_2 by an angle ϕ , while reverse operation is achieved when the bridge voltage v_1 lags v_2 by an angle ϕ , with $0 \leq |\phi| \leq 90^\circ$. Maximum output power is reached when $\phi = \pm 90^\circ$.

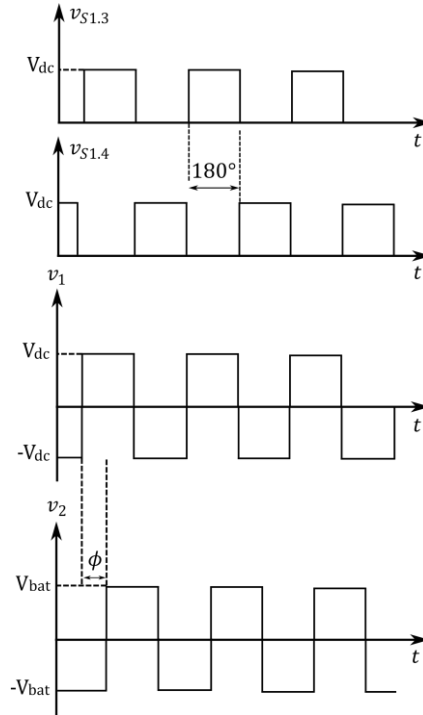


Figure 3.2: Single Phase-Shift (SPS) modulation, forward mode

3.2 State-variable description

To apply the cyclic-averaging method, the equivalent circuit of the converter must first be defined and the state-space representation must be determined. To simplify the definition of the state equations, the decomposition technique previously used for analysis of LCC converters in [3] and LLC converters in [4] will also be adopted here. For this analysis, the diagram of the DAB converter presented in Figure 3.1 is reduced to the equivalent circuits shown in Figure 3.3. The circuit is divided into two subsystems connected by a coupling equation, where the fast subsystem represents the elements with fast dynamics: the inductor and switching devices, while the slow subsystem is composed by the load and filter capacitor. The behaviour of the output bridge is represented by a coupling equation.

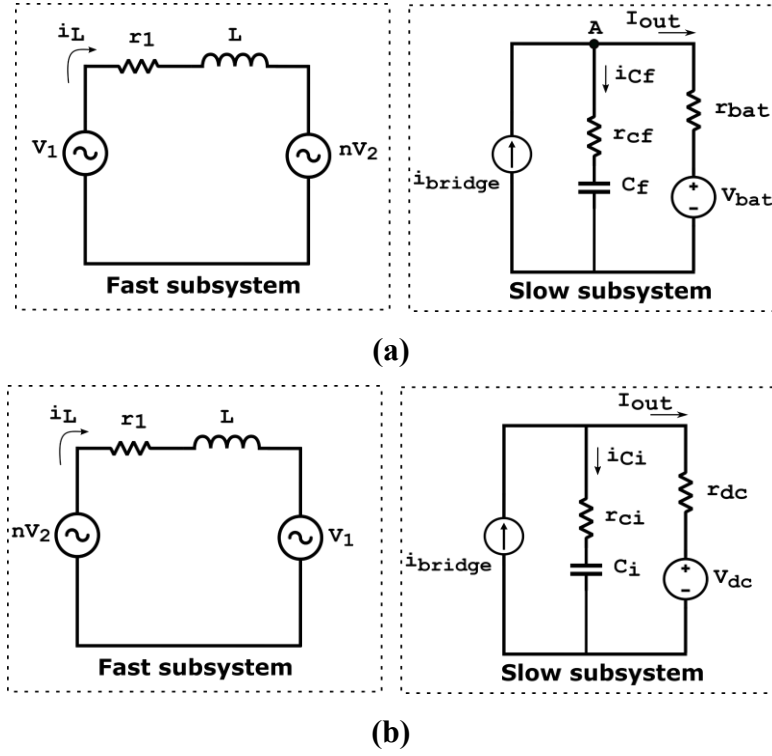


Figure 3.3: Equivalent circuits for DAB converter in (a) forward mode and (b) reverse mode

Here, the two cases of power flow direction (forward and reverse modes) are analysed separately and an equivalent circuit and equation description are obtained for each case. In forward operation, the fast subsystem is referred to primary while the slow subsystem is referred to the secondary of the transformer. For reverse operation, both fast and slow subsystems are referred to primary. The resistors r_1 and r_{cf}, r_{ci} represent the series resistance of the inductor and filter capacitors, respectively. The resistances of switching devices may be incorporated into the value of r_1 to increase accuracy. Resistors r_{dc} and r_{bat} are placed in series with the DC source and battery, respectively, representing their internal resistances or auxiliary resistances placed in the circuit for current measurement. These resistors are useful to simplify the calculation of the output current in the cyclic-averaging simulations and have a low value to prevent significant influence on the converter's output.

Considering a converter operating in forward mode, the following equation is defined from circuit analysis of the fast subsystem:

$$v_1 = v_{r1} + v_L + n v_2$$

$$v_L = L \frac{di_L}{dt} = v_1 - v_{r1} - nv_2$$

$$\frac{di_L}{dt} = \frac{v_1 - r_1 i_L - nv_2}{L}$$

(3.1)

Repeating the circuit analysis for the reverse mode circuit, the fast subsystem equation is also defined for reverse operation:

$$\frac{di_L}{dt} = \frac{nv_2 - r_1 i_L - v_1}{L}$$

(3.2)

From circuit analysis of the slow subsystem in forward mode:

$$v_{cf} + r_{cf} i_{cf} = V_{bat} + r_{bat} I_{out}$$

(3.3)

Isolating I_{out} from (3.3):

$$I_{out} = \frac{v_{cf} - V_{bat} + r_{cf} i_{cf}}{r_{bat}}$$

(3.4)

Applying Kirchhoff's current law for node A in Figure 3.3-a:

$$i_{bridge} = i_{cf} + I_{out}$$

$$i_{cf} = C_f \frac{dv_{cf}}{dt} = i_{bridge} - I_{out}$$

(3.5)

The state equation for the slow subsystem in forward mode is obtained substituting (3.4) in (3.5):

$$\frac{dv_{cf}}{dt} = \frac{V_{bat} + r_{bat} i_{bridge} - v_{cf}}{C_f (r_{bat} + r_{cf})}$$

(3.6)

Repeating the analysis for the reverse mode circuit results in:

$$\frac{dv_{Ci}}{dt} = \frac{V_{dc} + r_{dc}i_{bridge} - v_{Ci}}{C_i(r_{dc} + r_{Ci})} \quad (3.7)$$

In forward operation, the input current to the slow subsystem, i_{bridge} , is determined based on the operation of the secondary bridge. For converters operating under SPS modulation, the bridge voltages are perfect square waves, as previously shown in Figure 3.2. When the secondary bridge voltage is positive the input current to the output filter and load is equal to the inductor current referred to the secondary, but when the bridge voltage becomes negative, the input to the slow subsystem changes to the inverse of the inductor current referred to secondary. Therefore:

$$i_{bridge}(t) = \begin{cases} ni_L(t), & \text{when } v_2(t) > 0 \\ -ni_L(t), & \text{when } v_2(t) < 0 \end{cases} \quad (3.8)$$

Similar analysis is performed for reverse operation, now the output bridge is bridge 1 and the input current to the slow subsystem will depend on the state of voltage $v_1(t)$. Note that in this case the slow subsystem is referred to the primary side of the transformer.

$$i_{bridge}(t) = \begin{cases} i_L(t), & \text{when } v_1(t) > 0 \\ -i_L(t), & \text{when } v_1(t) < 0 \end{cases} \quad (3.9)$$

The differential equations obtained for fast and slow subsystems are now reorganized resulting in the following state-space representation for forward mode:

$$\frac{d}{dt} \begin{bmatrix} i_L(t) \\ v_{Cf}(t) \end{bmatrix} = \begin{bmatrix} -\frac{r_1}{L} & 0 \\ 0 & -\frac{1}{C_f(r_{bat} + r_{Cf})} \end{bmatrix} \begin{bmatrix} i_L(t) \\ v_{Cf}(t) \end{bmatrix} + \begin{bmatrix} \frac{v_1(t) - nv_2(t)}{L} \\ \frac{V_{bat} + r_{bat}i_{bridge}(t)}{C_f(r_{bat} + r_{Cf})} \end{bmatrix} \quad (3.10)$$

Similarly, for reverse mode:

$$\frac{d}{dt} \begin{bmatrix} i_L(t) \\ v_{Cf}(t) \end{bmatrix} = \begin{bmatrix} -\frac{r_1}{L} & 0 \\ 0 & -\frac{1}{C_i(r_{dc} + r_{ci})} \end{bmatrix} \begin{bmatrix} i_L(t) \\ v_{Ci}(t) \end{bmatrix} + \begin{bmatrix} \frac{nv_2(t) - v_1(t)}{L} \\ \frac{V_{dc} + r_{dc}i_{bridge}(t)}{C_i(r_{dc} + r_{ci})} \end{bmatrix} \quad (3.11)$$

The coupling equations for forward and reverse operation are given by equations (3.8) and (3.9), respectively. These are used to define the current $i_{bridge}(t)$ based on the polarity of bridge voltage $v_2(t)$ in forward operation or $v_1(t)$ in reverse operation. The behaviour of the bridge voltages is evaluated in the next section, where the converter operation will be analysed and the state-variable description here obtained will serve as base for application of the cyclic-averaging method.

3.3 Cyclic-averaging analysis

Once the state-variable model is defined, the periodic behaviour of the converter must be analysed in order to apply the cyclic-averaging method. The state-variable model obtained is a piecewise linear description that depends on the values of bridge voltages $v_1(t)$ and $v_2(t)$. The typical bridge voltages waveforms for a converter operating under SPS modulation are shown in Figure 3.4. It is observed that a cycle is divided into four operation modes: M_1 , M_2 , M_3 and M_4 . The start of a cycle in forward mode is determined by the transition of voltage v_1 from negative to positive, while for reverse operation the first mode starts when the polarity of v_2 becomes positive.

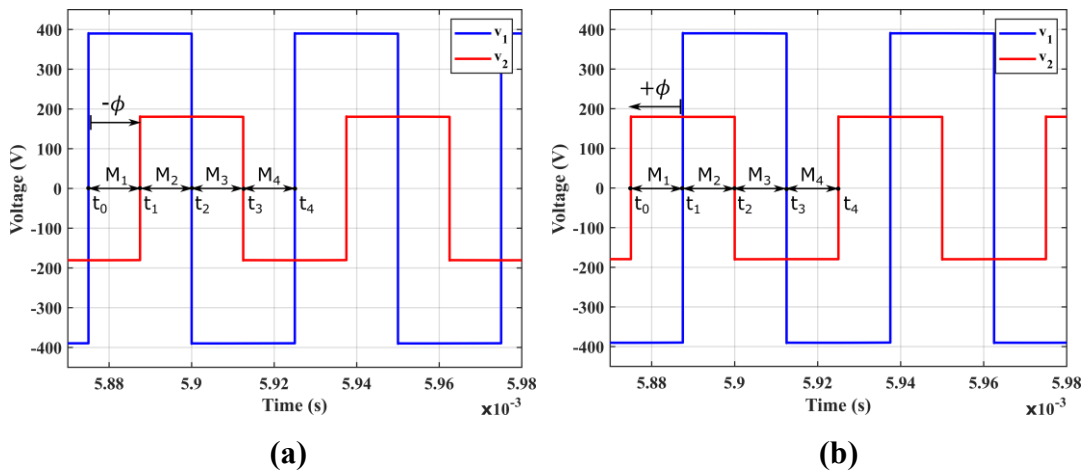


Figure 3.4: Typical waveforms of bridge voltages for DAB converters operating in (a) forward mode and (b) reverse mode

The states of variables v_1 , v_2 and i_{bridge} during each mode are defined in Tables 3.1 and 3.2. Since the resistances r_{dc} and r_{bat} are very small, the bridge voltages can be approximated to $v_1(t) = \pm V_{dc}$ and $v_2(t) = \pm V_{bat}$ for the calculation of the inductor current in the fast subsystem. Alternatively, the bridge voltage at the output side may also be approximated to $v_2(t) = \pm v_{cf}(t)$ (or $v_1(t) = \pm v_{ci}(t)$ in reverse mode) when neglecting the filter capacitor resistance. Initially, the assumption of $v_1(t) = \pm V_{dc}$ and $v_2(t) = \pm V_{bat}$ will be considered, later on, the validity of these approximations will be evaluated in the cyclic-averaging simulations and compared to the assumption of $v_2(t) = \pm v_{cf}(t)$ or $v_1(t) = \pm v_{ci}(t)$ to determine how this choice of approximation affects the results.

Table 3.1: Mode descriptions for DAB converter operating under SPS modulation, forward mode

Mode	$v_1(t)$	$v_2(t)$	$i_{bridge}(t)$ (from (3.8))
M_1	V_{dc}	$-V_{bat}$	$-ni_L(t)$
M_2	V_{dc}	V_{bat}	$ni_L(t)$
M_3	$-V_{dc}$	V_{bat}	$ni_L(t)$
M_4	$-V_{dc}$	$-V_{bat}$	$-ni_L(t)$

Table 3.2: Mode descriptions for DAB converter operating under SPS modulation, reverse mode

Mode	$v_1(t)$	$v_2(t)$	$i_{bridge}(t)$ (from (3.9))
M_1	$-V_{dc}$	V_{bat}	$-i_L(t)$
M_2	V_{dc}	V_{bat}	$i_L(t)$
M_3	V_{dc}	$-V_{bat}$	$i_L(t)$
M_4	$-V_{dc}$	$-V_{bat}$	$-i_L(t)$

The values of $v_1(t)$, $v_2(t)$ and $i_{bridge}(t)$ defined in the mode descriptions tables are now incorporated into equations (3.10) and (3.11) to obtain a linear state-variable description for each mode i as follows.

$$\frac{dx(t)}{dt} = A_i x(t) + B_i \quad (3.12)$$

where $i = 1, 2, 3, 4$ and the state-vector is $x(t) = \begin{bmatrix} i_L(t) \\ v_{Cf}(t) \end{bmatrix}$ for forward mode or $x(t) = \begin{bmatrix} i_L(t) \\ v_{Ci}(t) \end{bmatrix}$ for reverse mode.

A further requirement for the application of the cyclic-averaging method is the definition of the normalized time interval for each mode, also called duty cycle d_i . When operating under SPS modulation the values of duty cycle are easily determined based on the phase difference ϕ between primary and secondary bridge voltages. From analysis of the waveforms in Figure 3.4, the duty cycle for the first mode is defined as follows:

$$d_1 = \frac{|\phi|}{360} \quad (3.13)$$

where $0^\circ \leq |\phi| \leq 90^\circ$.

For the remaining modes, the duties are calculated from waveform symmetry:

$$d_2 = 0.5 - d_1, d_3 = d_1 \text{ and } d_4 = d_2 \quad (3.14)$$

Summarizing the analysis of the cyclic behaviour of a SPS modulated DAB converter, the dynamic and input matrices are defined as follows for a cycle starting at $t_0 = 0$, where A_{i_f} , B_{i_f} are the matrices used for forward operation and A_{i_r} , B_{i_r} for reverse operation.

Mode M_1 : when $t_0 < t < t_1 = d_1 T$:

$$A_{1_f} = \begin{bmatrix} -\frac{r_1}{L} & 0 \\ -\frac{r_{bat}n}{C_f(r_{bat} + r_{Cf})} & -\frac{1}{C_f(r_{bat} + r_{Cf})} \end{bmatrix}; B_{1_f} = \begin{bmatrix} \frac{V_{dc} + nV_{bat}}{L} \\ \frac{V_{bat}}{C_f(r_{bat} + r_{Cf})} \end{bmatrix}$$

$$A_{1_r} = \begin{bmatrix} -\frac{r_1}{L} & 0 \\ \frac{r_{dc}n}{C_i(r_{dc} + r_{ci})} & -\frac{1}{C_i(r_{dc} + r_{ci})} \end{bmatrix}; B_{1_r} = \begin{bmatrix} \frac{V_{dc} + nV_{bat}}{L} \\ V_{dc} \\ C_i(r_{dc} + r_{ci}) \end{bmatrix}$$

Mode M_2 : when $t_1 < t < t_2 = \frac{T}{2}$:

$$A_{2_f} = \begin{bmatrix} -\frac{r_1}{L} & 0 \\ \frac{r_{bat}n}{C_f(r_{bat} + r_{cf})} & -\frac{1}{C_f(r_{bat} + r_{cf})} \end{bmatrix}; B_{2_f} = \begin{bmatrix} \frac{V_{dc} - nV_{bat}}{L} \\ V_{bat} \\ C_f(r_{bat} + r_{cf}) \end{bmatrix}$$

$$A_{2_r} = \begin{bmatrix} -\frac{r_1}{L} & 0 \\ \frac{r_{dc}n}{C_i(r_{dc} + r_{ci})} & -\frac{1}{C_i(r_{dc} + r_{ci})} \end{bmatrix}; B_{2_r} = \begin{bmatrix} \frac{-V_{dc} + nV_{bat}}{L} \\ V_{dc} \\ C_i(r_{dc} + r_{ci}) \end{bmatrix}$$

Mode M_3 : when $t_2 < t < t_3 = d_1T + \frac{T}{2}$:

$$A_{3_f} = \begin{bmatrix} -\frac{r_1}{L} & 0 \\ \frac{r_{bat}n}{C_f(r_{bat} + r_{cf})} & -\frac{1}{C_f(r_{bat} + r_{cf})} \end{bmatrix}; B_{3_f} = \begin{bmatrix} \frac{-V_{dc} - nV_{bat}}{L} \\ V_{bat} \\ C_f(r_{bat} + r_{cf}) \end{bmatrix}$$

$$A_{3_r} = \begin{bmatrix} -\frac{r_1}{L} & 0 \\ \frac{r_{dc}n}{C_i(r_{dc} + r_{ci})} & -\frac{1}{C_i(r_{dc} + r_{ci})} \end{bmatrix}; B_{3_r} = \begin{bmatrix} \frac{-V_{dc} - nV_{bat}}{L} \\ V_{dc} \\ C_i(r_{dc} + r_{ci}) \end{bmatrix}$$

Mode M_4 : when $t_3 < t < t_4 = T$:

$$A_{4_f} = \begin{bmatrix} -\frac{r_1}{L} & 0 \\ \frac{r_{bat}n}{C_f(r_{bat} + r_{cf})} & -\frac{1}{C_f(r_{bat} + r_{cf})} \end{bmatrix}; B_{4_f} = \begin{bmatrix} \frac{-V_{dc} + nV_{bat}}{L} \\ V_{bat} \\ C_f(r_{bat} + r_{cf}) \end{bmatrix}$$

$$A_{4_r} = \begin{bmatrix} -\frac{r_1}{L} & 0 \\ \frac{r_{dc}n}{C_i(r_{dc} + r_{ci})} & -\frac{1}{C_i(r_{dc} + r_{ci})} \end{bmatrix}; B_{4_r} = \begin{bmatrix} \frac{V_{dc} - nV_{bat}}{L} \\ \frac{V_{dc}}{C_i(r_{dc} + r_{ci})} \end{bmatrix}$$

3.4 Simulation results

Once the duty ratios and dynamic and input matrices are defined for each mode and for both power flow directions, the equation description presented in Chapter 2 for application of the cyclic-averaging method can now be used, following the methodology described at the end of section 2.3.3. The simulation of the cyclic-averaging model is performed in the MATLAB environment.

The validation of the cyclic-averaging model results is performed through comparison with a Spice-based circuit simulation, using the software LTspice. The converter is simulated considering the transformer and switches ideal and neglecting the input and output filter capacitor resistances. The circuit parameters used in the simulation stage, listed in Table 3.3, are chosen based on the DAB design developed in [5] for a 7kW converter.

Table 3.3: Simulation parameters

Parameter	Value
DC link voltage (V_{dc})	390 V
Battery voltage (V_{bat})	180 V
Transformer turns ratio (n)	1
L	61.2 μH
r_1	0.11 Ω
r_{dc}, r_{bat}	0.01 Ω
C_i, C_f	3000 μF
f	20 kHz

Firstly, the average output current is measured considering forward and reverse operations, Spice and cyclic-averaging results are presented in Table 3.4. The phase-shift angle range analysed is from 10° to 90° with steps of 10 degrees. For the cyclic-averaging model implementation, the average value of the output filter capacitor voltage (state-variable v_{cf} or v_{ci}) is calculated and the output current is determined using equation (3.15).

$$I_{out_avg} = \frac{v_{cf_avg} - V_{bat}}{r_{bat}}, \text{ for forward operation}$$

$$I_{out_avg} = \frac{v_{ci_avg} - V_{dc}}{r_{dc}}, \text{ for reverse operation}$$

(3.15)

Table 3.4: Simulation results for SPS modulation

Phase-shift angle (ϕ)	Average output current (A)			
	Forward operation		Reverse operation	
	Spice	Cyclic-averaging	Spice	Cyclic-averaging
10°	8.655	8.668	3.541	3.531
20°	15.998	16.012	6.927	6.921
30°	22.341	22.355	9.850	9.848
40°	27.687	27.701	12.311	12.316
50°	32.037	32.051	14.314	14.323
60°	35.395	35.408	15.860	15.873
70°	37.764	37.774	16.949	16.965
80°	39.145	39.152	17.584	17.601
90°	39.541	39.545	17.767	17.782

The results from Table 3.4, also plotted in Figure 3.5, show that the cyclic-averaging model could successfully model the behaviour of the converter over the full range of SPS modulation, with accuracy similar to the Spice model. A maximum error of 0.28% was obtained when the cyclic-averaging model output current results were compared to Spice.

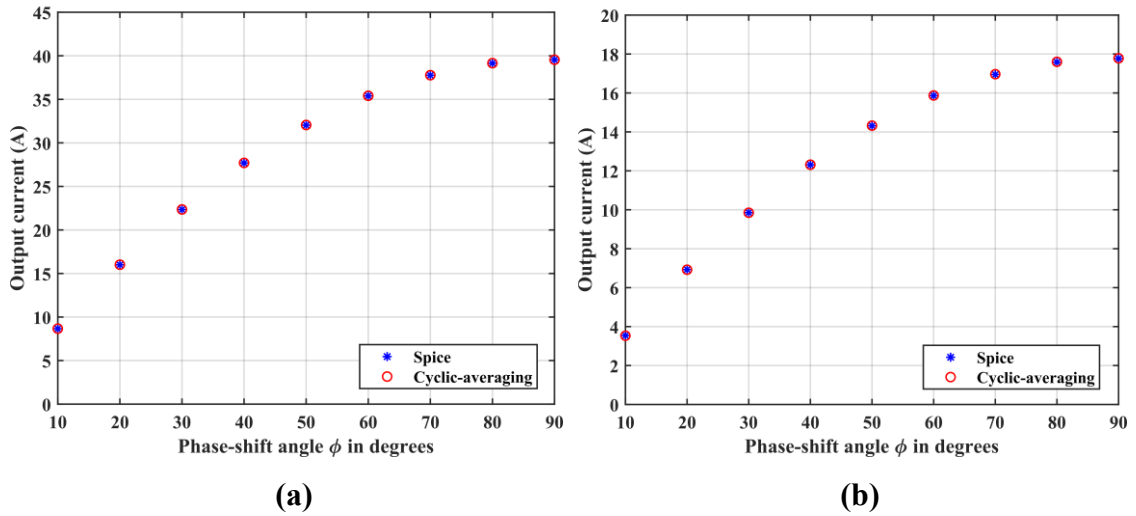


Figure 3.5: Simulation results for SPS modulation (a) forward mode and (b) reverse mode

The cyclic-averaging method is not only used to calculate the averaged state-vector and estimate the output current of the converter but can also be employed to measure the values of the state-variables over a full cycle. Following the verification of the converter's output current, the behaviour of the inductor current ($i_L(t)$) is analysed at the points of transition between the operation modes. The bridge voltages and inductor current waveforms obtained in Spice are presented in Figure 3.6 considering forward operation and two cases of modulation angles: $\phi = 90^\circ$ and $\phi = 45^\circ$.

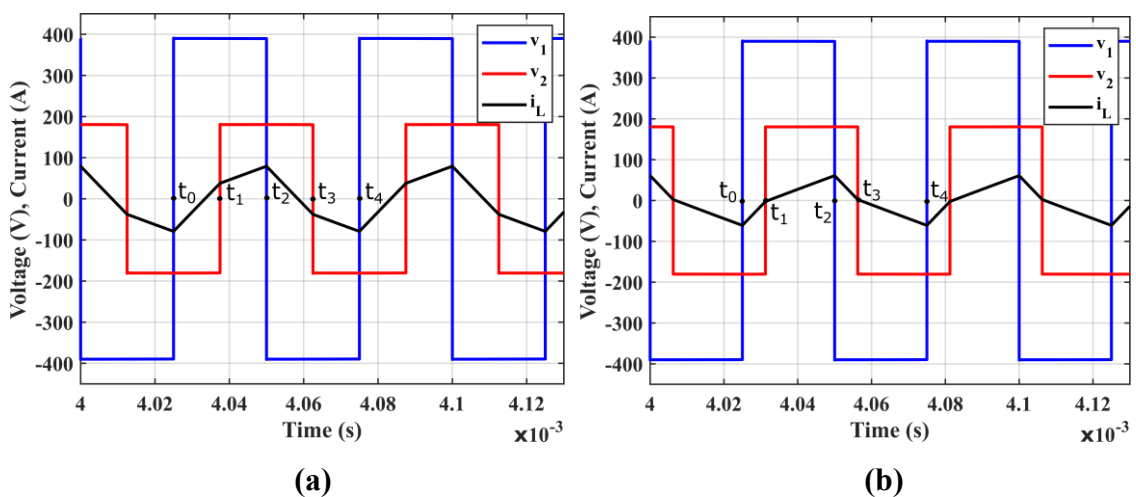


Figure 3.6: Bridge voltages and inductor current in forward operation for (a) $\phi = 90^\circ$ and (b) $\phi = 45^\circ$

The magnitude of the inductor current is measured at the times of transition between modes (t_0 , t_1 , t_2 , t_3 and t_4 in Figure 3.6). The comparison between Spice and cyclic-averaging results is shown in Table 3.5 for full modulation and in Table 3.6 when the modulation angle is reduced to 45° . The high accuracy of the cyclic-averaging model is confirmed again since results are close to Spice with maximum difference of 53mA in the instant current measurements. Therefore, this method can also be useful to quickly estimate the peak of the inductor current, which occurs at times t_0 , t_2 and t_4 .

Table 3.5: Inductor current states across a cycle considering forward operation and $\phi = 90^\circ$

	Spice				
	t_0	t_1	t_2	t_3	t_4
i_L (A)	-79.213	37.693	79.204	-37.702	-79.213
	Cyclic-averaging				
	t_0	t_1	t_2	t_3	t_4
i_L (A)	-79.230	37.653	79.230	-37.653	-79.230

Table 3.6: Inductor current states across a cycle considering forward operation and $\phi = 45^\circ$

	Spice				
	t_0	t_1	t_2	t_3	t_4
i_L (A)	-60.912	-2.350	60.903	2.341	-60.912
	Cyclic-averaging				
	t_0	t_1	t_2	t_3	t_4
i_L (A)	-60.956	-2.390	60.956	2.390	-60.956

The inductor current is also verified for a converter operating in reverse mode. The Spice waveforms for bridge voltages and inductor current are shown in Figure 3.7. Similar to forward operation, the current values for cyclic-averaging and Spice models are very close, as observed in Tables 3.7 and 3.8.

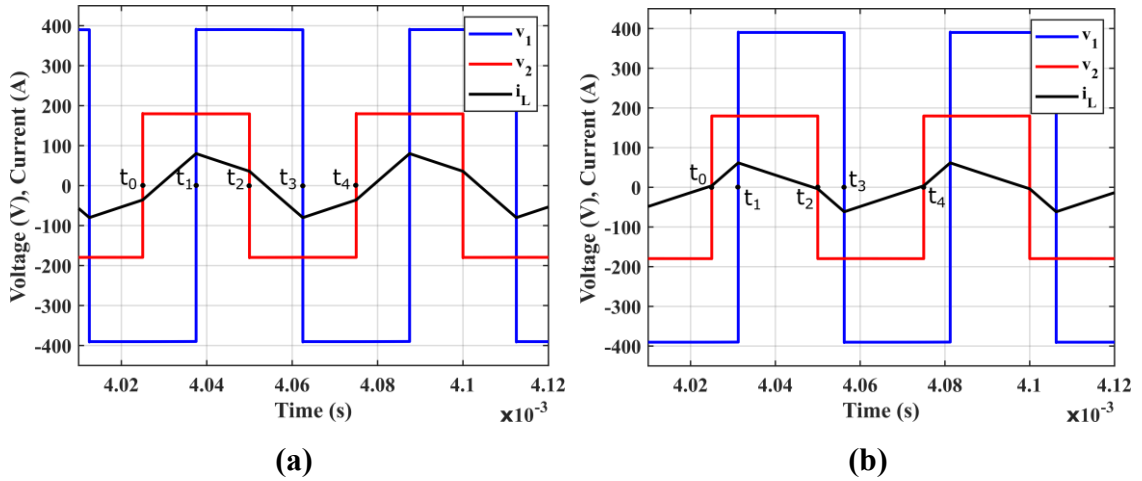


Figure 3.7: Bridge voltages and inductor current in reverse operation for (a) $\phi = 90^\circ$ and (b) $\phi = 45^\circ$

Table 3.7: Inductor current states across a cycle considering reverse operation and $\phi = 90^\circ$

	Spice				
	t_0	t_1	t_2	t_3	t_4
i_L (A)	-35.816	80.080	35.822	-80.071	-35.815
	Cyclic-averaging				
	t_0	t_1	t_2	t_3	t_4
i_L (A)	-35.864	80.056	35.864	-80.056	-35.864

Table 3.8: Inductor current states across a cycle considering forward operation and $\phi = 45^\circ$

	Spice - reverse mode, $\phi = 45^\circ$				
	t_0	t_1	t_2	t_3	t_4
i_L (A)	3.787	61.623	-3.778	-61.613	3.787
	Cyclic-averaging - reverse mode, $\phi = 45^\circ$				
	t_0	t_1	t_2	t_3	t_4
i_L (A)	3.732	61.575	-3.732	-61.575	3.732

The cyclic-averaging method is also useful to calculate the Fourier coefficients for all state-variables. Here, this method will be used to calculate the magnitude of

fundamental, third and fifth harmonics for the inductor current i_L . Due to waveform symmetry, the even order harmonics are null.

The RMS values of fundamental, third and fifth components obtained from the Spice and cyclic-averaging simulations are shown in Table 3.9 considering two phase-shift angles ($\phi = 90^\circ$ and $\phi = 45^\circ$) and forward operation. The results for both models are very close, confirming the accuracy of the cyclic-averaging method for harmonic analysis. Results also show that the magnitude of the Fourier coefficients decreases as the harmonic order increases.

Table 3.9: Harmonics analysis of inductor current i_L , forward mode

Component	RMS current (A)			
	$\phi = 90^\circ$		$\phi = 45^\circ$	
	Spice	Cyclic-averaging	Spice	Cyclic-averaging
Fundamental	50.280	50.279	34.148	34.172
3rd harmonic	5.586	5.587	6.929	6.929
5th harmonic	2.010	2.011	2.495	2.494

Once the coefficients are obtained, the waveform of the inductor current can be reconstructed following equation (3.16).

$$x(t) = \sum_{k=-\infty}^{\infty} c_k e^{jk\omega t} = c_0 + \sum_{k=1}^{\infty} (a_k \cos k\omega t + b_k \sin k\omega t) \quad (3.16)$$

where $a_k = 2\text{Re}(c_k)$ and $b_k = -2\text{Im}(c_k)$ and c_0 is the average value of i_L

Note that the number of coefficients is infinite, $k = 1, 2, \dots, \infty$. The higher the number of coefficients considered, the higher is the accuracy of the reconstructed function. As an example, the waveform for the inductor current obtained in Spice with modulation angle $\phi = 90^\circ$ is presented in Figure 3.8-a and compared to the current reconstructed considering only the 1st and 3rd components (Figure 3.8-b) and considering the 1st, 3rd, 5th, 7th and 9th components (Figure 3.8-c). These harmonic components were calculated using the cyclic-averaging method.

The shape and peak of the current waveform in Figure 3.8-c, considering 1st, 3rd, 5th, 7th and 9th harmonics, is clearly closer to the current waveform measured in Spice. Therefore, the results shown in Figure 3.8 confirm that accuracy increases as the number of harmonics accounted in the reconstruction process increases. The consideration of additional components beyond the 9th harmonic does not significantly affect the inductor current waveform since the magnitude of the high order coefficients is reduced.

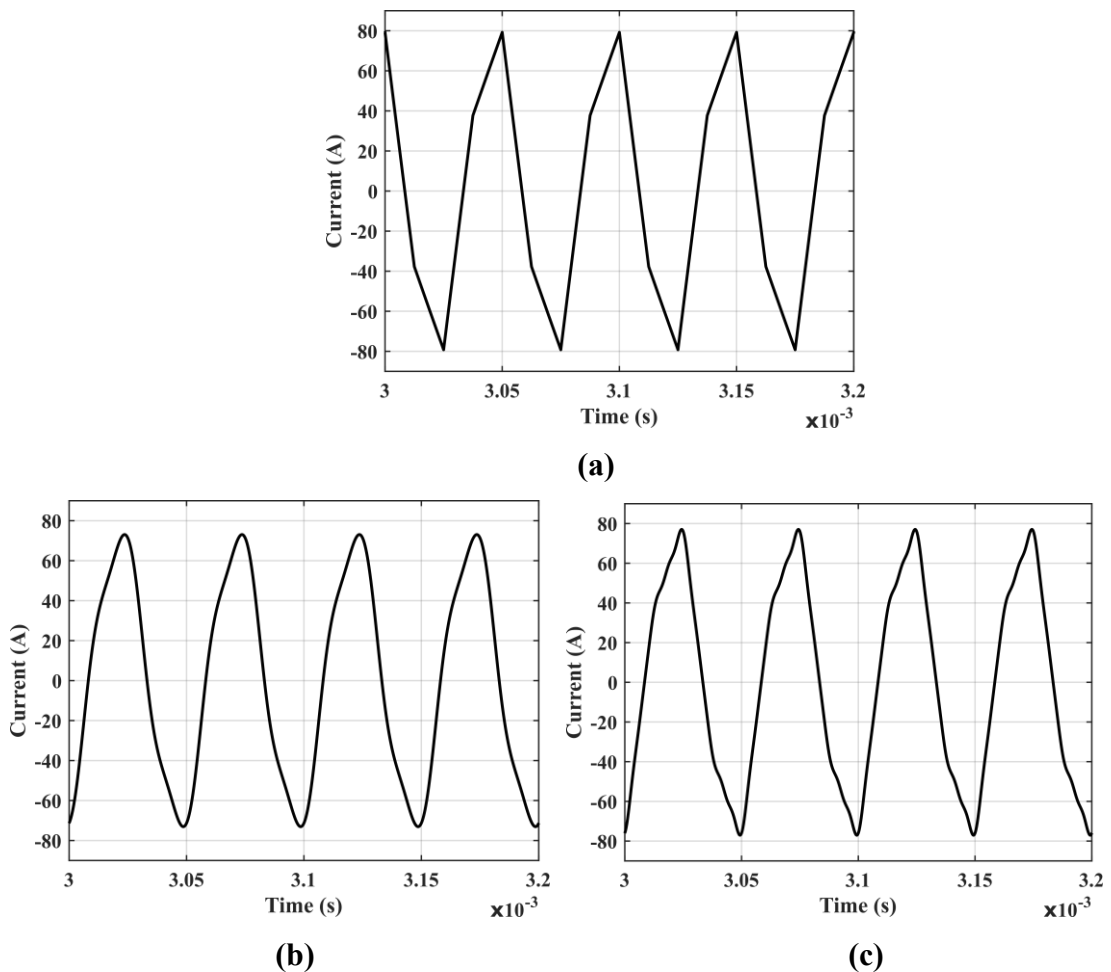


Figure 3.8: Inductor current waveform from (a) Spice (b) cyclic method with 1st, 3rd and 5th harmonics considered and (c) cyclic method with 1st, 3rd, 5th, 7th and 9th harmonics considered

The cyclic-averaging model results presented in this section were obtained using the approximation of $v_2(t) = \pm V_{bat}$ in forward mode and $v_1(t) = \pm V_{dc}$ in reverse mode. Simulations were also performed considering $v_2(t) = \pm v_{cf}(t)$ (and $v_1(t) = \pm v_{ci}(t)$ for reverse mode) and no significant difference was noticed. For the calculation of average output current a maximum difference of 0.001A was observed

when using $v_2(t) = \pm v_{cf}(t)$ instead of $v_2(t) = \pm V_{bat}$. A maximum error of 0.081A for the inductor current values over a cycle, and error of 0.023A for the harmonic components calculation were also observed when comparing the two possibilities of approximation. Therefore, it was confirmed that when resistances r_{bat} and r_{dc} have small values, in the order of milliohms, the influence of these resistors on converter operation is very reduced and either approximation can be used. In a case where the resistors have high values, the assumption of $v_2(t) = \pm v_{cf}(t)$ (or $v_1(t) = \pm v_{ci}(t)$) would give more accurate results. Those resistors, however, represent internal or measurement resistances which typically have low values.

The cyclic-averaging method has an average execution time of 0.755 seconds, compared to 24.675 seconds obtained with Spice. The simulation time of the Spice model considered here is 4 ms, where steady-state is reached around 3 ms. When the harmonic analysis is not performed, the execution time of the cyclic method drops to 0.149 seconds. Therefore, it was observed that the cyclic-averaging model has significantly faster execution compared to Spice.

3.5 Conclusions

In this chapter the cyclic-averaging modelling method was applied for analysis of a Dual Active Bridge converter operating under single phase-shift modulation. The model was employed for verification of the converter's output current, the inductor current cyclic behaviour and harmonic analysis. Simulations were performed under nearly ideal conditions (considering transformer and switches ideal) and results were verified against a Spice component-based simulation.

It was observed that the cyclic-averaging model could successfully predict the converter's behaviour for both power flow directions, showing similar accuracy to Spice. Additionally, the cyclic-averaging model benefits from significantly reduced execution time compared to the Spice.

In the following chapters, the cyclic-averaging method will be applied to analyse resonant CLLC converters operating under frequency and phase-shift modulations and a series-compensated IPT converter operating under phase-shift modulation. The cyclic-averaging results will also be compared to other modelling methods, as FMA, state-variable and Spice.

3.6 References

- [1] R. T. Naayagi and A. J. Forsyth, “Bidirectional DC-DC converter for aircraft electric energy storage systems,” in *5th IET International Conference on Power Electronics, Machines and Drives (PEMD 2010)*, 2010, pp. 1–6.
- [2] M. H. Kheraluwala, R. W. Gascoigne, D. M. Divan, and E. D. Baumann, “Performance Characterization of a High-Power Dual Active Bridge dc-to-dc Converter,” *IEEE Transactions on Industry Applications*, vol. 28, no. 6, pp. 1294–1301, 1992.
- [3] M. P. Foster, “Analysis and Design of High-order Resonant Power Converters,” PhD Thesis. University of Sheffield, 2003.
- [4] C. Gould, “Rapid Analysis and Design of CLL Resonant Power Converters,” PhD Thesis. University of Sheffield, 2006.
- [5] R. T. Naayagi, A. J. Forsyth, and R. Shuttleworth, “High-power bidirectional DC-DC converter for aerospace applications,” *IEEE Transactions on Power Electronics*, vol. 27, no. 11, pp. 4366–4379, 2012.

4 Modelling of Frequency Modulated CLLC Converter

4.1 Introduction

The cyclic-averaging method was applied in the previous chapter to model a Dual Active Bridge (DAB) converter operating under single phase-shift modulation. The application of this technique resulted in an accurate model of the converter's behaviour with the advantage of fast execution time compared to Spice.

Following the review of modelling techniques and resonant converters, performed in Chapter 2, and the application of cyclic-averaging to the non-resonant DAB in Chapter 3, a CLLC converter operating under frequency modulation will be analysed in this chapter. Fundamental Mode Approximation (FMA), state-variable and cyclic-averaging methods discussed in Chapter 2 will be used here to model the converter. The accuracy of the methods will be evaluated and compared through simulation. Furthermore, the execution time will be compared to confirm the rapid analysis provided by the cyclic-averaging technique. The models are validated against a Spice simulation and experimental results previously obtained from the literature.

Although this work is aimed at fixed-frequency converters, the models are applied to frequency modulated CLLC converters as a first step, since it is a more popular variant and due to a lack of this analysis in the literature. Additionally, since the focus of this research is on the phase-shift modulation variant, the design process will not be analysed for the frequency-modulated converter. For model validation, the FMA, state-variable and cyclic-averaging models will be developed and applied to the specification and design presented in [1].

4.2 Operation

The circuit diagram of a CLLC resonant converter is presented in Figure 4.1. The DC bus is represented by the voltage source V_{dc} and the battery is simply modelled also as a voltage source V_{bat} . Voltages v_1 and v_2 represent the output voltage of each bridge.

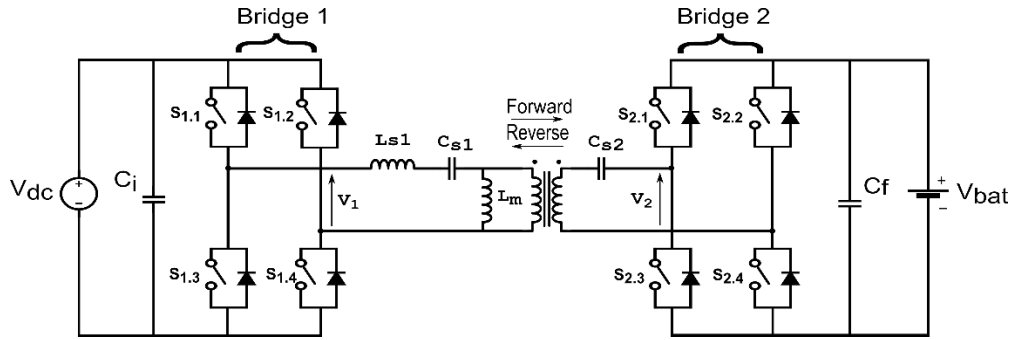


Figure 4.1: CLLC topology

For forward operation switches S1.1 to S1.4 form a full-bridge inverter while switches S2.1 to S2.4 work as a rectifier. For reverse operation the input inverter is formed by switches S2.1 to S2.4 and the output rectifier by S1.1 to S1.4. The switching signal is sent to the input stage switches while the output stage switches are always open, consequently, the diodes associated to the output switches form a rectifier bridge. Between the two bridges, a CLLC resonant network and a transformer are connected. The transformer is used to achieve galvanic isolation between input and output sides and the CLLC resonant tank is composed by inductances L_{s1} and L_m and capacitors C_{s1} and C_{s2} . The resonant capacitors also serve as blocking capacitors, eliminating DC voltage offset on voltages v_1 and v_2 [2].

The switching signal has a 50% fixed duty cycle and 180° phase-shift between switches in the same leg. Therefore, the input voltage to the resonant tank is a square wave with variable frequency. Here, the frequency is manipulated to control the converter's output current.

4.3 Fundamental Mode Approximation (FMA)

The first approach for analysis of the converter is the Fundamental Mode Approximation (FMA), a frequency-domain technique often used to model resonant converters. For the analysis in forward mode, the converter from Figure 4.1 can be

simplified to the equivalent circuit shown in Figure 4.2. For the reverse mode analysis, the equivalent circuit is presented on Figure 4.3. The circuits are referred to primary, therefore $C'_{s2} = C_{s2}/n^2$, considering an ideal transformer with turns ratio $n = N_1/N_2$, with N_1 and N_2 being the number of turns on primary and secondary windings respectively. The resistances of switches and resonant tank components are neglected for simplification of the circuit analysis. The input to the resonant tank is represented as a voltage source v_i and the output filter, rectifier and load are modelled as an equivalent resistor.

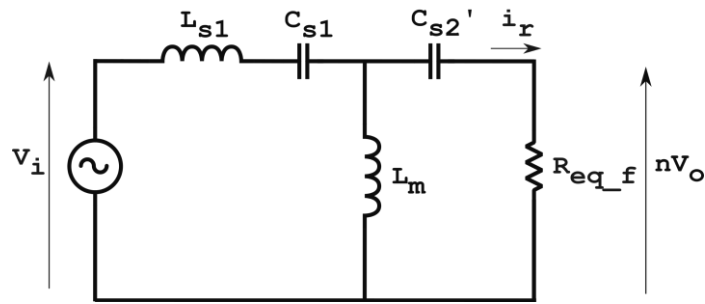


Figure 4.2: Equivalent circuit for FMA analysis in forward mode, referred to primary

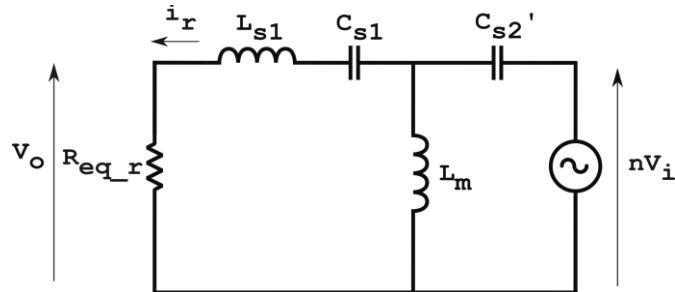


Figure 4.3: Equivalent circuit for FMA analysis in reverse mode, referred to primary

Based on the converter operation described in the previous section, the input voltage to the resonant tank is a square waveform $v_i(t)$ that alternates between $+V_{in}$ and $-V_{in}$. According to the Fourier series representation, $v_i(t)$ can be expressed as in (4.1), where i is harmonic number and f_s the switching frequency.

$$v_i(t) = \frac{4V_{in}}{\pi} \cdot \sum_{i=1,3,5}^{\infty} \frac{1}{i} \sin(2\pi i f_s t)$$

(4.1)

Additionally, the output voltage $v_o(t)$ of the resonant tank is also represented as a square wave phase-shifted from the input voltage and alternating between $+V_{out}$ and $-V_{out}$, as shown in equation (4.2).

$$v_o(t) = \frac{4V_{out}}{\pi} \cdot \sum_{i=1,3,5}^{\infty} \frac{1}{i} \sin(2\pi i f_s t - i\phi) \quad (4.2)$$

Notice that according to the topology diagram in Figure 4.1, for forward mode $v_i = v_1$, $V_{in} = V_{dc}$ and $v_o = v_2$, $V_{out} = V_{bat}$, while for reverse mode $v_i = v_2$, $V_{in} = V_{bat}$ and $v_o = v_1$, $V_{out} = V_{dc}$.

Following the FMA method, the resonant circuit is analysed assuming the waveforms of current and voltage can be approximated to its fundamental components and the load is modelled as an equivalent resistor. Therefore, the input voltage is reduced to the fundamental harmonic of $v_i(t)$. The fundamental component of $v_i(t)$ and the RMS value are shown in equation (4.3):

$$v_{i,FMA}(t) = \frac{4V_{in}}{\pi} \sin(2\pi f_s t)$$

$$V_{i,RMS} = \frac{4V_{in}}{\pi\sqrt{2}} = \frac{2\sqrt{2}V_{in}}{\pi} \quad (4.3)$$

Similarly, the output voltage $v_o(t)$ is reduced to its fundamental component:

$$v_{o,FMA}(t) = \frac{4V_{out}}{\pi} \sin(2\pi f_s t - \phi)$$

$$V_{o,RMS} = \frac{4V_{out}}{\pi\sqrt{2}} = \frac{2\sqrt{2}V_{out}}{\pi} \quad (4.4)$$

After the full wave rectifier stage, the average value of the output current, I_{out} , can be found calculating the average of $|i_{r,FMA}|$ as in (4.5) for forward mode and (4.6) for reverse mode.

$$I_{out} = \frac{1}{T} \int_0^T n |i_{r,FMA}| = I_{r,PEAK} \frac{2n}{\pi} = \frac{2\sqrt{2}nI_{r,RMS}}{\pi} \quad (4.5)$$

$$I_{out} = \frac{1}{T} \int_0^T |i_{r,FMA}| = I_{r,PEAK} \frac{2}{\pi} = \frac{2\sqrt{2}I_{r,RMS}}{\pi} \quad (4.6)$$

The equivalent load resistor referred to primary, at the output of the resonant tank, can be calculated as in (4.7) for forward mode and (4.8) for reverse mode.

$$R_{eq_f} = \frac{nV_{o,RMS}}{I_{R,RMS}} = \frac{2\sqrt{2}nV_{out}}{\pi} \cdot \frac{2\sqrt{2}}{\pi I_{out}/n} = \frac{8n^2 V_{out}}{\pi^2 I_{out}} = \frac{8n^2}{\pi^2} R_{load} \quad (4.7)$$

$$R_{eq_r} = \frac{V_{o,RMS}}{I_{R,RMS}} = \frac{2\sqrt{2}V_{out}}{\pi} \cdot \frac{2\sqrt{2}}{\pi I_o} = \frac{8 V_{out}}{\pi^2 I_{out}} = \frac{8}{\pi^2} R_{load} \quad (4.8)$$

where the output is represented as a load resistor $R_{load} = \frac{V_{out}}{I_{out}}$.

From circuit analysis, a transfer function can be calculated for forward and reverse modes, as in equations (4.9) and (4.10) respectively. The inclusion of components' resistances and parasitic inductances/capacitances would result in an increasingly complex circuit and transfer function, therefore, for simplification, these elements are not considered for the FMA analysis here.

$$\frac{V_{out}}{V_{in}} = \frac{V_{bat}}{V_{dc}} = \frac{1}{n} \cdot \frac{R_{eq_f}}{R_{eq_f} + Z_{cs2}} \cdot \frac{[Z_{Lm} // (Z_{cs2} + R_{eq_f})]}{Z_{ls1} + Z_{cs1} + [Z_{Lm} // (Z_{cs2} + R_{eq_f})]} \quad (4.9)$$

$$\frac{V_{out}}{V_{in}} = \frac{V_{dc}}{V_{bat}} = n \cdot \frac{R_{eq_r}}{R_{eq_r} + Z_{ls1} + Z_{cs1}} \cdot \frac{[Z_{Lm} // (Z_{ls1} + Z_{cs1} + R_{eq_r})]}{Z_{cs2} + [Z_{Lm} // (Z_{ls1} + Z_{cs1} + R_{eq_r})]} \quad (4.10)$$

From the transfer functions, the DC gain can be calculated as in (4.11) for forward mode and (4.12) for reverse mode.

$$DC_{Gain_f} = \left| \frac{V_{out}}{V_{in}} \right| = \frac{1}{\sqrt{A^2 + B^2}} \quad (4.11)$$

$$DC_{Gain_r} = \left| \frac{V_{out}}{V_{in}} \right| = \frac{1}{\sqrt{C^2 + D^2}} \quad (4.12)$$

where:

$$A = \frac{1}{h} + 1 - \frac{1}{h \cdot \omega_n^2}$$

$$C = 1 - \frac{1}{h \cdot g \cdot \omega_n^2}$$

$$B = D = Q_1 \left(\frac{1}{\omega_n} - \omega_n \right) + \frac{Q_1 \cdot (1 + h)}{g \cdot h \cdot \omega_n} - \frac{Q_1}{g \cdot h \cdot \omega_n^3}$$

Given:

$$\omega_{sr} = \frac{1}{\sqrt{L_{s1} \cdot C_{s1}}} \quad \omega_n = \frac{\omega_{sw}}{\omega_{sr}}$$

$$h = \frac{L_m}{L_{s1}} \quad g = \frac{C_{s2}}{C_{s1}}$$

$$Q_1 = \frac{\sqrt{\frac{L_{s1}}{C_{s1}}}}{R_{eq}}$$

where ω_{sr} is the series resonant frequency, ω_{sw} is the switching frequency, ω_n is normalized frequency, Q_1 quality factor, h is inductance ratio and g capacitance ratio.

For a frequency-modulated converter, the DC voltage gain versus frequency curve is an important tool for the design procedure, being previously used for this purpose in [1], [2]. During design, the voltage gain requirement must be met considering the specified input and output voltage range and bidirectional operation. Additionally, components values must be chosen to result in similar curves for both forward and reverse modes. Through the specified operation range, the gain curves must be

monotonically decreasing to guarantee a linear control, reducing the complexity for the controller implementation.

The FMA method allows easy implementation and results in a rapid solution but suffers from accuracy problems due to the circuit simplifications and the dominant fundamental harmonic assumption.

4.4 State-variable model

Following the FMA frequency-domain analysis, a non-linear state-variable model is developed for a time-domain analysis of the CLLC resonant converter. The equation description obtained by the end of this section will also serve as base for application of the cyclic-averaging method.

From the converter diagram presented in Figure 4.1, an equivalent circuit for state-variable analysis in forward mode is obtained, as shown in Figure 4.4. To facilitate the analysis, the technique previously employed in [3]–[5] for partitioning the converter circuit into decoupled subsystems will also be used here, with the circuit divided in two subsystems. The fast subsystem represents the dynamics of resonant tank and switching devices. The output filter capacitor composes the slow subsystem due to its slow response. The two subsystems are connected by coupling equations that represents the non-linear behaviour of the rectifier.

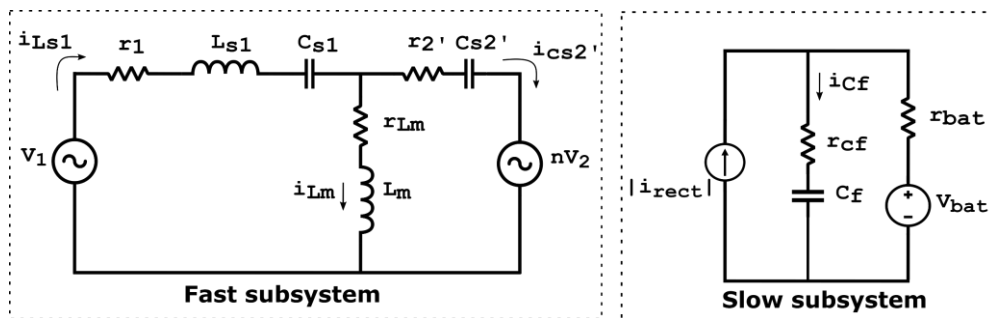


Figure 4.4: Equivalent circuit for state-variable analysis, forward mode

The output voltage of the primary bridge is represented by $v_1(t)$ and the input voltage to the rectifier, referred to the primary side of the transformer, is $nv_2(t)$, where n is the transformer's turns ratio. The primary resistance, secondary capacitance referred to primary and secondary resistance referred to primary are defined as follows:

$$r_1 = r_{Ls1} + r_{Cs1} + 2 \cdot r_{SWITCH}$$

$$C_{s2}' = \frac{C_{s2}}{n^2}$$

$$r_2' = n^2 r_{C2}$$

(4.13)

From circuit analysis of the fast subsystem the following equations are derived:

$$v_{Ls1} = L_{s1} \frac{di_{Ls1}}{dt} \rightarrow \frac{di_{Ls1}}{dt} = \frac{1}{L_{s1}} (v_1 - r_1 i_{Ls1} - v_{Cs1} - v_{Cs2}' - r_2' i_{Ls1} + r_2' i_{Lm} - n v_2)$$

(4.14)

$$i_{Cs1} = C_{s1} \frac{dv_{Cs1}}{dt} \rightarrow \frac{dv_{Cs1}}{dt} = \frac{1}{C_{s1}} (i_{Ls1})$$

(4.15)

$$v_{Lm} = L_m \frac{di_{Lm}}{dt} \rightarrow \frac{di_{Lm}}{dt} = \frac{1}{L_m} (-r_{Lm} i_{Lm} + v_{Cs2}' + n v_2 + r_2' i_{Ls1} - r_2' i_{Lm})$$

(4.16)

$$i_{Cs2}' = C_{s2}' \frac{dv_{Cs2}'}{dt} \rightarrow \frac{dv_{Cs2}'}{dt} = \frac{1}{C_{s2}'} (i_{Ls1} - i_{Lm})$$

(4.17)

For the slow subsystem:

$$i_{Cf} = C_f \frac{dv_{Cf}}{dt} \rightarrow \frac{dv_{Cf}}{dt} = \frac{1}{C_f (r_{bat} + r_{Cf})} (r_{bat} |i_{rect}| - v_{Cf} + V_{bat})$$

(4.18)

The output voltage and current can be defined as:

$$V_{out} = v_{Cf} + r_{Cf} i_{Cf}$$

$$I_{out} = \frac{V_{out} - V_{bat}}{r_{bat}}$$

(4.19)

The rectifier operation must be analysed to define the coupling equations. For CLLC converters operating under frequency modulation, the rectifier behaviour depends on the operating frequency. A typical graph of DC conversion gain in function of switching frequency for a CLLC converter, obtained from FMA analysis, is shown in Figure 4.5. It was observed in simulations that when the switching frequency, f_{sw} , is higher or equal to the frequency at the load independent point, f_{li} , the rectifier will always operate in the conduction state. In this case the output voltage of the tank is a perfect square wave. When the converter operates at frequencies lower than f_{li} , a non-conduction mode occurs when the output voltage of the resonant tank is not sufficient to turn on the diodes ($|v_2(t)| < V_{out} + 2V_d$, where V_d is the diode forward voltage), in this case the bridge rectifier is not conducting and the secondary current is zero.

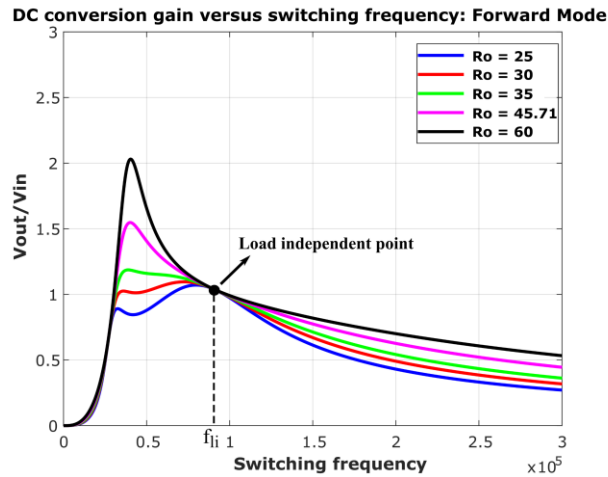


Figure 4.5: DC voltage gain versus switching frequency for CLLC converter in forward operation

For the LLC converter the load independent and unity gain points coincide and always occurs at the series resonant frequency but this premise cannot be applied to the CLLC converter case [6], [7]. In the example from Figure 4.5, the series resonant frequency is 73.16 kHz, the load independent point occurs around 91 kHz and the unity gain point is load dependent and placed in a range of 96 to 98 kHz for forward operation.

In Figure 4.6 typical inverter and rectifier bridge voltages and rectifier input current are shown for a converter operating with a switching frequency higher or equal to the load independent frequency ($f_{sw} \geq f_{li}$) and with switching frequency lower than

the load independent frequency ($f_{sw} < f_{li}$). The input voltage of the resonant tank, $v_1(t)$ for forward operation, is always a square wave with amplitude V_{dc} , but the behaviour of voltage $v_2(t)$ depends on the switching frequency range.

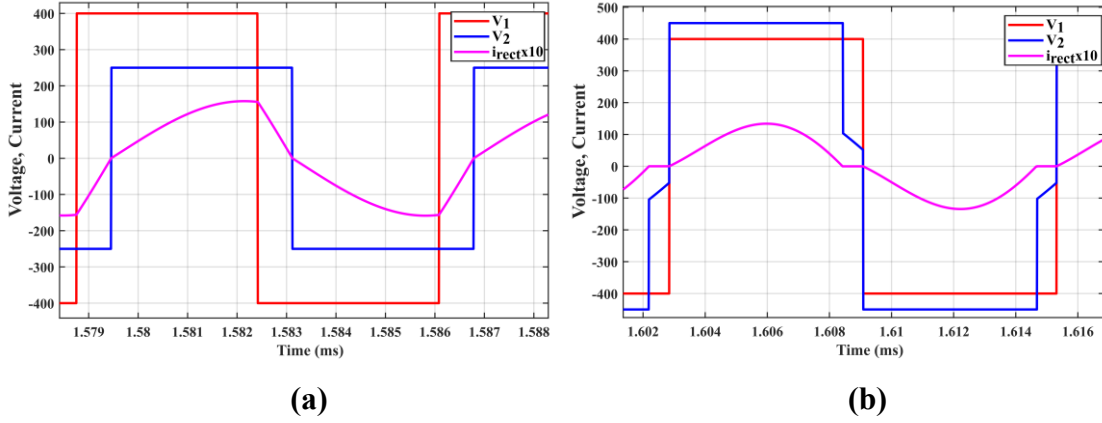


Figure 4.6: Typical bridge voltages and rectifier current in forward mode (a)

$f_{sw} \geq f_{li}$ (b) $f_{sw} < f_{li}$

For continuous conduction mode operation, $|v_2| \geq V_{out} + 2V_d$, the coupling equations are defined as:

$$nv_2(t) = n \cdot \text{sgn}(i_{CS2'}(t))(V_{out} + 2V_d + 2r_d|i_{rect}(t)|)$$

$$i_{rect}(t) = ni_{CS2'}(t) = n(i_{LS1}(t) - i_{Lm}(t))$$

(4.20)

where r_d is the forward-biased resistance of the diode.

During the non-conduction mode, the equivalent circuit of the fast subsystem behaves as shown in Figure 4.7. Since the diodes are not conducting in this case, no current flows through the secondary capacitor.

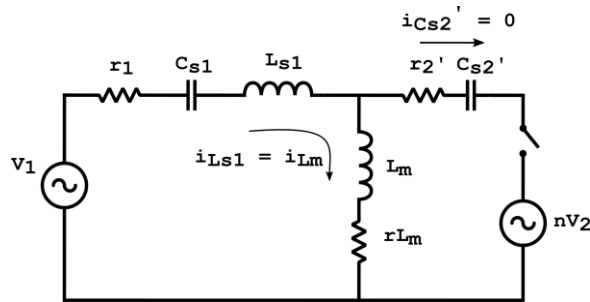


Figure 4.7: Equivalent circuit during non-conduction mode, forward operation

From circuit analysis, the input current and voltage of the rectifier are defined by equation (4.21).

$$nv_2(t) = \left[\frac{L_m}{L_m + L_{s1}} \left(v_1(t) - v_{cs1}(t) - r_1 i_{LS1}(t) + \frac{L_{s1}}{L_m} r_{Lm} i_{LS1}(t) \right) \right] - v_{cs2'}(t)$$

$$i_{rect}(t) = ni_{cs2'}(t) = n(i_{LS1}(t) - i_{Lm}(t)) = 0$$

(4.21)

The same analysis performed for converters operating in forward mode is now repeated for reverse mode operation. Here the input of the resonant tank is nv_2 while v_1 now is the rectifier input voltage, the equivalent circuit is shown in Figure 4.8:

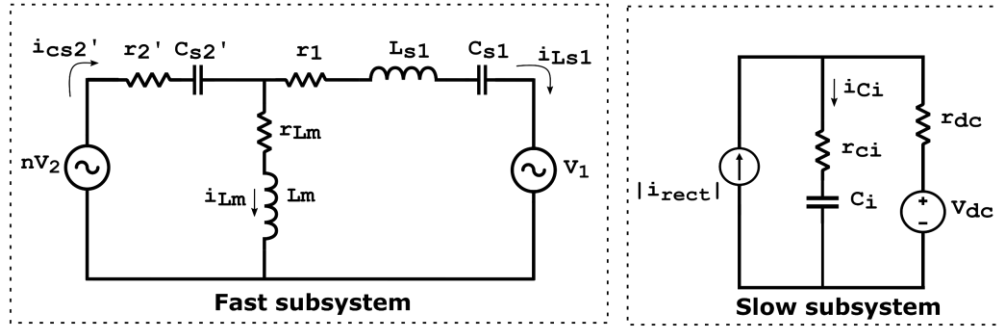


Figure 4.8: Equivalent circuit for state-variable analysis, reverse mode

From circuit analysis, the equations for the fast subsystem are defined as follows:

$$v_{LS1} = L_{s1} \frac{di_{LS1}}{dt} \rightarrow \frac{di_{LS1}}{dt} = \frac{1}{L_{s1}} (nv_2 - v_{cs2'} - r_2'(i_{LS1} + i_{Lm}) - r_1 i_{LS1} - v_{cs1} - v_1)$$

(4.22)

$$i_{CS1} = C_{s1} \frac{dv_{CS1}}{dt} \rightarrow \frac{dv_{CS1}}{dt} = \frac{1}{C_{s1}} (i_{LS1})$$

(4.23)

$$v_{Lm} = L_m \frac{di_{Lm}}{dt} \rightarrow \frac{di_{Lm}}{dt} = \frac{1}{L_m} (nv_2 - v_{cs2'} - r_2'(i_{LS1} + i_{Lm}) - r_{Lm} i_{Lm})$$

(4.24)

$$i_{Cs2'} = C_{s2'} \frac{dv_{Cs2'}}{dt} \rightarrow \frac{dv_{Cs2'}}{dt} = \frac{1}{C_{s2'}} (i_{Ls1} + i_{Lm}) \quad (4.25)$$

For the slow subsystem:

$$i_{Ci} = C_i \frac{dv_{Ci}}{dt} \rightarrow \frac{dv_{Ci}}{dt} = \frac{1}{C_i(r_{Ci} + r_{dc})} (r_{dc}|i_{rect}| - v_{Ci} + V_{dc}) \quad (4.26)$$

The output voltage is defined as:

$$V_{out} = v_{Ci} + r_{Ci}i_{Ci} \quad (4.27)$$

When the converter is operating in reverse mode, and $|v_1| \geq V_{out} + 2V_d$, the diodes are in a conduction state and the coupling equations are defined as:

$$\begin{aligned} v_1(t) &= \text{sgn}(i_{Ls1}(t))(V_{out} + 2V_d + 2r_d|i_{rect}(t)|) \\ i_{rect}(t) &= i_{Ls1}(t) \end{aligned} \quad (4.28)$$

When non-conduction mode occurs $|v_1| < V_{out} + 2V_d$ and the equivalent circuit is shown in Figure 4.9.

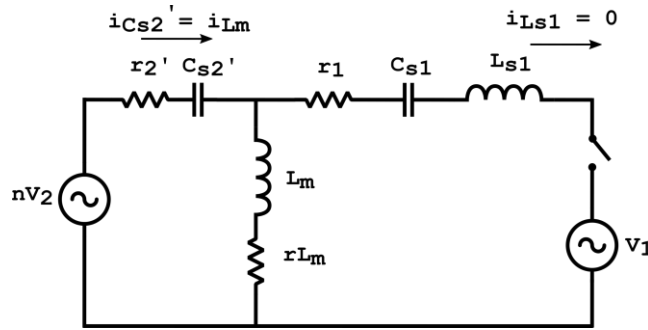


Figure 4.9: Equivalent circuit during non-conduction mode, reverse operation

In this case the diodes are not conducting, the inductor current is constant and equal to zero and consequently the primary resistor and inductor voltages are also equal to zero. From circuit analysis the coupling equations are given by:

$$v_1(t) = nv_2(t) - r_2'(i_{Ls1}(t) + i_{Lm}(t)) - v_{Cs2'}(t) - v_{Cs1}(t)$$

$$i_{rect}(t) = i_{Ls1}(t) = 0$$

(4.29)

4.4.1 Implementation in Simulink

Once the equation description is obtained, the piecewise linear state-variable model is implemented using the graphical programming environment Simulink for modelling and analysis of transient and steady-state behaviour of the converter. The block diagrams for the fast and slow subsystems, coupling equations and rectifier operation are shown in Figures 4.10, 4.11 and 4.12.

The fast and slow subsystem equations are implemented using mainly sum, gain and integration blocks. As shown in Figure 4.12, to implement the rectifier, the input current and voltage to the rectifier are monitored to determine if non-conduction mode occurs.

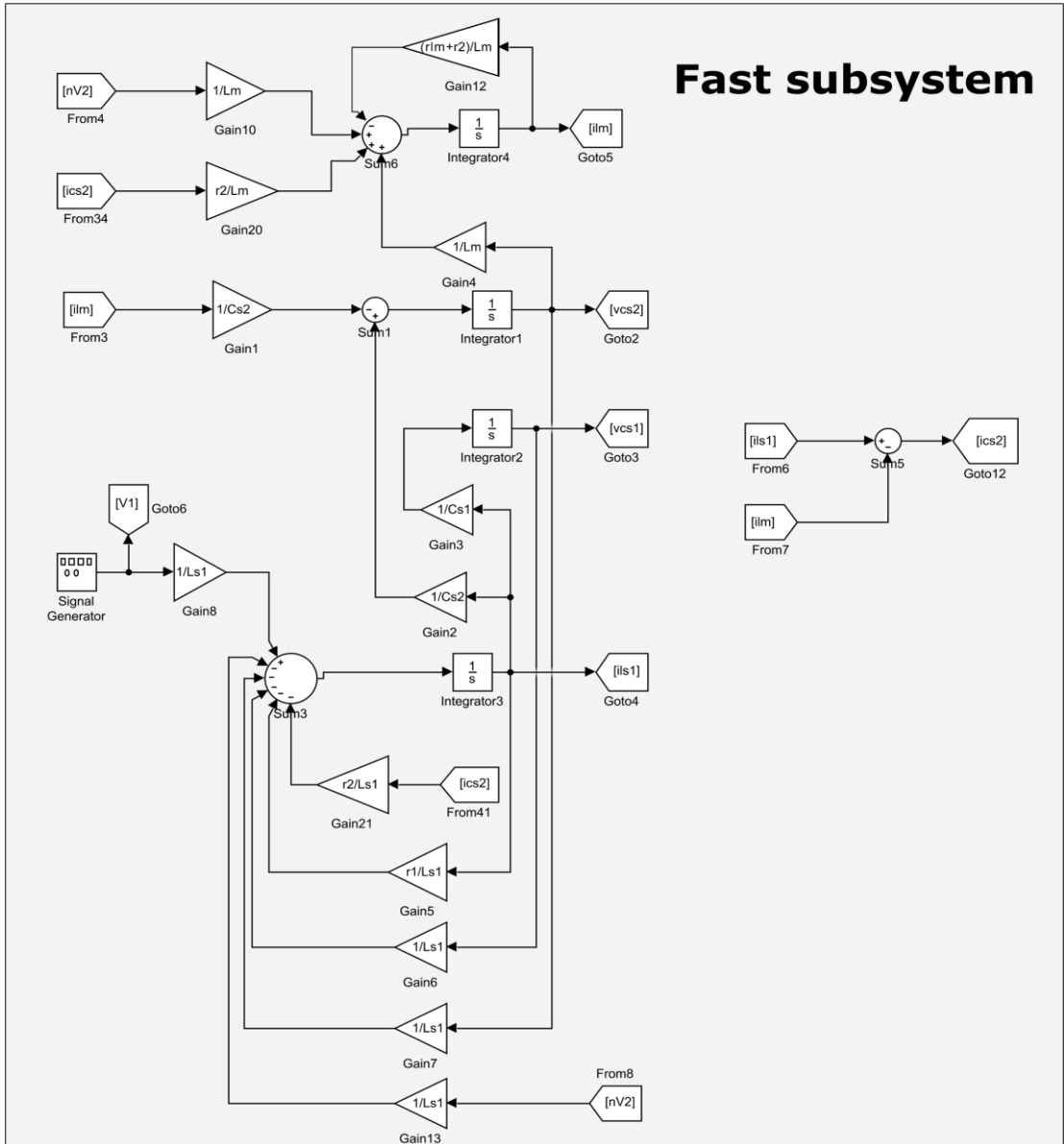


Figure 4.10: Fast subsystem, forward mode

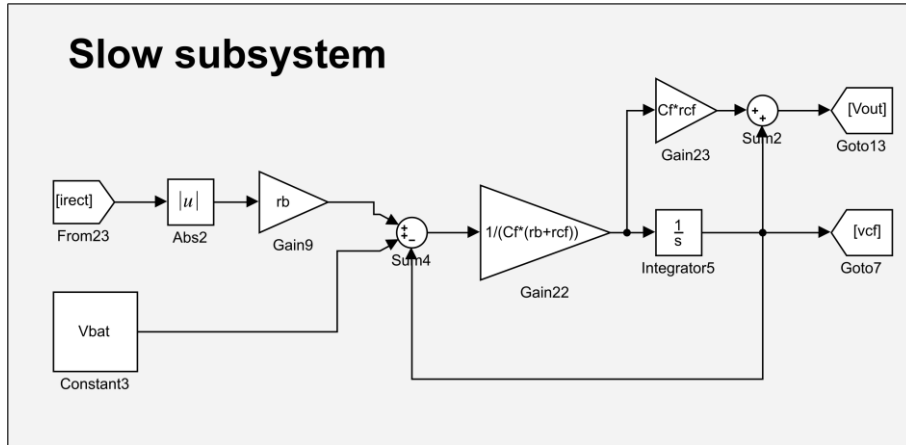


Figure 4.11: Slow subsystem, forward mode

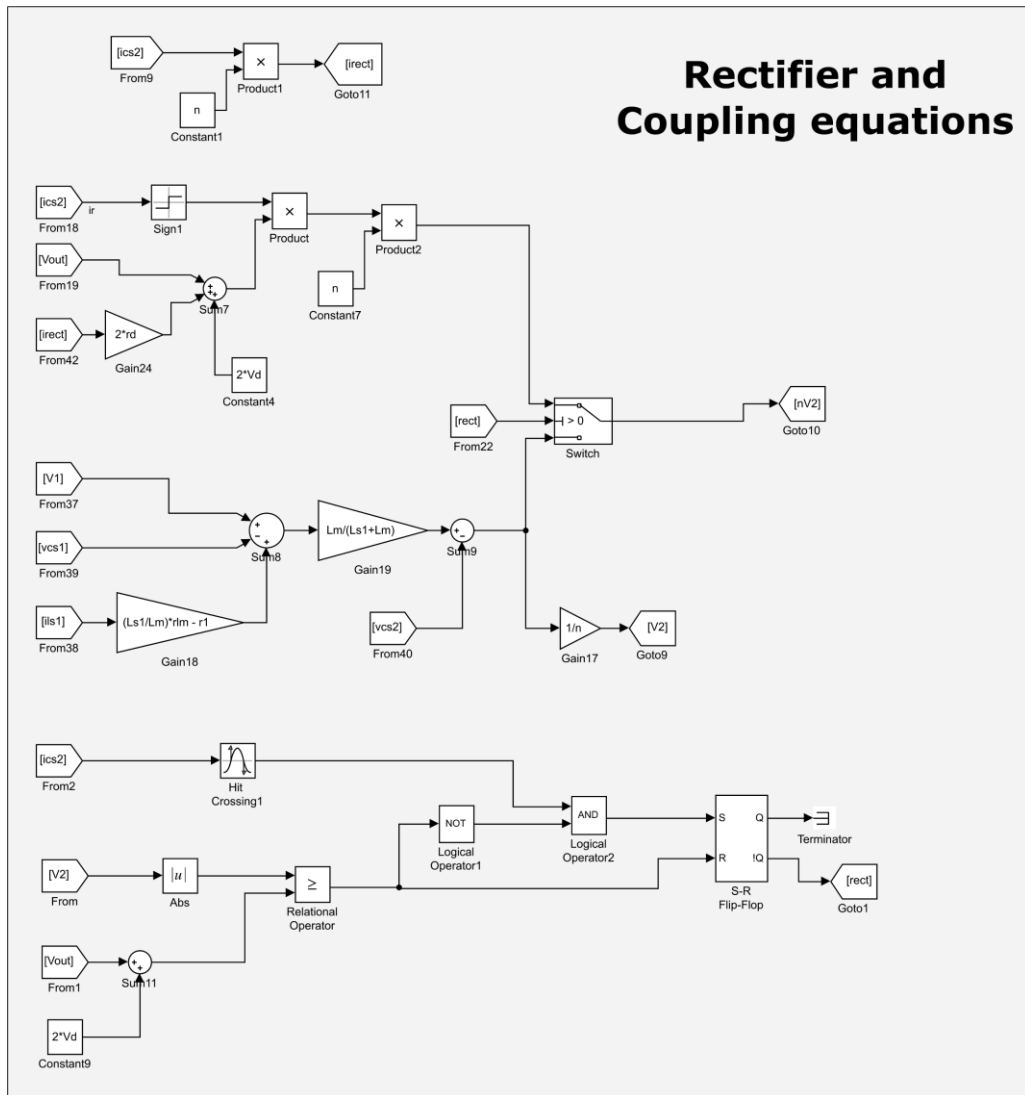


Figure 4.12: Rectifier and coupling equations, forward mode

4.5 Cyclic-averaging model

Based on the state-variable description obtained in section 4.4 and cyclic analysis presented in Chapter 2, the cyclic-averaging model is developed for steady-state analysis of the converter.

Combining the equations for fast and slow subsystems from the state-variable model previously obtained, the equation description can be presented also in matrix form as in (4.30):

$$\frac{d}{dt}x(t) = A \cdot x(t) + B \quad (4.30)$$

Where the state-vector $x(t)$, dynamic matrix A_f and input matrix B_f for forward mode are defined as follows:

$$x(t) = \begin{bmatrix} i_{Ls1}(t) \\ v_{Cs1}(t) \\ i_{Lm}(t) \\ v_{Cs2'}(t) \\ v_{Cf}(t) \end{bmatrix}$$

$$A_f = \begin{bmatrix} -\frac{(r_1 + r_2')}{L_{s1}} & -\frac{1}{L_{s1}} & \frac{r_2'}{L_{s1}} & -\frac{1}{L_{s1}} & 0 \\ \frac{1}{C_{s1}} & 0 & 0 & 0 & 0 \\ \frac{r_2'}{L_m} & 0 & -\frac{(r_{Lm} + r_2')}{L_m} & \frac{1}{L_m} & 0 \\ \frac{1}{C_{s2'}} & 0 & -\frac{1}{C_{s2'}} & 0 & 0 \\ 0 & 0 & 0 & 0 & -\frac{1}{C_f(r_{bat} + r_{cf})} \end{bmatrix}$$

$$B_f = \begin{bmatrix} \frac{v_1(t) - nv_2(t)}{L_{s1}} \\ 0 \\ \frac{nv_2(t)}{L_m} \\ 0 \\ \frac{r_{bat}|i_{rect}(t)| + V_{bat}}{C_f(r_{bat} + r_{cf})} \end{bmatrix}$$

Due to the presence of a non-conduction mode, the analysis is split in two cases: when the converter is operating in region I (switching frequency is higher or equal to load independent frequency: $f_{sw} \geq f_{li}$) and when it operates in region II (switching frequency is lower than load independent frequency: $f_{sw} < f_{li}$). Therefore, the coupling equations, are defined as follows:

a. Conduction mode (occurs when operating in regions I or II): $|v_2| \geq V_{out} + 2V_d$

$$nv_2(t) = n \cdot \text{sgn}(i_{cs2'}(t))(V_{out} + 2V_d + 2r_d|i_{rect}(t)|)$$

$$i_{rect}(t) = ni_{cs2'}(t) = n(i_{Ls1}(t) - i_{Lm}(t))$$

b. Non-conduction mode (occurs only when operating in region II): $|v_2| < V_{out} + 2V_d$

$$nv_2(t) = \left[\frac{L_m}{L_m + L_{s1}} \left(v_1(t) - v_{cs1}(t) - r_1 i_{Ls1}(t) + \frac{L_{s1}}{L_m} r_{Lm} i_{Ls1}(t) \right) \right] - v_{cs2'}(t)$$

$$i_{rect}(t) = ni_{cs2'}(t) = n(i_{Ls1}(t) - i_{Lm}(t)) = 0$$

To apply the cyclic-averaging method, the periodic behaviour of inverter/rectifier bridge voltages and rectifier current must be analysed. The typical voltage sequence in steady-state for a converter operating in region I is shown in Figure 4.13, where four modes of operation can be identified based on the state of variables $v_1(t)$, $v_2(t)$ and $i_{rect}(t)$. The start of a cycle is determined by the transition from negative to positive of input voltage $v_1(t)$.

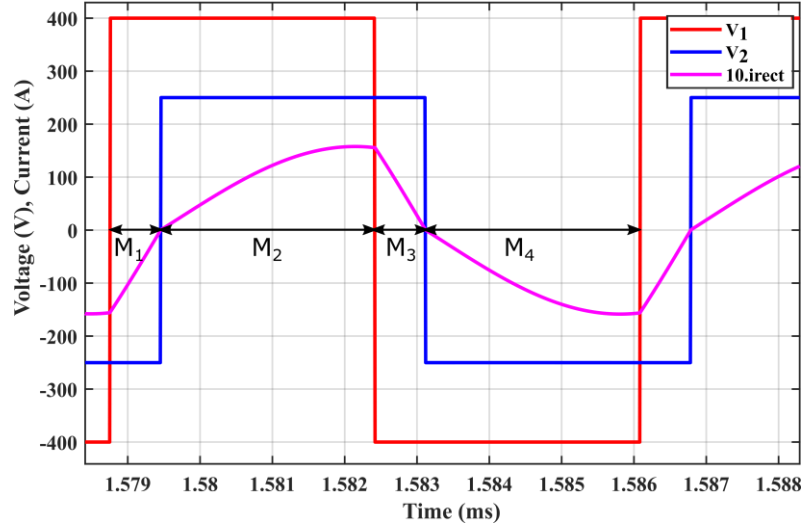


Figure 4.13: Typical voltage and current sequence for operation in region I, forward mode

From waveform analysis and coupling equations, the bridge voltages and rectified current can be defined for each mode as shown in Table 4.1.

Table 4.1: Mode descriptions for converter operating in region I, forward mode

Mode	$v_1(t)$	$nv_2(t)$	$ i_{rect}(t) $
M_1	V_{DC}	$-n(v_{Cf} + 2V_d + 2r_d i_{rect})$	$-n(i_{LS1} - i_{Lm})$
M_2	V_{DC}	$n(v_{Cf} + 2V_d + 2r_d i_{rect})$	$n(i_{LS1} - i_{Lm})$
M_3	$-V_{DC}$	$n(v_{Cf} + 2V_d + 2r_d i_{rect})$	$n(i_{LS1} - i_{Lm})$
M_4	$-V_{DC}$	$-n(v_{Cf} + 2V_d + 2r_d i_{rect})$	$-n(i_{LS1} - i_{Lm})$

The values of variables $v_1(t)$, $v_2(t)$ and $i_{rect}(t)$ for each mode M_n are incorporated into the state-variable equation (4.30) in order to obtain a set of piecewise linear equations for each mode. A set of matrices A_{n_f} and B_{n_f} will be used with the cyclic-averaging method equations from Chapter 2 to solve the system, where $n=1, 2, 3, 4$.

Similar analysis is performed for converters operating in region II. The typical voltage and current sequence is shown in Figure 4.14, note that non-conduction state occurs during two modes, M_2 and M_4 . Here the start of a cycle is determined by the transition from negative to positive of input voltage $v_1(t)$.

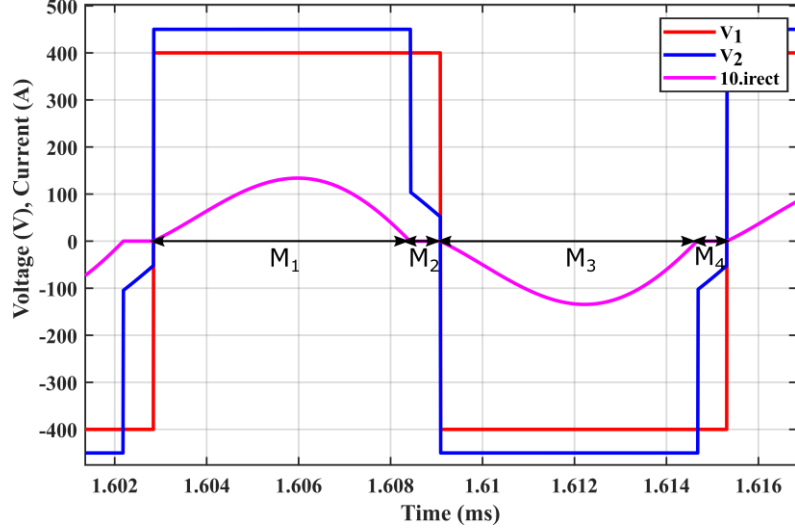


Figure 4.14: Typical voltage and current sequence for operation in region II, forward mode

The mode descriptions necessary to define the system over a cycle and apply the cyclic method equations are presented in Table 4.2.

Table 4.2: Mode descriptions for converter operating in region II, forward mode

Mode	$v_1(t)$	$nv_2(t)$	$ i_{rect}(t) $
M_1	V_{DC}	$n(v_{Cf} + 2V_d + 2r_d i_{rect})$	$n(i_{Ls1} - i_{Lm})$
M_2	V_{DC}	$\left[\frac{L_m}{L_m + L_{s1}} \left(v_1 - v_{cs1} - r_1 i_{Ls1} + \frac{L_{s1}}{L_m} r_{Lm} i_{Ls1} \right) \right] - v_{Cs2'}$	0
M_3	$-V_{DC}$	$-n(v_{Cf} + 2V_d + 2r_d i_{rect})$	$-n(i_{Ls1} - i_{Lm})$
M_4	$-V_{DC}$	$\left[\frac{L_m}{L_m + L_{s1}} \left(v_1 - v_{cs1} - r_1 i_{Ls1} + \frac{L_{s1}}{L_m} r_{Lm} i_{Ls1} \right) \right] - v_{Cs2'}$	0

Following the forward operation description, similar analysis is performed for reverse mode operation. The state-vector and matrices A_r and B_r are now given by:

$$x(t) = \begin{bmatrix} i_{Ls1}(t) \\ v_{Cs1}(t) \\ i_{Lm}(t) \\ v_{Cs2'}(t) \\ v_{Ci}(t) \end{bmatrix}$$

$$A_r = \begin{bmatrix} -\frac{(r_1 + r_2')}{L_{s1}} & -\frac{1}{L_{s1}} & -\frac{r_2'}{L_{s1}} & -\frac{1}{L_{s1}} & 0 \\ \frac{1}{C_{s1}} & 0 & 0 & 0 & 0 \\ -\frac{r_2'}{L_m} & 0 & \frac{-(r_{Lm} + r_2')}{L_m} & -\frac{1}{L_m} & 0 \\ \frac{1}{C_{s2'}} & 0 & \frac{1}{C_{s2'}} & 0 & 0 \\ 0 & 0 & 0 & 0 & -\frac{1}{C_i(r_{Ci} + r_{dc})} \end{bmatrix}$$

$$B_r = \begin{bmatrix} \frac{nv_2(t) - v_1(t)}{L_{s1}} \\ 0 \\ \frac{nv_2(t)}{L_m} \\ 0 \\ \frac{r_{dc}|i_{rect}(t)| + V_{dc}}{C_i(r_{Ci} + r_{dc})} \end{bmatrix}$$

Given the coupling equations:

a. Conduction mode: $|v_1| \geq V_{out} + 2V_d$

$$v_1(t) = \text{sgn}(i_{Ls1}(t))(V_{out} + 2V_d + 2r_d|i_{rect}(t)|)$$

$$i_{rect}(t) = i_{Ls1}(t)$$

b. Non-conduction mode: $|v_1| < V_{out} + 2V_d$

$$v_1(t) = nv_2(t) - r_2'(i_{Ls1}(t) + i_{Lm}(t)) - v_{Cs2'}(t) - v_{Cs1}(t)$$

$$i_{rect}(t) = i_{Ls1}(t) = 0$$

The voltages and current sequence for a converter operating in regions I and II for reverse mode are shown in Figures 4.15 and 4.16. Here the start of a cycle is defined by the transition from negative to positive of the input voltage v_2 .

Based on the coupling equations and waveform analysis, the mode descriptions for converters operating in reverse mode are shown in Tables 4.3 and 4.4.

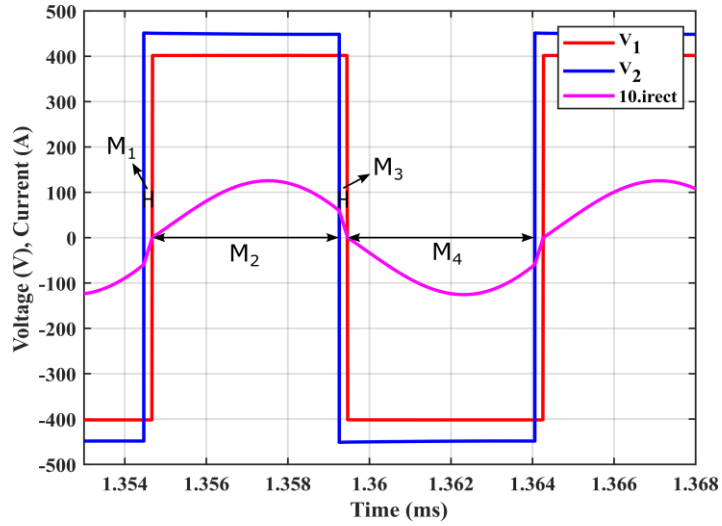


Figure 4.15: Typical voltage and current sequence for operation in region I, reverse mode

Table 4.3: Mode descriptions for converter operating in region I, reverse mode

Mode	$nv_2(t)$	$v_1(t)$	$ i_{rect}(t) $
M_1	nV_{bat}	$-(v_{Ci} + 2V_d + 2r_d i_{rect})$	$-i_{LS1}$
M_2	nV_{bat}	$(v_{Ci} + 2V_d + 2r_d i_{rect})$	i_{LS1}
M_3	$-nV_{bat}$	$(v_{Ci} + 2V_d + 2r_d i_{rect})$	i_{LS1}
M_4	$-nV_{bat}$	$-(v_{Ci} + 2V_d + 2r_d i_{rect})$	$-i_{LS1}$

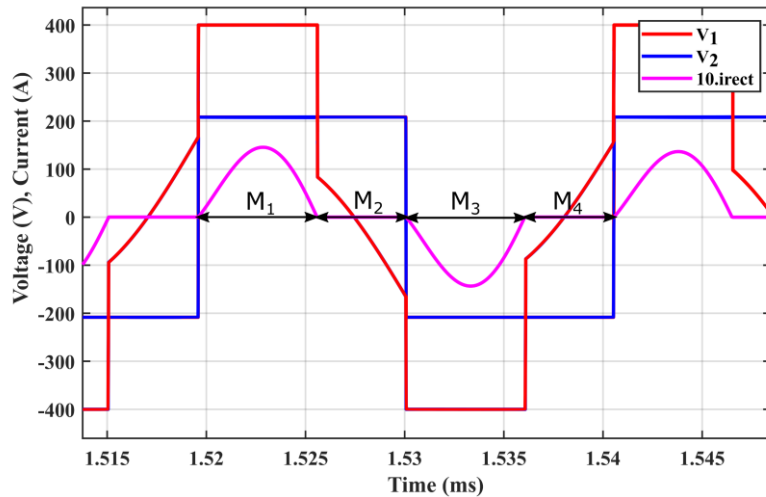


Figure 4.16: Typical voltage and current sequence for operation in region II, reverse mode

Table 4.4: Mode descriptions for converter operating in region II, reverse mode

Mode	$nv_2(t)$	$v_1(t)$	$ i_{rect}(t) $
M_1	nV_{bat}	$(v_{Ci} + 2V_d + 2r_d i_{rect})$	i_{LS1}
M_2	nV_{bat}	$nv_2 - r_2'(i_{LS1} + i_{Lm}) - v_{Cs2'} - v_{Cs1}$	0
M_3	$-nV_{bat}$	$-(v_{Ci} + 2V_d + 2r_d i_{rect})$	$-i_{LS1}$
M_4	$-nV_{bat}$	$nv_2 - r_2'(i_{LS1} + i_{Lm}) - v_{Cs2'} - v_{Cs1}$	0

Once the steady-state operating modes, and state-variable equations for each mode, are defined for forward and reverse operation, the next step is to determine the duration of each mode and calculate the duty cycles.

4.5.1 Estimation of duty cycle

In order to define the duty cycle for each mode, the phase-shift between the bridge voltages must be calculated. As demonstrated in the previous chapter, for phase-shift modulated converters, both primary and secondary bridges are active and the duties are easily calculated based on the defined modulation angle. When operating under frequency modulation, the secondary bridge functions as a diode rectifier bridge and the duration of each mode depends on the rectifier's operation and, consequently, the operating frequency range.

The phase-shift angle between the input and output of the resonant tank can be estimated based on FMA analysis. From the FMA equation description developed in section 4.3, the input and output voltage phasors are defined:

$$\begin{aligned}
 \mathbf{V}_i &= V_{i,RMS} \angle 0 = \frac{2\sqrt{2}}{\pi} V_{in} \angle 0 \\
 \mathbf{V}_o &= V_{o,RMS} \angle \phi = \frac{2\sqrt{2}}{\pi} V_{out} \angle \phi
 \end{aligned}
 \tag{4.31}$$

And based on the transfer functions defined in (4.9) and (4.10), the phase-shift angle between the input and output voltages can be calculated:

$$\phi = \tan^{-1} \left(-\frac{B}{A} \right), \text{ for forward operation}$$

$$\phi = \tan^{-1}\left(-\frac{D}{C}\right), \text{ for reverse operation}$$

where A, B, C and D are defined on equations (4.11) and (4.12) .

Considering a converter operating with continuous rectifier current (region I), the duty for the first mode is calculated from equation (4.32) while the duties for modes M2, M3 and M4 can be determined by symmetry, from d_1 .

$$d_1 = \frac{\phi}{2\pi}; d_2 = 0.5 - d_1; d_3 = d_1 \text{ and } d_4 = d_2 \quad (4.32)$$

When the converter is operating in region II the duties are calculated as in equation (4.33).

$$d_1 = 0.5 + 2\frac{\phi}{2\pi}; d_2 = 0.5 - d_1; d_3 = d_1 \text{ and } d_4 = d_2 \quad (4.33)$$

Due to accuracy limitations, the FMA analysis only gives an approximate angle value, therefore, an optimization method must be employed to obtain more precise values of the duties. From Figure 4.13, 4.14, 4.15 and 4.16 it is observed that the change from mode M1 to M2 occurs when $i_{rect} = 0$, which corresponds to $i_{Ls1} - i_{Lm} = 0$ for forward operation, or $i_{Ls1} = 0$ for reverse operation. Numerical analysis will be used here to find a more accurate duty value that fulfils the above mode transition conditions.

Based on the equations of cyclic-averaging model, the duty values are used to calculate the values of i_{Ls1} and i_{Lm} at each mode transition point and therefore depend on the value d_1 . For a converter operating in forward mode, a function can be defined as:

$$f(d_1) = i_{Ls1}(d_1) - i_{Lm}(d_1) \quad (4.34)$$

The Newton-Raphson recursive method will be used here to find the root of equation (4.34), that corresponds to the value of d_1 for $i_{Ls1} = i_{Lm}$. Using the cyclic model equations described in Chapter 2 for mode M1, i_{Ls1} and i_{Lm} are first calculated

using the initial guess of d_1 obtained from the FMA analysis in equations (4.32) and (4.33).

To calculate the derivative of $f(d_1)$, the function is next calculated for a small increment of δ to d_1 . Here the increment is defined as $\delta = 10^{-5}$.

$$f(d_1 + \delta) = i_{Ls1}(d_1 + \delta) - i_{Lm}(d_1 + \delta) \quad (4.35)$$

Therefore, an approximation for the derivative of $f(d_1)$ is given by equation (4.36).

$$f'(d_1) = \frac{f(d_1 + \delta) - f(d_1)}{\delta} \quad (4.36)$$

Based on Newton-Raphson's method definition, the new value of d_1 for next iteration is given by:

$$d_1[k] = d_1[k - 1] - \frac{f(d_1[k])}{f'(d_1[k - 1])} \quad (4.37)$$

Where $d_1[k]$ is the present time estimate for d_1 and $d_1[0]$ is the initial condition.

At the end of each iteration, the difference between i_{Ls1} and i_{Lm} is verified to check if this value is within a small error tolerance. For the converter analysis performed in this chapter, a tolerance of 0.001, or 1 mA, is considered sufficient to obtain accurate results.

The analysis for reverse mode is similar, the only difference is that the function is now defined as in (4.38), since now $i_{rect} = i_{Ls1}$.

$$f(d_1) = i_{Ls1}(d_1) \quad (4.38)$$

The recursive method is applied to find the value d_1 that results in $i_{Ls1} = 0$, which corresponds to the transition from mode M1 to M2.

When an acceptable value of duty is found, the recursive calculations are interrupted and cyclic-averaging equations are applied to calculate the average steady-state value of state-variables and output current. Since the series resistances of the filter capacitors are very small, they are considered negligible and the output current is approximated to:

$$I_{out,avg} = \frac{v_{Cf,avg} - V_{bat}}{r_b}, \text{ for forward operation}$$

$$I_{out,avg} = \frac{v_{Ci,avg} - V_{dc}}{r_{dc}}, \text{ for reverse operation}$$
(4.39)

Using this technique, the initial estimation from the FMA equations is optimized to obtain accurate values of duty cycle for the cyclic-averaging calculations.

4.6 Case study

To verify the models developed in the previous sections, simulations are performed based on the 3.5 kW CLLC converter design and operation proposed in [1]. The converter is designed to operate in the frequency range of 85 to 145 kHz in forward mode and 40 to 100 kHz in reverse mode. The DC link voltage is fixed at 400V and the battery operates in a voltage range of 250 to 450V.

For simulation purposes, the transformer and diodes are assumed to be ideal and capacitors' resistances are neglected, hence the converter is validated considering nearly ideal conditions. The converter's parameters used for all simulations in this chapter are listed on Table 4.5. Based on the defined parameters, the series resonant frequency (f_{sr}) for this converter is 73.16 kHz, where $\omega_{sr} = 2\pi f_{sr} = \frac{1}{\sqrt{L_{s1}C_{s1}}}$.

Table 4.5: Simulation parameters

Parameter	Value
V_{dc}	400 V
V_{bat}	250 to 450 V
C_f, C_i	300 μ F
L_{s1}	34.8 μ H
C_{s1}	136 nF
L_m	78.28 μ H
C_{s2}	200 nF
n (turns ratio)	0.8333
r_{bat}, r_{dc}	0.01 Ω
r_{SWITCH}	0.044 Ω
r_{Ls1}, r_{Lm}	0.1 Ω

The operation specification for forward and reverse modes is shown in Figure 4.17 and 4.18, where the output current is plotted against battery voltage. Here the frequency is the variable used to control the output current. In forward mode the battery is charged at a constant current of 10A whilst the battery voltage is lower than 350V. As the voltage increases beyond this point the current is reduced to maintain the converter maximum output power of 3.5 kW.

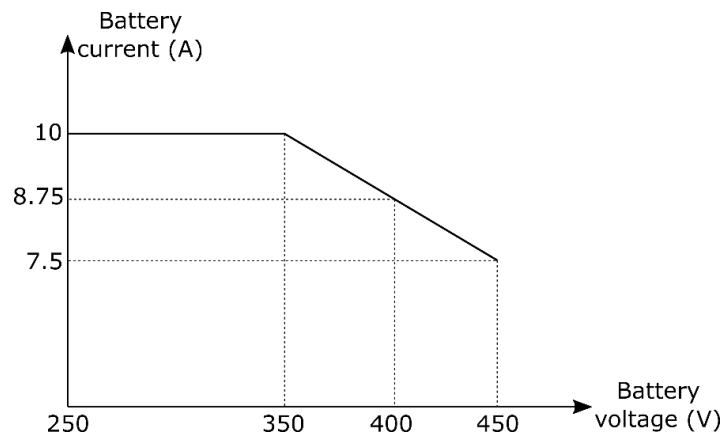


Figure 4.17: Battery current versus battery voltage for forward operation

In reverse mode the battery is supplying power to the DC bus, hence, the output voltage is now constant at 400V. While the battery voltage is in the range of 400 to 450V the output power is maintained close to maximum, at 3.4 kW. As the input battery voltage decreases the output power is reduced to avoid high RMS current in the resonant tank.

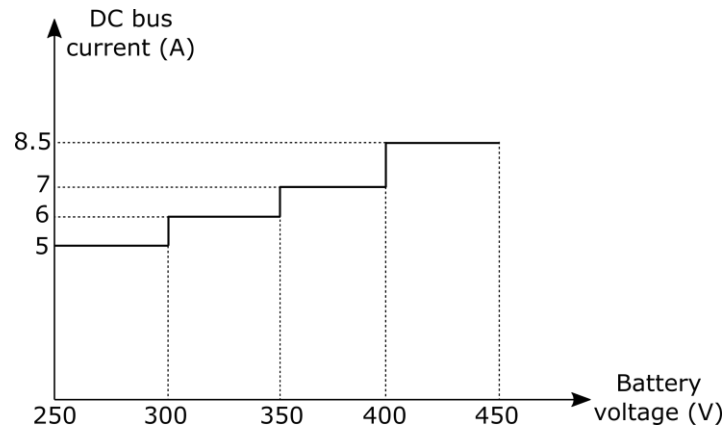


Figure 4.18: DC link current versus battery voltage for reverse operation

Based on the converter operation just described, five points are chosen for simulation and model comparison. Using the defined output voltage and current for each point, the output can be represented as a load resistor for the FMA analysis, where $R_{load} = V_{out}/I_{out}$. The values of R_{load} for the full range of operation points is shown in Table 4.6.

Table 4.6: Equivalent output load resistor across operating range

	Operation points				
	$V_{bat}=250V$	$V_{bat}=300V$	$V_{bat}=350V$	$V_{bat}=400V$	$V_{bat}=450V$
R_{load} (Ω) Forward mode	25	30	35	45.71	60
R_{load} (Ω) Reverse mode	80	66.67	57.14	47.06	47.06

4.7 Simulation results

Once the test points are defined, the models are simulated and validated using a Spice circuit-based simulation. The models are used to estimate the switching frequency necessary to provide the required output current for different values of battery voltage following the converter's designed operation.

Based on the FMA equation description from section 4.3, the DC voltage gain curves are plotted for all load configurations considering forward and reverse operation, as shown in Figure 4.19. Since the DC link voltage is constant (400V), the gain requirement for forward mode is in a range of 0.625 to 1.125, based on the battery voltage range. For reverse mode, the gain operation range is from 0.89 to 1.6. From the results shown, the gain requirement is accomplished and, for this operation range, the gain curves are monotonically decreasing which is an important characteristic for control purposes.

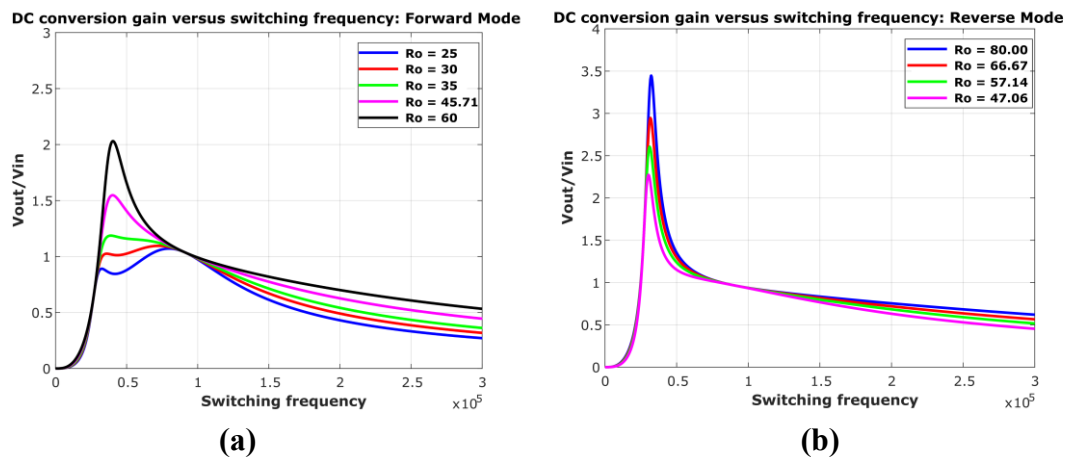


Figure 4.19: DC voltage gain versus switching frequency for converter operating in (a) forward mode and (b) reverse mode

The observation of the load independent point in the graphs is important to determine in which frequency range the non-conduction mode starts to occur. For this converter's design, the unity gain point is load dependent, close to the load independent point but not equal. The load independent point occurs around 91 kHz for both forward and reverse operation, while the unity gain point occurs between 96 and 98 kHz in forward mode and between 80 and 81.6 kHz in reverse mode.

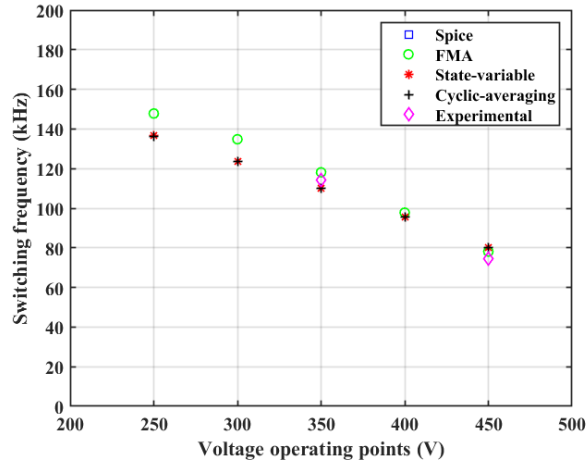
At first, the results obtained from model simulations are compared to Spice. Additionally, for the 350V and 450V operation points in forward mode and 250, 350 and 450V points in reverse mode, the results are also compared to the experimental results previously obtained in [1]. Results are shown in Tables 4.7 and 4.8 and plotted on Figure 4.20. The frequency at the load independent point, that marks the transition between regions I and II, is approximately 91.5 kHz in the Spice simulations, a result close to the value of 91 kHz obtained in the FMA analysis. Therefore, in forward mode, the converter operates in region II ($f_{sw} < f_{li}$) only when $V_{bat} = 450V$. For reverse mode, the converter operates mostly in region II, switching to region I ($f_{sw} \geq f_{li}$) when $V_{bat} = 450V$.

Table 4.7: Operation frequency forward mode

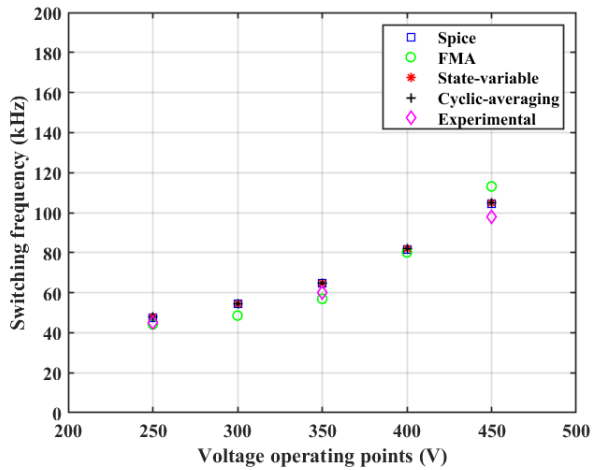
	Frequency (kHz)				
	$V_{bat}=250V$	$V_{bat}=300V$	$V_{bat}=350V$	$V_{bat}=400V$	$V_{bat}=450V$
FMA	147.80	134.80	118.10	97.77	78.10
Spice	136.10	123.14	109.30	94.81	79.75
State-variable	136.50	123.50	109.90	95.43	80.17
Cyclic-averaging	136.35	123.45	109.83	95.40	80.18
Experimental (literature)	-	-	114.39	-	74.34

Table 4.8: Operation frequency reverse mode

	Frequency (kHz)				
	$V_{bat}=250V$	$V_{bat}=300V$	$V_{bat}=350V$	$V_{bat}=400V$	$V_{bat}=450V$
FMA	44.16	48.57	56.92	80.12	113.10
Spice	47.60	54.26	64.50	81.38	104.27
State-variable	47.71	54.45	64.88	82.22	105.06
Cyclic-averaging	47.77	54.49	64.91	82.24	105.00
Experimental (literature)	45.27	-	59.85	-	97.75



(a)



(b)

Figure 4.20: Switching frequency for different battery voltage operation points for (a) forward and (b) reverse operation

The error between the frequency obtained from FMA, state-variable and cyclic-averaging models simulation and Spice is calculated and presented on Table 4.9 for forward operation and Table 4.10 for reverse operation.

Table 4.9: Percentage error between proposed models and Spice, forward mode

	Frequency (kHz)				
	$V_{bat}=250V$	$V_{bat}=300V$	$V_{bat}=350V$	$V_{bat}=400V$	$V_{bat}=450V$
FMA	8.60%	9.47%	8.05%	3.12%	2.07%
State-variable	0.29%	0.29%	0.55%	0.65%	0.53%
Cyclic-averaging	0.18%	0.25%	0.48%	0.62%	0.54%

Table 4.10: Percentage error between proposed models and Spice, reverse mode

	Frequency (kHz)				
	$V_{bat}=250V$	$V_{bat}=300V$	$V_{bat}=350V$	$V_{bat}=400V$	$V_{bat}=450V$
FMA	7.23%	10.49%	11.75%	1.55%	8.47%
State-variable	0.23%	0.35%	0.59%	1.03%	0.76%
Cyclic-averaging	0.36%	0.42%	0.64%	1.06%	0.70%

Results from cyclic-averaging and state-variable methods showed reduced errors compared to Spice, having a maximum error of nearly 1%, considering the whole range of forward and reverse mode operation. The FMA method shows increased error, a maximum of 11.75%, due to more significant model simplifications adopted when compared to the other methods.

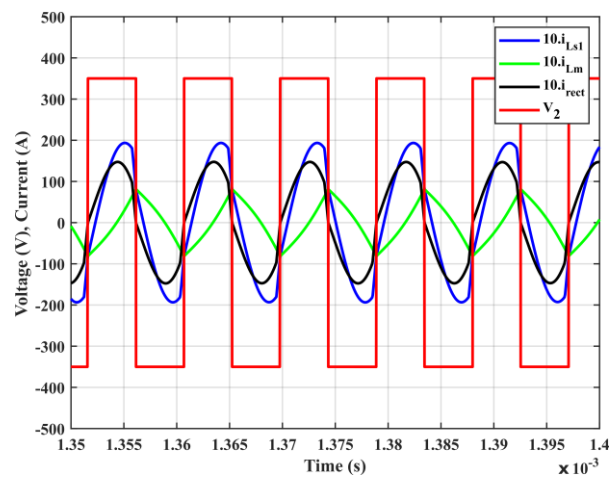
The models also showed reduced error when compared to the literature experimental results, with a maximum error of 8.45% for cyclic-averaging and 15.7% for FMA. The experimental results are affected by circuit resistances and parasitic elements while the model simulations were performed under nearly ideal conditions, resulting in increased error between simulations and practical results.

The closeness of the results for cyclic-averaging method and Spice show that the technique adopted in section 4.5.1 for calculation of duties, with initial estimation of duty value using FMA analysis and the Newton-Raphson method for optimization, gives accurate results. In Table 4.11 the results previously obtained are compared to a cyclic-averaging simulation where the duties are calculated considering only the FMA estimation. It is verified that estimation using only FMA is not accurate.

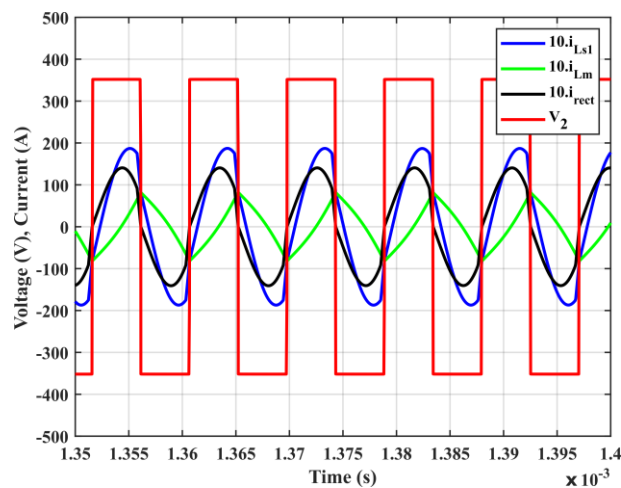
Table 4.11: Comparison of duty estimation techniques for cyclic-averaging implementation, forward mode

	Frequency (kHz)				
	$V_{bat}=250V$	$V_{bat}=300V$	$V_{bat}=350V$	$V_{bat}=400V$	$V_{bat}=450V$
Cyclic-averaging (only FMA)	149.75	139.07	125.33	108.01	60.21
Cyclic-averaging (FMA+Newton)	136.35	123.45	109.83	95.40	80.18
Spice	136.10	123.14	109.30	94.81	79.75

As a further investigation, the waveforms obtained with the proposed state-variable model are compared to Spice results. The currents flowing through inductors L_{S1} and L_m , the rectifier voltage and the input current to the rectifying bridge, i_{rect} , defined as $i_{rect} = n(i_{L_{S1}} - i_{L_m})$ for forward operation, are shown in Figure 4.21 for a converter operating at $V_{bat}=350V$. As confirmed by the current waveforms, the converter is operating in region I, consequently, non-conduction mode will not occur and the input and output of the resonant tank are square waves.



(a)



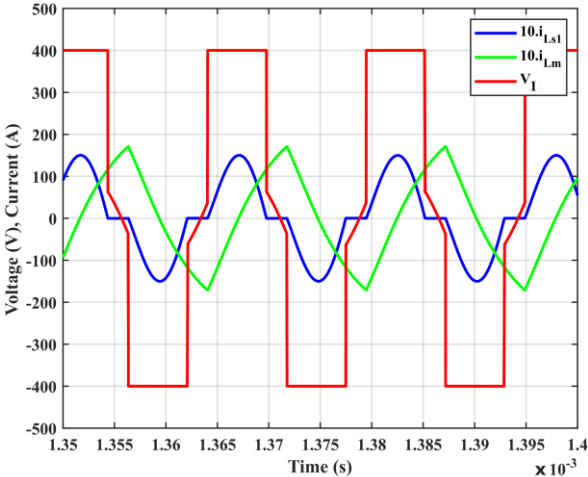
(b)

Figure 4.21: Waveforms comparison for (a) State-variable and (b) Spice simulations in forward mode and $V_{bat} = 350V$

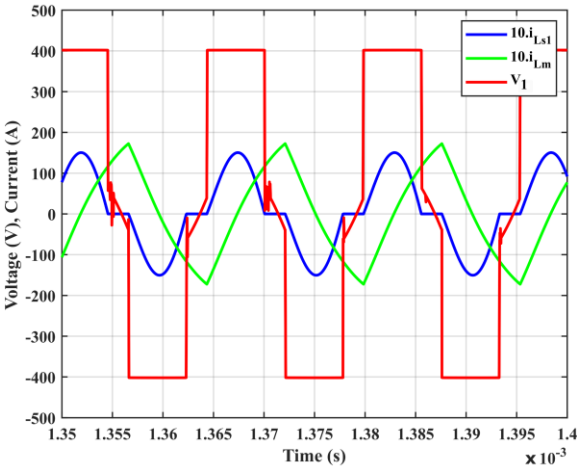
In Figure 4.22 the results are shown for a converter operating in reverse mode, also at $V_{bat} = 350V$, when the converter is operating in region II. Here the rectifier's input current is equal to $i_{L_{S1}}$ and, due to non-conduction mode occurrence, the rectifier

voltage is not a square wave as in the previous case. For the Spice simulation, noise is observed on the input voltage to the rectifier (v_1) during the non-conduction period.

For all cases analysed, waveforms obtained from Spice simulation are very similar to the state-variable results.



(a)



(b)

Figure 4.22: Waveforms comparison for (a) State-variable and (b) Spice simulations in reverse mode and $V_{bat} = 350V$

After verifying the accuracy of the models through simulation, the execution time for each method is compared. The average execution time for each model analysed is shown in Table 4.12. It is verified that cyclic-averaging is the fastest method, being nearly 37 times faster than Spice, the slowest method. Both Spice and state-variable

simulations are performed considering a simulation time of 3ms and maximum step size of 10 ns. Note that while FMA and cyclic-averaging methods directly calculate steady-state results, Spice and state-variable are time-domain models that include the transient response and simulation time must be adequately chosen to allow the system to reach steady-state.

Table 4.12: Execution time comparison

	Modelling technique			
	FMA	State-variable	Cyclic-averaging	Spice
Execution time (s)	2.045	5.888	0.165	6.084

4.8 Conclusions

In this chapter FMA, state-variable and cyclic-averaging models were developed for analysis of a 3.5kW CLLC bidirectional converter operating under frequency modulation.

Models were validated against Spice simulations and compared to experimental results available in the literature. From analysis of the obtained results, among the models here compared, cyclic-averaging and state-variable methods provide the most accurate response. Due to the increased number of simplifications and the representation of voltages and currents by only the fundamental component, the application of FMA method results in increased errors. FMA accuracy could be improved by adding to the model the effects of the resistances and parasitic elements associated to the resonant tank components and switches, but this would also result in more complex analysis and equation description.

Furthermore, it was confirmed that the use of cyclic-averaging techniques results in a rapid analysis, with the fastest execution time between the models tested.

In Chapter 5 the models developed here will be adapted for the analysis of a phase-shifted modulated variant of the CLLC converter.

4.9 References

- [1] Z. U. Zahid, Z. M. Dalala, R. Chen, B. Chen, and J. S. Lai, "Design of bidirectional DC-DC resonant converter for Vehicle-to-Grid (V2G) applications," *IEEE Transactions on Transportation Electrification*, vol. 1, no. 3, pp. 232–244, 2015.
- [2] W. Chen, P. Rong, and Z. Lu, "Snubberless bidirectional DC-DC converter with new CLLC resonant tank featuring minimized switching loss," *IEEE Transactions on Industrial Electronics*, vol. 57, no. 9, pp. 3075–3086, 2010.
- [3] J. Sun and H. Grotstollen, "Symbolic Analysis Methods for Averaged Modeling of Switching Power Converters," *IEEE Transactions on Power Electronics*, vol. 12, no. 3, pp. 537–546, 1997.
- [4] C. Gould, "Rapid Analysis and Design of CLL Resonant Power Converters," PhD Thesis. University of Sheffield, 2006.
- [5] M. P. Foster, "Analysis and Design of High-order Resonant Power Converters," PhD Thesis. University of Sheffield, 2003.
- [6] J. Deng, S. Li, S. Hu, C. C. Mi, and R. Ma, "Design Methodology of LLC Resonant Converters for Electric Vehicle Battery Chargers," *IEEE Transactions on Vehicular Technology*, vol. 63, no. 4, pp. 1581–1592, 2014.
- [7] B. Sen, Chaohui Liu, Jiabin Wang, C. Gould, and K. Colombage, "A CLLC Resonant Converter Based Bidirectional EV Charger with Maximum Efficiency Tracking," *8th IET International Conference on Power Electronics, Machines and Drives (PEMD 2016)*, pp. 1–6, 2016.

5 Modelling of Phase-shift Modulated CLLC Converter

5.1 Introduction

In the previous chapter the FMA, state-variable and cyclic-averaging modelling techniques were applied to analyse a bidirectional CLLC resonant converter operating under frequency modulation. From comparison of the results taken from each modelling approach with a Spice-based simulation, it was observed that cyclic-averaging and state-variable were the most accurate models, with the cyclic-averaging having the advantage of being the method with fastest execution time.

In this chapter similar analysis will be performed for the phase-shift modulated variant of the CLLC converter, considering bidirectional power transfer and two types of phase-shift modulation: Single Phase-Shift (SPS) and Pulse-Phase Modulation (PPM), also called Triple-Phase-Shift modulation (TPS).

From the results obtained in the previous chapter, it was observed that the FMA method suffers from accuracy problems, but due to its simple and easy implementation, this analysis will be applied here again to study the influence of phase-shift modulation angles on the converter's behaviour. A low-power converter design is presented and the state-variable and cyclic-averaging methods will be employed to estimate the average output current of a converter operating under SPS and PPM modulation. The results obtained from the aforementioned modelling methods will be verified against a Spice simulation and the execution time will be compared.

5.2 Phase-shift modulation technique

The bidirectional CLLC converter here analysed is the same topology investigated in the previous chapter, as presented in Figure 5.1.

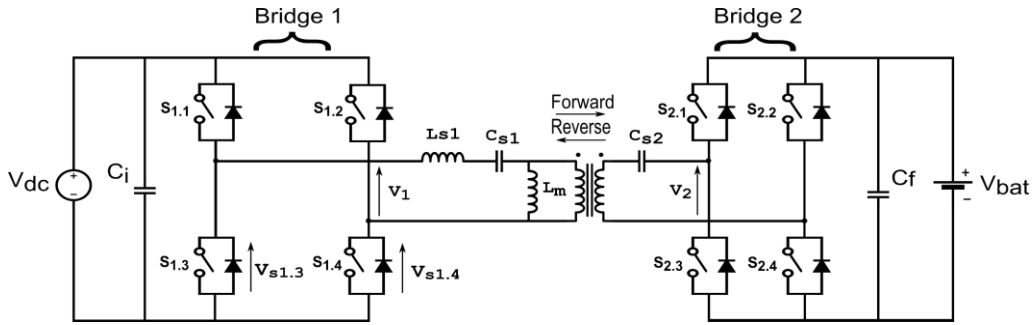


Figure 5.1: CLLC topology

In this chapter, two types of phase-shift modulation are considered for the operation of the CLLC converter. The first and simpler method analysed is the Single Phase-Shift (SPS) [1]–[3], the main advantage of this being easy implementation. In this configuration the switching frequency is fixed, duty cycle is kept constant at 50% for all switches, and a phase-shift angle ($-90^\circ \leq \phi \leq 90^\circ$) is introduced between the output voltages of bridge 1 and bridge 2 from Figure 5.1. Typical waveforms of bridge voltages v_1 and v_2 for a converter operating in reverse mode are shown in Figure 5.2-a. The output power magnitude and power flow direction are controlled using only the phase-shift angle, where positive values of ϕ (primary voltage v_1 lags secondary voltage v_2 by ϕ) result in forward operation while negative values (primary voltage v_1 leads secondary voltage v_2 by ϕ) are used for reverse mode implementation. The major drawback of SPS modulation is the high circulating current and, consequently, conduction losses when operating under partial loading [4], [5]. As the phase-shift angle decreases, the output current decreases but circulating current increases, resulting in increased losses.

As an alternative technique to reduce reactive currents, the Pulse-Phase Modulation (PPM) [6], [7], also known as Triple Phase-Shift method [8], [9] was proposed. In this case, the frequency is still constant but an additional phase-shift angle α_1 is introduced between the legs of the primary bridge, and angle α_2 between the legs of the secondary bridge, where $0 \leq \alpha_1, \alpha_2 \leq 180^\circ$. These angles are used to control the magnitude of output power. The phase-shift angle ϕ can also be used as control variable but, as operation degrades as this angle decreases, in most applications ϕ is fixed at $\pm 90^\circ$ and used only to control the power flow direction. The drain-source voltage of switches S1.3 and S1.4 for a converter operating under PPM modulation and the resulting bridge

voltages v_1 and v_2 from Figure 5.1 are shown in Figure 5.2-b. For a simpler control, α_1 is maintained equal to α_2 in many applications.

For a converter operating under phase-shift modulation, the maximum power transferred is reached when $\phi = \pm 90^\circ$ and $\alpha_1 = \alpha_2 = 180^\circ$.

Apart from the FMA analysis, where the influence of the phase-shift angles will be evaluated, when analysing the PPM modulation case for state-variable and cyclic-averaging models in this chapter the following considerations are made:

$$\alpha_1 = \alpha_2 = \alpha \text{ and } \phi = \pm 90^\circ$$

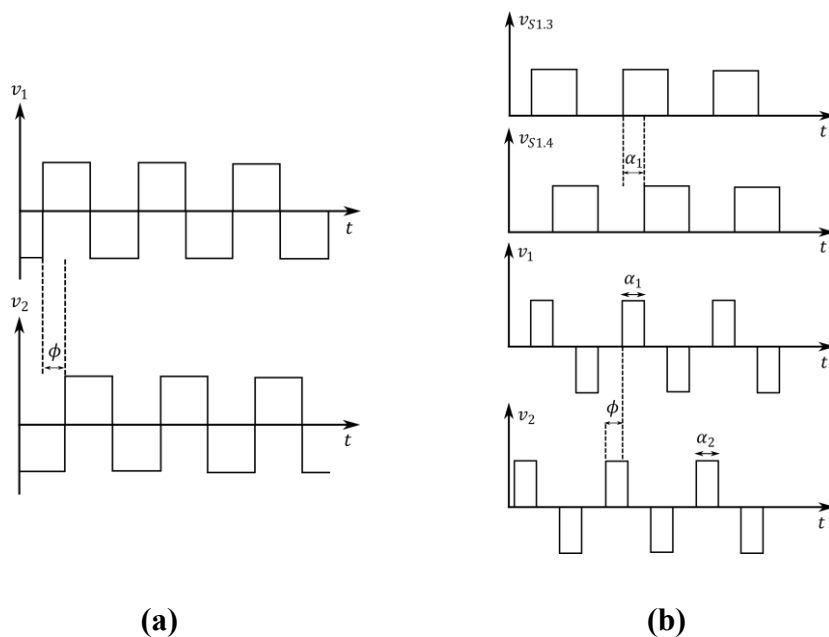


Figure 5.2: Bridge output voltages for (a) SPS modulation, operating in reverse mode and (b) PPM modulation, operating in forward mode

5.3 Fundamental Mode Approximation (FMA)

As shown in the previous chapter, the FMA technique is not the most accurate but provides simple and rapid analysis. Here this technique will be employed to quickly estimate the magnitude of the resonant tank currents and the output power. Based on the CLLC converter circuit presented in Figure 5.1, a simplified equivalent circuit is shown in Figure 5.3 for FMA analysis, where $C'_{s2} = C_{s2}/n^2$ and n is the transformer's turns ratio.

Based on the converter design procedure proposed in [10], inductor L_m resonates with $L_{s1}C_{s1}$ and C'_{s2} , as a result, the reactances in each leg of the T-network in Figure 5.3 are represented using a base reactance X_n , where $X_n = X_{C1} - X_{L1} = X_{Lm} = X_{C2'}$.

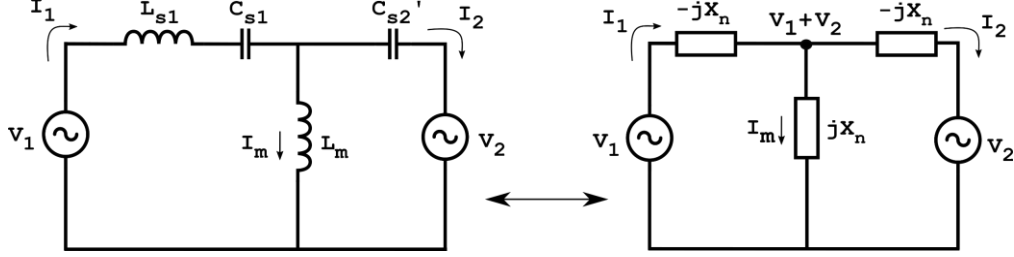


Figure 5.3: Simplified circuit for FMA analysis, referred to primary

Using the Fourier series representation, the bridge voltages referred to the primary are defined in (5.1). For the case of a converter operating under SPS modulation, the angles α_1 and α_2 are fixed and equal to 180° .

$$v_1(t) = \frac{4V_{DC}}{\pi} \sum_{i=1,3,\dots}^{\infty} \frac{1}{i} \cos(i\omega t) \sin\left(\frac{i\alpha_1}{2}\right)$$

$$v_2(t) = \frac{4nV_{bat}}{\pi} \sum_{i=1,3,\dots}^{\infty} \frac{1}{i} \cos(i\omega t + i\phi) \sin\left(\frac{i\alpha_2}{2}\right)$$
(5.1)

Applying FMA, only the fundamental component is considered, and the voltage phasors are defined as:

$$V_1 = \frac{4V_{DC}}{\pi\sqrt{2}} \sin\left(\frac{\alpha_1}{2}\right)$$

$$V_2 = \frac{4nV_{bat}}{\pi\sqrt{2}} \sin\left(\frac{\alpha_2}{2}\right) (\cos(\phi) + j \sin(\phi))$$
(5.2)

From circuit analysis, the resonant tank currents are calculated.

$$I_1 = \frac{V_2}{jX_n}$$

$$I_2 = -\frac{V_1}{jX_n}$$

$$I_m = \frac{V_1 + V_2}{jX_n} \quad (5.3)$$

The RMS values of currents are obtained calculating the magnitude of the phasors defined in (5.3). A generic phasor \mathbf{Z} is defined, composed of a real component a and imaginary part b .

$$\mathbf{Z} = a + jb \quad (5.4)$$

The magnitude of \mathbf{Z} is calculated as follows:

$$|\mathbf{Z}| = \sqrt{a^2 + b^2} \quad (5.5)$$

The magnitude of primary and secondary currents are presented in (5.6). Note that phasor \mathbf{I}_2 is referred to the primary side of the circuit, therefore, the magnitude of the secondary current (\mathbf{I}_{sec}) must be calculated considering the transformers turns ratio as in (5.6).

$$|\mathbf{I}_1| = \frac{4nV_{bat}}{\pi X_n \sqrt{2}} \sin\left(\frac{\alpha_2}{2}\right)$$

$$|\mathbf{I}_{sec}| = n|\mathbf{I}_2| = \frac{4nV_{DC}}{\pi X_n \sqrt{2}} \sin\left(\frac{\alpha_1}{2}\right) \quad (5.6)$$

The calculation of the magnetizing current from (5.3) results in a complex expression. This value is calculated at simulation stage using equation (5.3) and the MATLAB function $abs()$, which is employed to calculate the absolute value of a number X , or complex magnitude (or modulus) when X is a complex number.

For the FMA analysis, parasitic resistances are not considered and, consequently, the transferred power is calculated using (5.2), (5.3) and the active power equations $P = Re[\mathbf{V}_2 \mathbf{I}_2^*]$ or $P = Re[\mathbf{V}_1 \mathbf{I}_1^*]$, resulting in equation (5.7). Also, it was previously shown in [10] that, for a phase-shift modulated CLLC converter, most of the power is transferred by the fundamental component.

$$P_{out} = \frac{8nV_{DC}V_{bat}}{\pi^2 X_n} \sin(\phi) \sin\left(\frac{\alpha_1}{2}\right) \sin\left(\frac{\alpha_2}{2}\right) \quad (5.7)$$

From (5.7) it is confirmed that the maximum value of output power is obtained when $\phi = \pm 90^\circ$ and $\alpha_1 = \alpha_2 = 180^\circ$, as discussed in the previous section. In section 5.6.2 the equation description here obtained will be implemented using MATLAB and the output power and resonant tank currents will be calculated for different angles and compared to a Spice simulation.

5.4 State-variable analysis

The state-variable analysis for converters operating under phase-shift modulation is very similar to the study performed in the previous chapter for the frequency modulated variant, the main difference here is that the output bridge (bridge 2 for forward mode or bridge 1 for reverse mode, from Figure 5.1) no longer operates as a diode bridge rectifier as in the previous chapter. For the phase-shift modulated converter, both bridges are actively controlled and the bridge voltages $v_1(t)$ and $v_2(t)$ are determined following the SPS or PPM modulation description from section 5.2.

The equivalent circuit for a converter operating in forward mode is shown in Figure 5.4. The fast subsystem is referred to the primary side of the transformer while the slow subsystem is referred to the secondary, therefore $C_{s2}' = C_{s2}/n^2$. As previously discussed in Chapter 3, resistances r_{bat} and r_{dc} represent internal or measurement resistances, having a small value to not significantly influence the output of the converter. The primary and secondary resistances are defined as follows:

$$\begin{aligned} r_1 &= r_{Ls1} + r_{Cs1} + 2 \cdot r_{SWITCH} \\ r_2' &= n^2(r_{C2} + 2 \cdot r_{SWITCH}) \end{aligned} \quad (5.8)$$

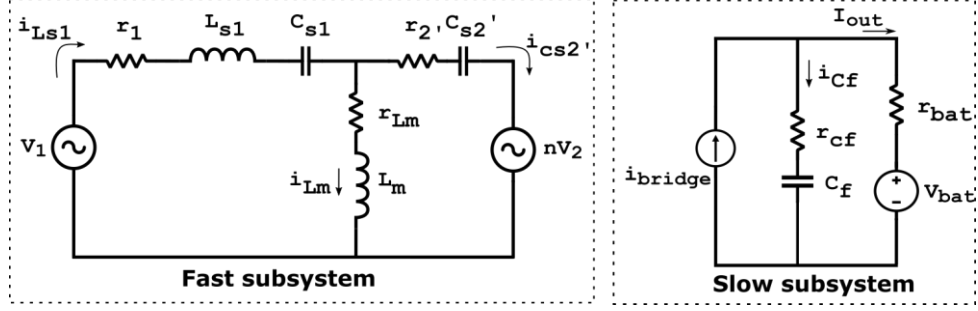


Figure 5.4: Equivalent circuit for state-variable analysis, forward mode

Similar to the bridge voltage definition performed in Chapter 3 for the DAB converter, for operation under SPS modulation, the output voltages of the H-bridges are simplified to square waves with amplitude dependent of the DC bus or battery voltages, as defined in (5.9). For the PPM modulation case, a zero-voltage level is added depending on the values of α_1 and α_2 , as previously shown in Figure 5.2.

$$v_1 = \pm V_{dc}$$

$$v_2 = \pm V_{bat}$$

(5.9)

To obtain the state-variable piecewise linear equation description, the fast and slow subsystems are analysed and the coupling equation is determined based on the equivalent circuit in Figure 5.4. From circuit analysis, the fast subsystem equations are given by:

$$\frac{di_{Ls1}}{dt} = \frac{v_1 - (r_1 + r_2')i_{Ls1} - v_{Cs1} + r_2' i_{Lm} - v_{Cs2'} - nv_2}{L_{s1}}$$

(5.10)

$$\frac{dv_{Cs1}}{dt} = \frac{i_{Ls1}}{C_{s1}}$$

(5.11)

$$\frac{di_{Lm}}{dt} = \frac{r_2' i_{Ls1} - (r_{Lm} + r_2')i_{Lm} + v_{Cs2'} + nv_2}{L_m}$$

(5.12)

$$\frac{dv_{Cs2'}}{dt} = \frac{i_{Ls1} - i_{Lm}}{C_{s2'}}$$

(5.13)

For the slow subsystem:

$$\frac{dv_{cf}}{dt} = \frac{V_{bat} + r_{bat}i_{bridge} - v_{cf}}{C_f(r_{bat} + r_{cf})} \quad (5.14)$$

The coupling equation is given by equation (5.15) and it is determined analysing the operation of the active bridge on the output side. Note that the case $v_2(t) = 0$ only occurs when the converter operates under PPM modulation.

$$i_{bridge}(t) = \begin{cases} n(i_{Ls1} - i_{Lm}), & \text{when } v_2(t) > 0 \\ -n(i_{Ls1} - i_{Lm}), & \text{when } v_2(t) < 0 \\ 0, & \text{when } v_2(t) = 0 \end{cases} \quad (5.15)$$

Once the equations for fast, slow and coupling systems are defined, the output voltage and current are calculated.

$$V_{out} = v_{cf} + r_{cf}i_{cf}$$

$$I_{out} = \frac{V_{out} - V_{bat}}{r_{bat}} \quad (5.16)$$

The same methodology adopted to obtain the state-variable description of a converter operating in forward mode is applied for the opposite power flow direction. The equivalent circuit in reverse mode is presented in Figure 5.5. The converter's output is now on the primary side of the transformer, therefore fast and slow subsystem are referred to primary.

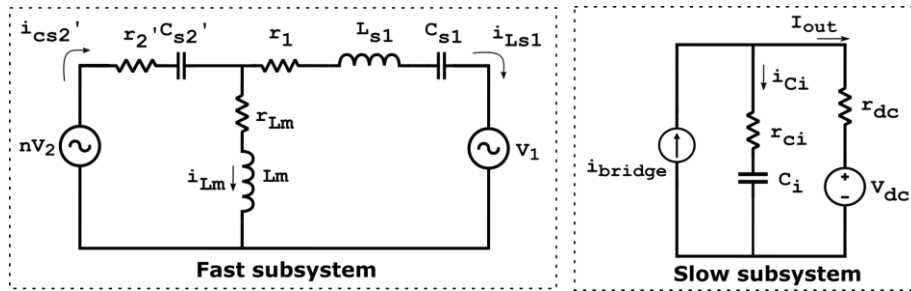


Figure 5.5: Equivalent circuit for state-variable analysis, reverse mode

Using basic circuit analysis, the fast subsystem equations are obtained:

$$\frac{di_{Ls1}}{dt} = \frac{nv_2 - (r_1 + r_2')i_{Ls1} - v_{Cs1} - r_2'i_{Lm} - v_{Cs2'} - v_1}{L_{s1}} \quad (5.17)$$

$$\frac{dv_{Cs1}}{dt} = \frac{i_{Ls1}}{C_{s1}} \quad (5.18)$$

$$\frac{di_{Lm}}{dt} = \frac{nv_2 - r_2'i_{Ls1} - (r_{Lm} + r_2')i_{Lm} - v_{Cs2'}}{L_m} \quad (5.19)$$

$$\frac{dv_{Cs2'}}{dt} = \frac{i_{Ls1} + i_{Lm}}{C_{s2'}} \quad (5.20)$$

The slow subsystem is described as:

$$\frac{dv_{Ci}}{dt} = \frac{V_{dc} + r_{dc}i_{bridge} - v_{Ci}}{C_i(r_{dc} + r_{Ci})} \quad (5.21)$$

The coupling equation is now defined based on the state of the output bridge voltage $v_1(t)$, the case of $v_1(t) = 0$ will only happen during PPM modulation.

$$i_{bridge}(t) = \begin{cases} i_{Ls1}, & \text{when } v_1(t) > 0 \\ -i_{Ls1}, & \text{when } v_1(t) < 0 \\ 0, & \text{when } v_1(t) = 0 \end{cases} \quad (5.22)$$

Ultimately, the output voltage and current are given by:

$$V_{out} = v_{Ci} + r_{Ci}i_{Ci}$$

$$I_{out} = \frac{V_{out} - V_{dc}}{r_{dc}} \quad (5.23)$$

5.4.1 Implementation in Simulink

After the set of piecewise linear equations is obtained for forward and reverse operation, the state-variable model is implemented in Simulink.

Firstly, the bridge voltages are defined as shown in Figure 5.6. The “pulse generator” and “variable time delay” blocks are used to implement the waveforms of $v_1(t)$ and $v_2(t)$ with a phase-shift between the legs of each bridge (angles α_1 and α_2) and between the primary and secondary bridge (angle ϕ).

Once the output voltages of the bridges are defined, the fast and slow subsystems and coupling equation are implemented as shown in Figures 5.7, 5.8 and 5.9.

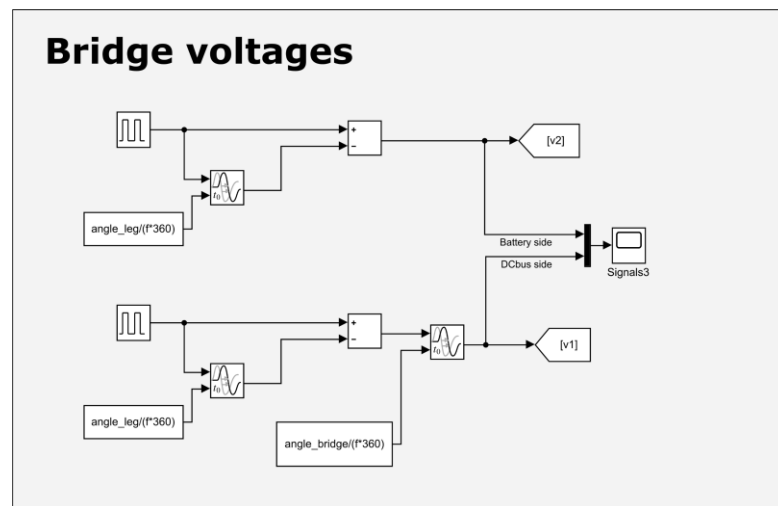


Figure 5.6: Definition of bridge voltages, forward mode

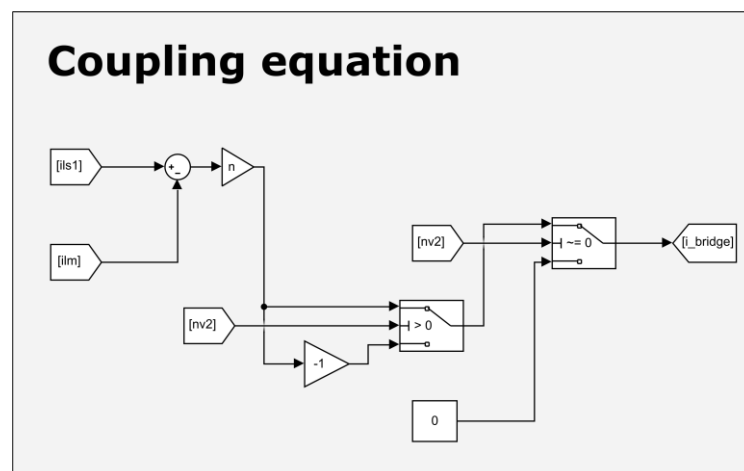


Figure 5.7: Coupling equation, forward mode

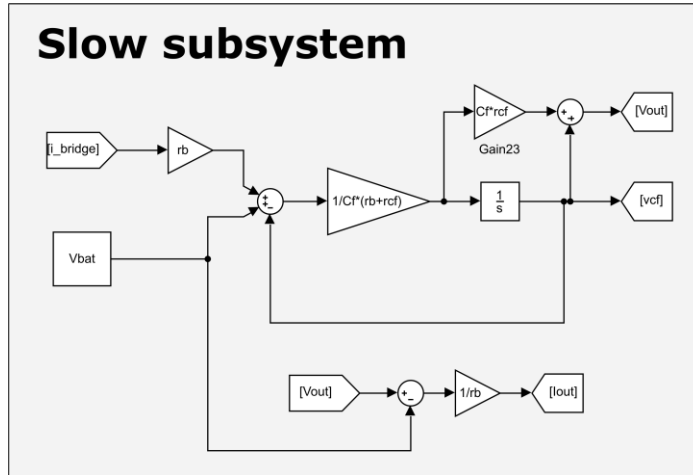


Figure 5.8: Slow subsystem, forward mode

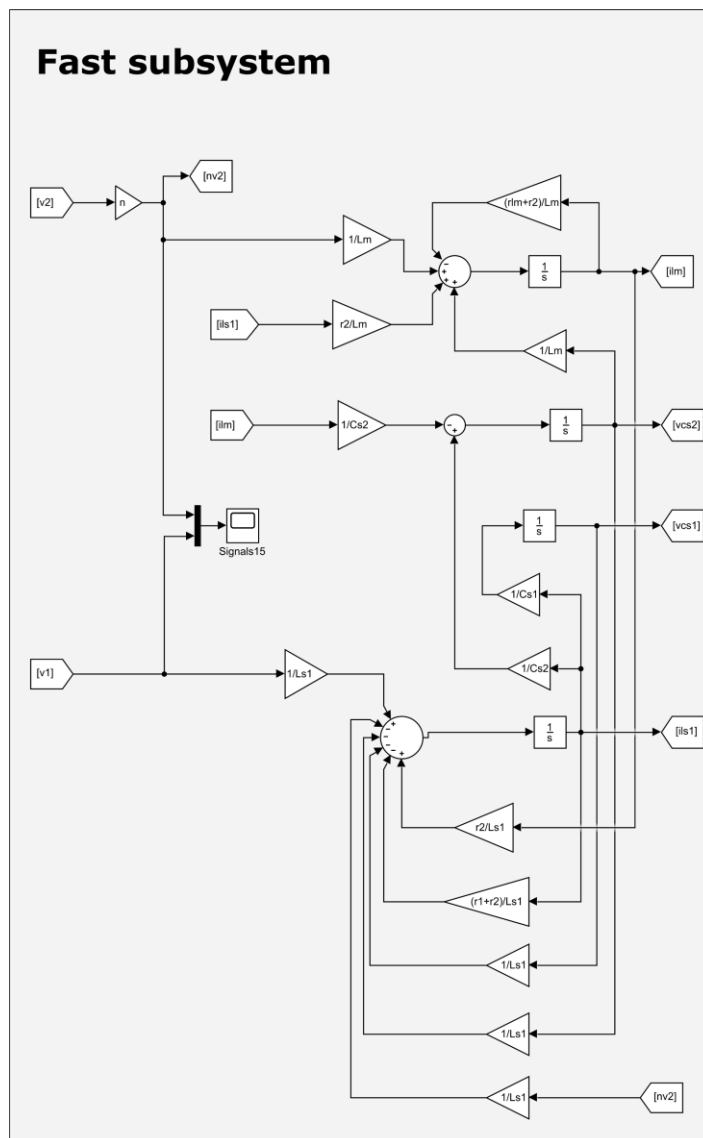


Figure 5.9: Fast subsystem, forward mode

5.5 Cyclic-averaging analysis

In the previous section a piecewise linear state-variable model was obtained, which will serve as base for application of the cyclic-averaging method. The set of equations for forward mode are reorganized for a matrix form representation:

$$\frac{d}{dt} \begin{bmatrix} i_{Ls1}(t) \\ v_{Cs1}(t) \\ i_{Lm}(t) \\ v_{Cs2'}(t) \\ v_{Cf}(t) \end{bmatrix} = A_f \begin{bmatrix} i_{Ls1}(t) \\ v_{Cs1}(t) \\ i_{Lm}(t) \\ v_{Cs2'}(t) \\ v_{Cf}(t) \end{bmatrix} + B_f \quad (5.24)$$

where:

$$A_f = \begin{bmatrix} -\frac{(r_1 + r_2')}{L_{s1}} & -\frac{1}{L_{s1}} & \frac{r_{c2'}}{L_{s1}} & -\frac{1}{L_{s1}} & 0 \\ \frac{1}{C_{s1}} & 0 & 0 & 0 & 0 \\ \frac{r_{c2'}}{L_m} & 0 & -\frac{(r_{Lm} + r_{c2}')}{L_m} & \frac{1}{L_m} & 0 \\ \frac{1}{C_{s2'}} & 0 & -\frac{1}{C_{s2'}} & 0 & 0 \\ 0 & 0 & 0 & 0 & -\frac{1}{C_f(r_{bat} + r_{cf})} \end{bmatrix}$$

$$B_f = \begin{bmatrix} \frac{(v_1(t) - nv_2(t))}{L_{s1}} \\ 0 \\ \frac{nv_2(t)}{L_m} \\ 0 \\ \frac{V_{bat} + r_{bat}i_{bridge}(t)}{C_f(r_{bat} + r_{cf})} \end{bmatrix}$$

Similarly, for reverse mode:

$$\frac{d}{dt} \begin{bmatrix} i_{Ls1}(t) \\ v_{Cs1}(t) \\ i_{Lm}(t) \\ v_{Cs2'}(t) \\ v_{Ci}(t) \end{bmatrix} = A_r \begin{bmatrix} i_{Ls1}(t) \\ v_{Cs1}(t) \\ i_{Lm}(t) \\ v_{Cs2'}(t) \\ v_{Ci}(t) \end{bmatrix} + B_r \quad (5.25)$$

where:

$$A_r = \begin{bmatrix} -\frac{(r_1 + r_2')}{L_{s1}} & -\frac{1}{L_{s1}} & -\frac{r_{c2'}}{L_{s1}} & -\frac{1}{L_{s1}} & 0 \\ \frac{1}{C_{s1}} & 0 & 0 & 0 & 0 \\ -\frac{r_{c2'}}{L_m} & 0 & -\frac{(r_{Lm} + r_{c2'})}{L_m} & -\frac{1}{L_m} & 0 \\ \frac{1}{C_{s2'}} & 0 & -\frac{1}{C_{s2'}} & 0 & 0 \\ 0 & 0 & 0 & 0 & -\frac{1}{C_i(r_{dc} + r_{ci})} \end{bmatrix}$$

$$B_r = \begin{bmatrix} \frac{(nv_2(t) - v_1(t))}{L_{s1}} \\ 0 \\ \frac{nv_2(t)}{L_m} \\ 0 \\ \frac{V_{dc} + r_{dc}i_{bridge}(t)}{C_i(r_{dc} + r_{ci})} \end{bmatrix}$$

To apply the cyclic-averaging method defined in Chapter 2, the converter's periodic behaviour is analysed and the state of variables $v_1(t)$, $v_2(t)$ and $i_{bridge}(t)$ through a full cycle are defined.

The typical bridge voltage and current sequence for a converter operating under SPS modulation is shown in Figure 5.10. The bridge voltages are square waves with two possible states, $\pm V_{dc}$ for v_1 and $\pm V_{bat}$ for $v_2(t)$, and the bridge current is calculated using (5.15) or (5.22) depending on the power flow direction. Four operation modes are identified for a cycle, considering the beginning of a cycle at the transition of the output bridge voltage (v_2 for forward operation or v_1 for reverse operation) from

negative to positive. The mode descriptions, containing the state of the bridge voltages and output current during each mode, is presented in Table 5.1 for forward operation and in Table 5.2 for reverse operation.

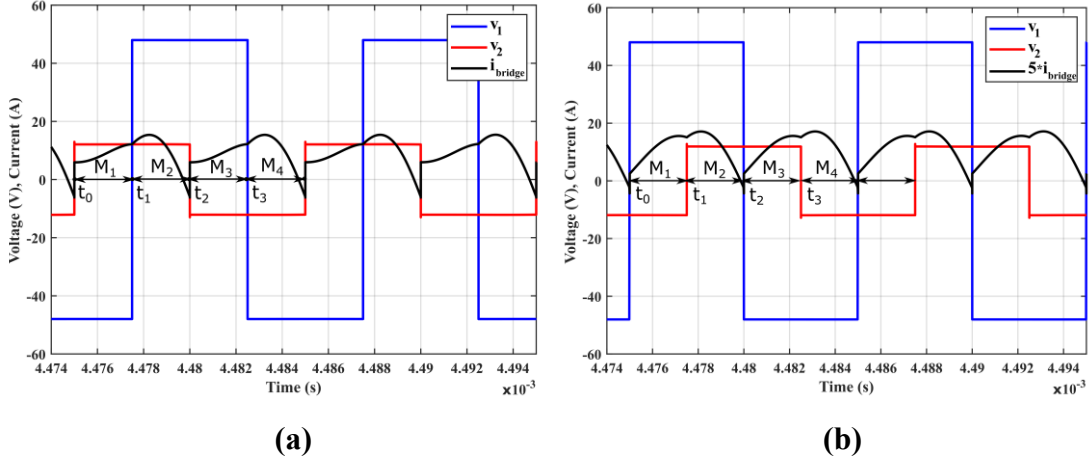


Figure 5.10: Typical bridge voltage and current sequence for SPS operation in (a) forward mode and (b) reverse mode

Table 5.1: Mode descriptions for SPS modulation, forward mode

Mode	$v_1(t)$	$v_2(t)$	$i_{bridge}(t)$
M_1	$-V_{dc}$	V_{bat}	$n(i_{LS1} - i_{Lm})$
M_2	V_{dc}	V_{bat}	$n(i_{LS1} - i_{Lm})$
M_3	V_{dc}	$-V_{bat}$	$-n(i_{LS1} - i_{Lm})$
M_4	$-V_{dc}$	$-V_{bat}$	$-n(i_{LS1} - i_{Lm})$

Table 5.2: Mode descriptions for SPS modulation, reverse mode

Mode	$v_1(t)$	$v_2(t)$	$i_{bridge}(t)$
M_1	V_{dc}	$-V_{bat}$	i_{LS1}
M_2	V_{dc}	V_{bat}	i_{LS1}
M_3	$-V_{dc}$	V_{bat}	$-i_{LS1}$
M_4	$-V_{dc}$	$-V_{bat}$	$-i_{LS1}$

For the PPM modulation case, the bridge voltages are no longer perfect square waves and have three possible states, 0 and $\pm V_{dc}$ for $v_1(t)$, and 0 and $\pm V_{bat}$ for $v_2(t)$. The occurrence and duration of the zero-voltage level depends on the phase-shift angle

α between the legs of each H-bridge, where $\alpha_1 = \alpha_2 = \alpha$. The phase-shift between the bridge output voltages, ϕ , is kept constant at $\pm 90^\circ$, where the sign determines the power flow direction.

To obtain the mode description of a converter operating under PPM modulation, two cases must be considered depending on the range of phase shift angle α and whether this angle is higher or lower than ϕ . The periodic behaviour of the bridge voltages and current when $90^\circ \leq \alpha \leq 180^\circ$ is shown in Figure 5.11, while the case $\alpha < 90^\circ$ is presented in Figure 5.12.

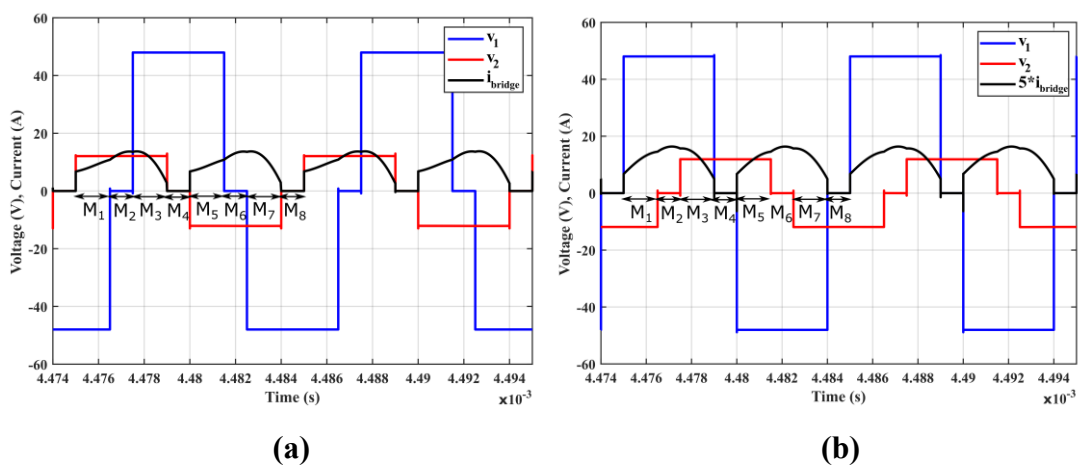


Figure 5.11: Typical bridge voltage and current sequence for PPM operation and $90^\circ \leq \alpha \leq 180^\circ$ in (a) forward mode and (b) reverse mode

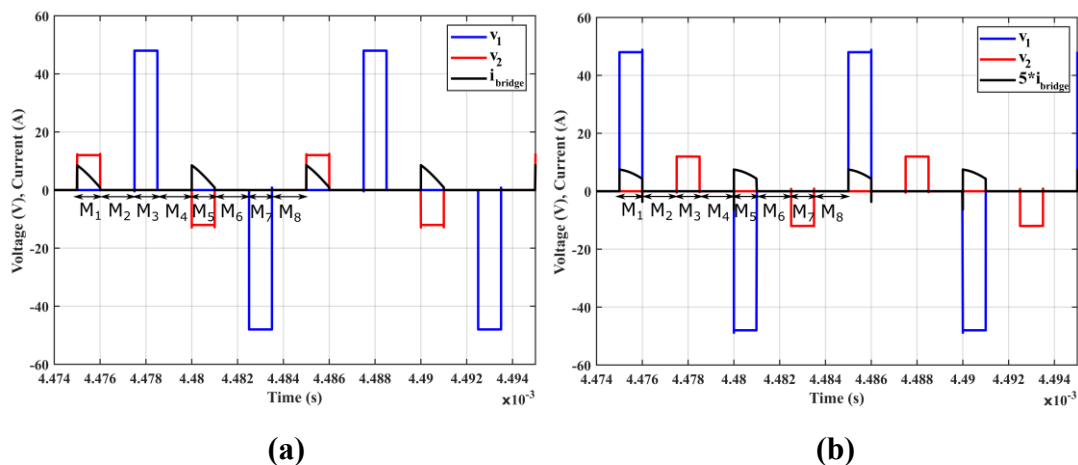


Figure 5.12: Typical bridge voltage and current sequence for PPM operation and $\alpha < 90^\circ$ in (a) forward mode and (b) reverse mode

For both cases, eight operation modes are identified and, considering the beginning of a cycle when the output bridge voltage (v_2 for forward and v_1 for reverse operation)

becomes positive, the mode descriptions for the full α range are presented in Tables 5.3, 5.4, 5.5 and 5.6.

Table 5.3: Mode descriptions for PPM modulation and $90^\circ \leq \alpha \leq 180^\circ$, forward mode

Mode	$v_1(t)$	$v_2(t)$	$i_{bridge}(t)$
M_1	$-V_{dc}$	V_{bat}	$n(i_{LS1} - i_{Lm})$
M_2	0	V_{bat}	$n(i_{LS1} - i_{Lm})$
M_3	V_{dc}	V_{bat}	$n(i_{LS1} - i_{Lm})$
M_4	V_{dc}	0	0
M_5	V_{dc}	$-V_{bat}$	$-n(i_{LS1} - i_{Lm})$
M_6	0	$-V_{bat}$	$-n(i_{LS1} - i_{Lm})$
M_7	$-V_{dc}$	$-V_{bat}$	$-n(i_{LS1} - i_{Lm})$
M_8	$-V_{dc}$	0	0

Table 5.4: Mode descriptions for PPM modulation and $90^\circ \leq \alpha \leq 180^\circ$, reverse mode

Mode	$v_1(t)$	$v_2(t)$	$i_{bridge}(t)$
M_1	V_{dc}	$-V_{bat}$	i_{LS1}
M_2	V_{dc}	0	i_{LS1}
M_3	V_{dc}	V_{bat}	i_{LS1}
M_4	0	V_{bat}	0
M_5	$-V_{dc}$	V_{bat}	$-i_{LS1}$
M_6	$-V_{dc}$	0	$-i_{LS1}$
M_7	$-V_{dc}$	$-V_{bat}$	$-i_{LS1}$
M_8	0	$-V_{bat}$	0

Table 5.5: Mode descriptions for PPM modulation and $\alpha \leq 90^\circ$, forward mode

Mode	$v_1(t)$	$v_2(t)$	$i_{bridge}(t)$
M_1	0	V_{bat}	$n(i_{Ls1} - i_{Lm})$
M_2	0	0	0
M_3	V_{dc}	0	0
M_4	0	0	0
M_5	0	$-V_{bat}$	$-n(i_{Ls1} - i_{Lm})$
M_6	0	0	0
M_7	$-V_{dc}$	0	0
M_8	0	0	0

Table 5.6: Mode descriptions for PPM modulation and $\alpha \leq 90^\circ$, reverse mode

Mode	$v_1(t)$	$v_2(t)$	$i_{bridge}(t)$
M_1	V_{dc}	0	i_{Ls1}
M_2	0	0	0
M_3	0	V_{bat}	0
M_4	0	0	0
M_5	$-V_{dc}$	0	$-i_{Ls1}$
M_6	0	0	0
M_7	0	$-V_{bat}$	0
M_8	0	0	0

Based on the mode descriptions, the values of $v_1(t)$, $v_2(t)$ and $i_{bridge}(t)$ are substituted on the state-variable equations (5.24) or (5.25) and the dynamic and input matrices, A_i and B_i respectively, are determined for each mode i , where $i = 1, 2, 3, 4$ for SPS modulation and $i = 1, 2, 3, 4, 5, 6, 7, 8$ for PPM modulation cases.

Once the state-variable description is determined for all modes, the duration of each mode, $d_i T$, must be calculated based on the period T calculated from the switching frequency and the duty cycle, or normalised time interval, for each mode, d_i .

As previously discussed in section 5.2, phase-shift modulated converters operate with fixed frequency and the two H-bridges are actively controlled by the phase-shift

angles α and ϕ . From waveform analysis, the duty cycles are calculated solely based on the leg and bridge phase-shift angles. Therefore, the duty cycle calculation here is significantly simpler when compared to the frequency modulated variant previously analysed in Chapter 4.

When operating under SPS modulation, as shown in Figure 5.10, the leg phase-shift angle, α , is kept constant at 180° and the duration of each mode is determined based on the phase-shift angle between the primary and secondary bridge, where $0^\circ \leq |\phi| \leq 90^\circ$. For the first mode:

$$d_1 = \frac{|\phi|}{360} \quad (5.26)$$

The remaining duty cycles are determined by waveforms symmetry:

$$d_2 = 0.5 - d_1, d_3 = d_1 \text{ and } d_4 = d_2 \quad (5.27)$$

For the PPM modulation case, the normalised time duration of each mode is determined analysing the waveforms from Figures 5.11 and 5.12. The bridge angle ϕ is now constant and, as a result, the duty values are calculated based on the values of the leg phase-shift angle α . When $90^\circ \leq \alpha \leq 180^\circ$, the duties are determined as in (5.28).

$$\begin{aligned} d_1 &= \frac{-90 + \alpha}{360} = d_3 = d_5 = d_7 \\ d_2 &= \frac{180 - \alpha}{360} = d_4 = d_6 = d_8 \end{aligned} \quad (5.28)$$

Now considering the case of $\alpha \leq 90^\circ$, the duty cycle values are calculated as follows:

$$\begin{aligned} d_1 &= \frac{\alpha}{360} = d_3 = d_5 = d_7 \\ d_2 &= \frac{90 - \alpha}{360} = d_4 = d_6 = d_8 \end{aligned} \quad (5.29)$$

When $\alpha = 90^\circ$ operation is reduced from eight to four modes. In this case either set of mode descriptions and duty calculation presented for PPM modulation can be used, since the extra modes will be eliminated in the calculation of the modes duration. According to the duty calculation equation (5.28), when $\alpha = 90^\circ$ the values of duties d_1, d_3, d_5 and d_7 will be equal to zero, cancelling modes M_1, M_3, M_5 and M_7 from Tables 5.3 and 5.4. Similarly, from (5.29) modes M_2, M_4, M_6 and M_8 , from Tables 5.5 and 5.6, are cancelled, resulting in the same mode description, as shown in Tables 5.7 and 5.8.

Table 5.7: Mode descriptions for PPM modulation and $\alpha = 90^\circ$, forward mode

Mode	$v_1(t)$	$v_2(t)$	$i_{bridge}(t)$
M_1	0	V_{bat}	$n(i_{LS1} - i_{Lm})$
M_2	V_{dc}	0	0
M_3	0	$-V_{bat}$	$-n(i_{LS1} - i_{Lm})$
M_4	$-V_{dc}$	0	0

Table 5.8: Mode descriptions for PPM modulation and $\alpha = 90^\circ$, reverse mode

Mode	$v_1(t)$	$v_2(t)$	$i_{bridge}(t)$
M_1	V_{dc}	0	i_{LS1}
M_2	0	V_{bat}	0
M_3	$-V_{dc}$	0	$-i_{LS1}$
M_4	0	$-V_{bat}$	0

After the state-variable equations, mode descriptions and duty cycles are determined for both types of phase-shift modulation, the cyclic method equations from Chapter 2 are used to model the converter and calculate the average value of the state-variables. Considering the resistances of the output filter capacitors (r_{Cf} and r_{Ci}) negligible, the average output current is calculated.

$$I_{out,avg} = \frac{v_{Cf,avg} - V_{bat}}{r_{bat}}, \text{ for forward operation}$$

$$I_{out,avg} = \frac{v_{Ci,avg} - V_{dc}}{r_{dc}}, \text{ for reverse operation}$$

5.6 Design and simulation

After the equation descriptions for FMA, state-variable and cyclic-averaging methods are obtained, the models are applied to a low power converter designed in this section.

The simulation of the state-variable model is performed in the Simulink graphical environment, as shown in section 5.4.1, while the FMA and cyclic-averaging equations are implemented using MATLAB scripts.

The FMA equations will be used to evaluate the influence of phase-shift angles on the converter operation, while the state-variable and cyclic-averaging models are used to estimate the converter's output current based on a predetermined range of phase-shift angles. The results obtained from the models' simulations are validated against a component-based Spice simulation.

In this chapter, at simulation stage the circuit is considered nearly ideal, the influence of resistances and parasitic elements will only be analysed in the next chapter with the construction of a prototype and comparison between simulation and experimental results.

5.6.1 Converter design

A low power converter is designed in this section following the design methodology developed in [10], where the phase-shift modulated CLLC topology was proposed and verified using a 50kHz, 4kW converter. Here a different specification is considered, where the switching frequency is set to 100 kHz, the DC bus voltage (V_{dc}) has a nominal value of 48V and a variation range of 42–55.2V while the battery voltage (V_{bat}) is in a range of 10.5–13.8 V with 12V nominal value. The output power is set to 110W when operating at nominal voltage.

The circuit used for state-variable, cyclic-averaging and Spice simulations is shown in Figure 5.13. The converter is considered nearly ideal, only a small resistance of 0.1Ω is considered at the input and output of the resonant tank (r_1 and r_2). Resistances r_{bat} and r_{dc} are used for measurement of the output current in the cyclic-averaging method

and have small values (0.01Ω) to not significantly influence the output power magnitude. Note that, as previously explained in section 5.3, for FMA analysis all resistances are neglected.

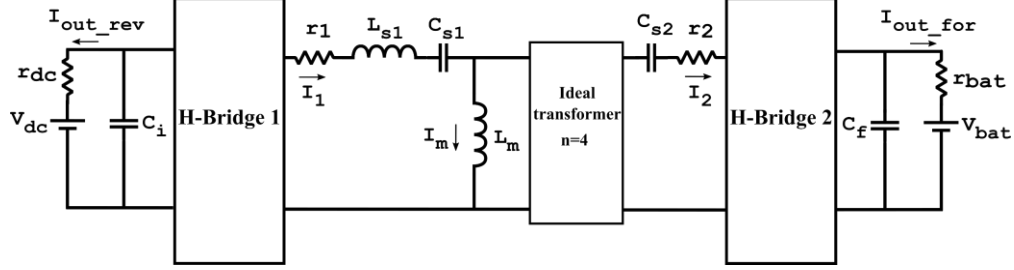


Figure 5.13: Final circuit for simulation of CLLC converter

Once the input and output voltages are specified, the DC voltage conversion ratio is calculated:

$$DC_{ratio} = n \frac{V_{bat}}{V_{dc}} \quad (5.31)$$

where n is the transformer turns ratio.

According to [10], converters operating under PPM modulation show reduced sensitivity to the DC voltage ratio value. For SPS modulated converters, however, a conversion ratio close to unity results in higher efficiency and smaller bridge currents, especially in low-power applications. For this reason, the DC voltage ratio is set to 1 and, based on the DC bus and battery nominal voltages (48-12V), the chosen value for the turns ratio is 4.

For the resonant frequency calculation, inductor L_m forms a resonator with $L_{s1}C_{s1}$ and C_{s2}/n^2 , consequently the resonant network is tuned to the switching frequency as follows.

$$\omega_r^2 = (2\pi f_s)^2 = \frac{1}{(L_{s1} + L_m)C_{s1}} = \frac{n^2}{L_m C_{s2}} \quad (5.32)$$

Additionally, each leg of the T-network is designed to have the same reactance, as defined in (5.33).

$$X_{C1} - X_{L1} = X_{Lm} = n^2 X_{C2} \quad (5.33)$$

Consequently, a base reactance X_n is defined in (5.34). For the calculation of L_{s1} and C_{s1} there is one degree of freedom, represented by k . In [10] values of k between 0 and 1 were analysed and it was observed that output power and bridge currents increase with small values of k . Here this analysis is extended for values higher than unity. In [9] a value of $k = 3.9$ is used in the prototype design, but the influence of k on the converter operation is not evaluated.

$$\begin{aligned} X_{Lm} &= n^2 X_{C2} = X_n \\ X_{C1} &= (1 + k) X_n \\ X_{L1} &= k X_n \end{aligned} \quad (5.34)$$

Before the calculation of the resonant components based on different values of k , the value of base reactance necessary to provide the specified output power of 110W is calculated. Ignoring circuit resistances and considering the fundamental component dominant, a FMA-based equation for maximum output power is obtained from (5.7), when considering the maximum values of phase-shift angles ($\phi = 90^\circ$ and $\alpha_1 = \alpha_2 = 180^\circ$).

$$P_{out_max} = \frac{8nV_{DC1}V_{DC2}}{\pi^2 X_n} \quad (5.35)$$

Considering the nominal voltage, turns ratio, and output power previously specified, the base reactance is calculated from (5.35) and $X_n = 16.98 \Omega$.

Substituting the value of X_n in (5.34) and using the reactance definition ($X_L = \omega L$ and $X_C = 1/\omega C$), the values of inductance and capacitances are calculated considering $k = 1, k = 2$ and $k = 5$, as shown in Table 5.9.

Table 5.9: Resonant tank parameters calculated for different values of k

Parameter	$k = 1$	$k = 2$	$k = 5$
L_{s1} (μH)	27.02	54.04	135.10
L_m (μH)	27.02	27.02	27.02
C_{s1} (nF)	46.86	31.24	15.62
C_{s2} (μF)	1.5	1.5	1.5

Using Spice simulation, the input/output power, efficiency, capacitors voltages resonant tank and output currents are calculated for each value of k and results are shown in Table 5.10. As k increases, the efficiency slightly increases but the output power, and consequently the output current, slightly decreases. The resonant tank currents also decrease when k is higher than 1. Additionally, the value of the primary capacitor (C_{s1}) decreases as k increases, resulting in higher voltage across C_{s1} and the necessity of components with higher voltage rating. A high value of k also results in a high value of L_{s1} (from $X_{L1} = kX_n$) increasing the size of the inductor and occasioning potential construction limitations. Therefore, in the process of selecting the value of k , the results show there is a trade-off between efficiency, output power and size to be considered.

For the present design, an intermediate value of $k = 2$ is chosen to slightly increase efficiency and reduce resonant tank currents, while keeping output power above the specified value of 110W. The inductor L_{s1} is also maintained at a reasonable value of 54.04 μH , not negatively affecting a future construction process.

Once the value of k is defined, all circuit elements are determined and the parameters obtained at the end of the design process are listed in Table 5.11.

Table 5.10: Spice simulation results for different values of k

	$k = 1$	$k = 2$	$k = 5$
Output Power (P_{out})	116.26 W	112.67 W	111.03 W
Input Power (P_{in})	118.03 W	114.30 W	112.63 W
Efficiency	98.50 %	98.56 %	98.58 %
Magnetizing RMS current ($I_{m,rms}$)	3.78 A	3.64 A	3.64 A
Primary RMS current ($I_{1,rms}$)	2.71 A	2.60 A	2.59 A
Secondary RMS current ($I_{2,rms}$)	11.21 A	10.42 A	10.27 A
Primary capacitor voltage ($V_{Cs1,rms}$)	89.44 V	131.81 V	263.79 V
Secondary capacitor voltage ($V_{Cs2,rms}$)	11.73 V	11.66 V	11.65 V
Average output current (I_{out})	9.77 A	9.32 A	9.24 A

Table 5.11: Design parameters

Parameter	Value
V_{dc}	48 V
V_{bat}	12 V
C_f, C_i	300 μ F
L_{s1}	54.04 μ H
C_{s1}	31.24 nF
L_m	27.02 μ H
C_{s2}	1.5 μ F
r_1, r_2'	0.1 Ω
r_{dc}, r_b	0.01 Ω

Similar to the phase-shift angles, the input and output voltage sources also affect the output power calculation and could be used as extra control variables. In Table 5.12 it is shown how the output power changes when the DC bus and battery voltages

deviate from nominal values, where a variation of 15% in the DC bus and battery voltages, simultaneously, results in a change of nearly 32% in the output power.

Table 5.12: Influence of voltage variations on output power

	Maximum output power (W)	
	Forward mode	Reverse mode
Nominal operation (48V – 12V)	112.67	108.76
Maximum DC bus/battery voltage (55.2V – 13.8V)	148.68	143.84
Minimum DC bus/battery voltage (42V – 10.5V)	86.072	83.27

5.6.2 Simulation results

Equations (5.3), (5.6) and (5.7) obtained during FMA analysis are now used to calculate the resonant tank currents and output power, evaluating the influence of phase-shift angles α_1 , α_2 and ϕ on the converter operation.

The angles α_1 and α_2 are tested for a range from 0 to 180°, with a step size of 5°. Three values of phase-shift angle ϕ were evaluated: 22.5°, 45° and 90°. The 3D graphs obtained for a converter operating in forward mode, with maximum ($\phi = 90^\circ$) and minimum ($\phi = 22.5^\circ$) values of bridge phase-shift angle are presented in Figures 5.14, 5.15, 5.16 and 5.17.

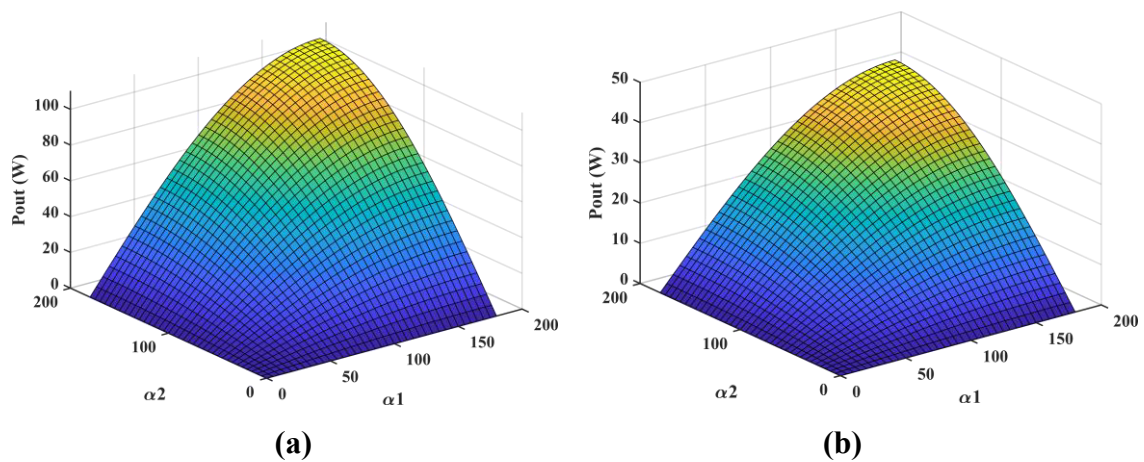


Figure 5.14: Output power versus α_1 and α_2 for (a) $\phi = 90^\circ$ (b) $\phi = 22.5^\circ$

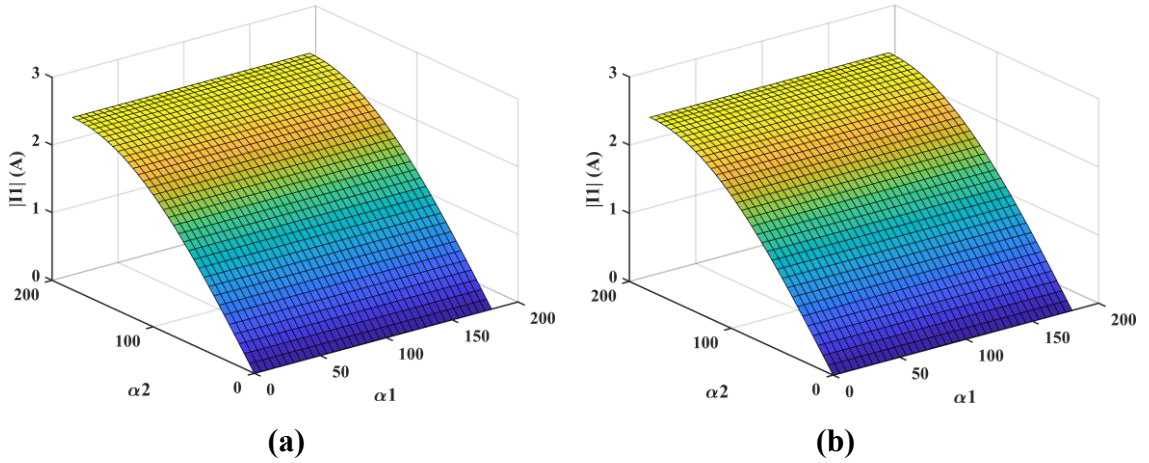


Figure 5.15: Primary current magnitude versus α_1 and α_2 for (a) $\phi = 90^\circ$ (b) $\phi = 22.5^\circ$

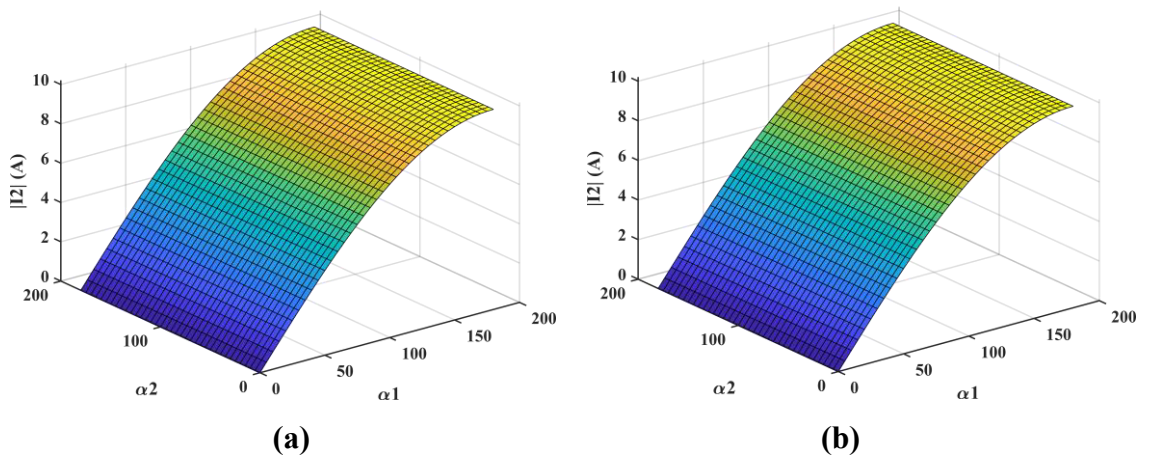


Figure 5.16: Secondary current magnitude versus α_1 and α_2 for (a) $\phi = 90^\circ$ (b) $\phi = 22.5^\circ$

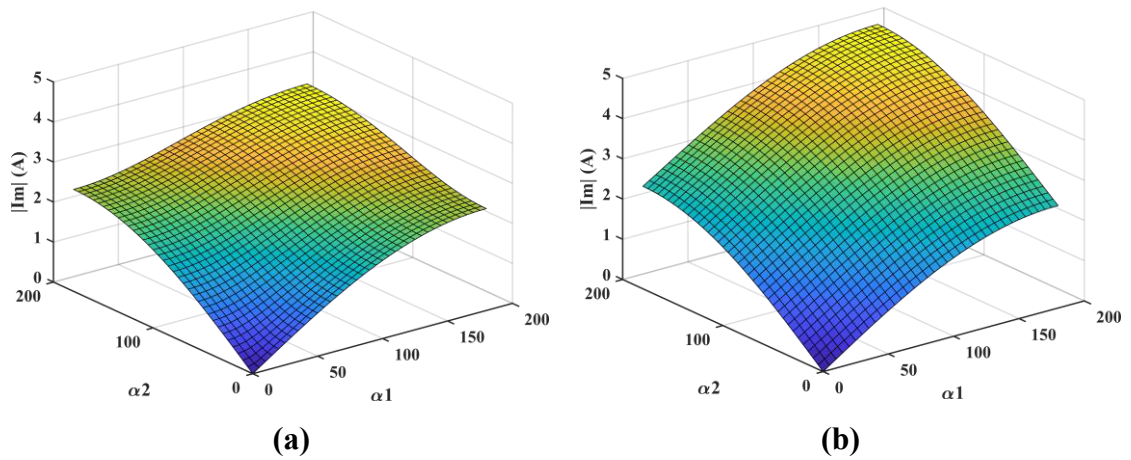


Figure 5.17: Magnetizing branch current magnitude versus α_1 and α_2 for (a) $\phi = 90^\circ$ (b) $\phi = 22.5^\circ$

The phase-shift angle between primary and secondary bridges, ϕ , functions as a control variable for the output current since, considering fixed input and output voltages, the output power decreases as the angle ϕ decreases. From the results presented it is also observed that the magnitude of primary and secondary currents is independent of the angle ϕ . The magnitude of the primary current only depends on the phase-shift angle between the legs of the secondary bridge (α_2) while the secondary current is dependent of α_1 , the phase-shift angle between the legs of the primary bridge.

This behaviour is one of the main disadvantages of the SPS modulation technique, where α_1 and α_2 are maintained at the maximum value (180°) and ϕ is the only control variable. In this case, for low values of ϕ the converter's output current decreases but the input and output currents of the resonant tank are not affected, their magnitude is always at maximum value, resulting in an increase of the circulating current, system losses and stress on switching devices.

To evaluate the accuracy of the FMA method, the results obtained are compared to a nearly ideal Spice simulation. Contrary to FMA, the Spice simulation is not ideal since this model includes the resistances r_1 , r_2 , r_{bat} and r_{dc} , as explained in section 5.6.1. The two models are compared considering the maximum bridge phase-shift ($\phi = 90^\circ$) and results are shown in Figures 5.18, 5.19, 5.20 and 5.21. Since when $\alpha_1 = 0$ or $\alpha_2 = 0$ the output power is nearly zero, the range here analysed is defined based on a converter operating with angles α_1 and α_2 from 18° to 180° , with a step size of 18° .

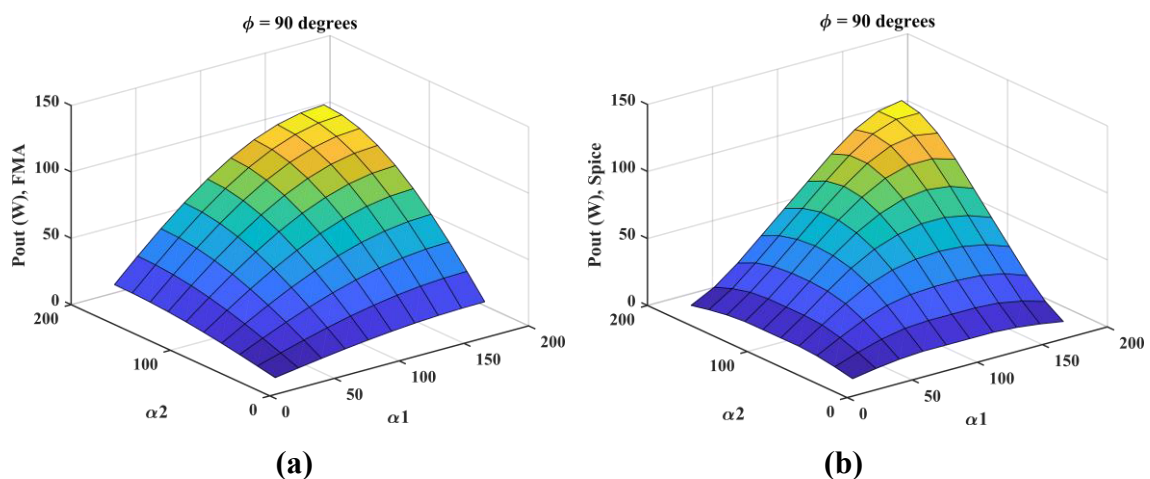


Figure 5.18: Output power for (a) FMA and (b) Spice simulations

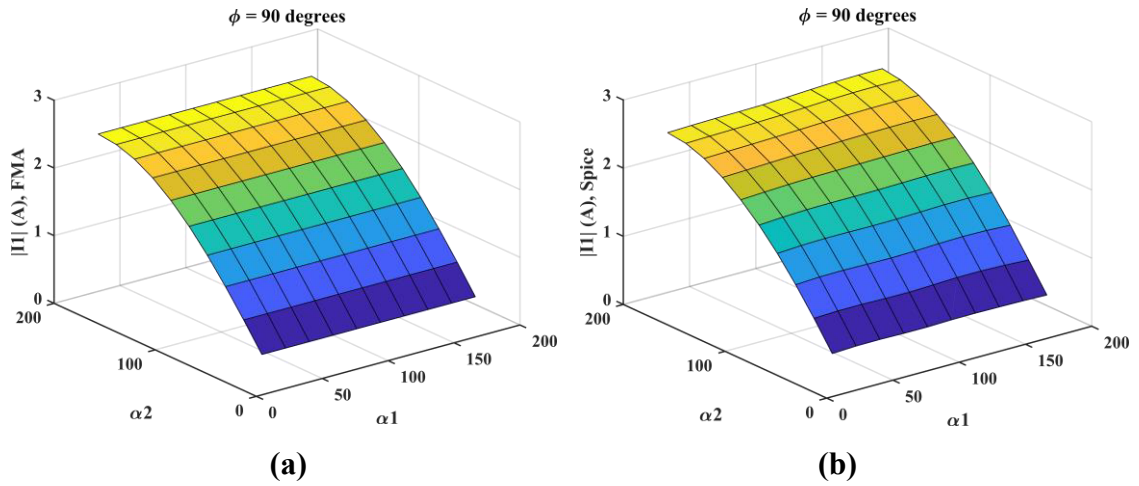


Figure 5.19: Primary current for (a) FMA and (b) Spice simulations

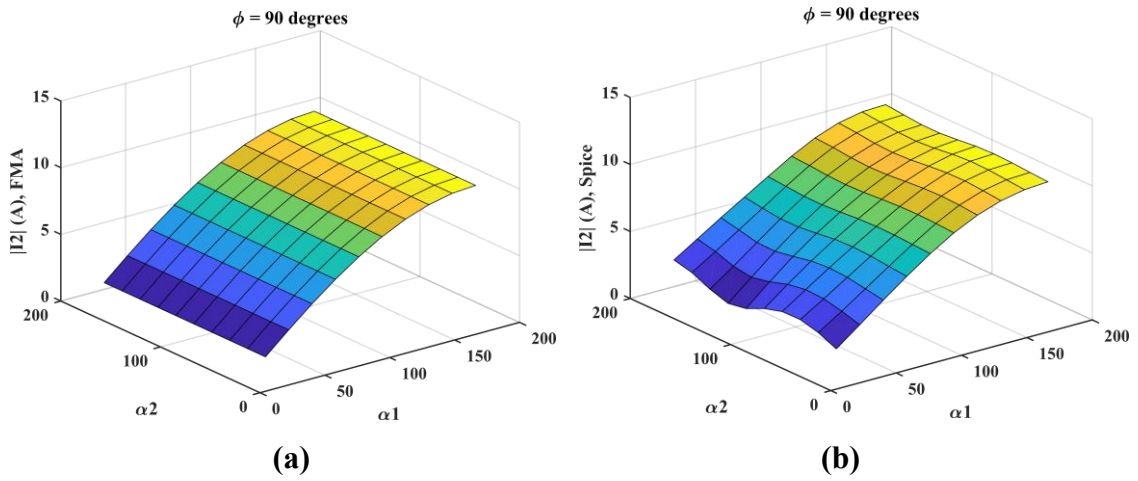


Figure 5.20: Secondary current for (a) FMA and (b) Spice simulations

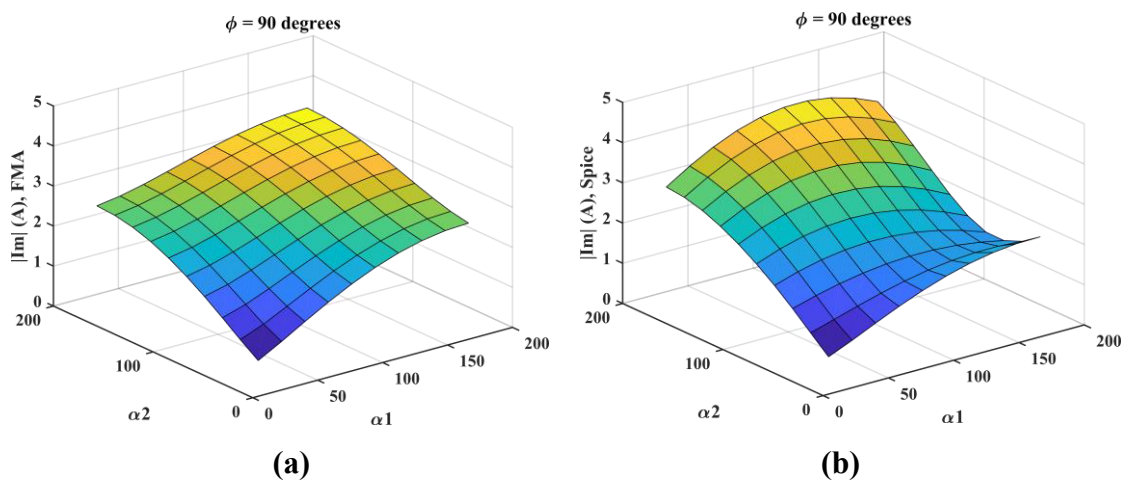


Figure 5.21: Magnetizing branch current for (a) FMA and (b) Spice simulations

Compared to FMA, the output power in Spice simulations decreases more rapidly as the phase-shift angles decrease. The magnitude of primary current is very similar for both models, but Spice results for secondary current are slightly dependent of α_2 , especially for low values of α_1 , while in FMA simulations the secondary current magnitude is independent of α_2 . A difference in shape was also noticed between Spice and FMA results for the magnitude of the magnetizing current in Figure 5.21. The differences between Spice and FMA are mainly due to the influence of the circuit resistances and the approximation adopted in the FMA method that ignores the influence of harmonics.

The relative error between Spice and FMA results was calculated for each point using equation (5.36) and results are shown in Tables A1.1, A1.2, A1.3 and A1.4, in Appendix A.1. Note that, in general, reduced error is obtained in the region of $\alpha_1 = \alpha_2$, and the discrepancy between Spice and FMA results tends to increase as the difference between α_1 and α_2 increases, especially for output power and magnetizing current results.

$$\text{Relative error (\%)} = \frac{X_{spice} - X_{fma.eq}}{X_{fma.eq}} \quad (5.36)$$

where X is the variable under analysis, which can be $|I_1|$, $|I_2|$, $|I_m|$ or P_{out} .

Overall, FMA is a simple and useful method for fast analysis but, as also observed in the previous chapter for the frequency modulated CLLC converter, this technique suffers from accuracy problems due to the fundamental and ideal circuit approximations.

Following the FMA analysis, to further evaluate the influence of the leg phase-shift angles α_1 and α_2 on the converter operation, a Spice simulation is used to calculate the converter's efficiency for the full operation range of α_1 and α_2 . The 3D plot obtained is shown in Figure 5.22 and the data points are listed in Table A1.5, in Appendix A.1.

The results show that the highest values of efficiency are obtained near the region of $\alpha_1 = \alpha_2$ and a considerable drop in efficiency is observed as the difference between α_1 and α_2 significantly increases. Therefore, for the next step of analysis and

verification of state-variable and cyclic-averaging models, the converter will be considered operating with $\alpha_1 = \alpha_2 = \alpha$ when applying the PPM modulation technique.

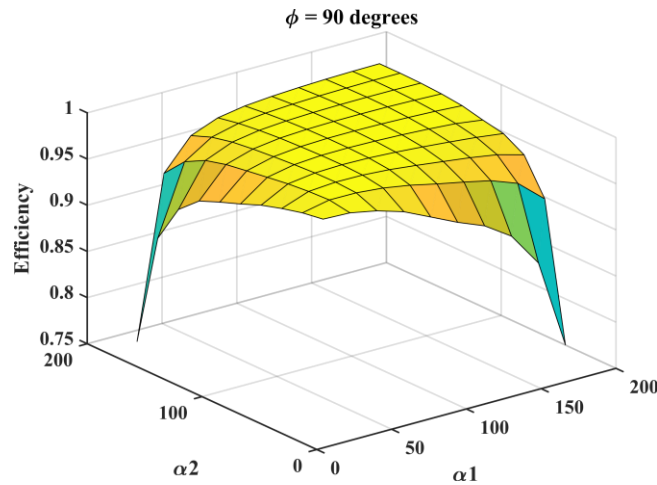


Figure 5.22: Efficiency from Spice simulation

Additionally, the efficiency also reduces as the bridge phase-shift angle decreases. When ϕ drops from 90° to 45° , while maintaining $\alpha_1 = \alpha_2 = 90^\circ$, the efficiency reduces from 98.56% to 97.83%. At 22.5° the efficiency drops to 95.89%.

At maximum modulation an efficiency of 98.56% is achieved. Note that the converter here evaluated is nearly ideal but, as the resistances in the circuit increase, an operation with low values of ϕ or far from the range of $\alpha_1 = \alpha_2$ results in significantly worse operation.

Following the FMA and efficiency analysis, the state-variable and cyclic-averaging models, obtained in sections 5.4 and 5.5 respectively, will be implemented and verified against a Spice simulation. The converter is analysed considering SPS and PPM modulation techniques and forward and reverse power flow directions.

For the SPS modulation analysis the angle α is fixed at 180° and the output current is measured as the phase-shift angle ϕ increases from 10° to 90° in steps on 10° . For the PPM modulation implementation, the angle ϕ is kept at its maximum value (90°) and the variation of the angle α is implemented using the normalized angle α_{ratio} , defined in (5.37), where the range of α_{ratio} evaluated is from 0.1 ($\alpha = 18^\circ$) to 1 ($\alpha = 180^\circ$), with a step size of 0.1.

$$\alpha_{ratio} = \frac{\alpha}{180} \tag{5.37}$$

The results obtained for the SPS modulation case are shown in Figure 5.23. The three models have very similar results and differences are hard to identify in the graph, therefore, for a meticulous analysis, the values of average output current for each value of modulation angle are listed in Table 5.13. The graphs obtained for PPM modulation are shown in Figure 5.24 while the data points are presented in Table 5.14.

Overall, it is observed that the application of both state-variable and cyclic-averaging models produce accurate results compared to Spice. An average error of 0.50% was observed between the Spice and cyclic-averaging models with a maximum value of 2.01% while, for state-variable, a similar average error of 0.48% was calculated compared to Spice, with maximum error of 1.06%.

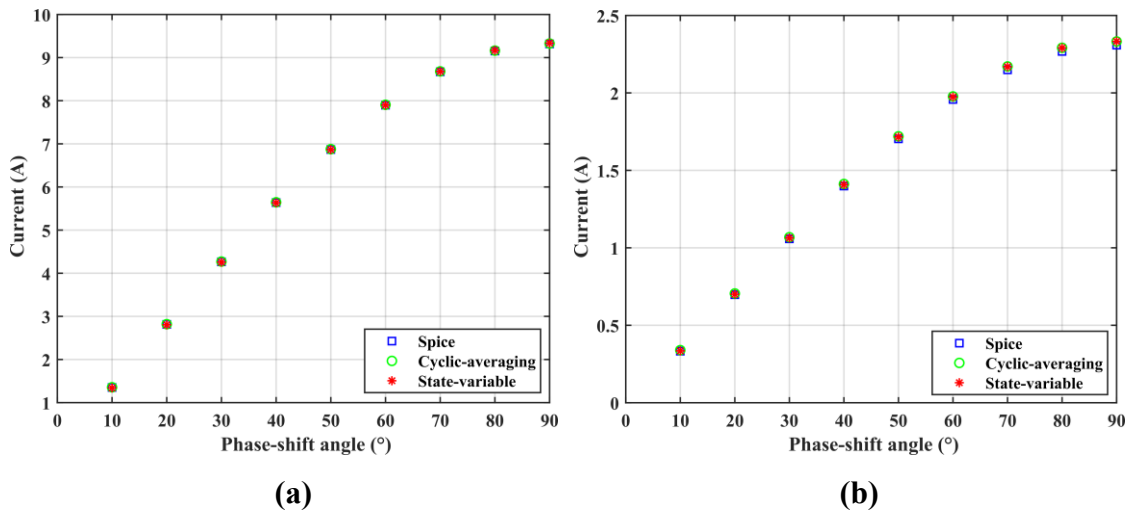


Figure 5.23: Simulation results for SPS modulation (a) forward mode and (b) reverse mode

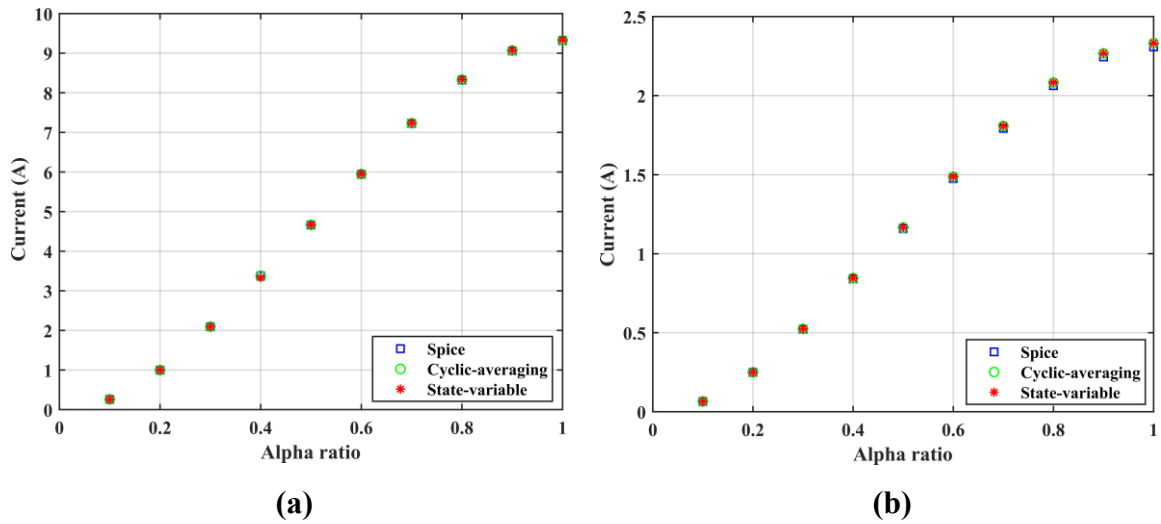


Figure 5.24: Simulation results for PPM modulation (a) forward mode and (b) reverse mode

Table 5.13: Simulation results for SPS modulation

Phase-shift angle (ϕ)	Average output current (A)					
	Forward operation			Reverse operation		
	Spice	Cyclic-averaging	State-variable	Spice	Cyclic-averaging	State-variable
10°	1.3515	1.3556	1.3420	0.3328	0.3395	0.3346
20°	2.8141	2.8188	2.8046	0.6973	0.7053	0.7003
30°	4.2650	4.2706	4.2569	1.0581	1.0683	1.0634
40°	5.6381	5.6449	5.6328	1.3989	1.4119	1.4074
50°	6.8687	6.8765	6.8671	1.7036	1.7198	1.7159
60°	7.8968	7.9054	7.8996	1.9578	1.9770	1.9741
70°	8.6710	8.6802	8.6789	2.1490	2.1707	2.1689
80°	9.1523	9.1618	9.1654	2.2677	2.2911	2.2905
90°	9.3161	9.3256	9.3344	2.3082	2.3320	2.3327

Table 5.14: Simulation results for PPM modulation

Alpha ratio (α_{ratio})	Average output current (A)					
	Forward operation			Reverse operation		
	Spice	Cyclic-averaging	State-variable	Spice	Cyclic-averaging	State-variable
0.1	0.2593	0.2597	0.2599	0.0648	0.0651	0.0650
0.2	0.9962	0.9971	0.9978	0.2489	0.2497	0.2497
0.3	2.0927	2.0941	2.0957	0.5220	0.5241	0.5241
0.4	3.3776	3.3793	3.3322	0.8410	0.8453	0.8455
0.5	4.6605	4.6628	4.6670	1.1587	1.1660	1.1663
0.6	5.9429	5.9463	5.9518	1.4756	1.4867	1.4871
0.7	7.2264	7.2315	7.2383	1.7925	1.8079	1.8084
0.8	8.3214	8.3285	8.3363	2.0626	2.0823	2.0829
0.9	9.0572	9.0659	9.0744	2.2442	2.2669	2.2676
1.0	9.3162	9.3256	9.3344	2.3082	2.3320	2.3327

For further verification, the behaviour of the circuit variables during a cycle is analysed and waveforms obtained from the state-variable simulation are compared to Spice. All state-variables and bridge voltages were verified for different points across the full range of phase-shift angles, considering forward and reverse operation. The graphs containing the bridge voltages v_1 and v_2 , primary inductor current $i_{L_{S1}}$ and magnetizing inductor current i_{L_m} for $\alpha_{ratio} = 0.25$ and $\phi = 90^\circ$ in forward mode are shown in Figure 5.25. From the results analysis, it is noticed a very similar behaviour between Spice and state-variable waveforms, confirming the accuracy of the state-variable method.

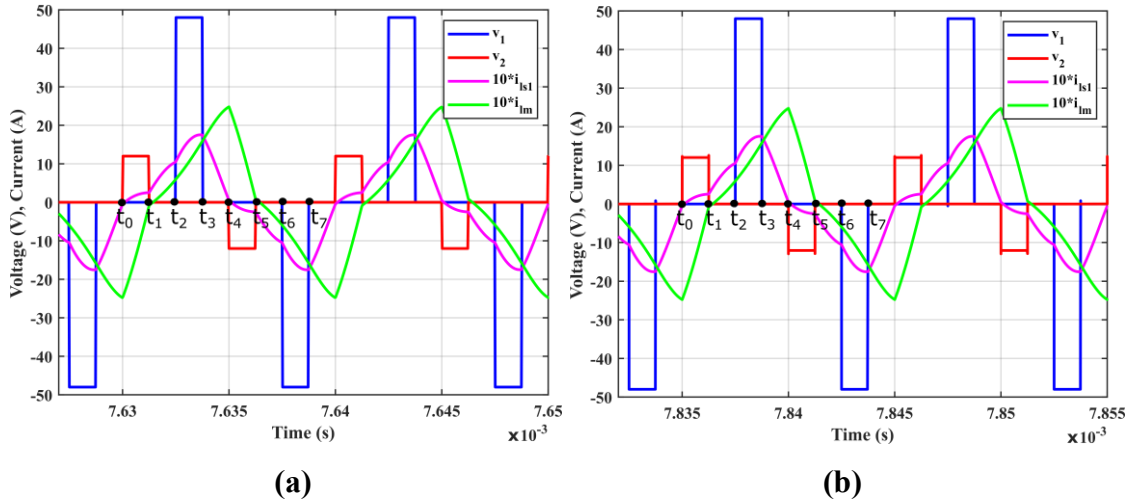


Figure 5.25: Waveform comparison for $\alpha_{ratio} = 0.25$ (a) state-variable and (b) Spice, forward mode

Based on the cyclic analysis and mode descriptions performed in section 5.5, a cycle is divided in 8 modes when operating under PPM modulation. To verify the accuracy of the cyclic-averaging method during a full cycle, the steady-state values of the resonant tank state-variables (i_{LS1} , v_{CS1} , i_{Lm} and v_{CS2}) are calculated at the beginning of each mode, points t_0 , t_1 , t_2 , t_3 , t_4 , t_5 , t_6 and t_7 from Figure 5.25. The values obtained from the cyclic-averaging simulation (Table 5.16) are compared to state-variable (Table 5.15) and Spice (Table 5.17) results considering $\alpha_{ratio} = 0.25$ and $\phi = 90^\circ$, in forward mode. This investigation, as well as the state-variable waveform analysis, were performed for different values of α_{ratio} and ϕ and results were similarly accurate across the full modulation range. Part of the error from Spice and state-variable results compared to cyclic-averaging is due to the dependency on the simulation step size and consequent difficulty in measuring the current and voltage values in the Spice and state-variable graphs at the exact point in time each mode starts.

Table 5.15: State-variable model results for variables states considering $\alpha_{ratio} = 0.25$, forward mode

	State-variable model							
	t_0	t_1	t_2	t_3	t_4	t_5	t_6	t_7
i_{Ls1} (A)	-0.038	0.258	1.050	1.739	0.052	-0.256	-1.049	-1.742
v_{Cs1} (V)	-66.970	-60.630	-31.930	29.720	66.980	60.720	32.070	-29.560
i_{Lm} (A)	-2.454	-0.071	0.596	1.588	2.473	0.073	-0.595	-1.588
v_{Cs2} (V)	-2.098	2.851	4.459	6.021	2.203	-2.858	-4.465	-6.025

Table 5.16: Cyclic-averaging model results for variables states considering $\alpha_{ratio} = 0.25$, forward mode

	Cyclic-averaging model							
	t_0	t_1	t_2	t_3	t_4	t_5	t_6	t_7
i_{Ls1} (A)	-0.047	0.254	1.049	1.744	0.047	-0.254	-1.049	-1.744
v_{Cs1} (V)	-66.913	-60.695	-31.819	29.383	66.913	60.695	31.819	-29.383
i_{Lm} (A)	-2.474	-0.080	0.591	1.580	2.474	0.080	-0.591	-1.580
v_{Cs2} (V)	-2.204	2.830	4.471	6.036	2.204	-2.830	-4.471	-6.036

Table 5.17: Spice model results for variables states considering $\alpha_{ratio} = 0.25$, forward mode

	Spice model							
	t_0	t_1	t_2	t_3	t_4	t_5	t_6	t_7
i_{Ls1} (A)	-0.051	0.256	1.057	1.748	0.050	-0.256	-1.054	-1.750
v_{Cs1} (V)	-67.174	-60.934	-31.837	29.322	67.134	60.955	32.065	-29.451
i_{Lm} (A)	-2.476	-0.076	0.598	1.584	2.477	0.075	-0.593	-1.584
v_{Cs2} (V)	-2.217	2.834	4.475	6.033	2.201	-2.829	-4.463	-6.040

After the accuracy of the models is verified, the execution time for the three methods is compared, as shown in Table 5.18. Six measurements were performed for each method and the average execution time is calculated. Both state-variable and Spice simulations are performed with simulation time of 8ms and step size of 10 ns. The

values calculated with the FMA and cyclic-averaging equation descriptions are directly steady-state, while Spice and state-variable simulations reach steady-state around 7 ms.

The execution time for the FMA and cyclic-averaging methods was measured considering the first time the code is compiled, to include the memory allocation time. After the first run, the variables are already defined and stored in memory and execution time drops to an average of 0.005 seconds for the cyclic method, nearly 4000 times faster than Spice, and 0.238 seconds for FMA. Since the execution of these methods is considerably fast, this allocation time significantly influences the calculation of average execution time, while for state-variable and Spice simulations no significant difference in execution time was observed between the first and subsequent executions.

Table 5.18: Execution time comparison

	Modelling technique			
	FMA	Cyclic-averaging	State-variable	Spice
Average execution time (s)	0.594	0.136	24.583	19.568

5.7 Conclusions

In this chapter three modelling techniques were employed to describe the operation of a bidirectional CLLC converter operating under phase-shift modulation. The equation descriptions for FMA, state-variable and cyclic-averaging models were obtained, and simulations were performed considering two types of phase-shift modulation techniques: Single Phase-Shift (SPS) and Pulse-Phase Modulation (PPM). For accuracy verification, the results were compared to a component-based Spice simulation.

From FMA analysis, it was shown that for higher values of α_1 and α_2 and in a range around $\alpha_1 = \alpha_2$ this technique shows accurate results compared to Spice. Still, the FMA method is not as accurate as the state-variable and cyclic-averaging techniques. For low values of α_1 and α_2 and as the difference between these angles increases the accuracy of the FMA model tends to reduce.

From Spice results it was also shown that efficiency reduces as the difference between α_1 and α_2 significantly increases and as ϕ , the bridge phase-shift angle, decreases. Therefore, it is concluded that better operation is obtained when using PPM modulation and with equal values of leg phase-shift angles of the primary and secondary bridge ($\alpha_1 = \alpha_2$).

The simulation results also show that state-variable and cyclic-averaging models could accurately predict the output current behaviour for both SPS and PPM modulation cases. As also observed for the frequency-modulated variant in the previous chapter, the cyclic-averaging method had the fastest execution time.

For the next chapter, a bidirectional phase-shift modulated CLLC converter prototype will be constructed and the models will be verified against experimental results.

5.8 References

- [1] S. Inoue and H. Akagi, "A bidirectional DC-DC converter for an energy storage system with galvanic isolation," *IEEE Transactions on Power Electronics*, vol. 22, no. 6, pp. 2299–2306, 2007.
- [2] R. T. Naayagi and A. J. Forsyth, "Bidirectional DC-DC converter for aircraft electric energy storage systems," in *5th IET International Conference on Power Electronics, Machines and Drives (PEMD 2010)*, 2010, pp. 1–6.
- [3] M. H. Kheraluwala, R. W. Gascoigne, D. M. Divan, and E. D. Baumann, "Performance Characterization of a High-Power Dual Active Bridge dc-to-dc Converter," *IEEE Transactions on Industry Applications*, vol. 28, no. 6, pp. 1294–1301, 1992.
- [4] H. Bai and C. Mi, "Eliminate reactive power and increase system efficiency of isolated bidirectional dual-active-bridge dc-dc converters using novel dual-phase-shift control," *IEEE Transactions on Power Electronics*, vol. 23, no. 6, pp. 2905–2914, 2008.
- [5] S. Zengin and M. Boztepe, "A Novel Current Modulation Method to Eliminate Low Frequency Harmonics in Single-Stage Dual Active Bridge AC/DC Converter," *IEEE Transactions on Industrial Electronics*, vol. 67, no. 2, pp. 1048–1058, 2019.
- [6] U. K. Madawala and D. J. Thrimawithana, "Current sourced bi-directional inductive power transfer system," *IET Power Electronics*, vol. 4, no. 4, pp. 471–480, 2011.

- [7] A. A. S. Mohamed, A. Berzoy, F. G. N. Nogueira de Almeida, and O. Mohammed, "Modeling and Assessment Analysis of Various Compensation Topologies in Bidirectional IWPT System for EV Applications," *IEEE Transactions on Industry Applications*, vol. 53, no. 5, pp. 4973–4984, 2017.
- [8] W. L. Malan, D. M. Vilathgamuwa, G. R. Walker, D. J. Thrimawithana, and U. K. Madawala, "Modeling and Control of a CLC Resonant Dual Active Bridge," *IEEE Transactions on Power Electronics*, vol. 31, no. 10, pp. 7297–7310, 2016.
- [9] W. L. Malan, D. M. Vilathgamuwa, G. R. Walker, D. J. Thrimawithana, and U. K. Madawala, "Novel modulation strategy for a CLC resonant dual active bridge," *9th International Conference on Power Electronics and ECCE Asia (ICPE-ECCE Asia)*, pp. 759–764, 2015.
- [10] R. P. Twiname, D. J. Thrimawithana, U. K. Madawala, and C. A. Baguley, "A Dual-Active Bridge Topology with a Tuned CLC Network," *IEEE Transactions on Power Electronics*, vol. 30, no. 12, pp. 6543–6550, 2015.

6 CLLC Converter Design and Prototype

6.1 Introduction

In the previous chapter FMA, state-variable and cyclic-averaging models were developed for a CLLC resonant converter operating under phase-shift modulation. It was verified that state-variable and cyclic-averaging are very accurate methods to model the converter's behaviour when compared to a Spice simulation. It was also previously observed that the use of the cyclic-averaging method results in the fastest execution for both frequency and phase-shift modulated converters.

Following the verification through simulation, the construction process for a low power prototype will be discussed in this chapter. The converter will be tested considering bidirectional power flow and operation under Single Phase-Shift (SPS) and Pulse-Phase (PPM) modulation. The experimental results obtained will be compared to a Spice and cyclic-averaging simulation.

A simplified diagram for the prototype construction is shown in Figure 6.1. The switching signals are produced using a microcontroller and inverting circuit. The H-bridge 1 connects a power supply to one side of the resonant tank while H-bridge 2 connects the other side of the resonant tank to a resistor load.

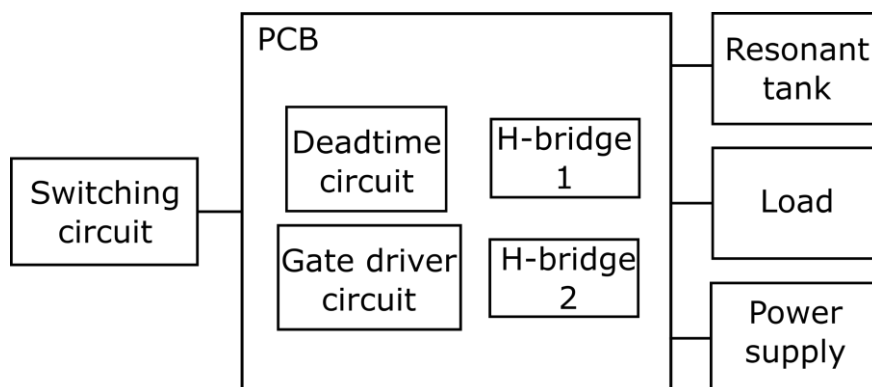


Figure 6.1: Simplified block diagram for prototype construction

6.2 Converter design

In this section the design procedure for each prototype subsystem from Figure 6.1 will be explained.

6.2.1 Switching circuit

The block diagram from Figure 6.2 illustrates how the switching circuit is implemented. The pulse signals are generated using the FRDM-KL25Z microcontroller development board. Each channel (Ch0 to Ch3) generates the phase-shifted switching signals to each leg of the two H-bridges. An inverting circuit is used to implement phase-shift angles greater than 180° . In Figure 6.3 the inverting circuit is presented in detail. The development board output has a voltage level of 3.3 V but the input signals for deadtime circuit in the PCB must be at 15V level. Therefore, before the switching signals are sent to the deadtime circuits, a voltage level shifter (CD4504B) is added.

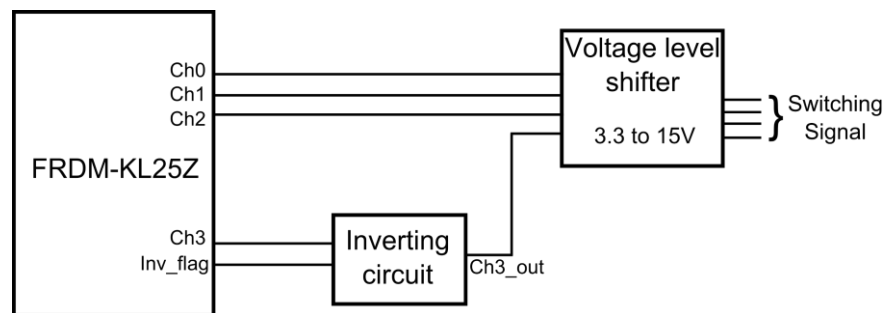


Figure 6.2: Switching circuit diagram

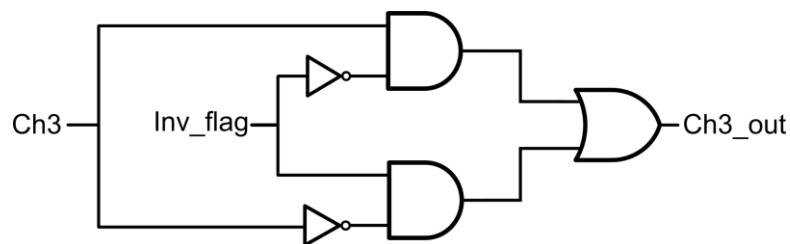


Figure 6.3: Inverting circuit

The FRDM-KL25Z board uses an ultra low-power KL25 microcontroller from the Kinetis L-series of ARM Cortex MCUs with Processor Expert support. Processor Expert is a tool with graphical user interface that generates code from embedded components as building blocks, allowing a fast and simplified development. To

generate the phase-shifted pulse waveforms the timer units are used in Output Compare mode, where the output is toggled when the counter matches a set value. To obtain a 100 kHz switching signal the timer frequency is set to 200 kHz. The timer counter goes from 0 to 104 and resets to zero, therefore, a full count is completed in 5 μ s for a frequency of 200 kHz.

For the four channels used (Ch0 to Ch3) the output value is zero at start. The counter starts at 0 and when it reaches the value of variable ChN_count the channel output value is inverted.

To implement a phase-shift angle between the channels, the variable $Ch0_count$, for channel 0, is fixed at zero as reference. For channels 1 to 3 the following equation is employed to obtain phase-shift angles between 0 and 180 degrees:

$$ChN_count = \frac{PS \cdot 104}{180} \quad (6.1)$$

where PS is the phase-shift angle.

For phase-shift angles greater than 180 degrees, the inverting circuit is activated, variable Inv_flag , from Figure 6.3, is changed from low to high and:

$$ChN_count = \frac{(PS - 180) \cdot 104}{180} \quad (6.2)$$

In Table 6.1 the values of Inv_flag , ChN_count and the resulting phase-shift angle relative to Ch0 are presented for different modulation cases. Note that variable ChN_count only accepts integer values, therefore an exact angle of 40° ($Ch2_count = 23.11$) cannot be implemented. Choosing the closest integer value (23) the phase-shift angle effectively implemented is 39.81°.

Table 6.1: Values of ChN_count and Inv_flag for different modulation cases,

Modulation case	$Ch0_count$	$Ch1_count$	$Ch2_count$	$Ch3_count$	Inv_flag
$\alpha = 180^\circ$ and $\phi = 90^\circ$	0	104 (180°)	52 (90°)	52 (270°)	1
$\alpha = 90^\circ$ and $\phi = 90^\circ$	0	52 (90°)	52 (90°)	104 (180°)	0
$\alpha = 180^\circ$ and $\phi = 40^\circ$	0	104 (180°)	23 (39.81°)	23 (219.81°)	1

The pulse waveform diagrams for phase-shift angles of 90, 180 and 270 degrees are shown in Figures 6.4, 6.5 and 6.6 respectively. This implementation results in a pulse waveform with period of $10\ \mu\text{s}$ and consequently, a frequency of 100 kHz.

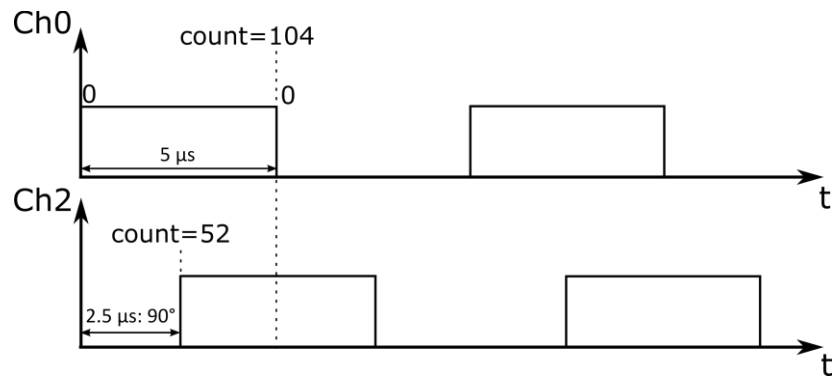


Figure 6.4: Implementation of 90 degrees phase-shift, $Ch2_count = 52$

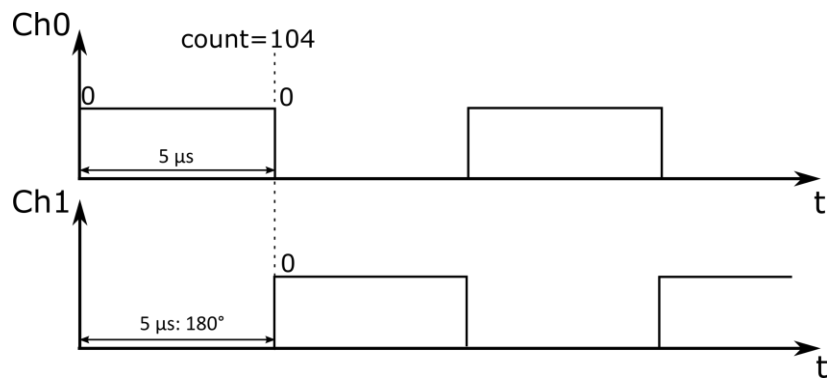


Figure 6.5: Implementation of 180 degrees phase-shift, $Ch1_count = 104$

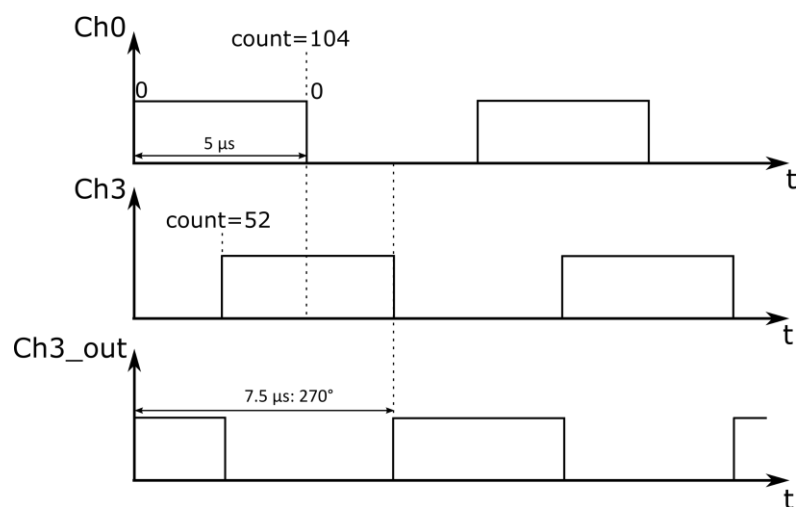


Figure 6.6: Implementation of angles greater than 180 degrees phase-shift, $Ch0_count = 0$, $Ch3_count = 104$ and $Inv_flag = 1$

Following the switching circuit implementation, the output signals will be connected to a voltage level shifter, producing 15V switching signals to the input of the deadtime circuit.

6.2.2 PCB: Deadtime, gate driver and H-bridge circuits

As shown in Figure 6.7 and from the CLLC topology description in Chapters 4 and 5, the CLLC converter is composed by two H-bridges connected to a resonant tank. Each leg of the bridge consists of two complementary switches. To avoid the activation of both switches in the same leg at the same time during transition, and consequently a short circuit, a deadtime circuit is used to introduce a delay.

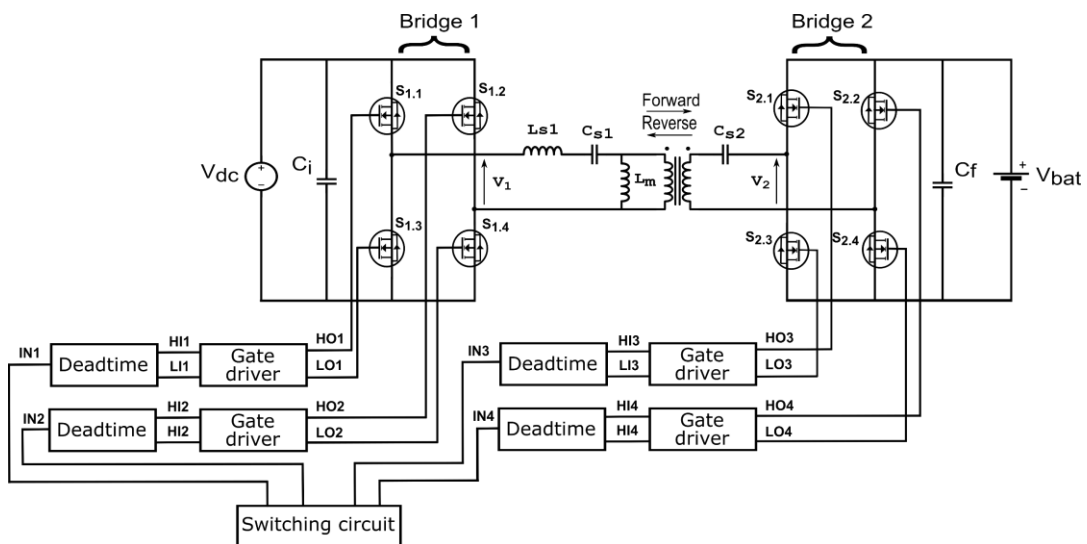


Figure 6.7: Implementation of CLLC converter

The deadtime circuit is shown in Figure 6.8, one circuit is used for each leg of the two bridges. From experimental tests, a deadtime of approximately 100 ns is sufficient to avoid short circuit. To obtain that delay, resistors $R_1 = R_2 = 3.3 \text{ k}\Omega$ and capacitors $C_1 = C_2 = 2.2 \text{ pF}$ were chosen for this application.

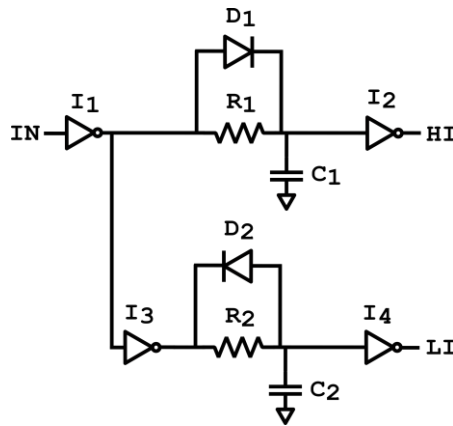


Figure 6.8: Deadtime circuit

The input signals for the deadtime circuit are provided by the switching circuit (microcontroller board + inverting circuit + voltage level shifter) described in the previous section. The output signals from the deadtime circuits are low power, therefore, a gate driver circuit must be used before connection to the MOSFET switches.

The IR2011 high power MOSFET driver is used to control the MOSFET switches. The output of the deadtime circuit is used as input to the gate driver circuit, as shown in Figure 6.9.

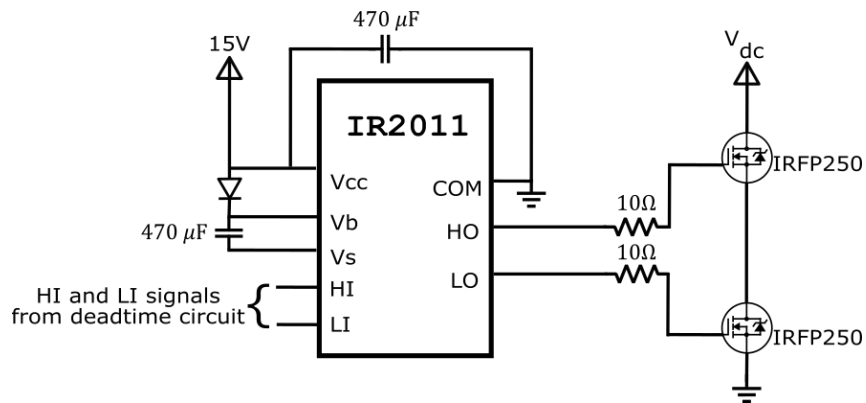


Figure 6.9: Gate driver circuit

For the implementation of the H-bridges, IRFP250 Power MOSFETs are chosen with 200V maximum drain source voltage, 30A maximum continuous drain current and $R_{DS(on)} = 0.085\Omega$. A high voltage/current rating was chosen with the intention of perform future tests at higher power levels after the validation of the 100W case. To reduce conduction losses, a device with low value of $R_{DS(on)}$ must be chosen.

Therefore, to further improve efficiency, devices using wide bandgap materials as Silicon Carbide (SiC) and Gallium Nitride (GaN) could be used due to their reduced on-resistance [1], [2].

6.2.3 Resonant tank design

The resonant tank circuit for a CLLC converter is shown in Figure 6.10. Considering the operating frequency of 100 kHz, ETD cores with ferrite material 3C90 are used for the construction of inductors and transformer. This material is recommended for applications with a frequency limit of 200 kHz.

The voltage and current values used in the design equations in this section are chosen based on the simulation results of the ideal converter presented in the previous chapter and considering a converter operating under maximum modulation.

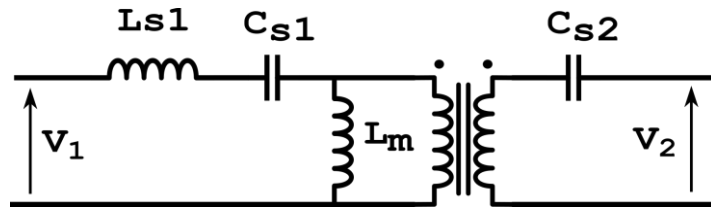


Figure 6.10: Resonant tank

For the inductors construction, the minimum number of turns is calculated based on equation (6.3).

$$N_{min} = \frac{LI}{B_{max}A_{core}} \quad (6.3)$$

where L is the inductance, B_{max} is the saturation flux density, A_{core} is the effective area of the core and I is the inductors' peak current.

The inductor gap l_g is calculated from equation (6.4).

$$l_g = \frac{N^2 A_{core} \mu_0}{L} \quad (6.4)$$

where μ_0 is the permeability of vacuum and N is the chosen number of turns.

The inductor L_{s1} is built with 10 turns in an ETD-34 core while for L_m an ETD-29 core is used with 8 turns. To reduce the skin depth effect, a litz wire composed of 19 strands of 0.4mm diameter, with total diameter of 2.5mm, was chosen to build the inductors and transformer. The inductance is measured with an LCR meter and the air gap l_g is adjusted to obtain a value of inductance closer to the design value.

The equivalent circuit for a real inductor is shown in Figure 6.11. Once the inductors are built, the inductance and parasitic components values are measured using the Bode 100 Vector Network Analyzer. The measurements were performed based on the Bode 100 application note for power inductor modelling [3]. The parameters values measured for inductor L_{s1} are shown in Table 6.2 while the values for inductor L_m are shown in Table 6.3.

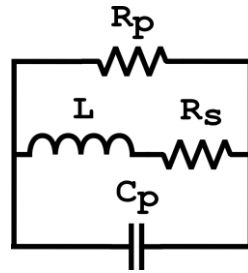


Figure 6.11: Inductor non-ideal model

Table 6.2: L_{s1} (design value: 54.04 μ H)

Parameter	Value
L	51.620 μ H
R_s	0.25 Ω
R_p	1.9 k Ω
C_p	2.52 pF

Table 6.3: L_m (design value: 27.02 μH)

Parameter	Value
L	32.089 μH
R_s	0.073 Ω
R_p	1.96 $\text{k}\Omega$
C_p	2.394 pF

The inductor's series resistance represents the winding losses. From the measurements performed with the Bode 100, shown in Figure 6.12, it is possible to observe that this resistance value is frequency-dependent, significantly increasing as the frequency increases. The series resistances were measured at the operating frequency, 100 kHz.

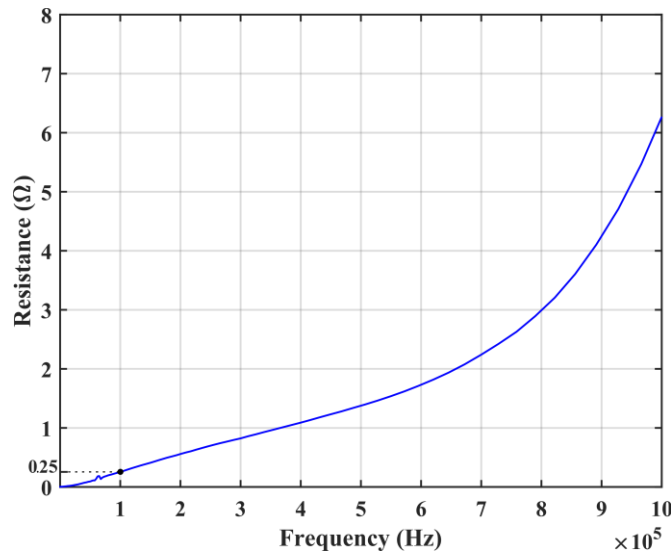


Figure 6.12: Series resistance of inductor in function of frequency

For the resonant tank capacitors, the values of capacitance were calculated in Chapter 5 considering the ideal values of inductance with the resonant circuit tuned to 100kHz. Based on the measured values of inductance, the values of capacitors C_{s1} and C_{s2} are recalculated to keep the resonant frequency at 100kHz. The value of C_{s1} drops from originally 31.24 nF to 29.70 nF, and C_{s2} changes from 1.5 μF to 1.25 μF . Polypropylene film capacitors were used due to the low-ESR, high power and frequency characteristics.

Here the real capacitor is modelled considering only the capacitance and an equivalent series resistance (ESR), as shown in Figure 6.13. The values of capacitance and series resistance are measured with the Bode 100 vector analyser, based on the Capacitor ESR measurement application note [4]. The results obtained are presented in Table 6.4 for the primary capacitor and in Table 6.5 for the secondary capacitor.

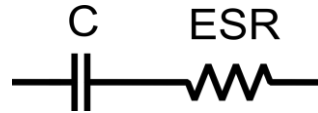


Figure 6.13: Capacitor non-ideal model

Table 6.4: C_{s1} (recalculated design value: 29.70 nF)

Parameter	Value
<i>ESR</i>	0.044Ω
C_s	28.354 nF

Table 6.5: C_{s2} (recalculated design value: 1.25 μF)

Parameter	Value
<i>ESR</i>	0.004 Ω
C_s	1.326 μF

For the transformer design, the minimum number of turns in the primary coil is calculated from equation (6.5).

$$N_1 > \frac{V \cdot \delta}{f \cdot 2 \cdot B_{max} \cdot A_{core}} \quad (6.5)$$

where V is the primary RMS voltage, f is the switching frequency and δ is the maximum duty cycle.

The transformer is built using an ETD-44 core and 20 turns on the primary winding and 5 turns on secondary, resulting in a turns ratio of 4. A short circuit test is performed with the Bode 100 to measure the leakage inductance and total winding resistance reflected to the primary at 100kHz. The open circuit test is employed to measure the

primary inductance, L_p . A gain measurement is used for calculation of the turns ratio and based on this value the secondary inductance, L_s , can be estimated for the Spice simulation as $L_s = \frac{L_p}{n^2}$. The transformer equivalent circuit is shown in Figure 6.14 and the parameters measured are presented in Table 6.6.

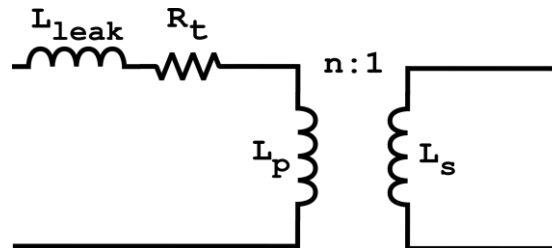


Figure 6.14: Transformer non-ideal model

Table 6.6: Measured transformer parameters

Parameter	Value
Gain	0.2501 ($n = 3.998$)
R_t	0.92 Ω
L_p	1.374 mH
L_{leak}	13.28 μ H

6.2.4 Load

The main objective in this chapter is to verify the accuracy of the models developed in Chapter 5 using an experimental set-up. Therefore, to simplify the model-prototype comparison, a load resistor, which is simpler to model, is used in place of the output battery. In Chapter 5 the battery is simply modelled as a voltage source. Using a resistor as load, the simulation and prototype results can be accurately compared without the need of developing a more accurate battery model for the simulations. The equivalent resistor is defined based on the output voltage and current for the maximum modulation case ($\alpha_{ratio} = 1$ and $\phi = 90^\circ$). From Spice simulation results obtained in Chapter 5, the output resistors are calculated for forward (R_{for}) and reverse (R_{rev}) operation:

$$R_{for} = \frac{V_{out}}{I_{out}} = \frac{12.093}{9.3162} = 1.298\Omega$$

$$R_{rev} = \frac{V_{out}}{I_{out}} = \frac{48.023}{2.3082} = 20.805\Omega$$

(6.6)

Based on commercial availability, a HS100 (100W) 0.5Ω resistor is used in series with a 1Ω resistor for forward operation, resulting in a measured resistance value that varies between 1.5 and 1.9Ω. Therefore, the average value of 1.7Ω is attributed to the output resistor in the simulation stage. In reverse operation, a HS100 12 Ω resistor and a 10 Ω resistor are connected in series, the multimeter measurement for resistance is in a range of 22.10 Ω to 22.65 Ω, resulting in an average value of 22.3 Ω.

The HS100 series are aluminium housed resistors designed to be used with heatsink for maximum performance, hence, as shown in Figure 6.15, the resistors are directly mounted in a heatsink with thermal compound. Wirewound resistors have a small inductance associated, however, it was observed in simulation that the inclusion of this value in the model did not significantly affect the average output current value.

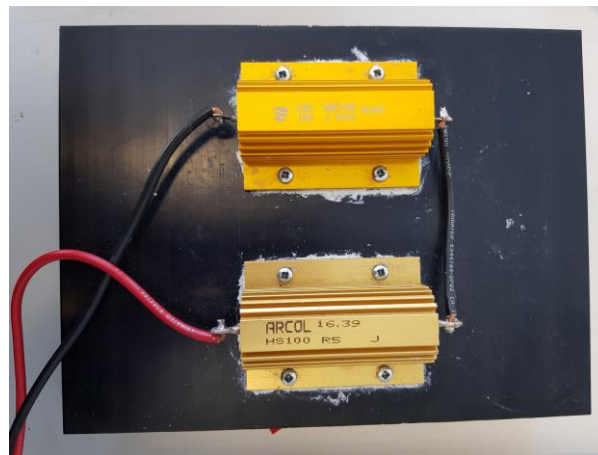


Figure 6.15: Load resistor for forward operation

6.3 Experimental results

In this section experimental results are presented and compared to cyclic-averaging and Spice models. In Chapter 5 simulations were performed considering a battery as output and an ideal model for the resonant tank. For comparison with the prototype, the

models are modified to include the output resistor load and the real values of the resonant circuit components (capacitors, inductors and transformer) measured in the previous section.

The cyclic-averaging model is derived from the state-variable model and consequently, as observed in Chapter 5, both models show very similar results and accuracy level. Therefore, only the cyclic-averaging and Spice model are now modified and compared to the experimental results. The state-variable equation description for the cyclic-averaging implementation, using equations (5.24) and (5.25), in the previous chapter was modified to place the equivalent load resistor (R_{for} or R_{rev}) at output in substitution of voltage source V_{bat} (or V_{dc} for reverse operation). The updated matrices A_f, A_r and B_f, B_r used for implementation of the cyclic model in this chapter are described in equations (6.7) - (6.10). The bridge voltages $v_1(t)$ and $v_2(t)$ are defined based on the modulation technique adopted (SPS or PPM) and, consequently, the modulation angles.

$$A_f = \begin{bmatrix} -\frac{(r_1 + r_2')}{L_{s1}} & -\frac{1}{L_{s1}} & \frac{r_{c2}'}{L_{s1}} & -\frac{1}{L_{s1}} & 0 \\ \frac{1}{C_{s1}} & 0 & 0 & 0 & 0 \\ \frac{r_{c2}'}{L_m} & 0 & -\frac{(r_{Lm} + r_{c2}')}{L_m} & \frac{1}{L_m} & 0 \\ \frac{1}{C_{s2}'} & 0 & -\frac{1}{C_{s2}'} & 0 & 0 \\ 0 & 0 & 0 & 0 & -\frac{1}{C_f R_{for}} \end{bmatrix}$$

$$B_f = \begin{bmatrix} \frac{(v_1(t) - nv_2(t))}{L_{s1}} \\ 0 \\ \frac{nv_2(t)}{L_m} \\ 0 \\ \frac{i_{bridge}(t)}{C_f} \end{bmatrix}$$

(6.7)

where:

$$v_1(t) = \pm V_{dc} \text{ or } 0 \text{ and } v_2(t) = \pm v_{cf}(t) \text{ or } 0$$

$$i_{bridge} = \begin{cases} n(i_{Ls1} - i_{Lm}), \text{ when } v_2(t) > 0 \\ -n(i_{Ls1} - i_{Lm}), \text{ when } v_2(t) < 0 \\ 0, \text{ when } v_2(t) = 0 \end{cases}$$

(6.8)

$$A_r = \begin{bmatrix} -\frac{(r_1 + r_2')}{L_{s1}} & -\frac{1}{L_{s1}} & -\frac{r_{c2'}}{L_{s1}} & -\frac{1}{L_{s1}} & 0 \\ \frac{1}{C_{s1}} & 0 & 0 & 0 & 0 \\ -\frac{r_{c2'}}{L_m} & 0 & -\frac{(r_{Lm} + r_{c2}')}{L_m} & -\frac{1}{L_m} & 0 \\ \frac{1}{C_{s2'}} & 0 & -\frac{1}{C_{s2'}} & 0 & 0 \\ 0 & 0 & 0 & 0 & -\frac{1}{C_i R_{rev}} \end{bmatrix}$$

$$B_r = \begin{bmatrix} \frac{(nv_2(t) - v_1(t))}{L_{s1}} \\ 0 \\ \frac{nv_2(t)}{L_m} \\ 0 \\ \frac{i_{bridge}(t)}{C_i} \end{bmatrix}$$

(6.9)

where:

$$v_1(t) = \pm v_{Ci} \text{ or } 0 \text{ and } v_2(t) = \pm V_{bat} \text{ or } 0$$

$$i_{bridge} = \begin{cases} i_{Ls1}, \text{ when } v_1 > 0 \\ -i_{Ls1}, \text{ when } v_1 < 0 \\ 0, \text{ when } v_1 = 0 \end{cases}$$

(6.10)

Once the experimental set-up is built, as shown in Figure 6.16, the system is tested using a 0-60V, 100A power supply as input.

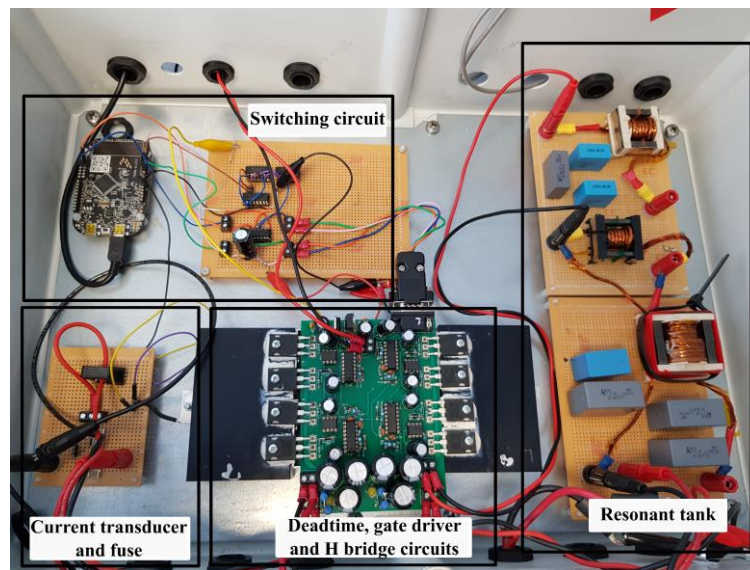


Figure 6.16: Experimental set-up

As shown in the previous section, the real inductor equivalent circuit comprises a series resistance, parallel resistance and capacitance. For the cyclic-averaging model developed in the previous chapter, the only loss element considered in the resonant circuit was the series resistance and the transformer was assumed to be ideal. To avoid further modifications in the model equations with the addition of these parallel and leakage elements, the cyclic averaging simulations are initially performed not considering the parallel capacitances and resistances, and the transformer's leakage inductance.

Since the modifications on the Spice model are easily implemented, simply adding the new components blocks, the Spice simulations are performed considering all measured parasitic elements. The resonant tank circuit diagrams used for Spice and cyclic-averaging simulations at this stage are presented in Figure 6.17.

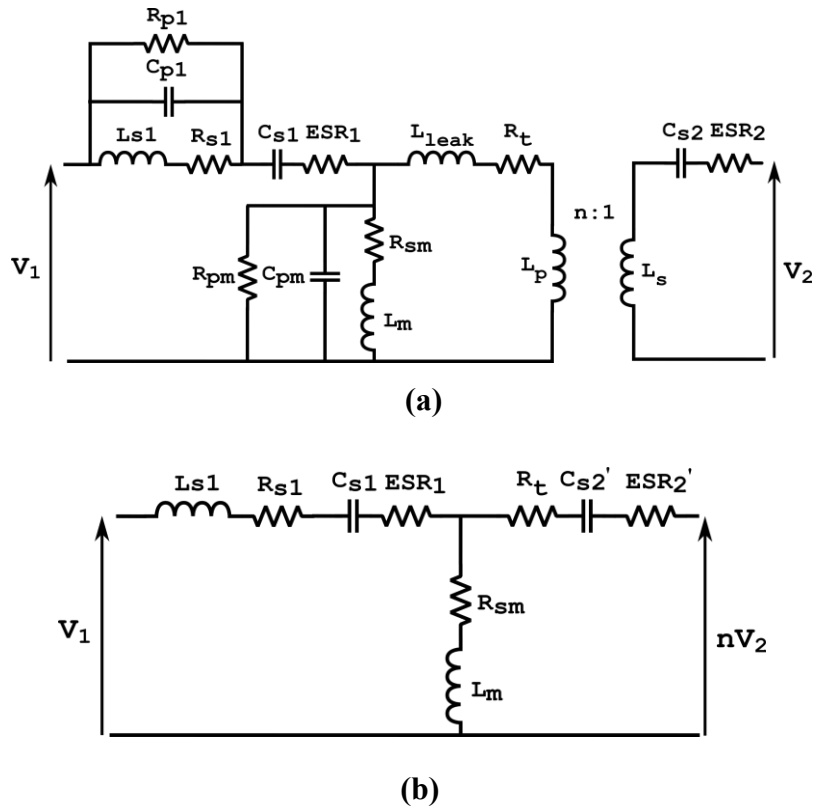


Figure 6.17: Resonant tank circuits employed for (a) Spice simulation and (b) cyclic-averaging simulation

Simulation and experimental results are compared in Figures 6.18 and 6.19, where the output DC current is plotted as function of the alpha ratio for PPM modulation and in function of the bridge phase-shift angle for SPS modulation.

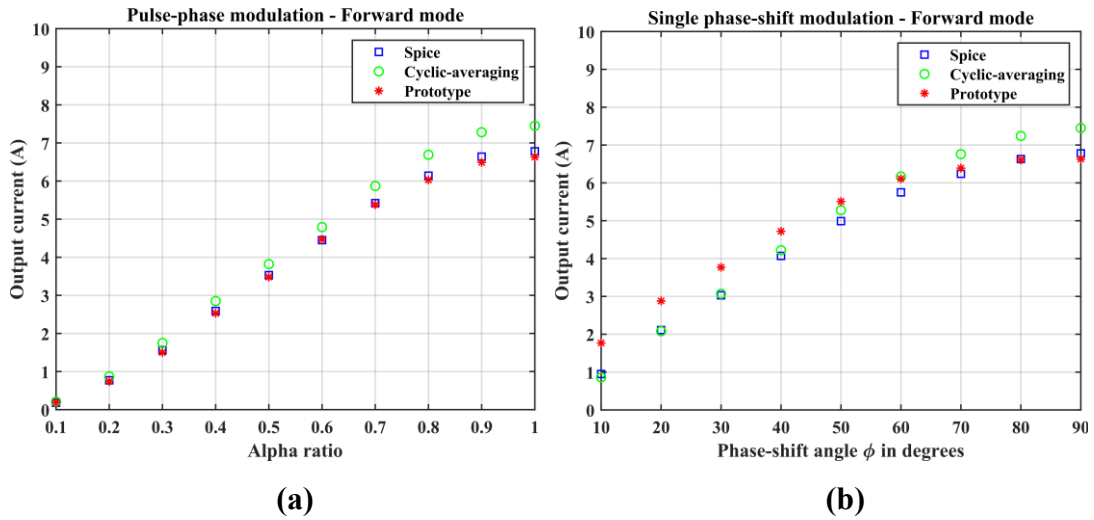


Figure 6.18: Spice, cyclic-averaging and prototype results comparison for (a) PPM modulation and (b) SPS modulation in forward operation

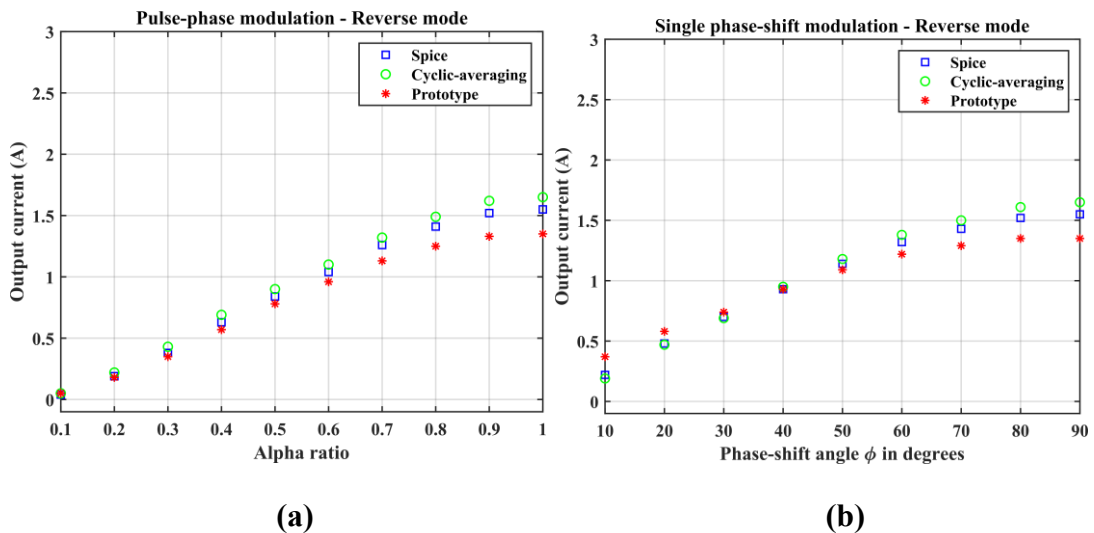


Figure 6.19: Spice, cyclic-averaging and prototype results comparison for (a) PPM modulation and (b) SPS modulation in reverse operation

For a converter operating under SPS modulation, as the bridge phase-shift angle decreases, the error between prototype and Spice results significantly increase. During experimental validation it was observed that implementation of small values of phase-shift angle ϕ are subject to reduced precision from the microcontroller and higher influence of deadtime and delays, contributing to increased errors between simulation and prototype results. Also, the operation of a converter under SPS modulation degrades as the phase-shift angle reduces and as the voltage mismatch between primary and secondary increases resulting in high circulation current, hard switching operation and large current spikes. For a converter operating under PPM modulation results were

not significantly affected by the reduction of leg phase-shift angles, even when testing small values of α_{ratio} .

The simulations were performed considering the bridge phase-shift angle value set by the microcontroller, thus to improve the accuracy of the simulations, the difference between the phase-shift angle of the switching signals and the real phase-shift at the output of the bridges must be incorporated into the models. The drain-source voltages v_{ds13} and v_{ds23} from Figure 6.20 are analysed with the oscilloscope, as shown in Figure 6.21. The phase-shift is measured for different SPS modulation cases and an average difference of 90.28ns is obtained between the set and real time difference, which corresponds to a 3.24° phase difference. Therefore, Spice and cyclic-averaging simulations are performed again adding 3.24° to the phase-shift angle ϕ previously used.

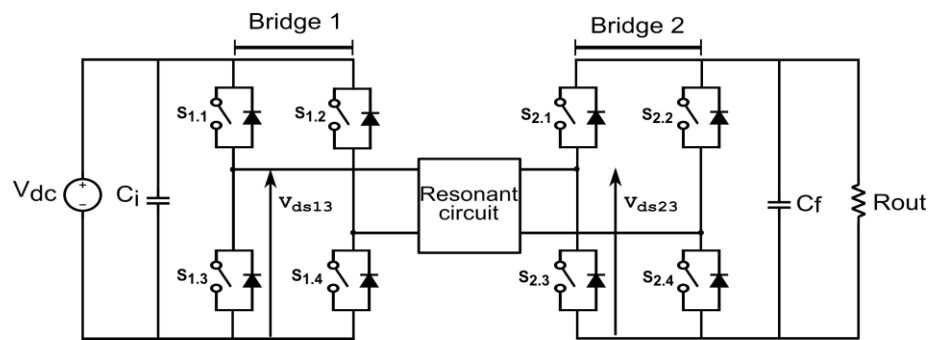


Figure 6.20: CLLC converter circuit

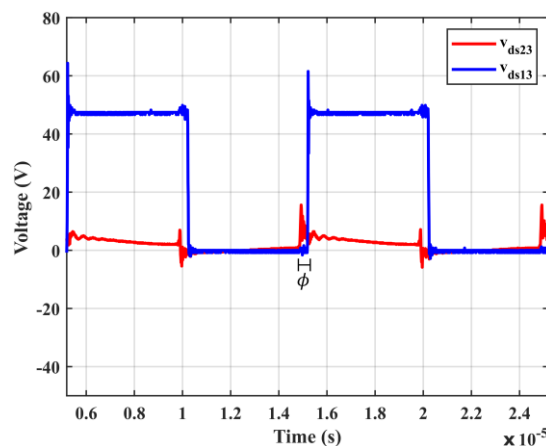


Figure 6.21: Drain source voltages for 10° phase-shift test case in forward mode

It was also observed in the first set of results in Figures 6.18 and 6.19 that the cyclic-averaging model was not as accurate as Spice, especially for high modulation angles. To further improve the accuracy of the cyclic-averaging method without changing the equation description, the non-ideal inductor circuit can be reduced to an equivalent inductive reactance in series with a resistor, as in Figure 6.22, and the leakage inductance of the transformer is incorporated to the reactance value of the secondary capacitor, Figure 6.23. This way, all parasitic elements considered in the Spice simulation are now also incorporated to the cyclic method, improving the comparison between the models.

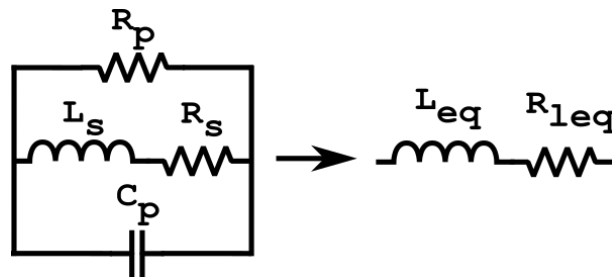


Figure 6.22: Inductor equivalent circuit for cyclic-averaging implementation

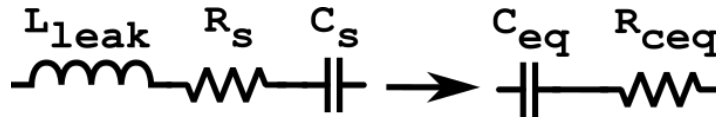


Figure 6.23: Secondary capacitor equivalent circuit for cyclic-averaging implementation

The equivalent impedances for the inductor, Z_{leq} , and for the secondary capacitor, Z_{ceq} , are defined in equation (6.11).

$$Z_{leq} = R_{leq} + j\omega L_{eq} = \frac{1}{\frac{1}{R_p} + \frac{1}{R_s + j\omega L} + j\omega C_p}$$

$$Z_{ceq} = R_{ceq} - j\frac{1}{\omega C_{eq}} = R_s + j\omega L_{leak} - \frac{j}{\omega C_{s2}'}$$

(6.11)

where, in the equivalent circuit for the secondary capacitor, R_s is obtained adding the capacitor's ESR to the transformer resistance, all referred to primary.

The calculated values for the equivalent circuit parameters, referred to the primary side of transformer, are shown in Table 6.7.

Table 6.7: Inductors and capacitor equivalent parameters referred to primary

Parameter	Inductor L_{s1}	Inductor L_m	Capacitor C_{s2}'
R_{leq} (for inductors) or R_{ceq} (for capacitor)	0.8033 Ω	0.2804 Ω	0.9839 Ω
L_{eq} (for inductors) or C_{eq} (for capacitor)	51.592 μH	32.084 μH	146.76 nF

After the phase-shift angle correction and cyclic-averaging accuracy modifications are implemented, simulation results are compared to experimental once again, as shown in Figures 6.24 and 6.25. The tables containing the numerical data for all tests performed can be found in Appendix A.2. After the model optimization the accuracy of the cyclic-averaging model was significantly improved, and results are very close to Spice for all modulation cases.

For maximum modulation in reverse mode, a difference of 200 mA (12.9%) is measured between Spice and prototype results of output current, while 150 mA (2.21%) difference is measured for forward mode.

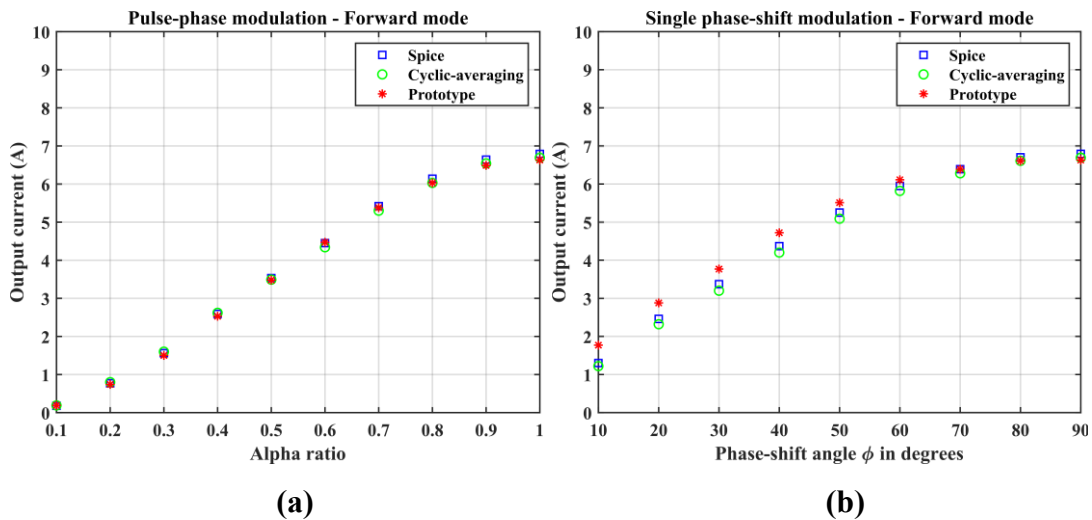


Figure 6.24: Optimized Spice, cyclic-averaging and prototype results comparison for (a) PPM modulation and (b) SPS modulation in forward operation

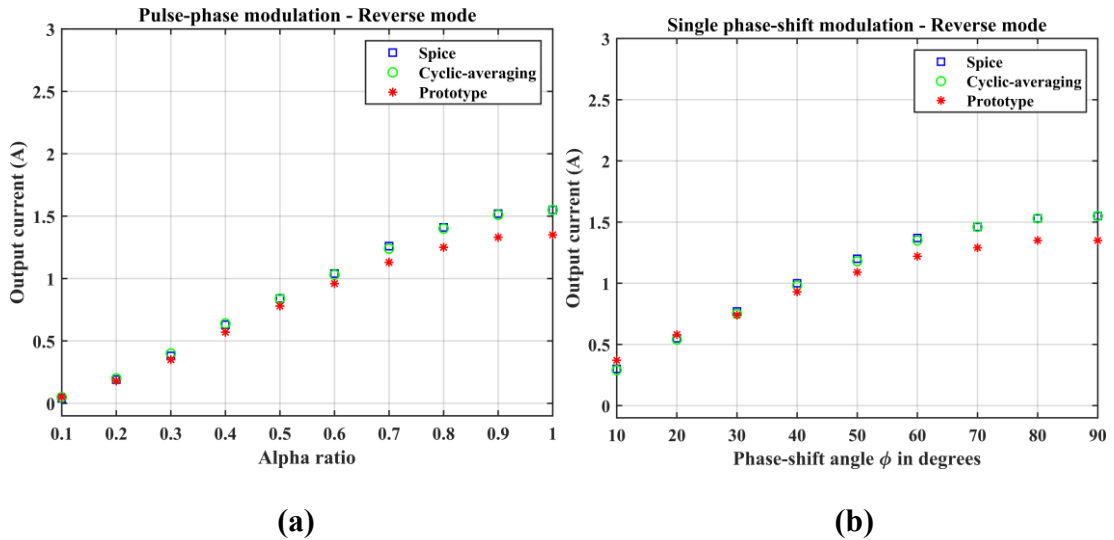


Figure 6.25: Optimized Spice, cyclic-averaging and prototype results comparison for (a) PPM modulation and (b) SPS modulation in reverse operation

The results for the SPS modulation case improved compared to the previous set of results, especially for small phase-shift angles. The simulation results are now closer to experimental due to the phase-shift angle compensation implemented. No significant difference is observed for the PPM modulation case from the addition of the compensation angle. Even with the basic delay compensation implemented on simulation models, errors are still higher for SPS modulation when operating with small values of phase-shift angle ϕ .

As a further verification, the waveforms obtained in the Spice simulation were analysed and compared to the experimental measurements. The results for a converter operating in reverse mode under maximum modulation ($\alpha = 1$ and $\phi = 90^\circ$) are shown in Figures 6.26, 6.27, 6.28 and 6.29. Measurements were made using an oscilloscope and a Rogowski current waveform transducer (CWTUM/ 015/B).

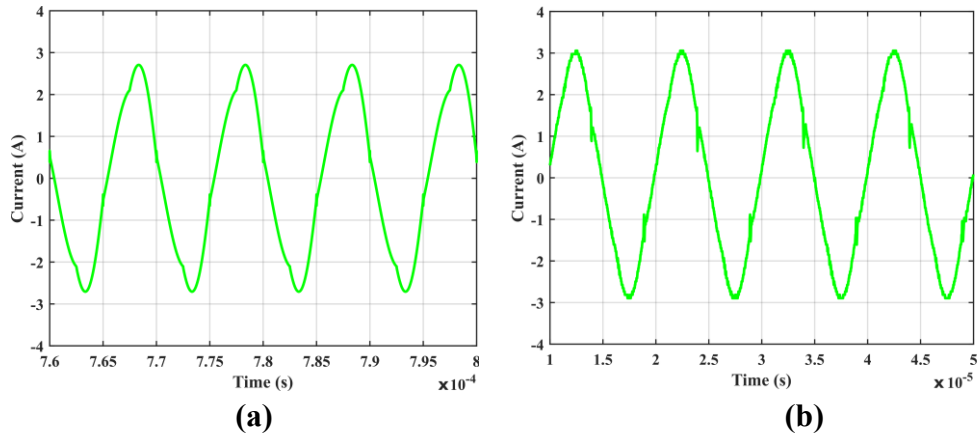


Figure 6.26: Comparison between (a) Spice and (b) experimental results for the primary current

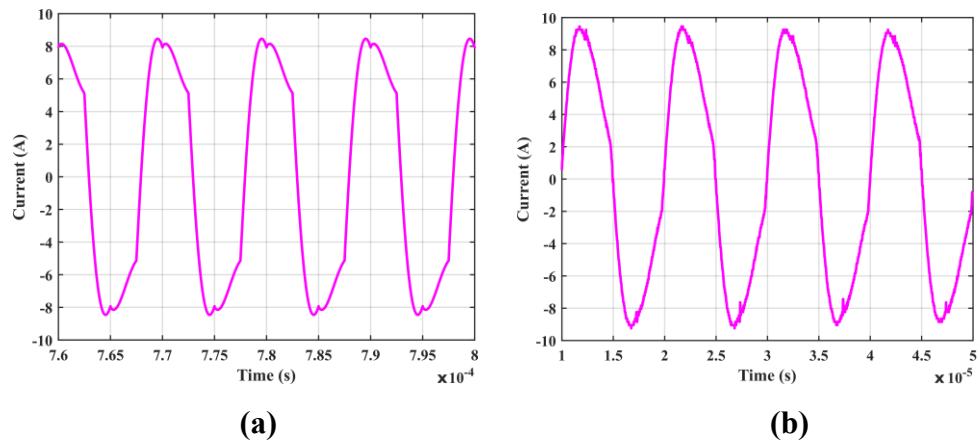


Figure 6.27: Comparison between (a) Spice and (b) experimental results for the secondary current

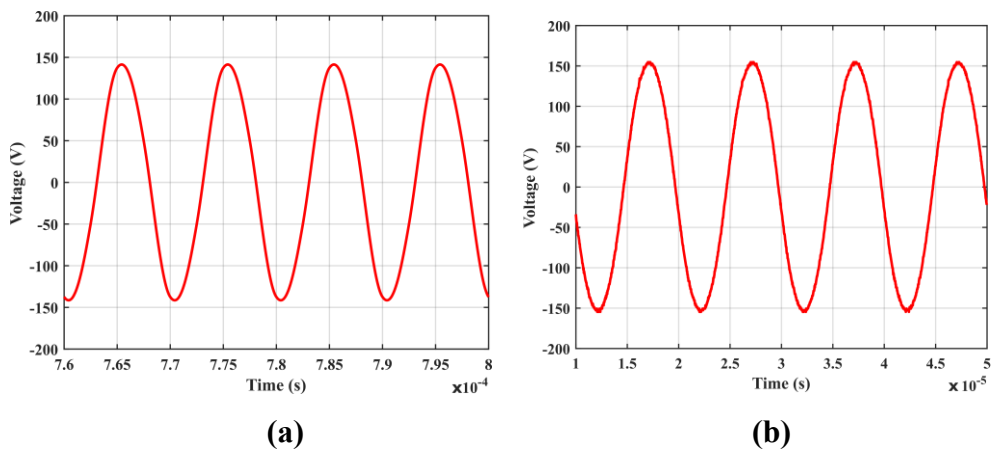


Figure 6.28: Comparison between (a) Spice and (b) experimental results for the primary capacitor voltage

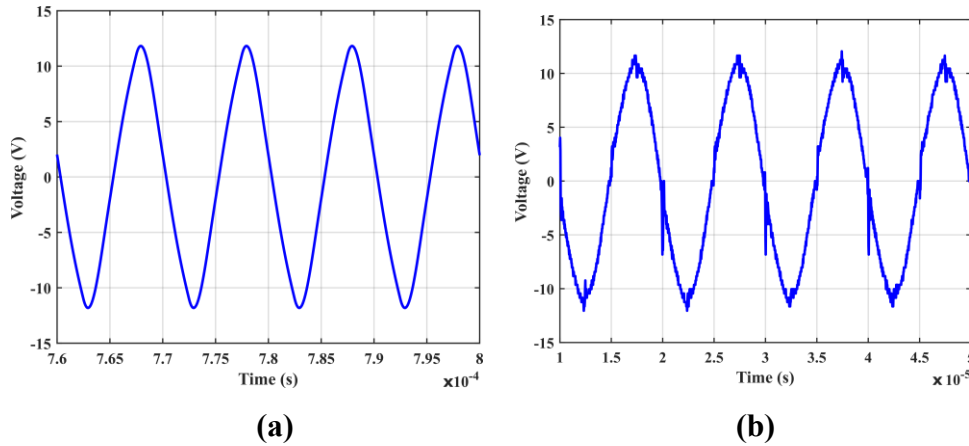


Figure 6.29: Comparison between (a) Spice and (b) experimental results for the secondary capacitor voltage

Overall, the experimental waveforms are also close to the simulation results. The values of rms voltages and currents obtained with the Spice and experimental measurements are compared in Table 6.8. From the waveforms results, it is observed that the peak value of the secondary current is higher for the experimental case, however, the experimental rms current value is lower. Furthermore, the experimental waveform for the secondary capacitor voltage shows increased noise, while in simulations this waveform is cleaner.

Table 6.8: Difference between Spice and experimental results in waveform analysis

Parameter	Spice	Experimental
Primary RMS current (A)	1.85	1.96
Secondary RMS current (A)	6.63	6.54
Primary capacitor RMS voltage (V)	101.19	110.49
Secondary capacitor RMS voltage (V)	7.84	7.63

The difference between simulation and experimental waveforms and average output current results are attributed to instrument error and additional loss elements in the circuit, as wire resistances and inductances, that were not previously included in simulation models. To analyse the influence of increased resistances on the output current results, new simulations are performed considering an addition of 100 mΩ on

the primary or secondary side of the resonant tank. Results are presented in Table 6.9, where the percentage error is calculated as follows:

$$\text{Percentage error} = \frac{\text{value after addition} - \text{base value}}{\text{base value}} \cdot 100\% \quad (6.12)$$

Table 6.9: Influence of additional resistances on output current

Parameter	Forward mode		Reverse mode	
	I_{out} (A)	Error (%)	I_{out} (A)	Error (%)
Addition of 100 mΩ on primary	6.7483	-0.53	1.5454	-0.15
Base value	6.7844	-	1.5477	-
Addition of 100 mΩ on secondary	6.7229	-0.91	1.4618	-5.55

The secondary is the low voltage/high current side of the circuit, therefore, increased resistances on this side results in higher current drop. From the results it is also verified that reverse mode results are more significantly affected by additional resistances in the secondary side of the resonant tank, in this case the resistor is introduced in the high current side which is also the input side.

Simulations are also performed to evaluate the circuit sensitivity to fluctuations in the values of circuit components and frequency. For the capacitors' analysis shown in Tables 6.10 and 6.11 a maximum variation of 5% was considered, since the components used have 5% tolerance. The inductors and frequency results are shown in Tables 6.12, 6.13 and 6.14 considering variations of $\pm 10\%$.

From the results obtained it is noticed that results are slightly affected by variations in the primary capacitor, inductors and frequency while variations on the secondary capacitor do not significantly affect the output current, with a difference in current inferior to 1% for a change of $\pm 5\%$ in the capacitor value.

Table 6.10: Influence of capacitor C_{s1} on output current

		Forward mode		Reverse mode	
Parameter		I_{out} (A)	Error (%)	I_{out} (A)	Error (%)
C_{s1}	+5%	7.1717	5.71	1.6074	3.86
	Base value	6.7844	-	1.5477	-
	-5%	6.3605	-6.25	1.4840	-4.12

Table 6.11: Influence of capacitor C_{s2} on output current

		Forward mode		Reverse mode	
Parameter		I_{out} (A)	Error (%)	I_{out} (A)	Error (%)
C_{s2}	+5%	6.7339	-0.74	1.5362	-0.74
	Base value	6.7844	-	1.5477	-
	-5%	6.8408	0.83	1.5602	0.81

Table 6.12: Influence of inductor L_{s1} on output current

		Forward mode		Reverse mode	
Parameter		I_{out} (A)	Error (%)	I_{out} (A)	Error (%)
L_{s1}	+10%	7.1930	6.02	1.6151	4.35
	Base value	6.7844	-	1.5477	-
	-10%	6.3615	-6.23	1.4826	-4.21

Table 6.13: Influence of inductor L_m on output current

		Forward mode		Reverse mode	
Parameter		I_{out} (A)	Error (%)	I_{out} (A)	Error (%)
L_m	+10%	6.5169	-3.94	1.4874	-3.90
	Base value	6.7844	-	1.5477	-
	-10%	7.0852	4.43	1.6247	4.97

Table 6.14: Influence of frequency on output current

		Forward mode		Reverse mode	
Parameter		I_{out} (A)	Error (%)	I_{out} (A)	Error (%)
Frequency	+5%	7.2262	6.51	1.6108	4.08
	Base value	6.7844	-	1.5477	-
	-5%	6.4297	-5.23	1.5288	-1.22

Simulations were previously performed considering the average value measured for the load resistor, therefore, the influence of this parameter is also examined through simulation considering the maximum and minimum values measured. As shown in Tables 6.15 and 6.16, fluctuations in the measurements of the value of the output resistor do not significantly affect the output current.

Table 6.15: Influence of output resistor on output current in forward mode

		Forward mode	
Parameter		I_{out} (A)	Error (%)
R_{for}	Maximum (1.9 Ω)	6.7244	-0.88
	Average (1.7 Ω)	6.7844	-
	Minimum (1.5 Ω)	6.8454	0.90

Table 6.16: Influence of output resistor on output current in reverse mode

		Reverse mode	
Parameter		I_{out} (A)	Error (%)
R_{rev}	Maximum (22.65 Ω)	1.5443	-0.22
	Average (22.30 Ω)	1.5477	-
	Minimum (22.10 Ω)	1.5497	0.13

Another factor that contributes to differences between simulation and experimental results is the MOSFET simulation model. The MOSFET switches are modelled in Spice considering the datasheet value of $R_{DS(on)}$, but during operation this value changes depending on parameters as temperature, gate-source voltage and drain current. Simulations results could be improved adopting a more accurate model for the

MOSFET including parasitic elements, instead of only $R_{DS(on)}$ and associated body diode, but this would also increase the complexity of the system, especially for cyclic-averaging implementation.

6.4 Conclusions

In this chapter a prototype for the CLLC converter was built to verify the accuracy of the Spice and cyclic-averaging models. The results show that both models analysed could successfully predict the converter's behaviour, with the confirmation that the phase-shift angles of the two H-bridges can be used to control the output current. Therefore, it is possible to use this converter as a charging/discharging system when connecting a battery to the output.

The models adopted in this chapter for representation of real inductors, capacitors, transformer, the associated resistances and parasitic elements are approximations and cannot perfectly represent the real system behaviour. Also, measurement errors, parameters variation and environment factors, as temperature, affect the results. Therefore, discrepancies between the models and experimental results still occur.

Errors between simulation and practical results are lower for the PPM modulation case, due to the increased sensitivity to delays and performance deterioration as the value of bridge phase-shift angle decreases when operating under SPS modulation, and finally, the difficulty to accurately incorporate the system's delays and all parasitic elements to the simulation models.

Furthermore, the influence of inductances and resistances associated to wires with considerable length connecting the resonant tank to the load and power supply was not considered in this chapter. The inclusion of these elements to the simulation model will be performed in the next chapter for the analysis of the wireless power transfer converter.

The influence of parasitic elements and transformer leakage inductance affects the resonant state, where a high value of transformer leakage inductance could result in a deviation from the point of resonance. Therefore, to improve performance, in [5] a construction process is suggested where the transformer is designed to incorporate the values of the resonant inductors. Consequently, to reduce the influence of the non-ideal

transformer to this system, the transformer could be designed to have leakage inductance equal to L_{s1} and magnetizing inductance equal to L_m . In the next chapter, a wireless variant of this converter will be analysed, where the resonant tank inductors originate from the wireless transformer equivalent circuit and no extra inductor is needed.

6.5 References

- [1] F. Xue, R. Yu, and A. Q. Huang, "A 98.3% Efficient GaN Isolated Bidirectional DC-DC Converter for DC Microgrid Energy Storage System Applications," *IEEE Transactions on Industrial Electronics*, vol. 64, no. 11, pp. 9094–9103, 2017.
- [2] J. Millan, P. Godignon, X. Perpina, A. Perez-Tomas, and J. Rebollo, "A survey of wide bandgap power semiconductor devices," *IEEE Transactions on Power Electronics*, vol. 29, no. 5, pp. 2155–2163, 2014.
- [3] M. Bitschnau, "Power Inductor Modelling," *Bode 100 Application Note*, 2017.
- [4] F. Hämmerle, "Capacitor ESR measurement technique," *Bode 100 Application Note*, 2017.
- [5] R. P. Twiname, D. J. Thrimawithana, U. K. Madawala, and C. A. Baguley, "A Dual-Active Bridge Topology with a Tuned CLC Network," *IEEE Transactions on Power Electronics*, vol. 30, no. 12, pp. 6543–6550, 2015.

7 Analysis of Series Compensated IPT converter

7.1 Introduction

The cyclic-averaging analysis approach was successfully applied in the previous chapters to model the bidirectional CLLC resonant converter. Here, this analysis is extended to evaluate an Inductive Power Transfer (IPT) wireless system. In the literature review conducted in Chapter 2, three topologies of compensation circuits were compared. The series compensated topology, shown in Figure 7.1, is chosen due to its simplicity, good performance and similarity to the previously analysed CLLC converter. FMA, state-variable and cyclic-averaging methods will now be applied to this circuit and verified against a Spice simulation. To simplify the analysis and construction processes, the IPT converter analysed in this chapter has a turns ratio, n , equal to one, therefore $L_1 = L_2$.

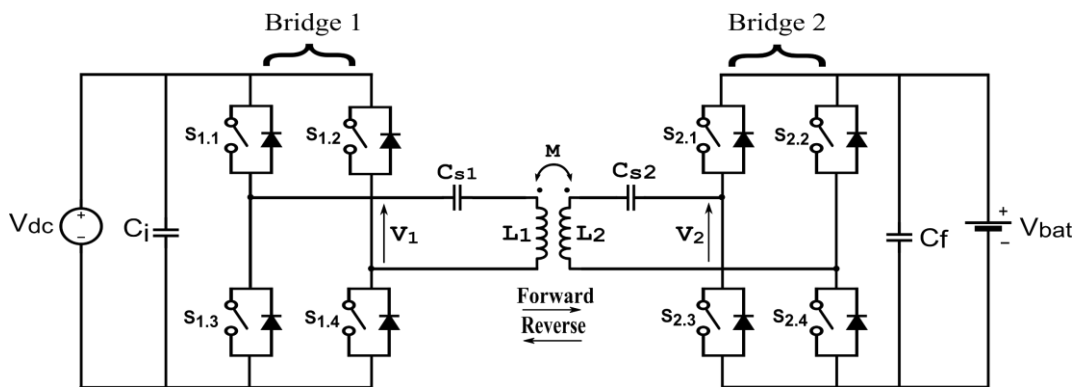


Figure 7.1: Series compensated IPT converter

Similar to the analysis performed in Chapters 5 and 6, Single Phase-Shift (SPS) and Pulse-Phase (PPM) modulation techniques will be adopted here for the analysis of the IPT converter.

The conventional transformer utilized in the previous chapters is now substituted by primary and secondary IPT coils, separated by a large air gap of 150mm. The values of inductance and coupling coefficient depends on the coil pad dimensions, material and the distance, or misalignment, between the pads. Using a 3D finite element analysis (FEA) simulation tool, the Double D coil pad structures will be designed and the influence of construction parameters and misalignment will be evaluated. The coil structures are built, tested for misalignment conditions, and results are compared to the FEA simulation.

Once the coil structures are validated, the pads are connected to the compensation capacitors and the prototype of the IPT converter is tested for experimental verification of the cyclic-averaging and Spice simulations.

7.2 Fundamental Mode Approximation (FMA) applied to inductive power transfer

The FMA analysis will be used in this chapter for calculation of the converter's output power and primary and secondary currents in the resonant tank. The converter diagram from Figure 7.1 can be simplified to the equivalent circuits shown in Figure 7.2. Circuit resistances and parasitic elements are not considered in the FMA analysis for simplification.

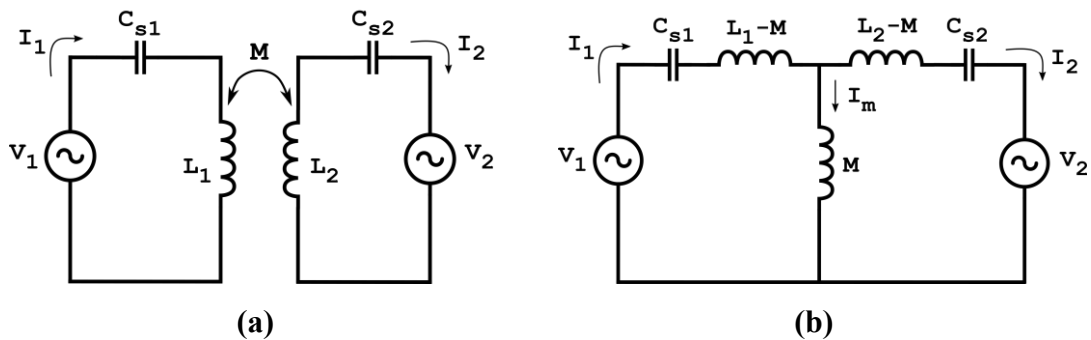


Figure 7.2: Equivalent circuits for series compensated IPT converter with (a) coupled inductors representation and (b) T-model representation

The mutual inductance M is calculated based on the value of self-inductances and the magnetic coupling between primary and secondary coil pads, as in (7.1).

$$M = k\sqrt{L_1L_2}$$

(7.1)

where k is the coupling coefficient, also called coupling factor.

The resonant frequency is defined in (7.2) based solely on the values of self-inductance and compensation capacitors, therefore, this frequency is independent from the coupling coefficient.

$$\omega_0 = 2\pi f_0 = \frac{1}{\sqrt{L_1 C_{s1}}} = \frac{1}{\sqrt{L_2 C_{s2}}} \quad (7.2)$$

From analysis of the equivalent circuit, Figure 7.2-b, the circuit impedances in the T-network are defined as follows:

$$Z_1 = j\omega(L_1 - M) - j\frac{1}{\omega C_{s1}}$$

$$Z_2 = j\omega(L_2 - M) - j\frac{1}{\omega C_{s2}}$$

$$Z_m = j\omega M$$

(7.3)

Since the converter operates under phase-shift modulation (SPS or PPM), the bridge voltages waveforms and the phasor voltages are defined the same way as in Chapter 5 (equations (5.1) and (5.2)), applying the fundamental approximation to the Fourier representation of functions $v_1(t)$ and $v_2(t)$. Therefore, the voltage phasors are given by:

$$\mathbf{V}_1 = \frac{4V_{DC}}{\pi\sqrt{2}} \sin\left(\frac{\alpha_1}{2}\right)$$

$$\mathbf{V}_2 = \frac{4V_{bat}}{\pi\sqrt{2}} \sin\left(\frac{\alpha_2}{2}\right) (\cos(\phi) + j \sin(\phi))$$

(7.4)

Once the voltage phasors are defined, the following equations are obtained analysing the circuit in Figure 7.2-b.

$$\begin{aligned}
V_1 &= Z_1 I_1 + Z_m I_m \\
I_1 &= I_2 + I_m \\
Z_m I_m &= Z_2 I_2 + V_2
\end{aligned}
\tag{7.5}$$

After solving the system of equations, the currents are obtained, as in (7.6).

$$\begin{aligned}
I_1 &= \frac{V_1(Z_2 + Z_m) - V_2 Z_m}{Z_1 Z_2 + Z_1 Z_m + Z_2 Z_m} \\
I_2 &= \frac{V_1 Z_m - V_2(Z_1 + Z_m)}{Z_1 Z_2 + Z_1 Z_m + Z_2 Z_m} \\
I_m &= \frac{V_1 Z_2 + V_2 Z_1}{Z_1 Z_2 + Z_1 Z_m + Z_2 Z_m}
\end{aligned}
\tag{7.6}$$

At simulation stage, MATLAB “abs()” function will be used with (7.6) to calculate the rms value of the primary and secondary currents.

No resistive losses are considered in the FMA model, therefore, the magnitude of the output active power is obtained calculating $Re(V_1 I_1^*)$ or $Re(V_2 I_2^*)$, resulting in the following equation:

$$P_{out} = \frac{8V_{dc}V_{bat}X_m \sin(\phi) \sin\left(\frac{\alpha_1}{2}\right) \sin\left(\frac{\alpha_2}{2}\right)}{\pi^2(X_1X_2 + X_1X_m + X_2X_m)}
\tag{7.7}$$

where $Z_1 = jX_1$, $Z_2 = jX_2$ and $Z_m = jX_m$.

The power equation can be simplified by substituting equation (7.2), which defines the resonant condition, into (7.7). The final expression for active power calculation is given by (7.8).

$$P_{out} = \frac{8V_{dc}V_{bat} \sin(\phi) \sin\left(\frac{\alpha_1}{2}\right) \sin\left(\frac{\alpha_2}{2}\right)}{\pi^2 \omega M} = \frac{8V_{dc}V_{bat} \sin(\phi) \sin\left(\frac{\alpha_1}{2}\right) \sin\left(\frac{\alpha_2}{2}\right)}{\pi^2 \omega k \sqrt{L_1 L_2}}
\tag{7.8}$$

The converter operates at resonant frequency $\omega = \omega_0$ and maximum output power is achieved when $\phi = \pm 90^\circ$ and $\alpha_1 = \alpha_2 = 180^\circ$. The output power equation is often used in the design process to dimension the inductors based on a defined range of input/output voltages, coupling coefficient and operating frequency.

7.3 State-variable and cyclic-averaging analysis

The equivalent circuit of the series compensated IPT converter, shown in Figure 7.2-b, is a CLLC network that resembles the CLLC converter analysed in Chapters 5 and 6. As shown in [1], a CLLC network can be reduced to an equivalent CLLC network. The transformation equations derived in [1] will be applied here to find the CLLC equivalent circuit for the resonant tank of the IPT converter. The circuit transformation is shown in Figure 7.3.

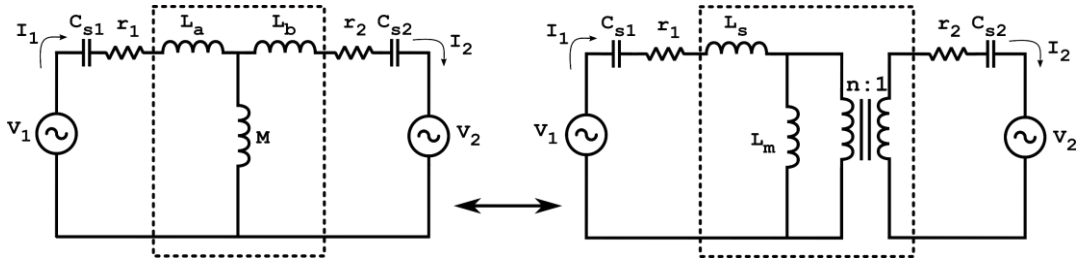


Figure 7.3: Equivalency between series compensated IPT converter and CLLC converter

Given $L_a = L_1 - M$ and $L_b = L_1 - M$, with M defined in (7.1), the inductances L_s , L_m and transformer turns ratio n for the equivalent CLLC circuit are calculated using the following equations:

$$L_s = \frac{(L_a + M)(L_b + M) - M^2}{(L_b + M)}$$

$$L_m = \frac{M^2}{(L_b + M)}$$

$$n = \frac{M}{(L_b + M)}$$

(7.9)

Once the equivalent CLLC converter is defined, the state-variable and cyclic-averaging models obtained in Chapter 5 for phase-shift modulated converters are

applied to describe the behaviour of the IPT converter. At simulation stage, the models will be used here to calculate the converter's output current, however, both state-variable and cyclic-averaging simulations can also be employed to analyse the behaviour of the primary and secondary currents and voltages across the primary and secondary capacitors, since the primary and secondary currents (I_1 and I_2) in the IPT resonant tank and CLLC resonant tank are equal.

The simulation results for the FMA, state-variable and cyclic-averaging models are discussed in the next section.

7.4 Simulation results

In this section, the FMA model defined in section 7.2 will be used to design a low power IPT converter, with 110W output power. Afterwards, the accuracy of the FMA method will be verified using a Spice simulation. Following the FMA analysis, the state-variable and cyclic-averaging models will be applied to a CLLC equivalent circuit of the IPT converter. For model verification, the results will be compared to a Spice simulation of the IPT converter and a simulation of the CLLC equivalent circuit.

7.4.1 Converter design based on FMA model

As discussed in the previous chapters, the FMA method is often used in the design process due to its simple and fast analysis. The design process here performed consists of the following steps:

1. Definition of circuit parameters as battery voltage, DC bus voltage and operating frequency;
2. Definition of coupling coefficient range and desired output power;
3. To simplify analysis and construction, the primary and secondary inductances are assumed to have the same value ($L_1 = L_2$).
4. The power equation (7.8) is used to calculate the value of inductances necessary to obtain the desired output power under maximum modulation condition;

5. The equation for resonance condition (7.2) is used to calculate the values of the compensation capacitors C_1 and C_2 ;

Here, the converter is designed considering the same operating frequency and voltage specification adopted for the verification of the CLLC converter in Chapters 5 and 6. Based on literature analysis and the previous work performed on loosely coupled transformers in [2], the design value of 0.3 was chosen for the coupling coefficient. The parameters used for the design process, as the inductors and capacitors calculated in steps 4 and 5, are listed in Table 7.1.

Table 7.1: Design parameters

Parameter	Value
P_{out}	110 W
V_{dc}	48 V
V_{bat}	12 V
f	100 kHz
k	0.3
L_1, L_2	21 μ H
C_{s1}, C_{s2}	120 nF

For the FMA simulations all resistances are neglected. The Spice, state-variable and cyclic-averaging simulations are conducted under nearly ideal conditions and the only resistances considered are the input and output resistances associated with the voltage sources ($r_{bat} = r_{dc} = 0.01 \Omega$) and series resistances of primary and secondary inductors ($r_1 = r_2 = 0.03 \Omega$).

7.4.2 Verification of FMA model

In the previous section the converter was designed to operate with coupling coefficient of 0.3 and primary and secondary self-inductances ($L = L_1 = L_2$) equal to 21 μ H in order to obtain output power close to 110W. Now the FMA model is used to estimate how the output power, primary and secondary currents behave with variations in the coupling coefficient and self-inductance. The results obtained will also be compared to a Spice simulation to verify the accuracy of the FMA model.

Figure 7.4 shows the primary current results obtained with the Spice and FMA models considering forward operation and maximum modulation. In Figure 7.4-a, the self-inductance of primary and secondary coils is kept constant at $21\mu H$ while the coupling coefficient varies in a range from 0.05 to 0.6, in steps of 0.05. In Figure 7.4-b, to analyse the effect of variations in the inductance value, the results were obtained maintaining the coupling coefficient constant at 0.3 and inductance values from $10\mu H$ to $50\mu H$ were tested in steps of $5\mu H$. For the results shown in Figure 7.4-b, the capacitances are changed according to the values of inductances tested to maintain the resonant frequency constant.

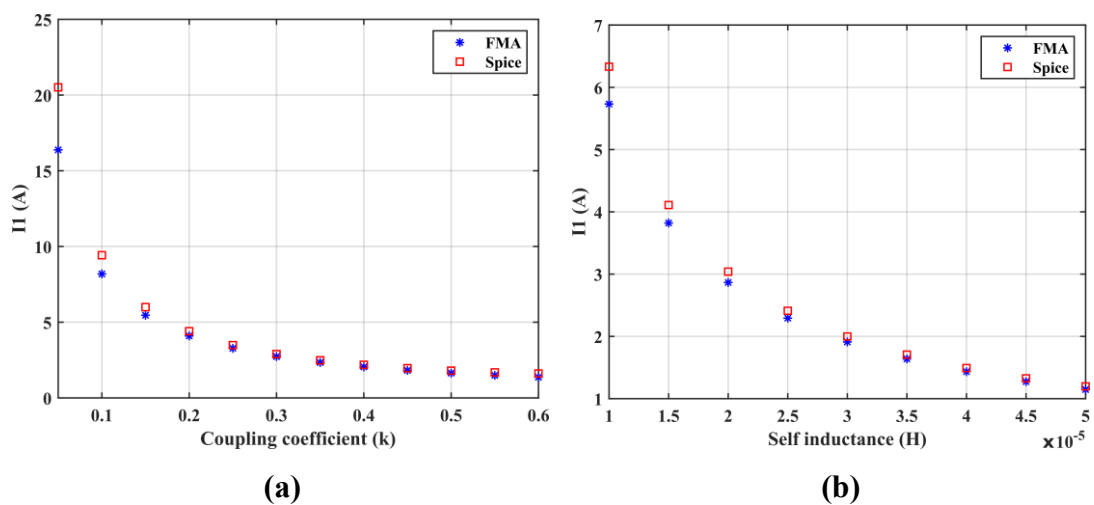


Figure 7.4: Spice and FMA results for RMS value of primary current in function of (a) coupling coefficient and (b) self-inductance

From the results analysis it is observed that, as the values of coupling coefficient and self-inductance increase, the magnitude of the primary current decreases, confirming the previous analysis of series compensated IPT converters performed in [3], [4]. Additionally, the error between Spice and FMA results is higher for lower values of coupling coefficient and inductance. However, when the coupling coefficient and self-inductance start to increase, the difference between the models reduces and results become very close. As stated in the previous section, the Spice model is simulated considering low values of circuit resistances, while in FMA these resistances are completely neglected. Therefore, the errors may be due to the fundamental approximation in the FMA model and to the increased resistances considered in the Spice model.

To identify the main source of error in the lower range of coupling coefficients and self-inductances, the Spice simulation is performed again reducing the values of resistances to get closer to an ideal circuit, r_{bat} and r_{dc} are reduced from 0.01 to 0.001 and r_1 and r_2 are reduced from 0.03 to 0.0003. Results are obtained for the first point of each graph ($k = 0.05$ in Figure 7.4-a and $L = 10 \mu H$ in Figure 7.4-b), where the error is the highest. Additionally, the fundamental component of the primary current is also measured in the Spice simulation to verify the contribution of the remaining harmonics. The results obtained are presented in Table 7.2.

Table 7.2: Comparison between Spice and FMA models for primary current (I_1)

Test case	Current measurement	RMS Value (A)	
		Low resistances	Nearly zero resistances
Case A (Figure 7.4-a) $k = 0.05$ and $L = 21 \mu H$	Spice: I_1	20.509	22.659
	Spice: I_1 - fundamental	20.512	16.370
	FMA: I_1	-	16.330
Case B (Figure 7.4-b) $k = 0.3$ and $L = 10 \mu H$	Spice: I_1	6.331	6.096
	Spice: I_1 - fundamental	6.244	5.790
	FMA: I_1	-	5.732

After analysing the data in Table 7.2 it is possible to conclude that when using low resistances the RMS value of the primary current is very close to the magnitude of the fundamental component. Once the circuit resistances were reduced to nearly zero, the difference between the magnitude of the primary current and its fundamental component significantly increases, indicating that other harmonics have higher contribution to the current waveform. Note that the value of the fundamental component in Spice when the resistances are closer to zero is now very close to the FMA result. Therefore, it is confirmed that the errors observed in Figure 7.4 are due to not only the increased resistances in the Spice model, but also to the lack of accuracy of the fundamental approximation to represent the primary current when the circuit resistances are very close to zero. This behaviour, however, was only significantly observed in the lower range of coupling coefficients and self-inductances analysed.

Following the analysis of the primary current, the Spice and FMA results for the secondary current are shown in Figure 7.5. In this case, FMA model shows good accuracy for the full range of coupling coefficients and inductances analysed.

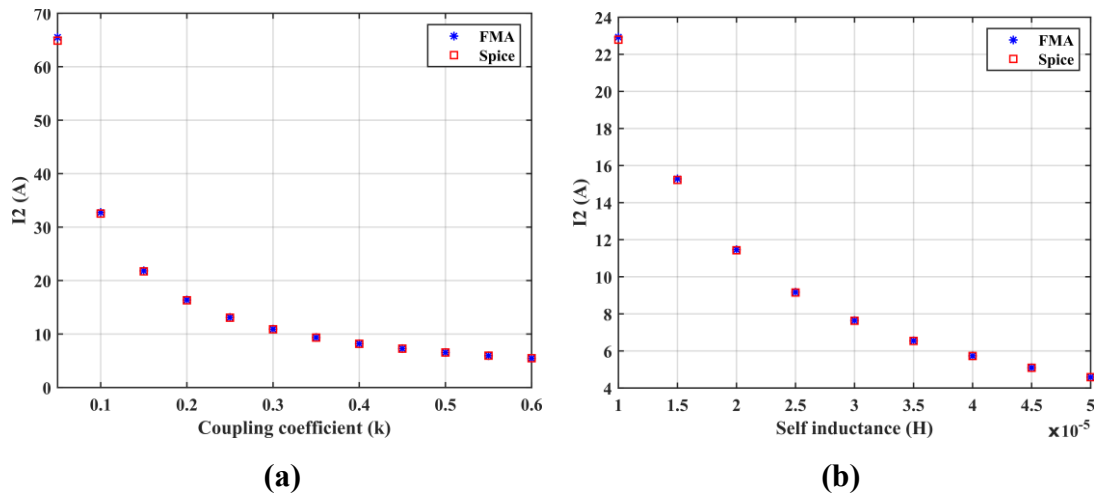


Figure 7.5: Spice and FMA results for secondary current in function of (a) coupling coefficient and (b) self-inductance

A similar investigation previously performed for the primary current is repeated to the secondary current. The results obtained are presented in Table 7.3. The secondary current waveform is always close to a perfect sine wave, therefore, the difference between the current values for Spice simulation with low resistance and FMA is reduced.

Table 7.3: Comparison between Spice and FMA models for current I_2

Test case	Current measurement	RMS Value (A)	
		Low resistances considered	Circuit resistances nearly zero
Case A (Figure 7.4-a) $k = 0.05$ and $L = 21\mu H$	Spice: I_2	64.184	67.218
	Spice: I_2 - fundamental	64.195	65.313
	FMA: I_2	-	65.335
Case B (Figure 7.4-b) $k = 0.3$ and $L = 10\mu H$	Spice: I_2	22.789	22.986
	Spice: I_2 - fundamental	22.777	22.935
	FMA: I_2	-	22.926

The results for output power are shown in Figure 7.6. Contrary to the parallel or LCL compensation topologies, for the series compensated converter ideal behaviour, an increase in the output power is observed as the coupling coefficient decreases, confirming the previous analysis found in the literature [3], [5]. For a practical converter, however, experimental results show that the power increases with the reduction of coupling coefficient until a certain point, but as the coupling furtherly decreases the output power starts to significantly drop, as discussed in [5].

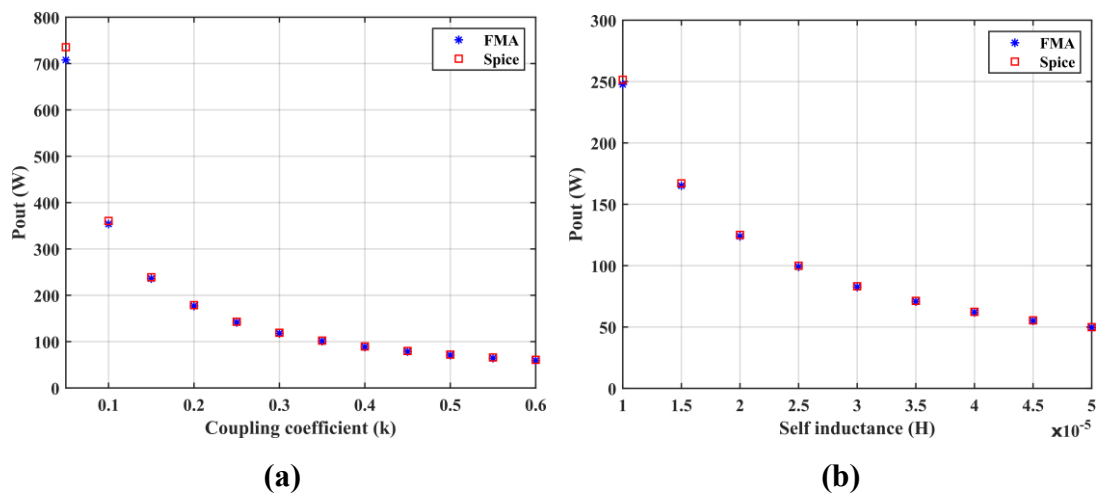


Figure 7.6: Spice and FMA results for output power in function of (a) coupling coefficient and (b) self-inductance

7.4.3 Verification of state-variable and cyclic-averaging method

As discussed in section 7.3, for the application of state-variable and cyclic-averaging models, a CLLC equivalent circuit is derived from the IPT converter. Therefore, results will be verified against two Spice simulations, the first model represents the series compensated IPT converter (Figure 7.7-a) and a second simulation is performed considering the equivalent CLLC circuit (Figure 7.7-b).

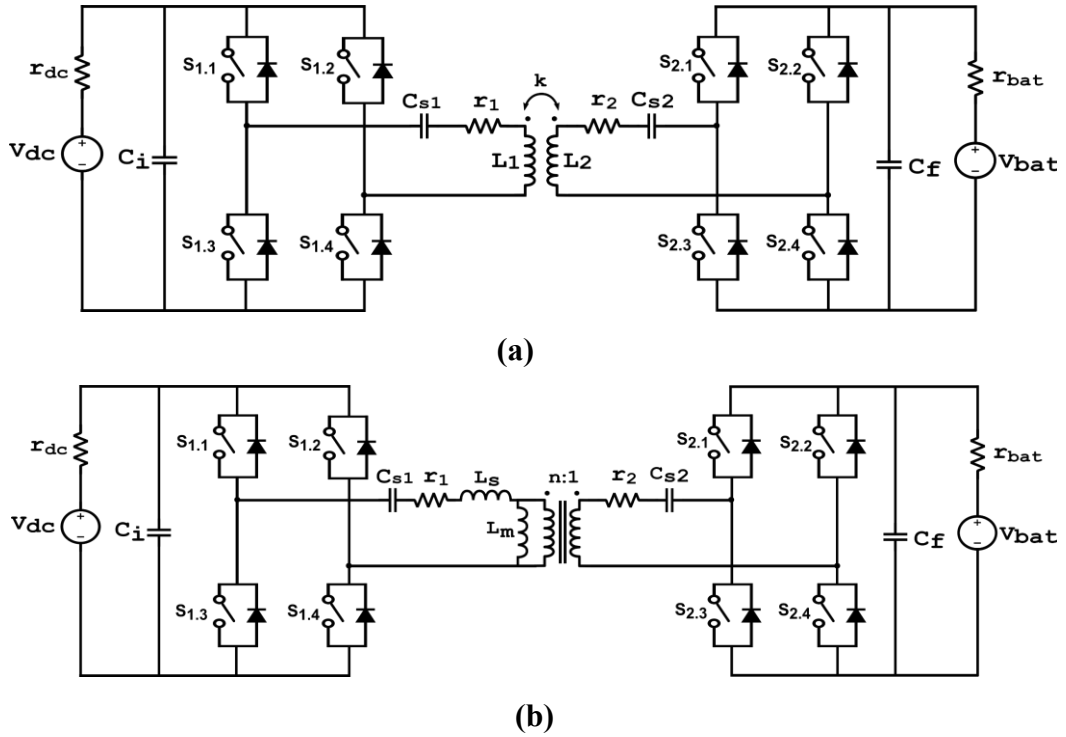


Figure 7.7: Equivalent circuits for Spice simulation (a) series compensated IPT converter and (b) CLLC equivalent circuit

The Spice simulation of the IPT converter is performed considering the circuit parameters from Table 7.1, obtained at the end of the design stage described in section 7.4.1. Substituting the IPT converter parameters in equation (7.9), the parameters for the CLLC equivalent circuit are calculated and listed in Table 7.4. The simulations are performed considering nearly ideal conditions, using ideal switches and low values of resonant tank resistances.

Table 7.4: Simulation parameters for IPT and CLLC-equivalent converters

Parameter	Value
C_{s1}, C_{s2}	120 nF
L_s	19.11 μH
L_m	1.89 μH
n	0.3
r_1, r_2	0.03 Ω
r_{bat}, r_{dc}	0.01 Ω

The results obtained for SPS and PPM modulation are shown in Figures 7.8 and 7.9, respectively.

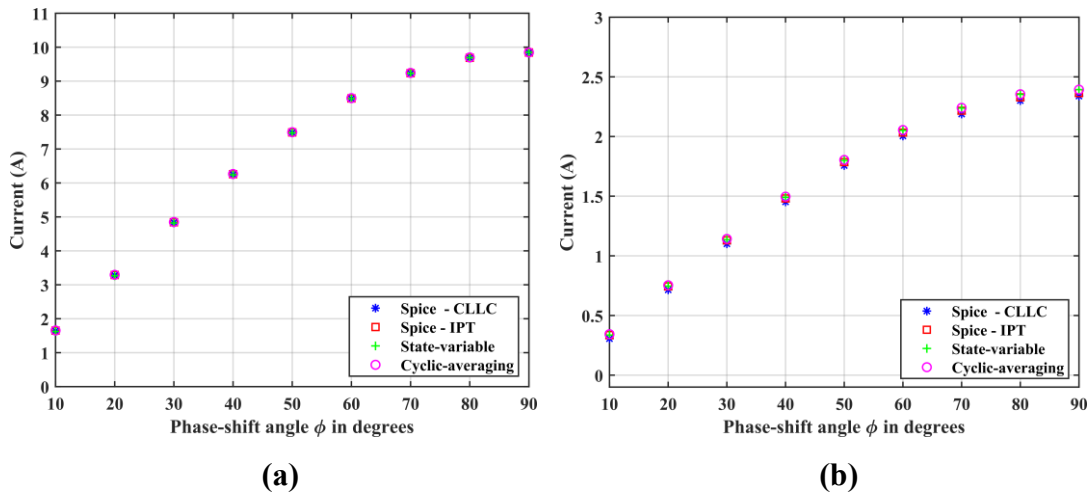


Figure 7.8: Model comparison SPS modulation (a) forward operation and (b) reverse operation

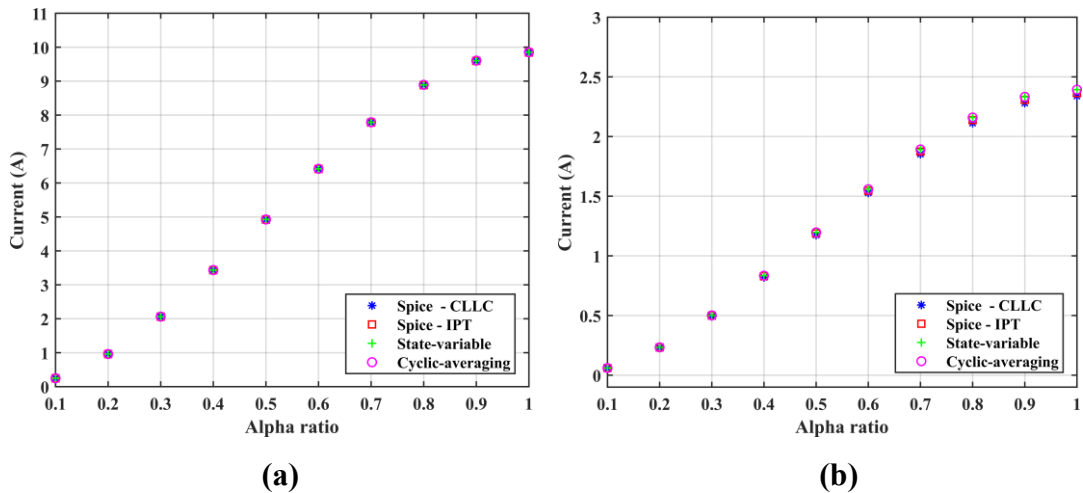


Figure 7.9: Model comparison PPM modulation (a) forward operation and (b) reverse operation

From results analysis it is possible to observe that the transformation of the IPT converter into a CLLC equivalent converter was accurate, where, between the two Spice simulations performed, the maximum difference in the output current was in the order of 30 mA. Furthermore, both state-variable and cyclic-averaging simulations could accurately model the behaviour of the converter's output current. The maximum error between the cyclic-averaging and the Spice simulation of the IPT converter is 2.23%, between state-variable and Spice, the maximum error is slightly lower, at 1.61%.

7.5 Magnetics design of coil pad structures

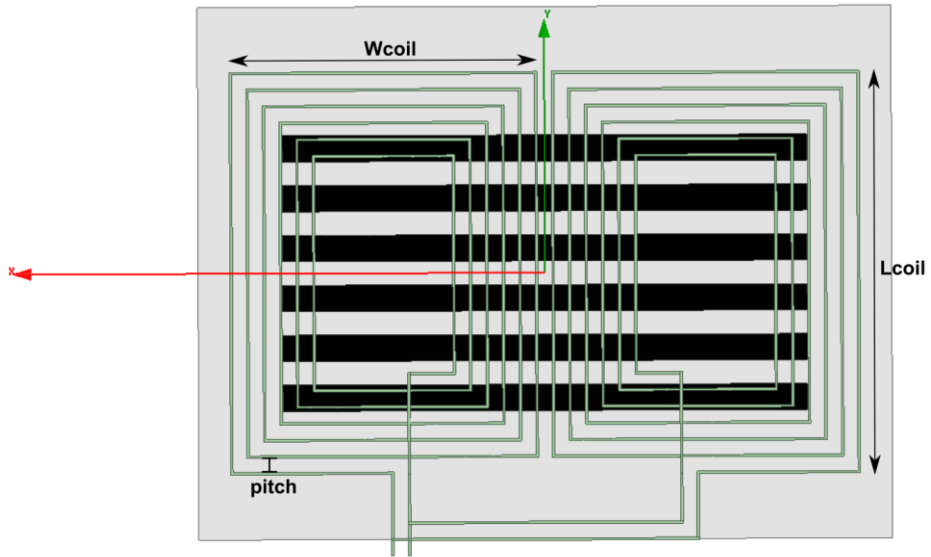
After the simulation analysis, a prototype is built for further verification of the cyclic-averaging and Spice models. The first step in the prototype construction process is the magnetic design of the primary and secondary coil pad structures. This design is performed using Ansys Maxwell, a simulation software that uses finite element analysis (FEA) to solve the electromagnetic field.

Based on the literature review conducted in Chapter 2, the Double D coil topology was chosen due to its simplicity and reduced sensitivity to misalignment compared to circular coils. The 3D model of the structures simulated in Ansys Maxwell is shown in Figure 7.10. The pad structure is shown in Figure 7.10-a and it is composed by two coils connected in parallel and mounted in an aluminium base. Rows of ferrite I cores (Figure 7.10-a, in black) with dimensions of 93x28x16 mm are used below the coil to increase the transferred power and direct the magnetic flux [6], [7].

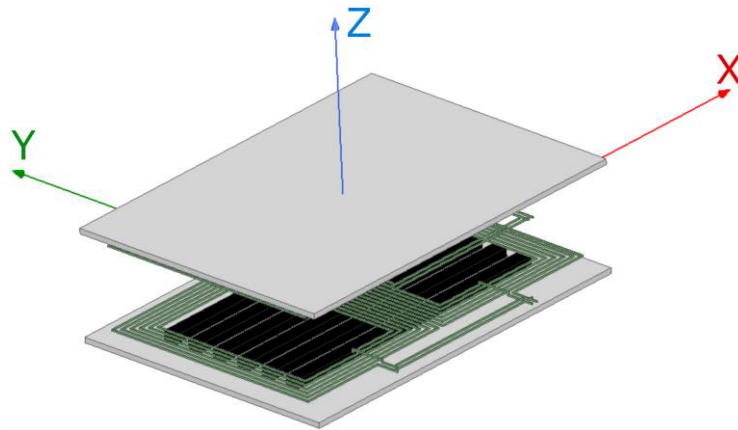
Each coil has 6 turns and uses a 2.6 mm diameter litz wire (Figure 7.10-a, in green), therefore, in the current excitation settings the option of stranded wire was chosen for the conductor type. The aluminium plate (Figure 7.10-a, in grey) is used as an electromagnetic shield and it also serves as support for the coil and ferrite bars. The aluminium shield is effective reducing leakage magnetic fields, however, the electrical performance will be affected since circulating eddy currents will be induced in the aluminium plate. The negative effects of the metallic shielding are minimized when using a ferrite layer between the coil and shield, with a metal shield thickness superior to the skin depth [8].

Following the SAE standard J2954 [9], the primary and secondary pads are designed to operate separated by a distance of 150 mm (Figure 7.10-b), this corresponds to a Z2 class, where the vertical distance between ground surface and the furthest coil is between 140 and 210 mm. The axis orientation for the 3D model implemented is shown in Figure 7.10-b.

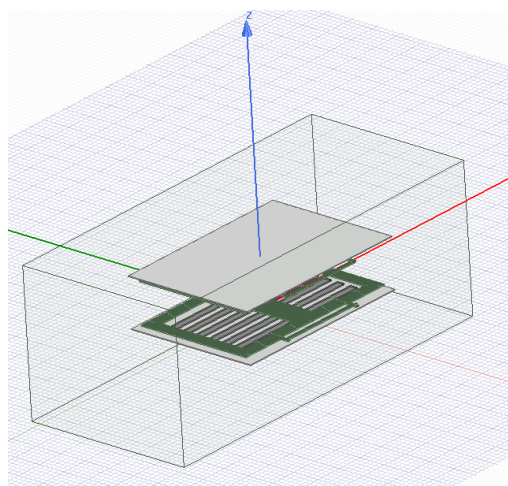
In Fig 7-c the region of simulation surrounding the coil pad structures is shown. The material of the region is set to air and the size of the region must be large enough to not impact the calculation of the electromagnetic fields near the structures implemented, here, accurate results were obtained using a region with volume around seven times the volume of the coil pad structures separated by 150mm air gap.



(a)



(b)



(c)

Figure 7.10: 3D model of double D coil (a) top view of coil pad (b) primary and secondary coil pads (c) coil pads + region

Once the 3D finite element model is implemented in Ansys Maxwell, the FEA analysis is employed to calculate the coupling coefficient and self-inductances using the eddy current solver, which gives a steady state solution for AC magnetic fields at the operating frequency of 100kHz. A sinusoidal current with peak value of 7A and 100kHz is assigned as excitation for each coil. Contrary to the magnetostatic solver, the operation frequency and skin effect are taken into consideration when using the eddy current solver. The solver also uses adaptive mesh refinement, where the mesh is automatically refined at each pass. Over-defining mesh can lead to long execution times without significant improvement of accuracy, therefore, accurate solutions can be obtained with adaptive mesh with faster execution. Here, two types of tests were performed, first using adaptive mesh and, secondly, manually defining the mesh. The solution using adaptive mesh showed good accuracy and improved execution time, therefore, this technique was chosen for the simulations presented in this section. The final mesh plot in the ZX plane obtained after the adaptive mesh refinement is shown in Figure 7.11. It is possible to observe how the mesh size is optimized along the region, where finer mesh is attributed to smaller elements and in the areas closer to the pad structures.

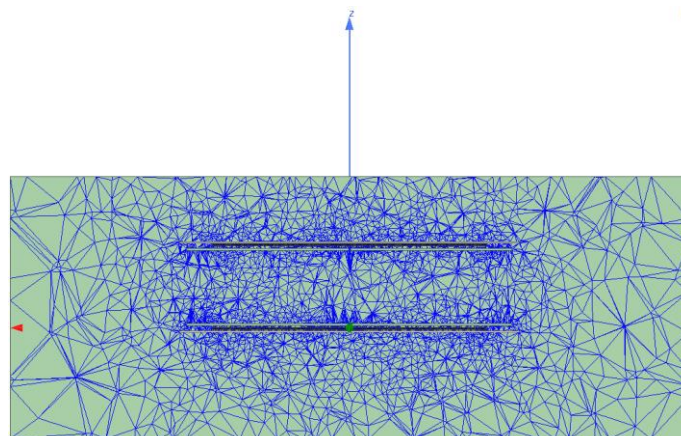


Figure 7.11: Mesh plot for coil pad structures, cross section area perpendicular to Y axis

Simulation is conducted using the initial pad dimensions listed in Table 7.5. The influence of each construction parameter on the inductance and coupling coefficient values will be evaluated for an optimization process to achieve the values of inductance and coupling coefficient defined in the converter specification, 21 μH and 0.3 respectively.

Table 7.5: Initial parameters for Double D coil in the FEA simulations

Parameter	Value
Coil width (W_{coil})	300 mm
Coil length (L_{coil})	300 mm
Number of ferrite cores per row	6
Distance between rows of ferrite cores	20 mm
Pitch	10 mm

The first parameters analysed are coil length and width, as shown in Figures 7.12 and 7.13. For each parameter variation, the remaining variables are kept constant following the values in Table 7.5. From the coil length and coil width results, it is possible to observe that inductance increases almost linearly as these parameters increase. The coupling coefficient is nearly constant for coil length higher than 375 mm and for coil width in a range of 275 to 375 mm. To maximize the coupling coefficient and increase the inductance, the values of 425 mm and 325 mm are chosen for coil length and coil width respectively.

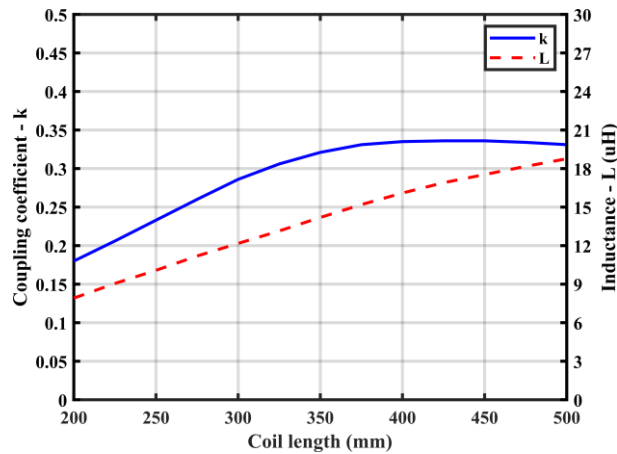


Figure 7.12: Coupling coefficient and self-inductance in function of coil length

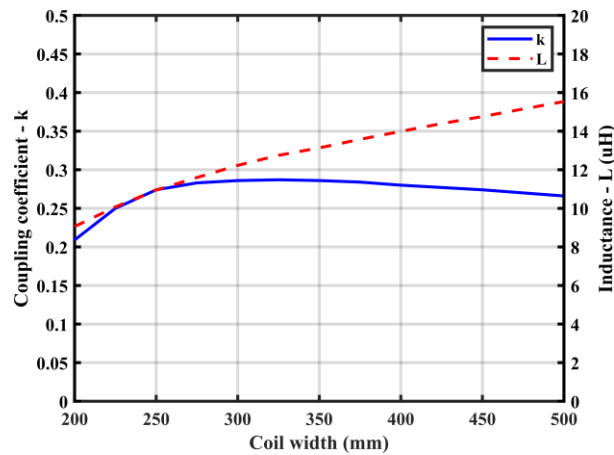


Figure 7.13: Coupling coefficient and self-inductance in function of coil width

The simulation is updated with the optimized coil dimensions and the influence of the number of ferrite cores per row and the distance between these rows is evaluated in Figures 7.14 and 7.15, respectively. The ferrite material is used in wireless power transfer applications to increase the power transfer capability and, as observed in Figure 7.14, the number of ferrite cores per row considerably affects the coupling coefficient, where the peak value is reached at 6 bars of ferrite cores per row. Therefore, this is the optimal number of bars, resulting in a total ferrite length of 558 mm per row, nearly 86% of the double D coil total width. When the total number of bars is increased to 7, the total ferrite length starts to surpass the double coil width and the coupling coefficient slightly decreases. As observed in Figure 7.15, the space between the rows of ferrite bars does not significantly influence the values of inductance and coupling coefficient, however, the peak value for both coupling coefficient and inductance occurs around 25mm, therefore, this value is preferred for the construction instead of the initial estimation of 20 mm.

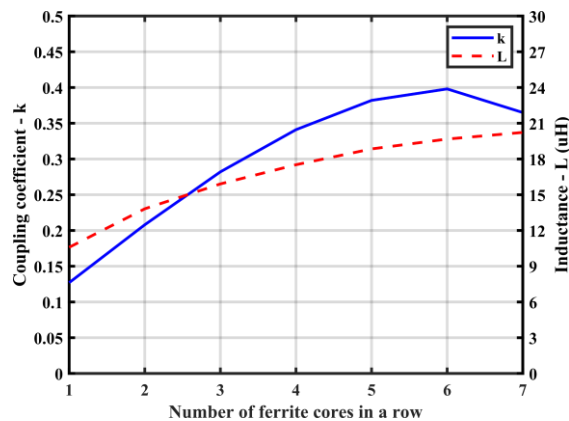


Figure 7.14: Coupling coefficient and self-inductance in function of number of ferrite cores per row

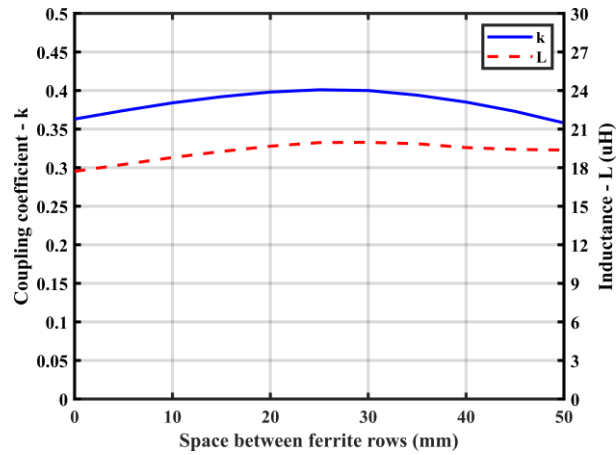


Figure 7.15: Coupling coefficient and self-inductance in function of space between rows of ferrite bars

The last parameter analysed is the pitch. As shown in Figure 7.16, the coupling coefficient is not significantly influenced by the pitch value, however, the inductance notably increases as the pitch decreases. The pitch value of 8 mm is chosen to keep the coupling coefficient close to the maximum value and achieve a value of inductance that meets the specification, resulting in pad structures with self-inductance of $21.792 \mu\text{H}$ and coupling coefficient of 0.398. Therefore, after the optimization process, the specification values of $21 \mu\text{H}$ for inductance and coupling coefficient of 0.3 are met. A comparison between the initial estimation and the optimized parameters is shown in Table 7.6.

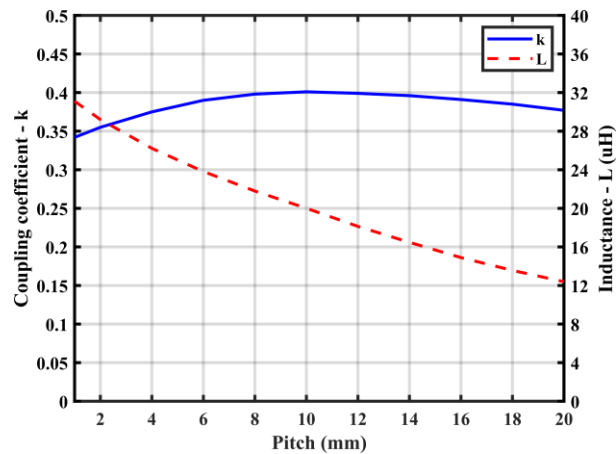


Figure 7.16: Coupling coefficient and self-inductance in function of pitch

Table 7.6: Parameters for Double D coil in the FEA simulations

Parameter	Initial value	Optimized value
Coil width (W_{coil})	300 mm	325 mm
Coil length (L_{coil})	300 mm	425 mm
Number of ferrite cores per row	6	6
Distance between rows of ferrite cores	20 mm	25 mm
Pitch	10 mm	8 mm

Another factor analysed in the magnetics design is the misalignment in the X and Y axis and influence of distance between the pads in the Z axis. Offsets in the X, Y or Z axis (Figure 7.10) do not have large influence in the inductance but the coupling coefficient is substantially affected.

First, the results for an offset in the X axis (Figure 7.17) are presented in Figure 7.18. It is possible to observe that, for an offset higher than approximately 80 mm, the coupling coefficient steeply drops. As previously discussed in Chapter 2 during the literature review, the Double D coil has improved performance for misalignment in the Y axis. To improve the behaviour of the coupling coefficient for misalignments in the X axis, Double D Quadrature or Bipolar coils should be used.

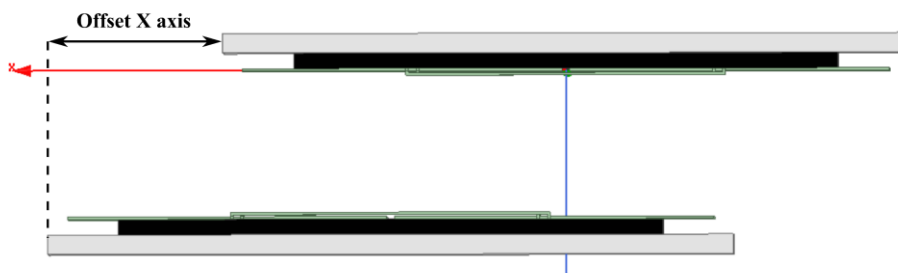


Figure 7.17: Implementation of offset in the X axis

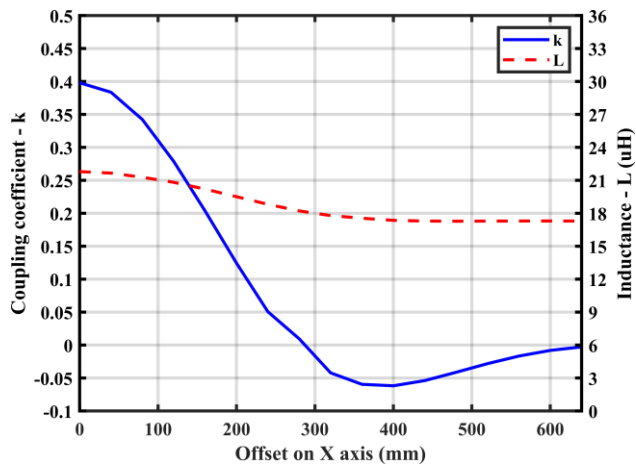


Figure 7.18: Coupling coefficient in function of distance between pads in the X axis

An offset in the Y axis (Figure 7.19) also influences the coupling coefficient, as shown in Figure 7.20, but not as significantly as in the X axis. For an offset of 200 mm in the Y axis, the coupling coefficient drops from 0.398 to 0.272. The same offset in the X axis causes a drop in the coupling coefficient from 0.398 to 0.124.

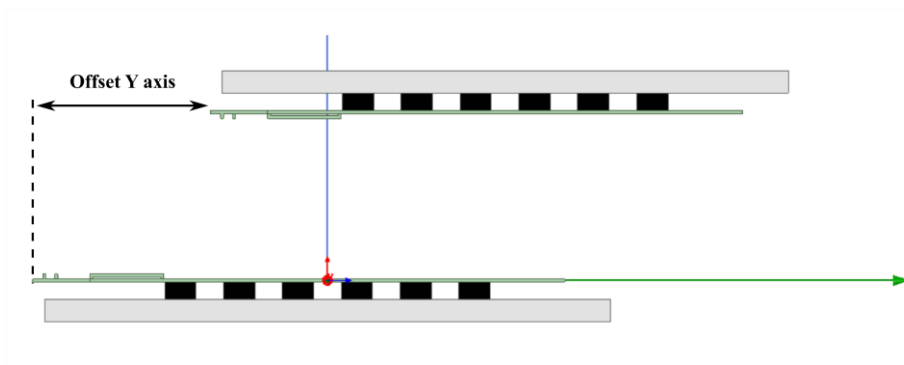


Figure 7.19: Implementation of offset in the Y axis

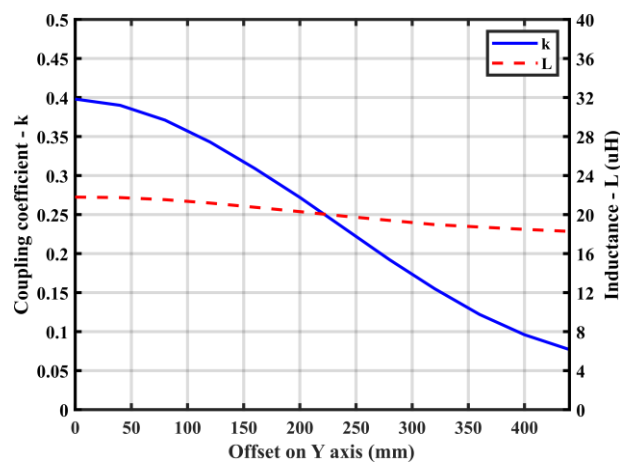


Figure 7.20: Coupling coefficient in function of distance between pads in the Y axis

The converter is designed to operate at a fixed distance of 150 mm between the primary and secondary coil pads. The influence of a variation of this distance (Figure 7.21) is shown in Figure 7.22. As expected, the coupling coefficient is increased when reducing the distance between the primary and secondary pads and, as this distance increases, the coupling coefficient decreases.

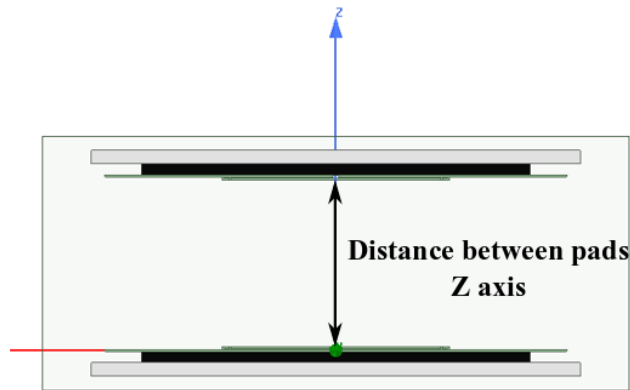


Figure 7.21: Implementation of offset in the Z axis

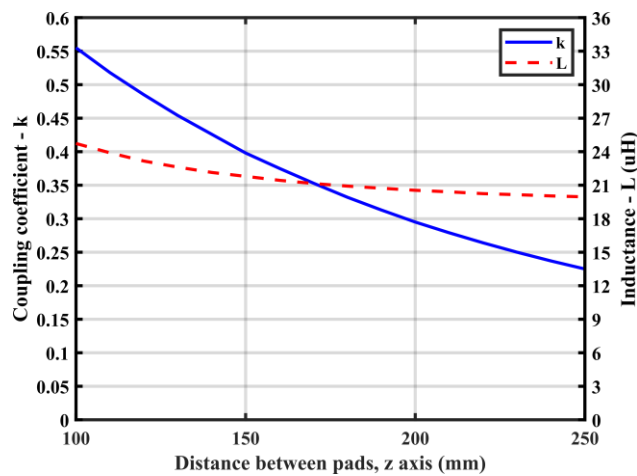


Figure 7.22: Coupling coefficient in function of distance between pads in the Z axis

When analysing the occurrence of misalignments, the behaviour of the coupling coefficient and inductance observed in the FEA simulation in this section is very similar to the results previously published in the literature.

In the construction process, due to market availability and price, ferrite plates with dimensions 43x28x4.1 mm and 3C95 material were used instead of the I93x28x16 cores used in the previous simulations. Since the new ferrite plates have reduced length compared to the I core, a higher number of cores per row (13 cores) is necessary to

obtain a length closest to the equivalent of using 6 I cores (558mm). Furthermore, due to availability in the university lab, the litz wire used in the construction stage has diameter of 4 mm (with strands of 0.4 mm). Consequently, the 3D FEA model was readjusted for the new dimensions of the ferrite core and wire.

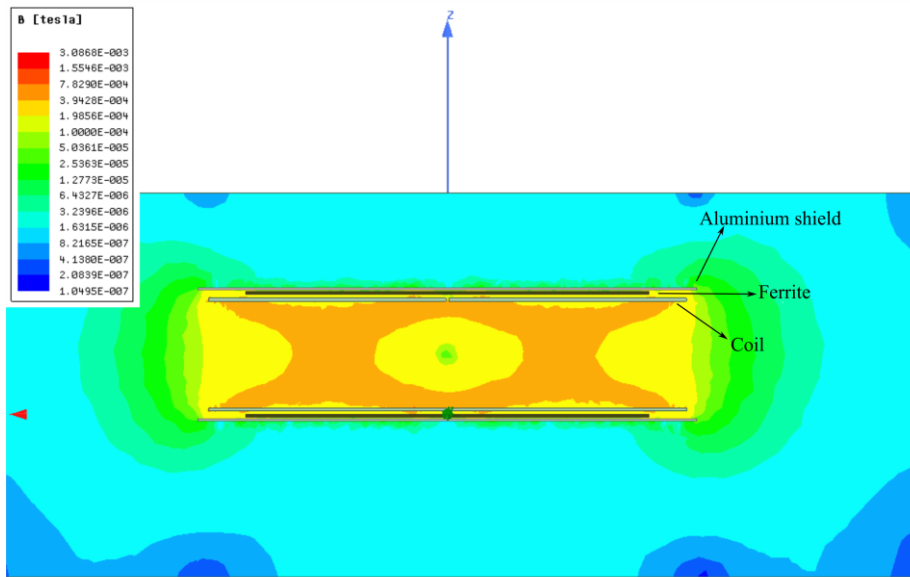
The updated simulation also includes additional construction parameters that were not previously considered, as the thickness of a 1mm polycarbonate (PC) sheet that serves as a holding structure for the coil and the thickness of tape used to attach the ferrite cores and coil to the PC sheet.

The pitch value was readjusted to 4mm in order to maintain the inductance close to 21 μ H, resulting in an inductance of 21.49 μ H and coupling coefficient of $k = 0.366$ in the final simulation. The updated construction parameters are shown in Table 7.7. In case the values of inductance or coupling coefficient are too distant from the desired values (inductance of 21 μ H and coupling coefficient of 0.3) during experimental verification, an extra layer of ferrite plates could be added increasing the thickness of the rows of ferrite bars or the pitch could be readjusted in order to get values closer to the specification.

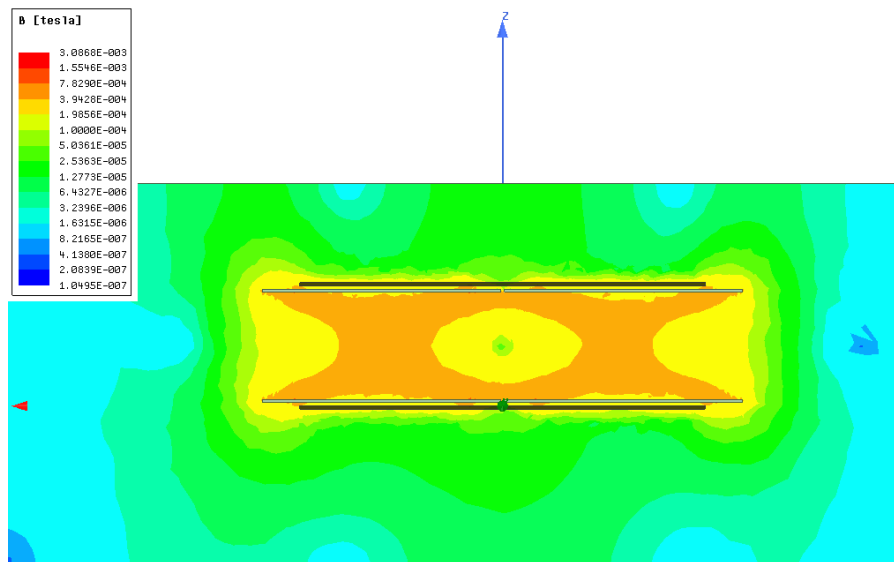
Table 7.7: Parameters used in Double D coil construction

Parameter	Value
Coil width (W_{coil})	325 mm
Coil length (L_{coil})	425 mm
Number of ferrite cores per row	13
Distance between rows of ferrite cores	25 mm
Pitch	4 mm

From the updated FEA simulation, the magnetic flux density distribution is analysed along the XZ plane as shown in Figure 7.23. The results for the updated model based on the construction parameters is shown in Figure 7.23-a, while in Figure 7.23-b the aluminium shield is removed from the model to verify its influence. It is possible to observe that the aluminium shield is effective suppressing the leakage magnetic field, since the flux density is significantly reduced in the areas below and above the inferior and superior shields, respectively.



(a)



(b)

Figure 7.23: Flux density distribution in the cross-section area perpendicular to Y axis (a) with aluminium shield (b) no aluminium shield placed

The current density distribution for the coils and aluminium shields in a cross-section area in the XZ plane is shown in Figure 7.24, where it is verified the presence induced currents in the aluminium shields (in green/yellow). Despite the eddy current occurrence in the shield structures, the metal shield is a simple and popular solution that still results in good performance when used in conjunction with a ferrite layer.

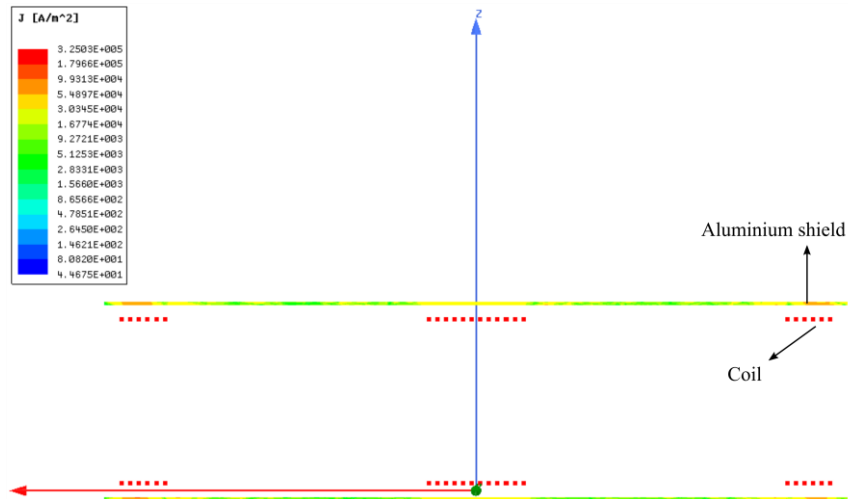


Figure 7.24: Current density distribution for primary and secondary coils and aluminium shields

The pad structures built will be further analysed in the next section, where the experimental results obtained for inductance and coupling coefficient will be compared to the FEA simulation.

7.6 Experimental results

In this section, results obtained with the built Double D coil pads will be compared to the FEA simulation. Once the coil structures are validated, they are connected to the compensation capacitors, H-bridges and switching circuit to test the IPT converter. The switching circuit and PCB containing the deadtime circuit, gate driver and H-bridges used for the implementation of the IPT converter in this chapter are the same as the circuits used for the CLLC converter, previously described in Chapter 6. At the end of this section the IPT converter prototype performance will be evaluated and experimental and simulation results will be compared.

7.6.1 Construction of coil pad structures

After the FEA simulations performed in section 7.5 for the magnetics design, the construction and experimental verification of the coil pad structures are evaluated in this section. The primary coil pad structure built is shown in Figure 7.25. The secondary pad is built with the same dimensions as the primary.

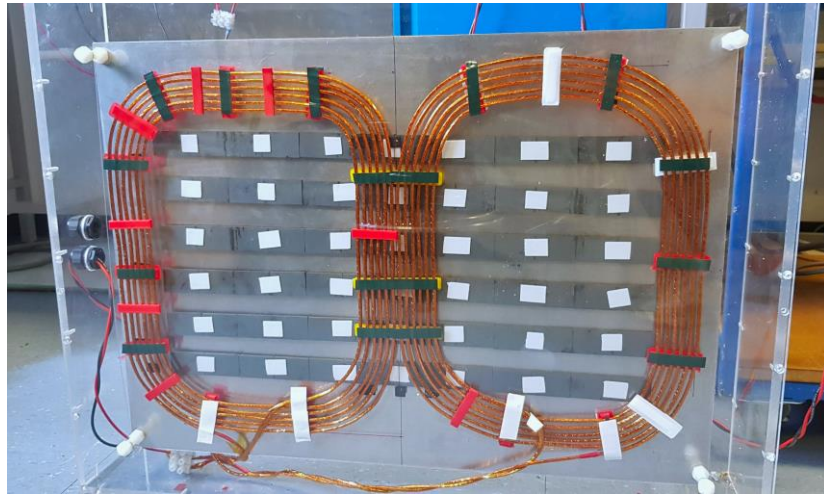


Figure 7.25: Coil pad structure

To maintain a fixed distance of 4 mm between each coil turn, the structure shown in Figure 7.26 was built using a 3D printer.

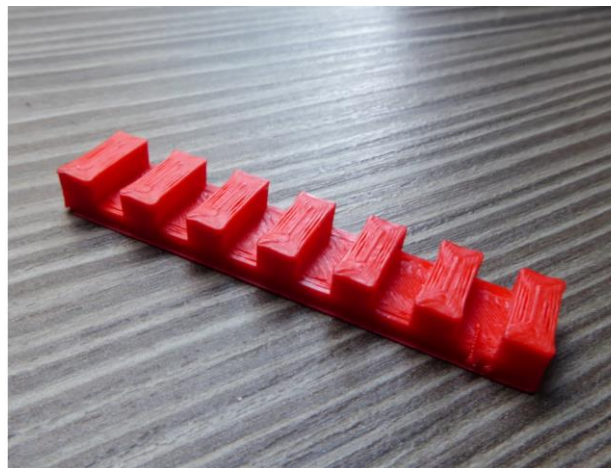


Figure 7.26: 3D printed structure to implement 4mm pitch

Before the coil pads are connected to the switching circuit, compensating capacitors and load for experimental verification of the converter, the coupling coefficient and primary and secondary inductances are measured to check if the coil pads parameters are close to the design values.

First, the self-inductance is measured using the Bode 100. The distance between the pads has a slight influence in the measured self-inductance as consequence of the proximity to the metal and magnetic material of the opposite pad. When the inductance is measured with primary and secondary pads considerably distant from each other, the value of inductance for the primary pad is 17.748 μH and for the secondary is 18.251

μH . Placing the primary and secondary pads at the position the system is designed to operate, separated by 150mm, the primary and secondary inductances raise to 18.462 μH and 18.952 μH respectively, resulting in a increase of nearly 0.7 μH .

For measurement of the coupling coefficient, three methods will be used and compared. The first and simplest method consists of measurement of the secondary-primary voltage ratio using the gain measurement in the Bode 100. The implementation of this technique was based on a Bode 100 article [10], where the equipment set-up information and derivation of the coupling factor equation are described. A typical gain curve measured with the Bode 100 is shown in Figure 7.27 and the following steps are undertaken for definition of the coupling coefficient using this method:

1. Placement of the coil pads at specified distance;
2. Measurement of self-inductances L_1 and L_2 ;
3. Measurement of gain magnitude for operating frequency (100kHz);
4. Use (7.10) to calculate the coupling coefficient k .

$$gain = \frac{V_2}{V_1} \approx k \sqrt{\frac{L_2}{L_1}}$$

(7.10)

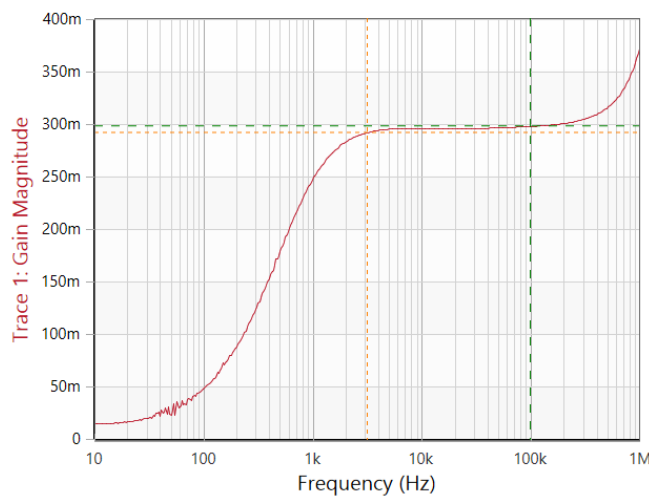


Figure 7.27: Gain curve measured with Bode 100

The second technique employed for measurement of coupling factor is the series-aiding series-opposing method, previously described in [11], [12]. The following methodology is used for the coupling coefficient calculation.

1. Placement of the coil pads at specified distance;
2. Measurement of self-inductances L_1 and L_2 ;
3. Inductance (L_{aid}) is measured when primary and secondary windings are connected in a series-aiding configuration, as in Figure 7.28-a;
4. Inductance (L_{op}) is measured when primary and secondary windings are connected in a series-opposing configuration, as in Figure 7.28-b;
5. Mutual inductance and coupling coefficient are calculated according to equation (7.11).

$$L_{aid} = L_1 + L_2 + 2M$$

$$L_{op} = L_1 + L_2 - 2M$$

$$M = \frac{L_{aid} - L_{op}}{4}$$

$$k = \frac{M}{\sqrt{L_1 L_2}}$$

(7.11)



Figure 7.28: Inductance measurement in (a) series-aiding and (b) series-opposing configurations

The third and last method is the short and open circuit technique, previously analysed in [11], [12]. The coupling coefficient is calculated taking the following steps.

1. Placement of the coil pads at specified distance;

2. Measurement of open circuit inductances in the primary (L_1) and secondary (L_2) sides;
3. Inductance of primary coil is measured when secondary coil is shorted (L_{short});
4. The coupling coefficient is calculated from (7.12).

$$k = \sqrt{1 - \frac{L_{short}}{L_1}} \quad (7.12)$$

Considering the pads separated by 150mm, the coupling coefficient values measured using each method are shown in Table 7.8. The average coupling coefficient value obtained is 0.296, very close to the design value of 0.3. Furthermore, the inductance values measured when pads are placed at 150 mm distance (18.462 μ H and 18.952 μ H) are also close to the design value of 21 μ H. Therefore, no further modifications were made to the prototype in order to improve the inductance or coupling coefficient values.

Table 7.8: Coupling coefficient when primary and secondary pads are separated by 150 mm

Method	Coupling coefficient
1. Gain method	0.2959
2. Series method	0.2938
3. Open/short circuit method	0.2988
Average	0.2962

Following the measurements for the standard, aligned placement of the pads, the influence of misalignment on the coupling coefficient is analysed. Experimental results considering the three measurement methods previously described are shown in Figure 7.29 for misalignment in the X axis, in Figure 7.30 for misalignment in the Y axis and in Figure 7.31 for the Z axis influence.

The open/short circuit method is the only measurement technique that gives only the absolute value of the coupling coefficient. Therefore, to facilitate the comparison

between the methods in Figure 7.29, the results for the open/short circuit method are plotted incorporating the sign information acquired with the gain and series methods.

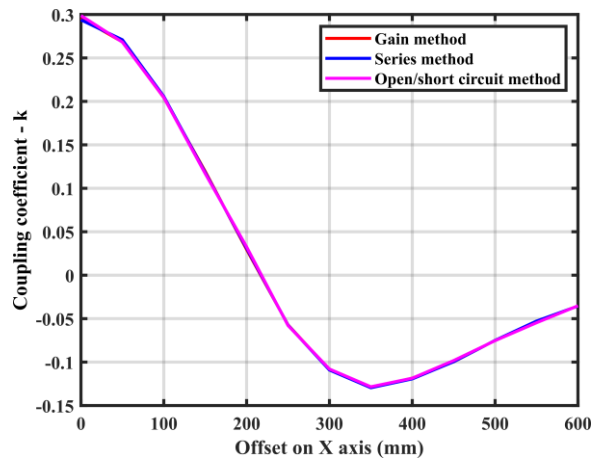


Figure 7.29: Experimental measurement of coupling coefficient in function of misalignment in the X axis

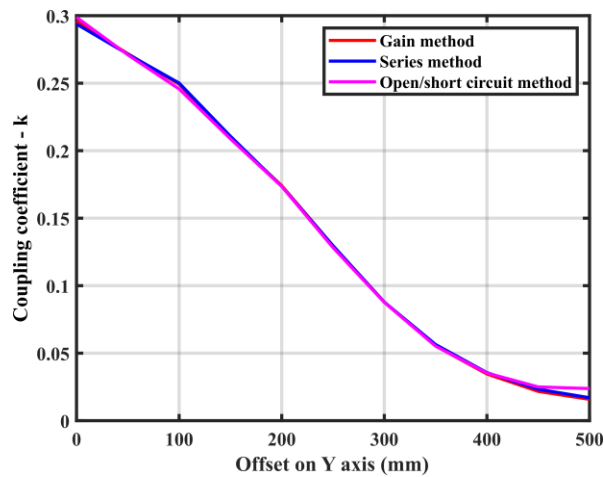


Figure 7.30: Experimental measurement of coupling coefficient in function of misalignment in the Y axis

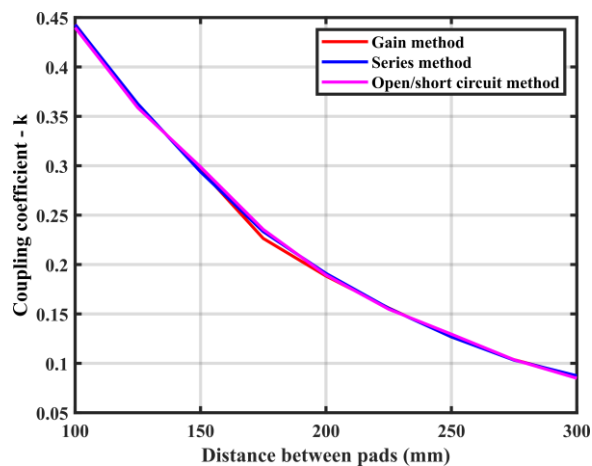


Figure 7.31: Experimental measurement of coupling coefficient in function of distance between pads in the Z axis

Analysing the misalignment graphs it is possible to conclude that results are very close between the three methods. Also, the behaviour of the coupling coefficient when subject to misalignment was similar to what was observed in the FEA simulations conducted in section 7.5.

From the experimental results obtained with the three methods, an average value of coupling coefficient was calculated and compared to results obtained in the updated FEA simulation, as shown in Figure 7.32. The data for each test point is presented in Tables 7.9, 7.10 and 7.11.

For the designed operation point, with no misalignment and distance of 150mm between pads, the difference between simulation (0.366) and experimental results (0.296) for coupling coefficient is 0.07. An average absolute difference of 0.078 is observed for Z axis measurements, 0.067 for Y axis and 0.080 for X axis misalignment.

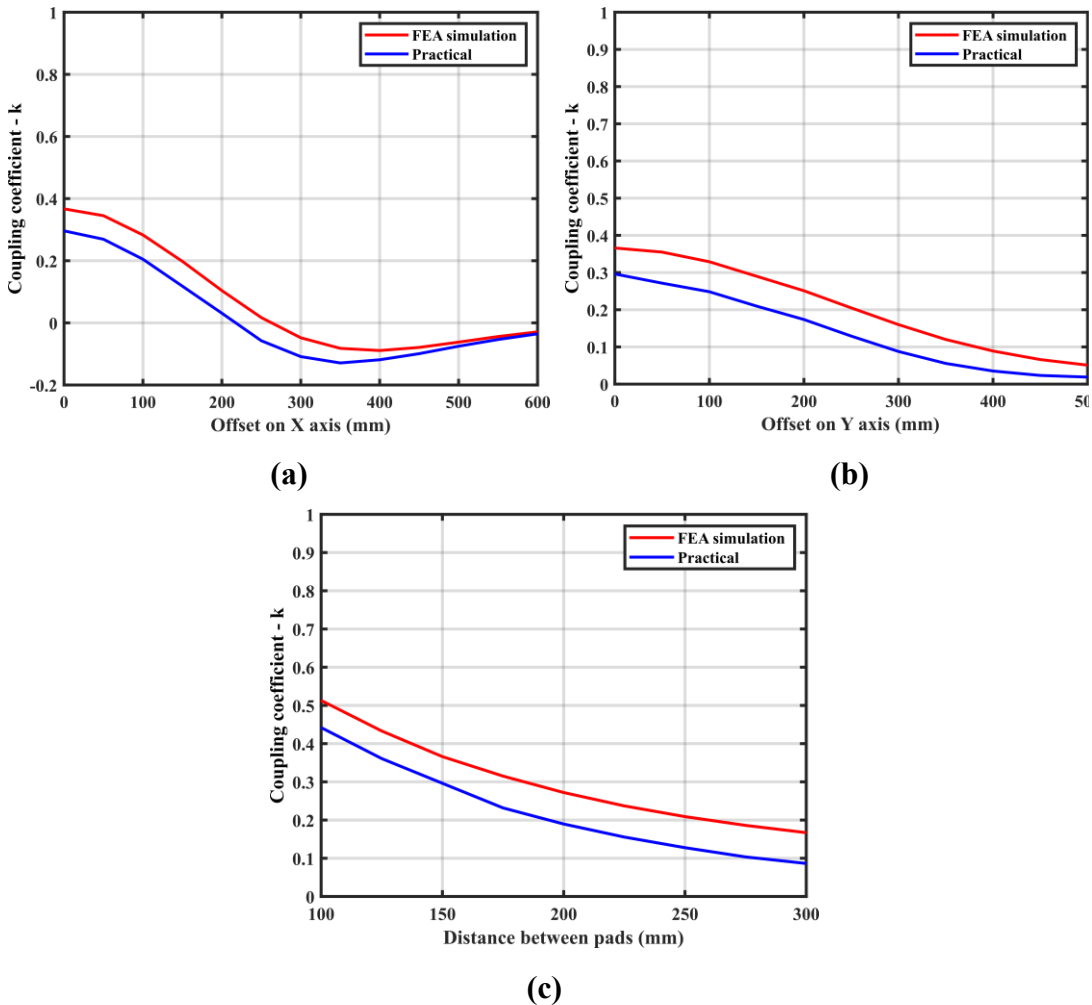


Figure 7.32: Coupling coefficient in function of (a) offset in X axis (b) offset in Y axis and (c) distance between pads in Z axis

A few practical factors contribute to the difference between simulation and experimental results. Overall, due to instrument and human errors in the construction process, the elements of the prototype will not have the exact same dimensions as in the FEA model. In simulation, the Double D coils have the shape of perfect rectangles, as previously shown in Figure 7.10, however, due to difficulties to reproduce that shape with a thick wire, the corners of the coils are slightly curved in the practical set-up (Figure 7.25). Also, during the misalignment tests, there is an error associated to the placement of the pads; in simulation the misalignment implemented is an exact value but in a practical situation there are small errors in the measurement of these distances that may influence the results.

Table 7.9: Coupling coefficient (k) in function of misalignment on X axis

Misalignment x axis	k experimental	k FEA simulation
0	0.296	0.366
50	0.269	0.345
100	0.205	0.283
150	0.118	0.198
200	0.031	0.104
250	0.057	0.017
300	0.109	-0.048
350	0.129	-0.082
400	0.119	-0.089
450	-0.099	-0.079
500	-0.075	-0.062
550	-0.054	-0.044
600	-0.035	-0.029

Table 7.10: Coupling coefficient (k) in function of misalignment on Y axis

Misalignment Y axis	k experimental	k FEA simulation
0	0.296	0.366
50	0.271	0.355
100	0.248	0.329
150	0.210	0.293
200	0.174	0.251
250	0.129	0.205
300	0.088	0.160
350	0.056	0.120
400	0.035	0.089
450	0.023	0.066
500	0.019	0.051

Table 7.11: Coupling coefficient (k) in function of distance between pads

Distance between pads Z axis	k experimental	k FEA simulation
100	0.442	0.513
125	0.361	0.433
150	0.296	0.366
175	0.232	0.315
200	0.190	0.272
225	0.155	0.237
250	0.128	0.209
275	0.103	0.186
300	0.086	0.167

7.6.2 Evaluation of converter operation

Once the coils are tested and inductances and coupling coefficient are measured, these structures are ready to be connected to compensation capacitors, H-bridges and the switching circuit for the converter validation.

Since the experimental values of the inductors were slightly lower than what was calculated in the design stage, the value of compensation capacitors is recalculated using equation (7.2) to maintain the resonant frequency at 100 kHz. Consequently, the design value increases from 120 nF to approximately 134 nF. The measured values for total compensation capacitance (Figure 7.33) are 133 nF for primary and 132 nF to the secondary side.

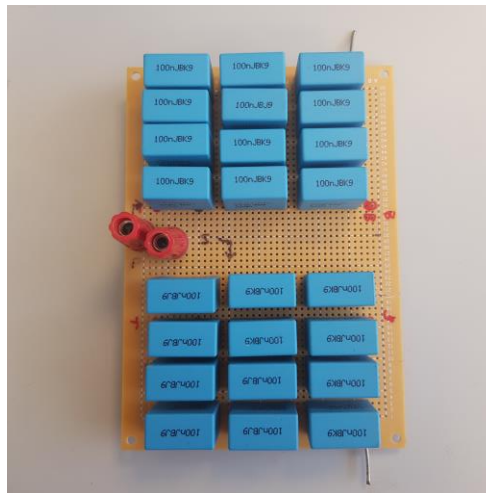


Figure 7.33: Primary and secondary compensation capacitors

For the converter experimental validation, resistances and parasitic elements are measured with the Bode 100 and incorporated to the circuit used for Spice and cyclic-averaging simulations. The equivalent circuit for the resonant tank is shown in Figure 7.34-a. The equivalent circuit for the inductor, described by equation (7.13), is the same used in the experimental analysis of the CLLC converter in Chapter 6, considering an inductance connected to a series resistance, parasitic capacitance in parallel and parallel resistance.

The capacitor is modelled by a capacitance connected to a series resistance (ESR). Additionally, in this chapter the resistances and inductances of the wires (R_{w1} , R_{w2} and L_{w1} , L_{w2}) that connect the resonant tank to the H-bridges are measured and

incorporated to the simulation model for comparison. As shown in equation (7.14), these values are incorporated into the equivalent circuit of the capacitor. Simplifying the equivalent circuit for the inductors to a Z_{leq} , as in (7.13) and capacitors to a Z_{ceq} , as in (7.14), the resonant tank circuit can be reduced to the equivalent shown in Figure 7.34-b. In this circuit, the equivalent resistances are obtained adding the resistance of the equivalent inductor (R_{leq}) to the resistance of the equivalent capacitor (R_{ceq}), as shown in equation (7.15). Once this reduced IPT resonant circuit is defined, equations (7.1) and (7.9) can be used to obtain the CLLC equivalent circuit for the cyclic-averaging simulation.

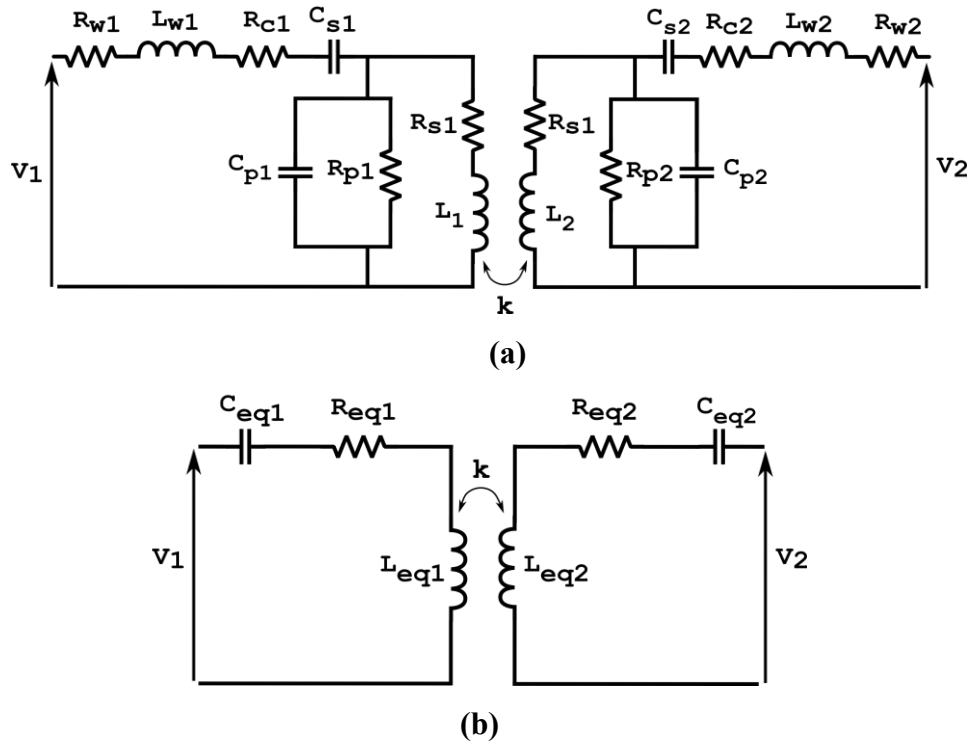


Figure 7.34: Experimental and theoretical coupling coefficients in function of (a) offset in X axis (b) offset in Y axis

$$Z_{leq} = R_{leq} + j\omega L_{leq} = \frac{1}{\frac{1}{R_p} + \frac{1}{R_s + j\omega L} + j\omega C_p} \quad (7.13)$$

$$Z_{ceq} = R_{ceq} - j\frac{1}{\omega C_{ceq}} = R_c + R_w + j\omega L_w - \frac{j}{\omega C_{s2}} \quad (7.14)$$

$$R_{eq1} = R_{ceq1} + R_{leq1}$$

$$R_{eq2} = R_{ceq2} + R_{leq2} \quad (7.15)$$

The measured values for all elements of the circuit from Figure 7.34-a are listed in Table 7.12. The elements of the simplified circuit from Figure 7.34-b and CLLC equivalent circuit for the cyclic-averaging simulation are listed in Table 7.13.

Table 7.12: Equivalent circuit parameters measured with Bode 100

Parameter		Value
Primary Capacitor	C_{s1}	133 nF
	R_{c1}	0.06 Ω
Secondary Capacitor	C_{s2}	132 nF
	R_{c2}	0.04 Ω
Primary Inductor	L_1	18.42 μ H
	R_{s1}	0.155 Ω
	R_{p1}	2.1 k Ω
	C_{p1}	205.88 pF
Secondary Inductor	L_2	18.87 μ H
	R_{s2}	0.166 Ω
	R_{p2}	2.75 k Ω
	C_{p2}	201.44 pF
Wire primary	L_{w1}	1.09 μ H
	R_{w1}	0.140 Ω
Wire secondary	L_{w2}	1.12 μ H
	R_{w2}	0.120 Ω

Table 7.13: Equivalent circuit parameters for reduced IPT converter and CLLC converter

Parameter		Value
IPT circuit	L_{eq1}	18.44 μ H
	R_{eq1}	0.420 Ω
	L_{eq2}	18.90 μ H
	R_{eq2}	0.378 Ω
	C_{eq1}	141.07 nF
	C_{eq2}	140.18 nF
CLLC equivalent circuit	L_{s1}	16.83 μ H
	L_m	1.62 μ H
	n	0.292

For the experimental verification, the output of the converter (battery in forward operation or DC bus in reverse operation) is modelled as an equivalent load. As in Chapter 6, these values are calculated using the simulation results at maximum modulation, where $R_{load} = \frac{V_{out}}{I_{out}}$. The design and practical values of resistance obtained are shown in Table 7.14.

Table 7.14: Load definition for forward and reverse tests

Method	Load - theoretical	Load - measured
Forward operation (48V – 12V)	1.14 Ω	1.20 Ω
Reverse operation (12V – 48V)	31.26 Ω	30.20 Ω

Once all parameters are defined, experimental results are compared to Spice simulations of the IPT converter and cyclic-averaging simulations of the equivalent CLLC converter. Results for SPS modulation are presented in Figure 7.35 while the PPM modulation case is analysed in Figure 7.36. The data for each test point is presented in Tables 7.15 and 7.16.

From analysis of the results, it is possible to conclude that both Spice and cyclic-averaging methods can accurately represent the converter's behaviour. At maximum

modulation, the error between Spice and experimental results is 50 mA, or 0.47%, for forward operation and 70 mA, or 5.43%, in reverse operation. Comparing experimental to cyclic-averaging results, also at maximum modulation, the error is equal to 40 mA, or 0.38%, in forward operation and 70mA, or 5.43%, in reverse operation.

Overall, the errors between simulation and experimental results are lower when operating with PPM modulation. As the modulation angle decreases in operation with SPS modulation, the difference between simulation and experimental results increases. It was observed in simulation that this is not solely due to the influence of delays in the system, as observed in Chapter 6. When using SPS modulation, the output current is more sensitive to the resonant tank components, and consequently the primary and secondary wire inductance values. For a phase-shift angle of 10 degrees, the output current in forward mode would drop from 2.68 to 2.01 (670 mA difference) if the wire inductance was not considered in the Spice simulation. For the PPM modulation case, the same comparison, at the lowest modulation angle, would result in a difference of only 25 mA.

The error between experimental and simulation results in this chapter was reduced compared to the analysis made in the previous chapter for the CLLC converter. This is mainly due to the addition of the primary and secondary wire resistances and inductances to the simulation of the IPT converter, while in Chapter 6 the influence of long wires was neglected.

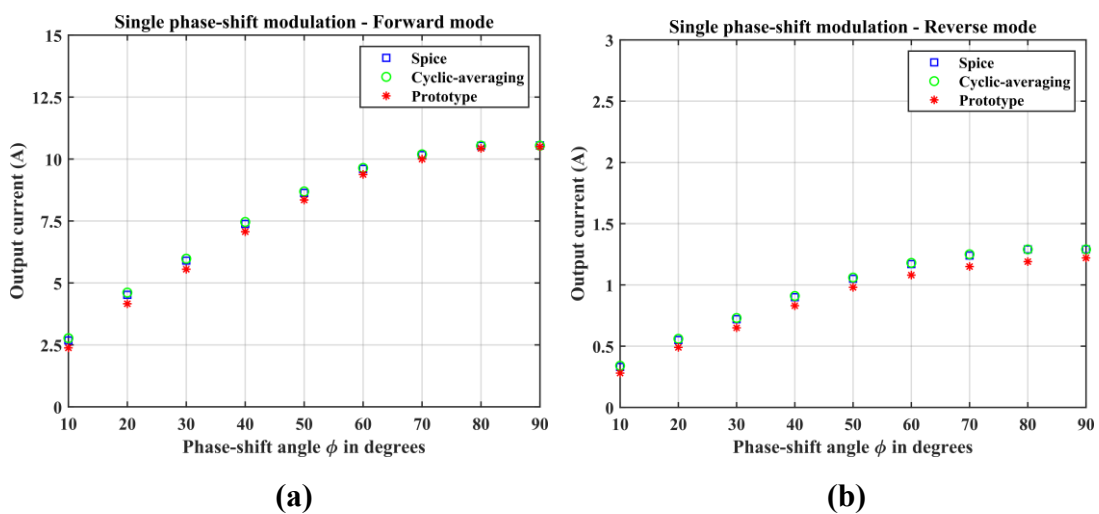


Figure 7.35: Experimental and simulation results for 48-12V SPS modulated converter operating in (a) forward and (b) reverse modes

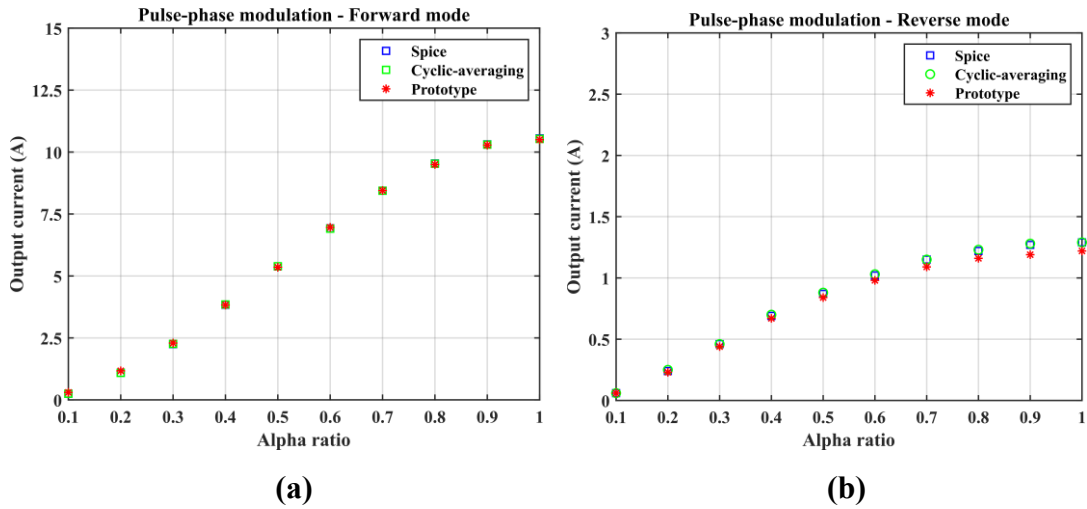


Figure 7.36: Experimental and simulation results for 48-12V PPM modulated converter operating in (a) forward and (b) reverse modes

Table 7.15: Results for SPS modulation (48 – 12 V)

Demanded phase-shift angle in degrees (ϕ)	Average output current (A)					
	Forward operation			Reverse operation		
	Cyclic-averaging	Spice	Prototype	Cyclic-averaging	Spice	Prototype
10.04	2.77	2.68	2.38	0.34	0.33	0.28
20.77	4.61	4.52	4.16	0.56	0.55	0.49
29.42	5.98	5.90	5.55	0.73	0.72	0.65
39.81	7.46	7.38	7.07	0.91	0.90	0.83
50.19	8.69	8.63	8.35	1.06	1.05	0.98
60.58	9.64	9.60	9.38	1.18	1.17	1.08
69.23	10.19	10.16	10.00	1.25	1.24	1.15
79.61	10.54	10.53	10.43	1.29	1.29	1.19
90	10.54	10.55	10.50	1.29	1.29	1.22

Table 7.16: Results for PPM modulation (48 – 12 V)

Demanded alpha ratio (α)	Average output current (A)					
	Forward operation			Reverse operation		
	Cyclic- averaging	Spice	Prototype	Cyclic- averaging	Spice	Prototype
0.096	0.25	0.25	0.30	0.06	0.06	0.06
0.202	1.09	1.09	1.17	0.25	0.24	0.23
0.298	2.26	2.25	2.29	0.46	0.46	0.44
0.404	3.85	3.84	3.83	0.70	0.69	0.67
0.5	5.39	5.39	5.35	0.88	0.87	0.84
0.596	6.91	6.92	6.96	1.03	1.02	0.98
0.702	8.44	8.44	8.45	1.15	1.15	1.09
0.798	9.53	9.54	9.50	1.23	1.22	1.16
0.904	10.30	10.31	10.28	1.28	1.27	1.19
1.0	10.54	10.55	10.50	1.29	1.29	1.22

During experimental verification it was observed that output power and efficiency were significantly reduced when operating in reverse mode. At maximum modulation in forward mode, the measured output power is 130.206 W with efficiency of 56.6%, while in reverse mode the output power dropped to 44.65 W with efficiency of 40.6%.

While in a nearly ideal simulation both forward and reverse operations have similar output power and high efficiency, when the resistances and parasitic elements from the real circuit are added to the simulation model, the output power and efficiency in reverse mode are considerably reduced. Tests were performed using the Spice simulation with voltage sources at input and output sides, to verify the influence of the input-output voltage ratio in the converter's behaviour. According to the simulation results shown in Table 7.17, when the input and output voltage match, the results for forward and reverse operation are very similar and the efficiency is increased. As the difference between input and output voltages increase, the output power in reverse mode is considerably lower than in forward mode and the efficiency drops, more significantly for reverse operation.

Table 7.17: Influence of converter voltage ratio in the output power and efficiency of the system at maximum modulation

Voltage	Output Power (W)		Efficiency (%)	
	Forward	Reverse	Forward	Reverse
$V_{dc} = 48V, V_{bat} = 12V$	126.910	45.115	59.4	32.5
$V_{dc} = 48V, V_{bat} = 48V$	437.720	443.340	71.2	71.6
$V_{dc} = 12V, V_{bat} = 12V$	27.303	27.643	70.6	70.9
$V_{dc} = 24V, V_{bat} = 24V$	109.210	110.570	70.6	70.9

In this research project, the converters were not built to achieve maximum efficiency. The primary objective here is to verify the accuracy of the models in the representation of the converter behaviour. Therefore, provided that most of the losses are incorporated into the simulation and the models give accurate results, it is acceptable to have a low efficiency converter. For converters built with optimized efficiency, the voltage mismatch would not be a problem, since when the losses are significantly reduced both forward and reverse modes perform well. Improved efficiency can be achieved reducing the quantity and length of wires in the circuit, using SiC or GaN MOSFETs with reduced on-resistance and prioritizing efficiency in the inductor design and construction process.

To verify the case of unity voltage conversion ratio, maintaining a maximum output of approximately 110 W at maximum modulation, the input and output voltages of the converter are changed to 24 V. The new values of equivalent load used for these tests are shown in Table 7.18.

Table 7.18: Load definition for forward and reverse tests for 24-24V tests

Power flow direction	Load - theoretical	Load - measured
Forward operation (24V – 24V)	4.97 Ω	5.39 Ω
Reverse operation (24V – 24V)	4.97 Ω	5.39 Ω

Experimental and simulation results are compared, as shown in Figures 7.37 and 7.38, and the values of output current for each test point are presented in Tables 7.19 and 7.20. Now the graphs for forward operation are nearly identical to the reverse

operation results. At maximum modulation in forward mode, the current error between experimental and Spice and cyclic-averaging simulations is 60 mA (1.32%), while in reverse mode the difference is 30 mA (0.65%) to Spice results, and 40 mA (0.87%) to the cyclic-averaging results.

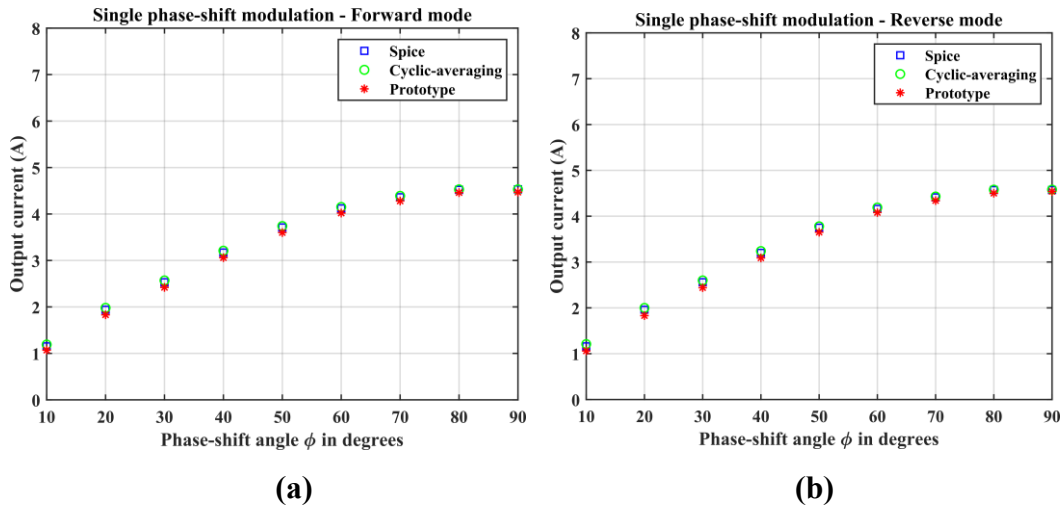


Figure 7.37: Experimental and simulation results for 24-24V SPS modulated converter operating in (a) forward and (b) reverse modes

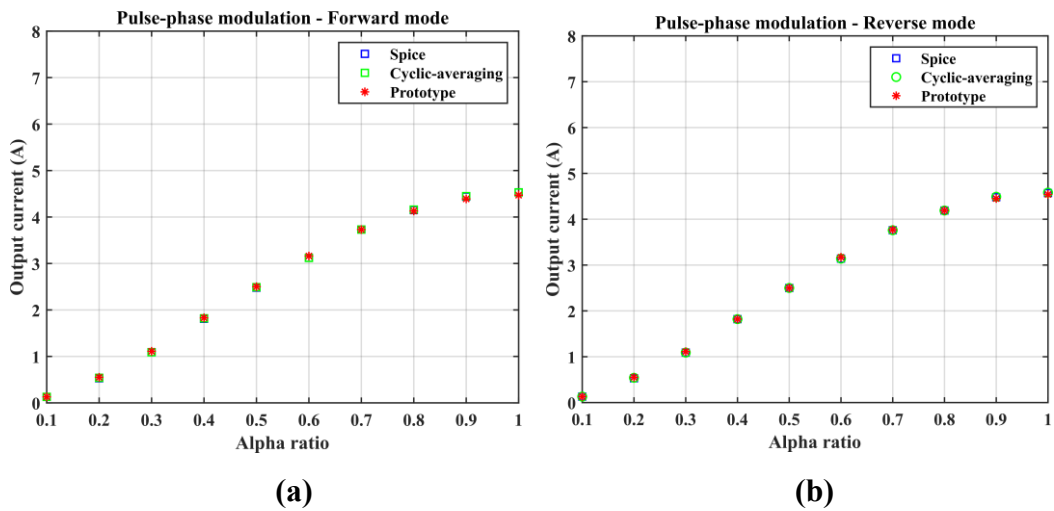


Figure 7.38: Experimental and simulation results for 24-24V PPM modulated converter operating in (a) forward and (b) reverse modes

Table 7.19: Results for SPS modulation (24 – 24 V)

Demanded phase-shift angle in degrees (ϕ)	Average output current (A)					
	Forward operation			Reverse operation		
	Cyclic-averaging	Spice	Prototype	Cyclic-averaging	Spice	Prototype
10.04	1.19	1.15	1.07	1.21	1.16	1.06
20.77	1.98	1.94	1.83	2.00	1.96	1.83
29.42	2.57	2.53	2.42	2.60	2.56	2.44
39.81	3.21	3.17	3.06	3.24	3.20	3.09
50.19	3.74	3.71	3.60	3.78	3.75	3.65
60.58	4.15	4.12	4.02	4.19	4.16	4.08
69.23	4.39	4.36	4.28	4.43	4.41	4.34
79.61	4.53	4.52	4.46	4.58	4.57	4.50
90	4.53	4.53	4.47	4.58	4.57	4.54

Table 7.20: Results for PPM modulation (24 – 24 V)

Demanded alpha ratio (α)	Average output current (A)					
	Forward operation			Reverse operation		
	Cyclic-averaging	Spice	Prototype	Cyclic-averaging	Spice	Prototype
0.096	0.13	0.13	0.13	0.13	0.13	0.13
0.202	0.54	0.53	0.55	0.54	0.53	0.55
0.298	1.09	1.09	1.11	1.09	1.09	1.11
0.404	1.82	1.81	1.83	1.82	1.82	1.82
0.5	2.49	2.48	2.50	2.50	2.50	2.50
0.596	3.12	3.12	3.16	3.14	3.14	3.17
0.702	3.73	3.73	3.73	3.76	3.76	3.77
0.798	4.16	4.15	4.13	4.19	4.19	4.19
0.904	4.45	4.44	4.39	4.49	4.48	4.45
1.0	4.53	4.53	4.47	4.58	4.57	4.54

The input and output signals measured at maximum modulation and forward operation are shown in Figures 7.39 and 7.40. Due to inaccuracies inherent of

experimental tests, as instrument errors, influence of the temperature in the measurements, and the fact the measured load value (5.39 Ω) is not exactly the same as the theoretical load value (4.97 Ω), the experimental voltage conversion ratio is not equal to one, but still very close, as shown in (7.16).

$$\text{conversion ratio} = \frac{V_{out}}{V_{in}} = \frac{24.559}{23.795} = 1.03 \quad (7.16)$$

In the experimental tests, an output power of 109.78 W was measured in forward mode at maximum modulation, while 109.69 W was the power for reverse mode operation. An efficiency of 67% was obtained for both forward and reverse modes. Therefore, operation with a voltage conversion ratio close to unity resulted in an improvement of efficiency and nearly equal output power for both forward and reverse operations.

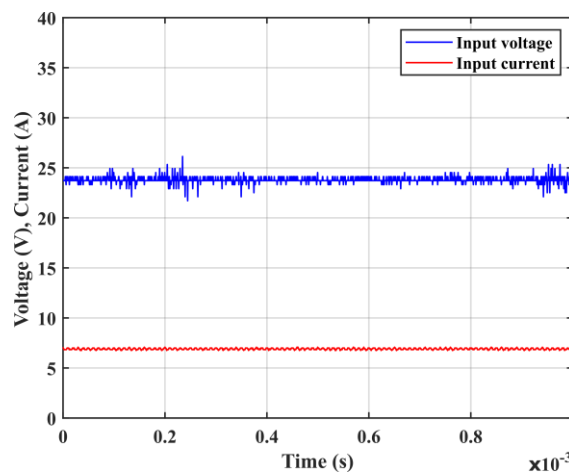


Figure 7.39: Prototype tests: input voltage and current

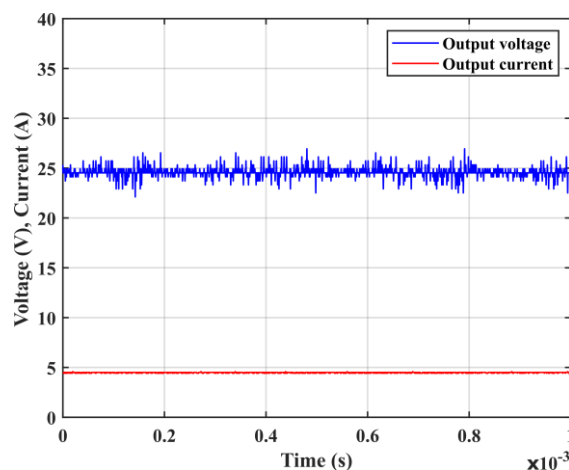


Figure 7.40: Prototype tests: output voltage and current

7.7 Conclusions

In this chapter a series compensated IPT converter was analysed. A FMA model was derived and employed in the converter design. From simulation results, it was observed that FMA still suffers from accuracy problems due to the fundamental approximation, especially when analysing the primary current. For the secondary current and output power analysis in a low loss circuit, the FMA model performed well.

For the application of state-variable and cyclic-averaging methods, an equivalent CLLC circuit was obtained and the modelling equations from Chapter 5 were used to predict the IPT converter output. At simulation stage, it was confirmed that both state-variable and cyclic-averaging methods could accurately model the IPT converter's behaviour.

For the design of the primary and secondary coils, a finite element analysis (FEA) simulation was performed and the influence of construction parameters and misalignment was analysed. In both simulation and experimental results, it was verified that the Double D coil is more sensitive to misalignments in the X axis. To achieve good performance for misalignments in both X and Y axis, more complex coils can be used, as Double D Quadrature or Bipolar coils.

The parameters of the experimental set-up were measured, incorporated to the simulation models and results obtained were compared to Spice and cyclic-averaging simulations. The simulation model for the prototype verification in this chapter was improved compared to Chapter 6, with the addition of wire resistances and inductances (for long wires connecting primary and secondary side of resonant tank to the remaining circuit), resulting in better accuracy for both Spice and cyclic-averaging models.

Finally, the influence of the voltage conversion ratio in the output power and efficiency of the converter was evaluated. It was observed that, when the converter has increased loss, performance in reverse mode deteriorates as the conversion ratio diverges from unity, with reduced output power and efficiency compared to forward mode results. The prototype was then tested with an input-output voltage ratio close to one, which resulted in better performance in reverse mode and overall improvement of efficiency.

7.8 References

- [1] Z. U. Zahid, Z. M. Dalala, R. Chen, B. Chen, and J. S. Lai, "Design of bidirectional DC-DC resonant converter for Vehicle-to-Grid (V2G) applications," *IEEE Transactions on Transportation Electrification*, vol. 1, no. 3, pp. 232–244, 2015.
- [2] A. A. S. Mohamed, A. Berzoy, and O. Mohammad, "Magnetic design considerations of bidirectional inductive wireless power transfer system for EV applications," *IEEE Transactions on Magnetics*, vol. 53, no. 6, pp. 1–5, 2017.
- [3] A. A. S. Mohamed, A. Berzoy, F. G. N. Nogueira de Almeida, and O. Mohammed, "Modeling and Assessment Analysis of Various Compensation Topologies in Bidirectional IWPT System for EV Applications," *IEEE Transactions on Industry Applications*, vol. 53, no. 5, pp. 4973–4984, 2017.
- [4] Y. Zhang, T. Kan, Z. Yan, and C. C. Mi, "Frequency and Voltage Tuning of Series-Series Compensated Wireless Power Transfer System to Sustain Rated Power under Various Conditions," *IEEE Journal of Emerging and Selected Topics in Power Electronics*, vol. 7, no. 2, pp. 1311–1317, 2019.
- [5] S. Wang, J. Chen, Z. Hu, C. Rong, and M. Liu, "Optimisation design for series–series dynamic WPT system maintaining stable transfer power," *IET Power Electronics*, vol. 10, no. 9, pp. 987–995, 2017.
- [6] A. Zaheer, D. Kacprzak, and G. A. Covic, "A bipolar receiver pad in a lumped IPT system for electric vehicle charging applications," *2012 IEEE Energy Conversion Congress and Exposition, ECCE 2012*, pp. 283–290, 2012.
- [7] G. a. Covic and J. T. Boys, "Inductive Power Transfer," *Proceedings of the IEEE*, vol. 101, no. 6, pp. 1276–1289, 2013.
- [8] J. Kim *et al.*, "Coil design and shielding methods for a magnetic resonant wireless power transfer system," *Proceedings of the IEEE*, vol. 101, no. 6, pp. 1332–1342, 2013.
- [9] SAE International, "J2954™ Wireless Power Transfer for Light-Duty Plug-In/Electric Vehicles and Alignment Methodology," *Surface Vehicle Information Report*, 2016.
- [10] L. Heinzle, "Measuring the Mutual Interaction between Coaxial Cylindrical Coils with the Bode 100," *Bode 100 Article*, pp. 1–11, 2013.
- [11] K. Hata, T. Imura, and Y. Hori, "Simplified measuring method of kQ product for wireless power transfer via magnetic resonance coupling based on input impedance measurement," *IECON 2017 - 43rd Annual Conference of the IEEE Industrial Electronics Society*, pp. 6974–6979, 2017.
- [12] B. Hesterman, "Analysis and Modeling of Magnetic Coupling," *Denver Chapter Seminar, IEEE Power Electronics Society*, pp. 1–93, 2007.

8 Conclusions and Further Work

8.1 Conclusions

In this thesis the cyclic-averaging method was successfully applied to model a DAB converter, a 4th order CLLC resonant converter and a series compensated IPT converter. The technique showed good performance, accuracy and significantly faster execution time compared to more traditional methods of analysis as FMA, state-variable and Spice. Here the novel cyclic-averaging model was mainly used to evaluate the influence of the control variables (phase-shift angles in Chapters 3, 5, 6 and 7 or frequency in Chapter 4) on the converter's behaviour. However, the models developed in this thesis can also be applied to analyse the influence of the circuit components in order to obtain a faster design process.

In Chapter 2 popular topologies of DC-DC converters for V2G applications and modelling techniques were analysed. Despite the requirement of complex modulation techniques to maintain good performance, the DAB is still a popular topology for bidirectional chargers and serves as base for various resonant converters. Among the converters analysed, the CLLC resonant topology had the best features for conventional bidirectional chargers, while IPT converters with series or LCL compensation were the best options for wireless systems. Based on previous research on converter modelling, the FMA method is the most popular due to its simple and fast implementation, but the fundamental approximation may cause accuracy problems when the resonant tank voltages/currents are not sinusoidal. The cyclic-averaging method, despite requiring a more complex analysis, stands out due to its fast execution and good accuracy.

The Dual Active Bridge converter operating under Single Phase-Shift (SPS) modulation was analysed in Chapter 3, considering bidirectional operation. The operation modes of the converter were defined and the cyclic-averaging method was applied for calculation of the converter's output current in function of the phase-shift angles, resulting in a rapid analysis with accuracy similar to Spice. The cyclic method

was also successfully employed to perform a harmonic analysis of the state-variables, where harmonic components were calculated and used for waveform reconstruction. The waveforms obtained from the harmonic analysis were very close to the Spice simulation results. The main benefit observed for the cyclic-averaging method was the fast execution, being nearly 33 times faster than Spice for calculation of the converter's output and the state-variables harmonics or nearly 166 times faster when the harmonic analysis and waveform reconstruction are not performed.

In Chapter 4 FMA, state-variable and cyclic-averaging techniques were applied to model a frequency modulated CLLC converter. Among the models analysed, state-variable, with maximum error of 1.03%, and cyclic-averaging, with maximum error of 1.06%, showed the best accuracy compared to Spice. For the cyclic analysis of the phase-shift modulated DAB converter the duty cycle values were easily calculated from the modulation angle. For the frequency modulated CLLC converter, however, FMA equations are used for the angle estimation followed by a numerical optimization with the Newton-Raphson method. It was observed during simulation that results obtained when using only FMA for duty calculation were not sufficiently accurate, therefore, the optimization method proposed in Chapter 4 is essential to achieve accurate results with the cyclic-averaging method. A drawback of cyclic-averaging applied to frequency modulated topologies is the complexity in the analysis and duty calculation, with the necessity of auxiliary methods to obtain an accurate solution. Furthermore, the converter operating modes and switching frequency must be carefully analysed, since non-conduction mode occurs when operating in a frequency range lower than the load independent point frequency.

A phase-shift modulated CLLC converter was analysed in Chapter 5. The operating modes were defined considering two types of modulation: Single Phase-Shift (SPS) and Pulse-Phase Modulation (PPM). The influence of phase-shift angles on the converter operation was analysed and results showed that efficiency is higher when operating with equal leg phase-shift angles ($\alpha_1 = \alpha_2$) and bridge phase-shift angle (ϕ) fixed at $\pm 90^\circ$. Similar to the previous chapter results, the FMA model has reduced accuracy when compared to cyclic-averaging or state-variable methods. Here, the cyclic-averaging technique applied to calculation of the output current has an average error of 0.5% compared to Spice, with execution 180 times faster than the state-variable simulation and nearly 144 times faster than Spice.

Following the validation of the CLLC converter models through simulation, the prototype construction of a phase-shift modulated CLLC converter and experimental verification were described in Chapter 6. Since the simulations in Chapter 5 were performed for a nearly ideal converter, the cyclic-averaging and Spice models were modified to include loss elements from the experimental system and increase the accuracy when comparing the models' simulations and prototype results. Overall, both Spice and cyclic-averaging models had a good performance modelling the behaviour of the bidirectional CLLC converter considering SPS and PPM modulation. Higher output current error was identified for operation using SPS modulation with reduced phase-shift angles due to the increased sensitivity to delays and to variations in the resonant tank elements observed when implementing this modulation method.

In Chapter 7 the design, construction and validation of a series-compensated IPT converter were evaluated. Using circuit transformation to obtain an equivalent CLLC circuit, the state-variable and cyclic-averaging models developed for the CLLC converter in Chapters 5 and 6 were used to model the IPT converter. The models were validated against a Spice simulation and could accurately predict the behaviour of the IPT converter, with maximum error of 2.23% for cyclic-averaging and 1.61% for state-variable.

For the experimental verification conducted in Chapter 7, additional elements from the real circuit (resistances and inductances of long wires connecting the resonant tank to the H-bridges) were considered in the simulation models, improving the accuracy of both Spice and cyclic-averaging models compared to the results obtained in Chapter 5, especially for operation with small phase-shift angles in SPS modulation. A study of the influence of the conversion gain on the bidirectional operation was also performed in this chapter, showing that, for high efficiency converters, the variation of conversion gain has no significant effect. For higher loss converters, however, performance in reverse mode and overall efficiency degrade when the converter gain is not close to unity. From the experimental verification performed, increased efficiency and improved reverse operation were achieved when operating with voltage gain close to unity.

Analysing the cyclic-averaging implementation for the DAB and CLLC converters, it was possible to conclude that the complexity of the cyclic-averaging model increases for higher order resonant networks and is highly dependent of the modulation technique

chosen. More complex modulation techniques will result in more variables affecting the converter's behaviour and, consequently, more operating modes to be analysed. Therefore, despite the benefits of rapid and accurate analysis, the implementation of this method may become too complicated for converters with significantly more complex resonant networks or when intricate modulation methods are used.

In this thesis the models were validated with the construction of a small-scale prototype (100 W converter). The application of cyclic-averaging models for converters operating at higher power levels was verified only through simulation in Chapter 3, for a 7kW converter, and in Chapter 4, for a 3.5 kW converter, also resulting in an accurate analysis. The cyclic-averaging models here developed are still valid for converters used in EV charging applications that operate at higher power levels as long as the loss and parasitic elements are measured and incorporated into the equivalent circuits following the same methodology used to verify the low power prototypes in Chapters 6 and 7.

8.2 Further work

Based on the research conducted in this thesis, possibilities of further investigation were identified and will be discussed in this section.

In this thesis the cyclic-averaging method was applied for the simplest type of phase-shift modulation for the DAB converter and for the most popular modulation techniques for the CLLC and IPT series compensated converters. Depending on the modulation technique utilized, the converter operation must be reanalysed for the definition of the operating modes and duty cycles. Therefore, the cyclic analysis here developed has the potential to be adapted for various modulation techniques and converters topologies that were not considered in this research.

In Chapters 4, 5, 6 and 7 the cyclic-averaging method was employed mainly for calculation of the converter's output current and instant values of state-variables at each operating mode transition, while in Chapter 3 the technique was also used to perform a harmonic analysis of the DAB converter. Therefore, further work can be conducted to extend the harmonic analysis to the more complex CLLC converter and, with the application of circuit transformation, to the series compensated IPT converter.

Despite being a popular method for analysis of resonant converters, accuracy limitations were identified for the FMA model in this thesis. To obtain an improved

frequency-domain analysis, the RTFMA method [1], [2], that propose modifications to the conventional FMA technique to achieve increased accuracy, can be investigated for the converter topologies here analysed.

Since one of the challenges of wireless topologies is the efficiency improvement, an efficiency study can be conducted to the series compensated IPT converter prototype in order to improve operation. As shown in Figure 8.1, the coil AC resistance significantly decreases with reduction of frequency. A change in frequency, however, also affects other systems parameters, as the size of magnetic components. Therefore, the influence of the operating frequency and magnetic materials in the overall system's losses can be furtherly investigated for an improvement of the converter's efficiency. Additionally, the reorganization of the system for reduction or elimination of wires, use of SiC and GaN switching devices with reduced on-resistance and use of litz wire with thinner strands should also result in an improvement of efficiency.

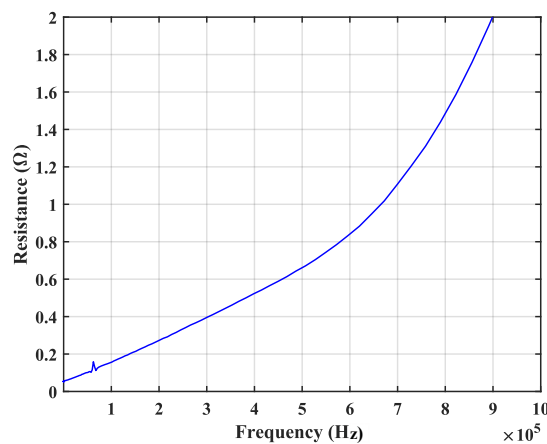


Figure 8.1: Coil resistance versus frequency

8.3 References

- [1] H. I. Sewell, M. P. Foster, C. M. Bingham, D. A. Stone, D. Hente, and D. Howe, “Analysis of voltage output LCC resonant converters, including boost mode operation,” *IEE Proceedings - Electric Power Applications*, vol. 150, no. 6, pp. 673–679, 2003.
- [2] M. P. Foster, “Analysis and Design of High-order Resonant Power Converters,” PhD Thesis. University of Sheffield, 2003.

Appendix A.1

The relative errors between FMA and Spice simulations from chapter 5, for the following variables: output power, primary current, secondary current and magnetizing current, are shown in Tables A1.1 to A1.4.

The efficiency as function of leg phase-shift angles α_1 and α_2 obtained from the Spice simulation is presented in Table A1.5.

Table A1.1: Output power relative error (%) between FMA and Spice considering $\phi = 90^\circ$, where: Green: <5%, Orange : 5-10% and Red: >10%

	α_2									
α_1	18	36	54	72	90	108	126	144	162	180
18	14.48	9.71	0.64	-12.10	-27.57	-37.08	-43.40	-54.71	-69.95	-87.49
36	12.41	13.08	8.81	0.01	-12.50	-23.75	-30.99	-39.21	-51.74	-67.45
54	4.42	9.90	10.40	5.99	-2.79	-12.39	-20.62	-28.25	-37.88	-51.24
72	-8.06	1.54	6.51	6.60	1.99	-4.67	-11.61	-19.23	-27.61	-38.22
90	-23.72	-10.91	-2.06	2.25	1.88	-1.20	-5.63	-11.75	-19.52	-28.60
108	-33.43	-22.25	-11.64	-4.31	-1.05	-0.58	-1.99	-5.75	-11.88	-20.06
126	-39.53	-29.43	-19.83	-11.16	-5.37	-1.85	-0.22	-1.19	-5.00	-11.45
144	-50.24	-37.37	-27.30	-18.66	-11.36	-5.47	-1.03	0.91	-0.15	-4.25
162	-64.79	-49.50	-36.67	-26.87	-18.99	-11.47	-4.688	0.02	1.86	0.52
180	-81.96	-64.97	-49.84	-37.34	-27.99	-19.58	-11.07	-3.99	0.63	2.20

Table A1.2: Primary current ($|I_1|$) relative error (%) between FMA and Spice, considering $\phi = 90^\circ$, where: Green: <5%, Orange: 5-10% and Red: >10%

	α_2									
α_1	18	36	54	72	90	108	126	144	162	180
18	8.89	5.37	3.75	2.48	1.43	0.67	0.41	0.47	0.64	0.72
36	12.97	7.14	5.28	3.90	2.65	1.57	0.97	0.88	1.04	1.16
54	13.63	7.19	5.64	4.56	3.46	2.38	1.60	1.27	1.33	1.46
72	12.10	6.24	5.15	4.47	3.71	2.85	2.14	1.71	1.58	1.63
90	11.78	5.95	4.77	4.23	3.69	3.08	2.56	2.22	2.01	1.88
108	14.38	7.44	5.39	4.46	3.85	3.33	2.98	2.79	2.66	2.47
126	14.98	9.17	6.57	5.12	4.22	3.61	3.32	3.28	3.30	3.20
144	14.02	9.27	7.34	5.81	4.66	3.88	3.54	3.57	3.74	3.81
162	12.78	7.94	6.87	5.95	4.91	4.04	3.62	3.63	3.88	4.11
180	10.35	5.66	5.31	5.09	4.60	3.91	3.49	3.47	3.73	4.05

Table A1.3: Secondary current ($|I_2|$) relative error (%) between FMA and Spice considering $\phi = 90^\circ$, where: Green: <5%, Orange: 5-10% and Red: >10%

	α_2									
α_1	18	36	54	72	90	108	126	144	162	180
18	26.34	64.23	86.17	84.81	60.22	21.39	6.77	34.65	73.61	93.84
36	6.38	18.76	28.61	30.64	23.50	9.851	1.04	7.61	22.73	32.97
54	1.78	6.80	11.88	13.90	11.51	5.49	0.46	1.31	8.23	14.53
72	0.39	2.48	4.98	6.20	5.29	2.41	-0.15	-0.15	2.76	6.30
90	0.35	1.41	2.48	2.87	2.18	0.58	-0.58	-0.24	1.43	3.00
108	0.81	1.86	2.38	2.17	1.26	-0.004	-0.56	0.18	1.72	2.65
126	0.85	2.31	2.95	2.523	1.36	-0.01	-0.49	0.41	2.06	3.04
144	0.65	2.14	3.22	3.04	1.80	0.22	-0.48	0.28	1.98	3.18
162	0.44	1.64	2.83	3.15	2.17	0.52	-0.489	-0.04	1.52	2.86
180	0.31	1.17	2.14	2.63	2.16	0.72	-0.458	-0.36	0.91	2.21

Table A1.4: Magnetizing current ($|I_m|$) relative error (%) between FMA and Spice considering $\phi = 90^\circ$, where: Green: <5%, Orange: 5-10% and Red: >10%

	α_2									
α_1	18	36	54	72	90	108	126	144	162	180
18	6.28	12.49	13.62	13.44	13.11	13.05	13.36	13.96	14.65	15.16
36	-3.48	4.70	11.04	14.75	17.09	18.89	20.56	22.22	23.79	25.07
54	-8.31	-4.18	3.39	9.90	14.91	18.92	22.34	25.41	28.15	30.44
72	-10.88	-11.12	-5.02	2.39	9.17	15.02	20.11	24.60	28.56	31.92
90	-12.42	-16.28	-12.71	-5.79	1.73	8.83	15.26	21.02	26.11	30.46
108	-13.48	-20.24	-19.46	-13.86	-6.36	1.42	8.82	15.62	21.72	26.99
126	-14.30	-23.43	-25.41	-21.59	-14.67	-6.66	1.39	9.02	15.99	22.11
144	-14.99	-26.18	-30.83	-29.05	-23.07	-15.16	-6.71	1.56	9.28	16.18
162	-15.60	-28.62	-35.92	-36.40	-31.62	-24.01	-15.34	-6.55	1.81	9.41
180	-16.13	-30.85	-40.80	-43.79	-40.46	-33.28	-24.46	-15.234	-6.30	1.94

Table A1.5: Efficiency in Spice considering $\phi = 90^\circ$, where: Green: ≥ 0.98 , Orange: 0.95-0.98 and Red <0.95

	α_2									
α_1	18	36	54	72	90	108	126	144	162	180
18	0.9812	0.9777	0.9721	0.9654	0.9564	0.9481	0.939	0.9195	0.878	0.7562
36	0.9801	0.9838	0.9827	0.9806	0.9774	0.9741	0.9706	0.9647	0.9531	0.9302
54	0.9744	0.9836	0.9849	0.9845	0.9832	0.9815	0.9795	0.9767	0.9717	0.9631
72	0.9655	0.9809	0.9846	0.9855	0.9853	0.9845	0.9834	0.9815	0.9788	0.9745
90	0.9519	0.976	0.9826	0.9849	0.9856	0.9856	0.985	0.9838	0.9819	0.9794
108	0.9382	0.9695	0.9793	0.9833	0.985	0.9857	0.9857	0.985	0.9837	0.9819
126	0.9265	0.9636	0.9756	0.9811	0.9839	0.9853	0.9858	0.9856	0.9848	0.9835
144	0.9074	0.9572	0.9718	0.9785	0.9823	0.9844	0.9856	0.9858	0.9854	0.9846
162	0.8705	0.9464	0.9671	0.9756	0.9802	0.9832	0.9849	0.9857	0.9858	0.9853
180	0.774	0.9217	0.9591	0.9718	0.9762	0.9814	0.9839	0.9852	0.9857	0.9856

Appendix A.2

The experimental results obtained for the CLLC resonant converter operating under SPS and PPM modulation are presented in Tables A2.1, A2.2, A2.3 and A2.4. The input voltages applied to the system for each test point are shown in Tables A2.5 and A2.6.

As explained in chapter 6, to verify the accuracy of the models, evaluating the influence of loss elements and time delays, three test cases are considered for the simulations:

Test A: real component loss elements not fully considered and deadtime not considered (test case exclusive to cyclic-averaging simulations);

Test B: all measured loss elements incorporated into model, deadtime influence not considered;

Test C: all measured losses elements incorporated into model, deadtime compensation implemented.

Table A2.1: Results for single phase-shift modulation forward operation

Demanded Phase-shift Angle (ϕ)	Average Output Current (A)					
	Cyclic-averaging			Spice		Prototype
	Test A	Test B	Test C	Test B	Test C	
10.04°	0.86	0.89	1.22	0.95	1.30	1.77
20.77°	2.08	1.99	2.32	2.11	2.46	2.88
29.42°	3.07	2.87	3.20	3.03	3.37	3.77
39.81°	4.22	3.90	4.20	4.07	4.37	4.72
50.19°	5.28	4.83	5.09	4.99	5.25	5.51
60.58°	6.17	5.61	5.82	5.75	5.95	6.11
69.23°	6.76	6.12	6.28	6.24	6.39	6.39
79.61°	7.24	6.53	6.61	6.63	6.70	6.61
90°	7.45	6.70	6.69	6.79	6.78	6.63

Table A2.2: Results for single phase-shift modulation reverse operation

Demanded Phase-shift Angle (ϕ)	Average Output Current (A)					
	Cyclic-averaging			Spice		Prototype
	Test A	Test B	Test C	Test B	Test C	
10.04°	0.19	0.21	0.29	0.22	0.30	0.37
20.77°	0.47	0.46	0.54	0.48	0.55	0.58
29.42°	0.69	0.67	0.75	0.70	0.77	0.74
39.81°	0.95	0.91	0.98	0.93	1.00	0.93
50.19°	1.18	1.12	1.18	1.14	1.20	1.09
60.58°	1.38	1.30	1.35	1.32	1.37	1.22
69.23°	1.50	1.42	1.46	1.43	1.46	1.29
79.61°	1.61	1.51	1.53	1.52	1.53	1.35
90°	1.65	1.55	1.55	1.55	1.55	1.35

Table A2.3: Results for pulse-phase modulation forward operation

Demanded Alpha Ratio (α)	Average Output Current (A)					
	Cyclic-averaging			Spice		Prototype
	Test A	Test B	Test C	Test B	Test C	
0.096	0.21	0.19	0.19	0.18	0.18	0.19
0.202	0.87	0.80	0.80	0.77	0.77	0.74
0.298	1.75	1.60	1.60	1.56	1.56	1.50
0.404	2.85	2.62	2.62	2.59	2.59	2.53
0.5	3.82	3.49	3.49	3.53	3.53	3.48
0.596	4.79	4.34	4.34	4.45	4.45	4.47
0.702	5.87	5.30	5.30	5.42	5.42	5.38
0.798	6.69	6.03	6.03	6.14	6.14	6.03
0.904	7.28	6.54	6.54	6.64	6.64	6.49
1.0	7.45	6.70	6.69	6.79	6.78	6.63

Table A2.4: Results for pulse-phase modulation reverse operation

Demanded Alpha Ratio (α)	Average Output Current (A)					
	Cyclic-averaging			Spice		Prototype
	Test A	Test B	Test C	Test B	Test C	
0.096	0.05	0.05	0.05	0.04	0.04	0.05
0.202	0.22	0.20	0.20	0.19	0.19	0.18
0.298	0.43	0.40	0.40	0.38	0.38	0.35
0.404	0.69	0.64	0.64	0.63	0.63	0.57
0.5	0.90	0.84	0.84	0.84	0.84	0.78
0.596	1.10	1.03	1.03	1.04	1.04	0.96
0.702	1.32	1.24	1.24	1.26	1.26	1.13
0.798	1.49	1.40	1.40	1.41	1.41	1.25
0.904	1.62	1.52	1.51	1.52	1.52	1.33
1.0	1.65	1.55	1.55	1.55	1.55	1.35

Table A2.5: Measured input voltage SPS tests

Demanded Phase-shift Angle (ϕ)	Input Voltage Forward Mode (V)	Input Voltage Reverse Mode (V)
10.04°	47.96	11.95
20.77°	47.95	11.94
29.42°	47.94	11.93
39.81°	47.92	11.91
50.19°	47.91	11.88
60.58°	47.89	11.86
69.23°	47.87	11.84
79.61°	47.86	11.82
90°	47.87	11.78

Table A2.6: Measured input voltage PPM tests

Demanded Alpha Ratio (α)	Input voltage forward mode (V)	Input voltage reverse mode (V)
0.096	48.00	11.99
0.202	48.00	11.99
0.298	47.99	11.98
0.404	47.98	11.96
0.5	47.97	11.93
0.596	47.94	11.90
0.702	47.92	11.87
0.798	47.90	11.84
0.904	47.88	11.82
1.0	47.87	11.78